APPLICATION OF LASERS IN ATOMIC NUCLEI RESEARCH

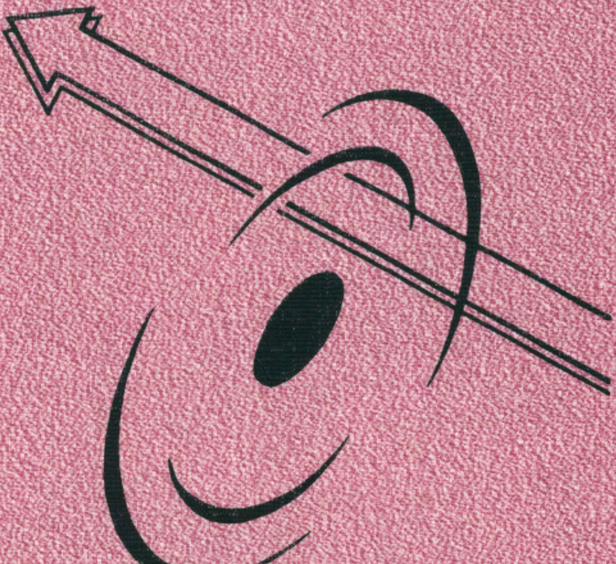

ПРИМЕНЕНИЕ ЛАЗЕРОВ В ИССЛЕДОВАНИИ АТОМНЫХ ЯДЕР

Joint Institute for Nuclear Research

APPLICATION OF LASERS IN ATOMIC NUCLEI RESEARCH

PROSPECTS FOR THE DEVELOPMENT OF LASER METHODS IN THE STUDY OF NUCLEAR MATTER

Proceedings of the V International Workshop

Poznań, Poland, May 28–31, 2001

Dubna 2002

УДК [539.14 : 535.21] (063)
ББК [22.383.4 + 22.344.1] я 431
A67

The contributions are reproduced directly from the originals presented by the Organizing Committee.

Application of Lasers in Atomic Nuclei Research. Prospects for the Development of Laser Methods in the Study of Nuclear Matter: Proceedings of the V International Workshop (Poznan, Poland, May 28–31, 2001) — Dubna: JINR, 2002. — 253 p.
A67
ISBN 5-85165-701-4

The reports are presented given at the V International Workshop «Application of Lasers in Atomic Nuclei Research» (May 28–31, 2001, Poznan, Poland), dedicated to the prospects for laser techniques in research on the properties of nuclear matter. A promising line of that research involves laser spectroscopic experiments on beams of radioactive nuclei. Laser techniques allow the size and shape of nuclei, the nuclear moments, nucleon distributions for ground and isomer states of nuclides to be studied as well as other characteristics to be determined. A number of talks include experimental and theoretical data on nuclear hyperfine interactions and anapole moments; data on atomic clusters are discussed. Some talks on applied techniques for investigating the properties of matter (trace, track and magneto-optical methods, radiotherapy, etc.) are also presented.

Применение лазеров в исследовании атомных ядер. Перспективы развития лазерных методов исследования ядерной материи: Труды V международного рабочего совещания (Познань, Польша, 28–31 мая 2001 г.) — Дубна: ОИЯИ, 2002. — 253 с.
ISBN 5-85165-701-4

В сборнике представлены доклады участников V международного рабочего совещания «Применение лазеров в исследовании атомных ядер» (28–31 мая 2001 г., Познань, Польша), посвященного перспективам развития лазерных методов для изучения свойств ядерной материи. Одним из важных перспективных направлений таких исследований является проведение на основе лазерной спектроскопии экспериментов на пучках радиоактивных ядер. Лазерные методы позволяют определять размеры и форму ядер, ядерные моменты, нуклонные распределения в основном и изомерном состояниях исследуемых нуклидов и другие характеристики. В ряде докладов приводятся экспериментальные и теоретические данные по сверхтонким взаимодействиям и анапольным моментам в атомных ядрах, даны сообщения по атомным кластерам. Представлены также доклады по прикладным методам исследования свойств материи (следовые, трековые и магнитооптические методы, радиотерапия и др.).

УДК [539.14 : 535.21] (063)
ББК [22.383.4 + 22.344.1] я 431
A67

ISBN 5-85165-701-4

PREFACE

In accordance with the plan of the international collaboration between the Flerov Laboratory of Nuclear Reactions (Joint Institute for Nuclear Research, Dubna, Russia) and the Faculty of Physics (Adam Mickiewicz University, Poznan, Poland), the V Workshop on the Application of Lasers in Atomic Nuclei Research was held in Morasco (vicinity of Poznań) on May 28 – 31, 2001. Several different fields of the nuclear structure investigations of radioactive nuclei, using laser radiation, were discussed at the Workshop. The scientific programme of the Workshop covered the following main topics:

- Trends in research of nuclear matter by laser methods
- Laser spectroscopy on beams of fission fragments and radioactive nuclei
- Study of nuclear structure by off- and on-line laser methods
- Charge distribution and nuclear moments
- Hyperfine magnetic anomaly and radii of valence nucleons
- Properties of atoms clusters and nuclei
- Radiotherapy, track and spectrometric methods
- Experimental laser methods and applied research

The programme of the Workshop also included a trip to Warsaw (June 1 – 2, 2001). The participants of the Workshop visited the Laboratory of Heavy Ions of Warsaw University where they have acquainted themselves with the heavy ion cyclotron U-200P and its physical set-ups. The scientific programme and results of investigation with the use of the U-200P were presented.

The working language of the Workshop was English.

Scientists from 7 countries participated in the Workshop, from scientific centers of Prague (Czech Republic), Orsay (France), Darmstadt, Mainz, Marburg (Germany), Warsaw, Poznań, Kielce, Krakov (Poland), Moscow, St. Petersburg, Dubna (Russia), Kristianstad (Sweden), Birmingham, Manchester (UK).

Organizing Committee:

Prof.Z.Blaszczak *(Poznań,Poland)* – **Chairman**
Dr.B.N.Markov *(Dubna, Russia)* – **Scientific Secretary**
Prof.J.Dembczyńsky *(Poznań,Poland)*
Prof.W.Nawrocik *(Poznań,Poland)*
Prof.S.Chojnacki *(Warsaw,Poland)*
Prof.A.Kopystyńska *(Warsaw,Poland)*
Prof.Yu.P.Gangrsky *(Dubna, Russia)*
Prof.Yu.E.Penionzhkevich *(Dubna, Russia)*
Dr.M.Halas *(Poznań,Poland)* – **Secretary**
Dr.I.Iwaszkiewicz-Kostka *(Poznań,Poland)* – **Secretary**

Organizers: Faculty of Physics, Adam Mickiewicz University, Poznań, Poland,
Flerov Laboratory of Nuclear Reactions JINR, Dubna, Russia

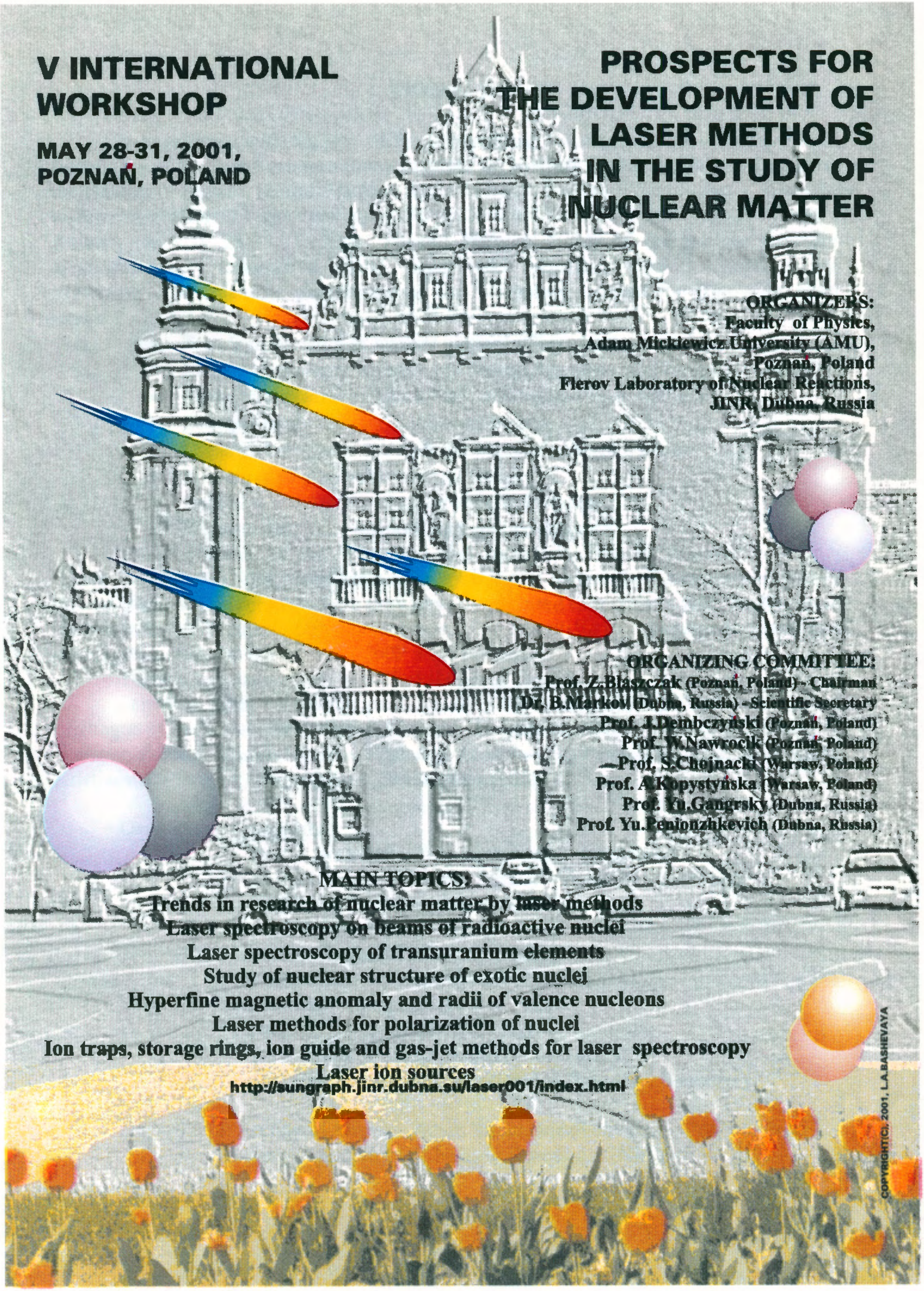

V INTERNATIONAL WORKSHOP

MAY 28-31, 2001,
POZNAŃ, POLAND

PROSPECTS FOR THE DEVELOPMENT OF LASER METHODS IN THE STUDY OF NUCLEAR MATTER

ORGANIZERS:
Faculty of Physics,
Adam Mickiewicz University (AMU),
Poznań, Poland
Flerov Laboratory of Nuclear Reactions,
JINR, Dubna, Russia

ORGANIZING COMMITTEE:
Prof. Z.Blaszczak (Poznań, Poland) - Chairman
Dr. B.Markov (Dubna, Russia) - Scientific Secretary
Prof. J.Dembczyński (Poznań, Poland)
Prof. W.Nawrocik (Poznań, Poland)
Prof. S.Chojnacki (Warsaw, Poland)
Prof. A.Kopystyńska (Warsaw, Poland)
Prof. Yu.Gangrsky (Dubna, Russia)
Prof. Yu.Penionzhkevich (Dubna, Russia)

MAIN TOPICS:
Trends in research of nuclear matter by laser methods
Laser spectroscopy on beams of radioactive nuclei
Laser spectroscopy of transuranium elements
Study of nuclear structure of exotic nuclei
Hyperfine magnetic anomaly and radii of valence nucleons
Laser methods for polarization of nuclei
Ion traps, storage rings, ion guide and gas-jet methods for laser spectroscopy
Laser ion sources

http://sungraph.jinr.dubna.su/laser001/index.html

CONTENTS

WELCOME ADDRESS

Ladies and Gentlemen,

It is my great honour and pleasure to welcome all participants and the guests of our regular Workshop in Poznań. I am doing this not only in my name but also on behalf of the whole Organizing Committee. I am pleased to see among us Professor Yu.P. Gangrsky, a leading expert in the field of laser spectroscopy at the Flerov Laboratory of Nuclear Reactions, JINR (Dubna, Russia), Professor J. Dembczyński, Rector of the Poznań University of Technology, Professor A. Dobek, Dean of the Faculty of Physics and Professor B. Mróz, Director of the Institute of Physics of Adam Mickiewicz University (AMU), Professor H. Hühnermann from the Philippe University (Marburg, Germany), Professor W. Nörtershäuser from GSI (Darmstadt, Germany) and many other distinguished participants and guests who honoured the opening of the Workshop by their presence.

I would like to remind that three years ago we celebrated the 80th anniversary of our University. It has developed from a small college to one of the greatest science and cultural centers.

The Faculty of Physics is one of 11 faculties of our University. Adam Mickiewicz University belongs to the largest Polish universities. More than 2,000 academic teachers teach more than 30,000 students.

The Faculty of Physics consists of three units:

- the Institute of Physics,
- the Institute of Acoustic,
- Astronomical Observatory.

We teach more than 800 students in different specializations:

- experimental and theoretical physics,
- biophysics,
- acoustic,
- astronomy,
- didactics of physics,
- medical physics,
- physics of the Earth and its atmosphere,
- physics and informatics.

Our Institute of Physics consists of 20 departments and laboratories, specializing in both experimental and theoretical research, employs 150 research workers and teachers. In the section of experimental physics the main fields of interest are solid state properties and structure, nonlinear optics, nuclear magnetic resonance (NMR), electron paramagnetic resonance (EPR), molecular biophysics. Theoretical investigations concentrate on the solid state theory including superconductivity phenomena, theory of magnetism, nonlinear optics, surface physics and mathematical physics. We are open to co-operate in all these fields, and we have established many permanent links with some leading universities in quite a few countries.

After this short information about our Faculty of Physics AMU I would like to say a few words of the history of the Poznań Workshop on the Application of Lasers in Atomic Nuclear Research. The idea was born in Dubna, where the first conference took place; the subsequent conferences were organized in Poznań. The people most devotedly engaged in organising the conferences here were: our friends from Dubna Professor Gangrsky and Dr. Markov, and, from our side, Professor Nawrocik and myself. Let me remind you of the titles of these Workshops, shown in the Table. Each time the conference grew in status and in the number of participants from an increasing number of countries. At this conference, which will be the first in the 21st century and in the 3th millennium as well, you will meet over 50 participants from 7 countries.

This fifth Workshop is devoted to prospects for the development of laser methods in the study of nuclear matter. One of these prospects is the experiments on beams of accelerated radioactive nuclei. This is a very interesting field of nuclear physics; now developed in many research centers. The advanced equipment for generation of radioactive beams is or will soon be in operation at many research centers. At the Flerov Laboratory of the Joint Institute for Nuclear Research a project named DRIBs (Dubna Radioactive Ion Beams) has been proposed. The project includes production of two kinds of the exotic radioactive beam – light neutron-rich nuclei and fission fragments. A heavy ion cyclotrons and an electron accelerator-microtron, will be used for this purpose. Several reports concerning this project are to be presented at our Workshop. These reports deal with the obtaining of beam of radioactive nuclei and different experimental methods for their study. The laser spectroscopy method is the most promising for the study of such nuclei. It allows determination of the size and the shape of the nuclei studied and the nucleon configurations of the ground or isomeric states. This is a very important source of information about nucleon interaction in the nuclei far from β-stability. I hope that discussion of the presented reports will be useful in selecting the most suitable techniques and in planning future experiments.

Let me wish you successful and fruitful discussions and many interesting contacts. The weather is beautiful and we hope that it will stay like that throughout case during the whole Workshop, the organizers will also do their best to make sure you will never regret coming here.

Let me officially declare the conference open.

Professor Z. Blaszczak
Chairman of the Organizing Committee

Table

Dubna – Poznań International Workshop

I. **Laser Spectroscopy of Atomic Nuclei**
Dubna, December 18 – 20, 1990

II. **Charge and Nucleon Radii of Exotic Nuclei**
Poznań, Poland, May 29 – 31, 1995

III. **Hyperfine Structure and Nuclear Moments of Exotic Nuclei by Laser Spectroscopy**
Poznań, Poland, February 3 – 5, 1997

IV. **Laser Spectroscopy on Beams of Radioactive Nuclei**
Poznań, Poland, May 24 – 27, 1999

V. **Prospects for the Development of Laser Methods in the Study of Nuclear Matter**
Poznań, Poland, May 28 – 31, 2001

STUDY OF FISSION FRAGMENTS STRUCTURE IN PROJECT DRIBs (Dubna)

Yu.P.Gangrsky, D.V.Karaivanov, K.P.Marinova, B.N.Markov, L.M.Melnikova, G.V.Mishinsky, Yu.E.Penionzhkevich, S.G.Zemlyanoi, V.I.Zhemenik

Joint Institute for Nuclear Research, Dubna, Russia

The prospects of the study of the nuclear structure fission fragments by resonance laser spectroscopy methods are discussed. Research in this field is currently being carried out as part of the DRIBs Project, which is under development in the Laboratory of Nuclear Reactions JINR. The fission fragments under study are mainly very neutron-rich nuclei near the proton (Z = 50) and neutron (N = 50 and 82) closed shells, the region of strongly deformed nuclei (N > 60 and N > 90) and nuclei with high spin isomeric states. Resonance laser spectroscopy is used successfully in the study of the structure of such nuclei. It allows one to determine a number of nuclear parameters (mean-square charge radius, magnetic dipole and electric quadrupole moments) and to make a conclusion about the collective and singleparticle properties of nuclei.

PECULIARITIES OF FISSION FRAGMENT NUCLEAR STRUCTURE

Fission fragments of heavy nuclei (Z > 90) are neutron-rich isotopes of the elements from Zn (Z = 30) to Nd (Z = 60) with a neutron number of 45 – 90. The location of the fission fragment region on the nuclide chart is shown in Fig.1. The large neutron excess in the fission fragments under study (in some cases there are 10 – 15 more neutrons, than in the nuclei situated in the β-stability valley) could lead to an essential change in their structure and radioactive decay characteristics. The anomal ratio of protons and neutrons in such nuclei reflects on spin-orbit interactions and can lead to another order of nucleon shell filling. This change will manifest itself in the appearance of new magic numbers of protons or neutrons, new regions of deformation, of new islands of isomerism. A striking example of such phenomena is found in light neutron-rich nuclei of ^{31}Na and ^{32}Mg at the magic number N = 20. Contrary to our knowledge about nuclear structure, these nuclei are strongly deformed [1,2]. The same situation could occur in

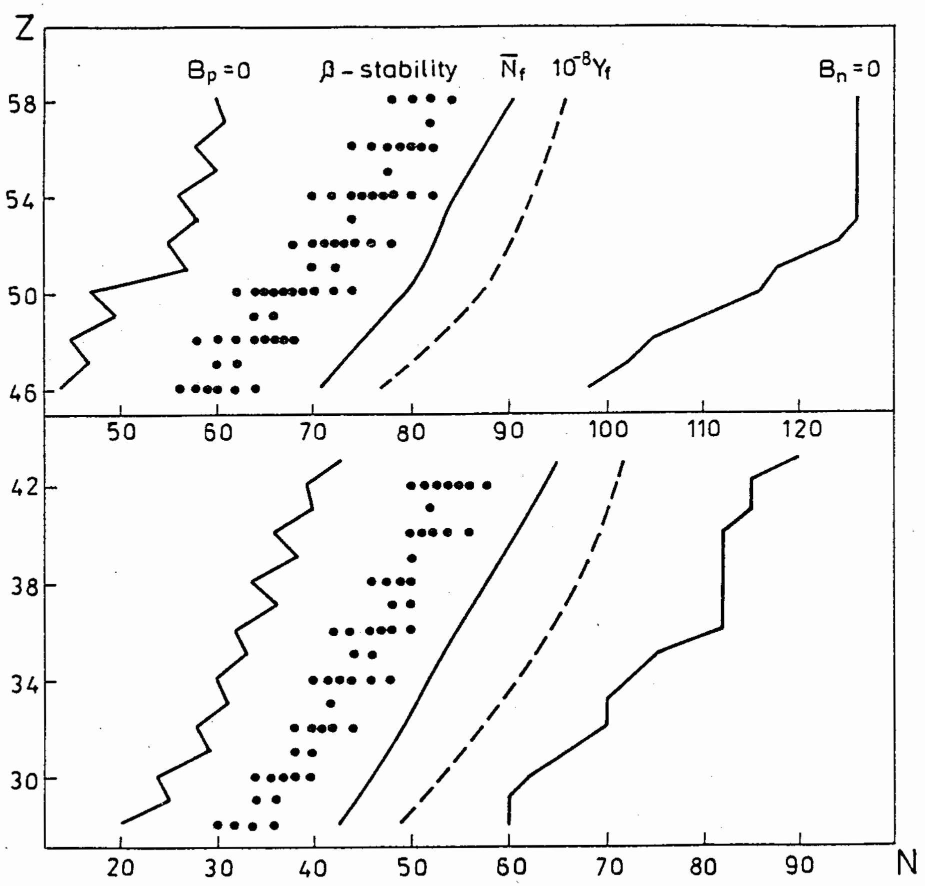

Fig. 1. The part of a nuclide chart that corresponds to the fission fragment atoms. The dots represent stable atoms; the curves show the drip-lines, the average neutron number of the fission fragments and their yield of 10^{-8} per fission event.

the case of very neutron-rich isotopes of Cu and Zn near N = 50 as well as Ag and Cd near N = 82.

It is also possible that there is an unusual change in nuclear structure on the boundary deformation regions. In the between-initial part of the known region at N = 90, the quadrupole deformation parameter increases in a different way for various elements: there is a sharp jump in the β-stability valley (isotopes of Nd, Sm, Eu, Gd) and a smooth growth outside it (neutron-rich isotopes of Ba and neutrondeficient isotopes of Yb [3]). At the same time the octupole deformation parameter decreases in these nuclei. The nuclei on the boundary of another deformation region are studied much less. It is only known that there is a sharp jump in quadrupole deformation at N = 60 in the isotopes from Kr (Z = 36) to Mo (Z = 42). It manifests itsell by the strong change in their charge radii [4] and the reduced probabilities of electric quadrupole transitions [5].

A change in nuclear structure can also occur in the know islands of isomerism (nuclei with N < 50 and N < 82). Highspin levels $g_{9/2}$ and $h_{11/2}$ can be shifted and their decay characteristic will change.

The peculiarity of fission fragment decay is the high energy of the β-decay and low neutron binding energy on the dauther nuclei. $Q_\beta > 5$ MeV and $B_n < 5$ MeV in the primary fragments formed directly in fission. Therefore the wide spectrum of excited levels of different nature is populated in the β^--decay of fission fragments. Neutron emission accompanies γ-radiation in the deexcitation of these levels. About 100 delayed neutron emitters are known up to now [6]. The values of neutron emission probability allow one to get new information about the wave function of excited levels.

The high energy of β-decay can result in the appearance of new, much rarer, modes of radioactive decay. They are emission of a neutron pair or an α-particle after β-decay (β2n or βα). These decay modes are an important source of new information about nuclear structure.

Thus the spectroscopic properties of fission fragments are very various. They are relatively poorly known, and researching them measurement of the nuclear moments, the level spectra, the decay schemes etc.) allows one to establish the way in which nuclear structure changes with the increasing neutron excess. A wide set of experimental devices should be used to obtain this information.

DRIBs PROJECT — DUBNA RADIOACTIVE ION BEAMS

Study of the nuclear structure of fission fragments is one of the main directions of the DRIBs project, being developed in the Flerov Laboratory of Nuclear Reactions,JINR. The aim of this project is the production of intense beams of accelerated radioactive nuclei in a wide range of Z and A – from He to rare-earth elements. Light neutron-rich nuclei (up to Na) will be obtained in the fragmentation of bombarding ions on the 4-meter isochronous cyclotron U-400M, and nuclei of a medium mass number – in the fission of uranium on the electron accelerator microtron MT-25 .

Nuclei chosen for study will be mass-separated and transported to be accelerated in another 4-meter isochronous, cyclotron U-400. A scheme of such an accelerating complex is shown in Fig.2.

Study of reactions induced by neutron-rich or neutron-deficient nuclei essentially enlarges information about their structure. It is impossible to judge some details of this structure from radioactive decay characteristics. A striking example is observation of an unusual wide space distribution of neutrons in some neutron-rich nuclei (neutron halo), first in ^{11}Li and then in others [7]. These data were obtained from measurement of cross-sections for different reactions (fusion, stripping, nucleon exchange) with neutron-rich nuclei. Such multidirection investigation of the properties of nuclei far from the β-stability valley definitely widens our knowledge about the changes in nuclear structure with the growing neutron excess and about the appearing of new phenomena.

Reactions with neutron-rich nuclei can be also used for obtaining more neutron-rich nuclei. Really, the compound-nuclei formed in these reactions contain the neutron excess, and the evaporation of charged particles increases this excess. By this technique it is possible to get the most neutron-rich nuclei and to draw near the boundary of nucleon stability.

THE YIELDS OF FRAGMENTS IN PHOTOFISSION

The success of study of the structure of fission fragments, especially the most neutron-rich fragments, depends to a great degree on their yields. These are determined by their distribution on mass and atomic numbers (A and Z). But there is poor information about these parameters in photofission as compared with neutron fission. Worthy of mention are only investigations performed in Gent (Belgium) [8,9].

The main contribution to the photofission fragment yield is made by the energy range of 10 – 15 MeV (it is the position of the giant dipole resonance in heavy nuclei). This energy range also determines the excitation

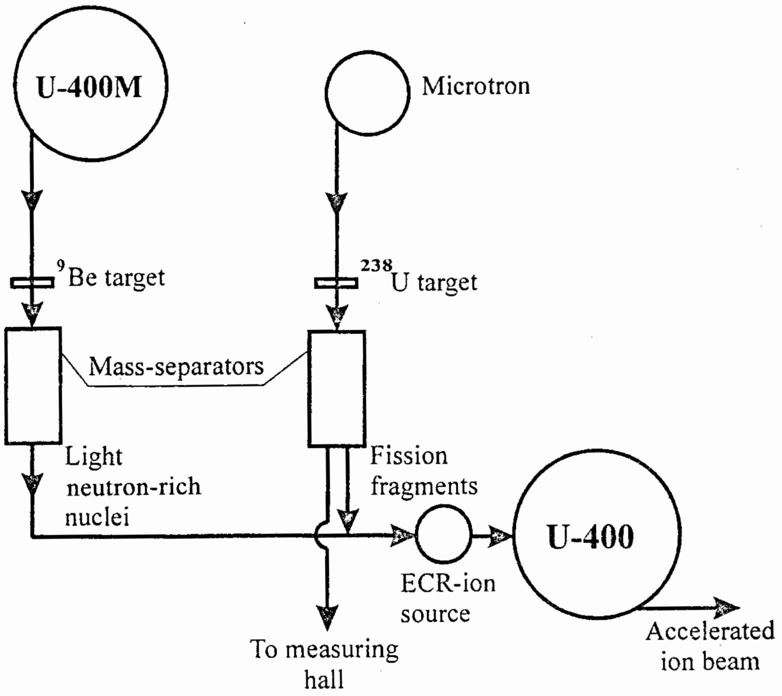

Fig. 2. A block diagram of the complex for accelerating radioactive nuclei (the DRIBs project).

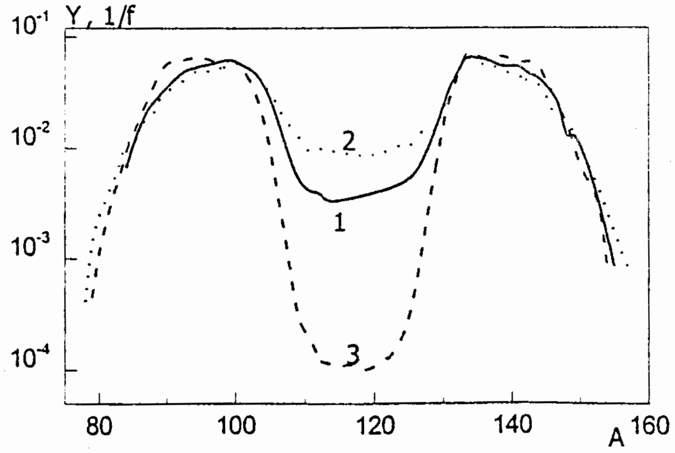

Fig. 3. The fragment mass distributions for the fission of ^{238}U induced: 1, by 15 MeV γ-quanta; 2, by 14.7 MeV neutrons and for the fission of ^{235}U induced by thermal neutrons: 3.

energy of fissioning nuclei. At such excitation energy, the mass spectra of the photofission fragments are asymmetric with the mean mass numbers 99 and 139 for the light and heavy groups of fragments. This spectrum and the analogous ones for neutron fission (thermal and 14.7 MeV neutrons) are presented in Fig.3. It is seen that photofission dependence is intermediate between these neutron fission dependences (the ratio of pike-valley is ~ 100). Each mass number in these spectra corresponds to some set of nuclides with different atomic numbers Z formed in the rupture of fissioning nuclei. The atomic number distribution of these nuclides is described by the Gauss curve with the half-width $\sigma \sim 1.0 - 1.2$. The nuclides formed in one or several β-decay transitions are added to these nuclides.

To get more detailed information about the isotopic yields, we measured the isotopic distributions of Kr and Xe fragments in the photofission of ^{238}U and other heavy nuclei by bremstrahlung with the boundary energy of 25 MeV [10]. The method of transporting fission fragments by a gas flow and stopping in a cryostat with liquid nitrogen was used. The isotopic distributions of Xe fission fragments obtained by this technique are presented in Fig.4 (the same distributions for fission by thermal and 14.7 MeV neutrons are shown for comparison). It is seen that the distributions for the fission by γ-rays and 14.7 MeV neutrons are similar. But an enhanced yield of the most neutron-rich nuclides is observed in photofission as compared with thermal neutron fission, this difference increased with the growing neutron excess.

It is possible to conclude from the presented results that we can use a great body of information about neutron fission for obtaining the isotopic distributions for photofission. By this means the independent and cumulative yields for a number of elements in ^{238}U photofission were calculated (they are presented in Fig.5). It is seen that these isotopic distributions are wide enough; they include up to 10 isotopes which have relative yields of more than 1% as compared with the maximal yield.

Some examples of these yields are presented in the table. They are interesting from the point of view of their nuclear structure (number of protons or neutrons close to the magic numbers, large quadrupole deformation, unusual mode of radioactive decay). We can see that these yields are large enough, and that they allow one to perform successful investigations of such nuclides.

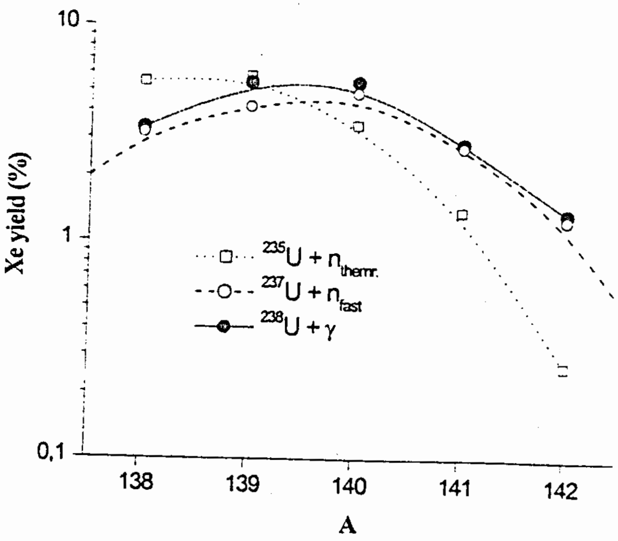

Fig 4. The mass number Xe fragment distributions for the fission of ^{238}U.

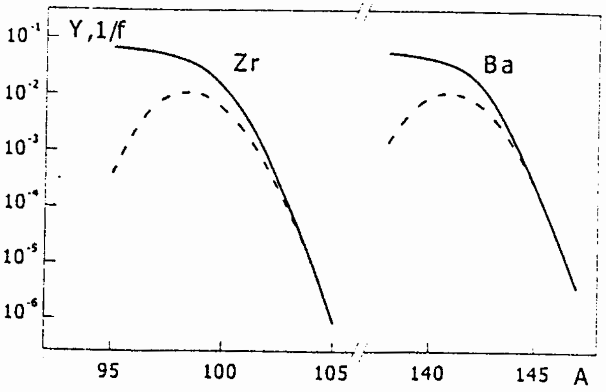

Fig. 5. The cumulative (solid curve) and independent (dashed curve) yields of fragments of Zr and Ba isotopes for the photofission of ^{238}U.

Fission fragment and its peculiarities	Y, 1/f	Y, 1/s (DRIBs)
^{80}Zn – closed neutron shell N=50	10^{-6}	10^{5}
^{81}Ge – closed neutron shell N=50	$3\cdot10^{-5}$	$3\cdot10^{6}$
^{131}In – closed neutron shell N=82	10^{-3}	10^{8}
^{132}Sn – duble magic nuclei Z=50, N=82	$3\cdot10^{-3}$	$3\cdot10^{8}$
^{134}Sn – 2 neutrons over closed shell	$8\cdot10^{-4}$	10^{7}
^{100}Zr – beginning of deformation region	10^{-2}	10^{9}
^{104}Zr – strongly deformed nuclei	$5\cdot10^{-4}$	$5\cdot10^{7}$
^{160}Sm – strongly deformed nuclei	10^{-4}	10^{7}
^{134}Sb – delayed two-neutron emitter	10^{-6}	10^{5}
^{140}J – delayed α-emitter	10^{-5}	10^{6}

Thus photofission reactions of heavy nuclei are a very handy and promising way for the production of intense beams of the most neutron-rich nuclides. The small penetrating power of the γ-rays allows one to use thick targets. But the low excitation energy of the fissioning nuclei and of the fission fragments results in the small values of the evaporated neutrons. This compensates for the phtofission cross-sections being smaller as compared with the cross-sections for fission induced by charged particles and neutrons. Moreover electron accelerators are simpler and much cheaper than charged particle accelerators and atomic reactors.

TRANSPORT AND SEPARATION OF FISSION FRAGMENTS

Fission fragments very far from the β-stability valley and most interesting from the point of view of their nuclear structure are very shortlived as a rule (their half-lives are less than 1 s). The half-lives of the Zr isotope chain (experimental and calculated values [12]) are presented in Fig.6 as an example. It is seen that for the most neutron-rich nuclei the values of $T_{1/2}$ are situated in the millisecond range. Therefore fast and effective transport of fission fragments to measuring devices is necessary for them to be successfully investigated. Although in a number of science centers, are now used spectrometers of unslowed fission fragments (a review of these set-ups is presented in [13]) with a transport time of less than 1 μs for a distance of several metres, their efficiency is very low ($< 10^{-4}$) and able targets are very thin (< 1 mg/cm^2). Therefore their capabilities in study of fission fragment structure are limited and it is necessary to search for other ways.

One of such methods is transport of fission fragments with a gas flow. Fragments that have escaped from the target are slowed down in an inert

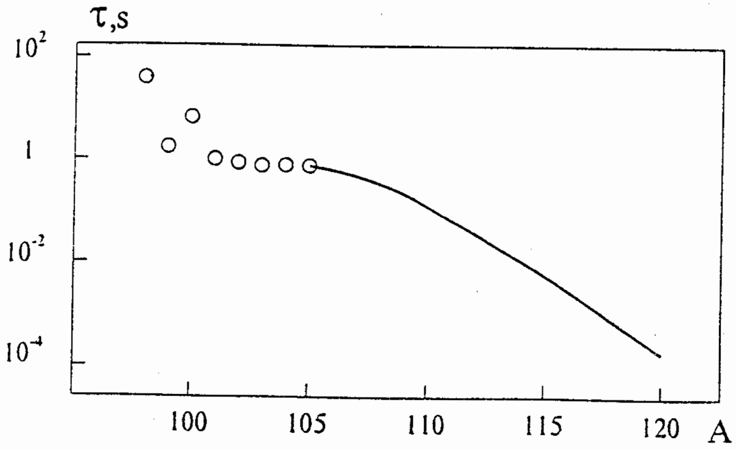

Fig. 6. Lifetimes of the Zr isotope sequence: open circles - experimental, line – theoretical.

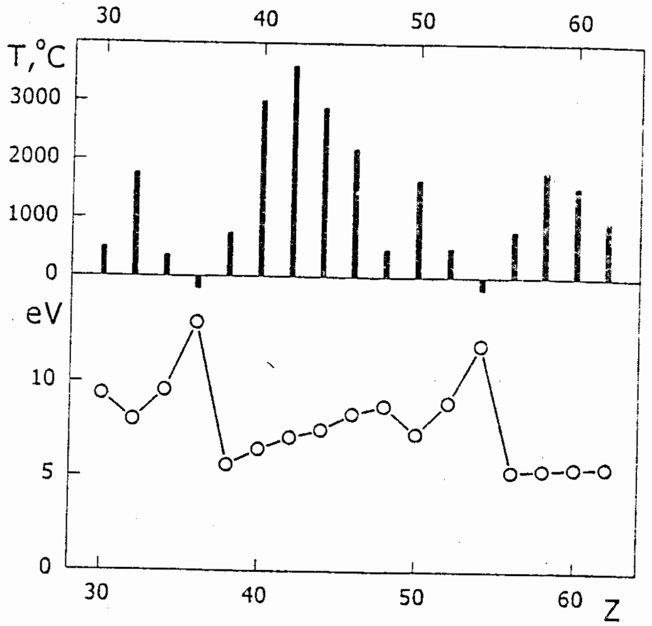

Fig. 7. The temperatures that correspond to a saturated vapour pressure of 100 Pa (above) and the ionisation potentials of the fragment atoms (below).

gas, adsorbed by aerosols and carried through a capillary to the measuring devices. In a set-up of this kind, developed in FLNR,JINR, the transport time is 0.2 s for a distance of 1 m and 3.5 s for a distance of 30 m at the efficiency of up to 70% [14]. The thickness of usable targets corresponds to the range of fission fragments in uranium (~ 10 mg/cm^2). It is much larger than in spectrometers of unslowed fragments, but much smaller than the range of bombarding particles in a substance and their capabilities are not used eintirely.

As is known, a very large number of different nuclides is formed in fission (more than 100 with yields of more than 1% relatively to the number of fission events). Therefore it is necessary to separate the studied nuclides from the other fission fragments, which are elements from 9 periods of the Mendeleev table. Their properties (chemical, thermophysical, electrical), are very various, therefore essentially different methods of separation are required. In some cases it is possible to use this difference in the properties. For example, in the above-mentioned methods of fission fragment transport by a gas flow, Kr and Xe inert gases are stopped in a cryostat, but all the other nuclides – by a filter [10].

The most effective method of fission fragment separation according to their mass number (A) is the use of electromagnetic mass-separators. In on-line experiments, the irradiated target is part of the ion source. This target must be thick enough (up to several tens of grams) to increase the yield of fission fragments. This thickness is much larger than the range of fragments, and they leave the target due to thermal diffusion while the target is heated. The efficiency of the extraction of fragments from the target and the ionization probability are determined by their thermal properties (melting and boiling temperatures, saturated vapour pressure) and by the ionization potential. These parameters for fission fragments are presented in Fig.7. It is seen that in the whole region of elements (Y – Pd) this temperature is higher than 2000°C, and this circumstance makes it difficult for them to be atomized. On the other hand a number of volatite elements (As, Se Br, Sb, Te, J) and the inert gases have very high ionization potential (> 8 eV). This is the reason, why it is impossible to develop a universal ion source which is efficient enough for all fission fragments. Therefore ion sources of various types are used for different groups of elements: surface ionization sources for alkaline, alkaline-earth and rare-earth elements and gas discharge sources for inert gases and for a number of volatile elements. But for the above-mentioned group of refractory elements, an efficient ion source has not been created up to now. In some cases, it is possible to avoid this difficalty, if refractory elements are formed after the β-decay of alkaline or alkaline-earth elements (for example Zr after the β-decay of Rb or Sr). Then the evaporation from the uranium target, ionization, separation and collection of the daughter products are performed.

LASER METHODS IN THE STUDY OF FISSION FRAGMENTS

One of the directions of nuclear structure research is obtaining information about the space distribution of the electric charge and current in nuclei. The radial distribution of these values is determined by mean radii and the azimutal distribution by multiple moments. The high resolution laser resonance spectroscopy methods are used effectively for measurement of these nuclear parameters [15-17]. These methods are based on excitation of electron levels of the atoms and on precise measurement of the energies of these levels. The electron levels of atoms or ions are very sensitive to a number of nuclear parameters. The finite dimension of the nucleus results in a shift of the atomic levels and nuclear moments – their splitting. In the spite of the very small perturbations of level energies (their relative values are less than 10^{-5}) modern optical methods allow successful measurement. These methods are the most efficient when spectoroscopic laser is used. The pecularity of laser methods is that measurement is carried out of the energy of (or the wave-length) laser resonance radiation rather than measuring emitted radiation. The intensity of this radiation is many orders higher, therefore measurement is much more precise. It is possible to observe the appearance of the resonance by a number of signes: a sharp increase in scattered photon intensity, the formation of electron – ion pairs, the occurrence of nuclear radiation anisotropy. The use of tuned lasers characterized by high intensity and very narrow spectral lines allows one to raise the accuracy and especially the sensitivity of measurement as compared with traditional optical methods and to study the nuclei situated on the nucleon drip-line, which are formed with a very low yield. The following examples show the ultimate capabilities of laser spectroscopy methods:

1. The highest sensitivity was reached for spontaneously fissioning isomers of Am – the yield of isomeric nuclei was only 10 1/s [18].
2. The most short-lived nuclide was the isomer ^{87}Rb with a half-live of 10^{-6} s (it was obtained in the β-decay of ^{87}Kr) [19].
3. The highest accuracy was realized in isotopic shift measurement of a hydrogen-deuterium pair 10^{-8} [20].

These examples confirm the efficiency of laser methods in the study of a wide number of nuclei in ground and isomeric states with half-lives up to the nanosecond range.

OPTICAL PROPERTIES OF FISSION FRAGMENTS

The success of laser methods in the study of fission fragments is determined essentially by their optical characteristics. As laser method are based on excitation of atomic levels, the initial state must be the ground stste or a long-lived metastable state. Moreover it is necessary that one of the states (the initial or final state) be sensitive to measured nuclear parameters. In measurement of charge radii this state must contain a large admixture of $s_{1/2}$ or $p_{1/2}$ electron configuration (or in transition, the screening of these electrons by the internal atomic shells must change). In the case of nuclear multipole moments the requirements to atomic level configurations are not so strict. However the orbital moment of level l must correspond to the multipolarity of the measured moment (for instance for the electric quadrupole moment it is necessary that $l \geq 1$).

Measurement of the aboveconsidered nuclear parameters will be the most efficient, if the exciting laser radiation is situated in the visible, nearinfrared or nearultraviolet regions of the spectrum. An analysis of fission fragment optical spectra was performed in our previous paper [21]. It turned out that the elements of the I, II, III, IV and VIII groups of the Mendeleev table satisfy these requirements. They make up largest part of the fission fragment region. In atoms of V, VI and VII groups the transitions convenient for measurement lie at high excitation energies (as a rule more, than 40000 cm^{-1}). But in some of these elements the initial levels of these transitions are metastable and they can be populated at the neutralization of ions. Thus it is possible to conclude that the optical properties of fission fragments allow one to study their nuclear structure by laser spectroscopy in the most interesting regions.

PROSPECTS OF THE STUDY OF FISSION FRAGMENT NUCLEAR STRUCTURE BY LASER METHODS

As it is discussed earlier, measuring nuclear characteristics by laser methods allows one to judge both the singleparticle (spin and magnetic dipole moment) and collective (charge radius, electric quadpupole moment properties of nuclei). These values determine the nucleon configurations of ground and isomeric states, the size and shape of a nucleus; they identify the levels in the scheme of a nuclear model. It is very important to establish how these nuclear properties change with increasing neutron excess and as the neutron drip-line is reached. It is possible to choose the most interesting regions and directions of investigation of fission fragments.

1. The nuclei near closed neutron shells: N = 50 (isotopes of Zn, Ge, Ga) and N = 82 (isotopes of Cd, In, Sn). It is known that the regularity of charge radii changes in the chain of isotopes in the β-stability valley: nuclide with a magic neutron number has the smallest radius (or the most compact shape). But it is known that there is an exception for neutron-rich nuclei of ^{31}Na and ^{32}Mg with N = 20. It is very interesting to find similar exceptions for fission fragments.
2. The nuclei on the boundary of the deformation region with N > 60 (isotopes of Zr, Nb, Mo, Tc). In the known deformation region (N > 90) a change in a nucleus shape is quite different for different atomic numbers. A sharp jump in deformation is observed at N = 60 in nuclei with Z ≤ 40, but it is unclear what will happen in nuclei with Z > 40.
3. Shape isomers in fission fragments. In some nuclei there exist excited states with unusual large quadrupole deformation (the deformation parameter $\beta \geq 0.6$). In nuclei with $Z \geq 92$ these states are isomeric (spontaneously fissioning isomers [23]). In other regions of nuclei, excited rotational bands with quadrupole deformation that is much more than in the ground state (the super- and hyperdeformation [24]) are observed. But the lowest state of these bands has not been observed yet. Probably this state is isomeric with a long enough half-life. It is possible that such states exist in fission fragments (they are predicted in the nuclei around ^{78}Zn and ^{114}Ru). The population of such states, probably, is favored in fission, since fissioning nuclei and formed fragments have very large deformation during and after rupture. The identification of such isomeric states can be based on their very large isomeric shift of the optical lines, measured by laser methods.
4. The difference in the space distribution of electrical charge and nuclear matter. The large excess of neutrons in fission fragments can result in a great difference in proton and neutron radii. Usually this difference is obtained from a comparison of the cross-sections for elastic scattering and charge-exchange reactions induced by studied nuclei. Experiments of this kind are planned to be carried out on beams of accelerated fission fragments in the DRIBs project. But it is possible to get similar information in experiments with laser radiation. The method to be used is based on the Bohr – Weisskopf effect [24] – the influence of nuclear magnetism distribution on the hyperfine splitting of atomic levels. It is known that a magnetic moment is formed by unpaired nucleons. They are neutrons in odd-neutron nuclei.

These examples show the wide field of activity in the study of the neutron-rich nuclei structure, and the DRIBs project is the first step on this way.

The authors would like to thank Alexander von Humbold Foundation, INTAS (grant N 00-00463) and RFFI (grant N 00-02-16674 and N 01-02-97038) for financial support.

References

1. G.Huber, F.Touchard, S.Büttgenbach et. al., Phys. Rev., **C18**(1978)2342.
2. D.Gillemaud-Müeller, C.Detraz, M.Langevin et. al., Nucl. Phys., **A426**(1984)37.
3. Yu.P.Gangrsky, Particles and Nuclei, **23**(1991)1616.
4. F.Buchinger, E.B.Ramsay, E.Arnold et. al., Phys. Rev., **C41**(1990)2883.
5. S.Raman, C.H.Malarkey, W.T.Milner et. al., ADNDT, **36**(1987)1.
6. L.Tomlinson, ADNDT, **12**(1973)179.
7. I.Tanihata, H.Hamagaki, O.Mashimoto et. al., Phys. Rev. Lett., **55**(1985)2676.
8. H.Jacobs, H.Tierens, D. De Frenne et. al., Phys. Rev., **C21**(1980)237.
9. D. De Frenne, H.Tierens, B.Proot et. al., Phys. Rev., **C26**(1982)1356.
10. Yu.P.Gangrsky, S.N.Dmitriev, V.I.Zhemenik et al., Particles and Nuclei Letters, **6**(2000)5.
11. E.A.C.Crouch, ADNDT, **19**(1977)417.
12. M.Hirsh, A.Stauch, H.V.Klapdor-Kleingrothaus, ADNDT, **51**(1992)263.
13. Yu.P.Gangrsky, B.N.Markov, V.P.Pereligin, Detection and Spectroscopy of Fission Fragments, Energatomizdat, Moscow, 1992.
14. Yu.P.Gangrsky, V.P.Dmitriev, V.I.Zhemenik et. al., Preprint JINR, P13-2001-66, 2001, Dubna.
15. E.W.Otten, Treatise on Heavy Ion Science, **8**(1989)517.
16. V.S.Letokhov, V.P.Chebotaev, Nonlinear Highresolution Laser Spectroscopy, Fizmatiz, Moscow, 1990.
17. J.Billowes, P.Campbell, J. Phys. G, **21**(1995)707.
18. H.Backe, M.Hies, H.Kunz et. al., Phys. Rev. Lett., **80**(1998)920.
19. G.Shimkaaveg, W.Quiwers, R.Dasari et. al., Phys. Rev. Lett., **53**(1984)2231.
20. F.Schmidt-Kaler, D.Liebfried, M.W.Weitz, T.W.Hänsch, Phys. Rev. Lett., **70**(1993)2261.
21. Yu.P.Gangrsky, D.V.Karaivanov, K.P.Marinova et. al., Application of Laser in Atomic Nuclei Research, P.46, 1999, Poznan.
22. Yu.P.Gangrsky, S.G.Zemlyanoi, B.Markov et. al., Izvestiya RAN, ser. fiz., **64**(2000)899.
23. H.C.Britt, ADNDT, **12**(1973)407.
24. P.J.Nolan, P.J.Twin, Annu. Nucl. Part. Sci., **38**(1998)533.
25. A.Bohr, V.F. Weisskopf, Phys. Rev., **70**(1950)94.

RECENT RESULTS ON NEUTRON RICH TIN ISOTOPES BY LASER SPECTROSCOPY

B. Roussière[1], L. Cabaret[2], J.E. Crawford[3], S. Essabaa[1], V. Fedoseyev[4], W. Geithner[5], J. Genevey[6], M. Girod[7], G. Huber[5], R. Horn[5], S. Kappertz[5], J. Lassen[5], F. Le Blanc[1], J.K.P. Lee[3], G. Le Scornet[8], J. Lettry[9], V. Mishin[4], R. Neugart[5], J. Obert[1], J. Oms[1], A. Ouchrif[1], S. Péru[7], J. Pinard[2], H. Ravn[9], J. Sauvage[1], D. Verney[1] and the ISOLDE collaboration

1 Institut de Physique Nucléaire, IN2P3-CNRS, 91406 Orsay Cedex, France
2 Laboratoire Aimé Cotton, 91405 Orsay Cedex, France
3 Physics Department, McGill University, H3A2T8 Montréal, Canada
4 Institute of Spectroscopy, Troitsk, Russia
5 Institut für Physik der Universität Mainz, 55099 Mainz, Germany
6 Institut des Sciences Nucléaires, IN2P3-CNRS, 38026 Grenoble Cedex, France
7 Service de Physique et Techniques Nucléaires, DAM-CEA, BP 12, 91680 Bruyères-le-Châtel, France
8 Centre de Spectrométrie Nucléaire et de Spectrométrie de Masse, IN2P3-CNRS, 91405 Orsay Cedex, France
9 EP Division, CERN, 1211 Geneva 23, Switzerland

Abstract

Laser spectroscopy measurements have been performed on neutron rich tin isotopes using the COMPLIS experimental setup. The nuclear charge radii of the even-even isotopes from A = 108 to 132 are compared to the results of macroscopic and microscopic calculations. The improvements and optimizations needed to perform the isotope shift measurement on ^{134}Sn are presented.

1. Introduction

The study of optical transitions through long isotopic chains is a very useful tool to determine the global properties of the ground and isomeric states of nuclei far from stability. It enables the measurement of *i)* the change in the mean square charge radius ($\delta <r_c^2>$) from the isotope shift, and *ii)* the magnetic moment (μ) and the spectroscopic quadrupole moment (Q_S) from the hyperfine structure. This type of measurement requires high resolution laser spectroscopy. For tin isotopes, the atomic transition used has a wavelength of 286.4 nm ($5p^2\ ^3P_0 \rightarrow 5p6s\ ^3P_1$) corresponding to a frequency of 10^6 GHz. For this transition, the isotope shift between two adjacent masses is around 100 MHz [1], which means that the effect we want to measure is of the order of 10^{-7}.

In this paper, we present the first laser spectroscopy results obtained on the neutron rich tin isotopes. First, the motivation for this work will be indicated and second the experimental methods used will be described. Then the charge radii of the even-even tin isotopes will be compared to the results of macroscopic and microscopic theoretical models. Finally the future prospects of this study will be discussed.

2. The physics case

Magic and doubly magic nuclei are of great interest in nuclear physics. The properties of the stable doubly magic nuclei (e.g., binding energy, neutron separation energy, radius) have been widely used to determine the parameters of the effective nuclear interactions used in the mean field calculations. The proton-magic tin isotope series contains the doubly magic nucleus ^{132}Sn which is located far from stability. Thus observables in this nucleus, such as radius, can be used to improve the nuclear effective interaction in order to get better predictions for nuclei far from stability. Since the radii of the stable tin isotopes have been determined from muonic atom experiments [2], the measurement of the isotope shift in tin isotopes gives access to the tin radii, and especially to the radius of ^{132}Sn.

Figure 1 shows the energy of the first excited 2^+ state in the even-even nuclei of some isotopic series near the magic proton number Z = 50, as well as the change in the mean square charge radius already measured. The energy of this 2^+ state indicates if the nucleus is deformed or spherical: one expects a 2^+ state located at high energy in spherical nuclei and at low energy in deformed nuclei. Moreover a nucleus is all the more difficult to deform as its nucleon number is close to closed shells, in this region Z = 50 for protons and N = 50 or 82 for neutrons. For Cd and Te which have two protons less or more than Sn (Z =50), when the neutron number increases up to N = 82, the energy of the 2^+ state first decreases slightly, then is almost constant, and after that increases. In Ba and Xe, for which the proton numbers are farther from Z = 50, the 2^+ energy shows a minimum for the middle of the neutron shell indicating a maximum of the deformation, then its energy increases with N up to N = 82. In the spherical proton-magic tin isotopes, the 2^+ energy is quite constant between N = 52 and 80 and very similar to the values observed

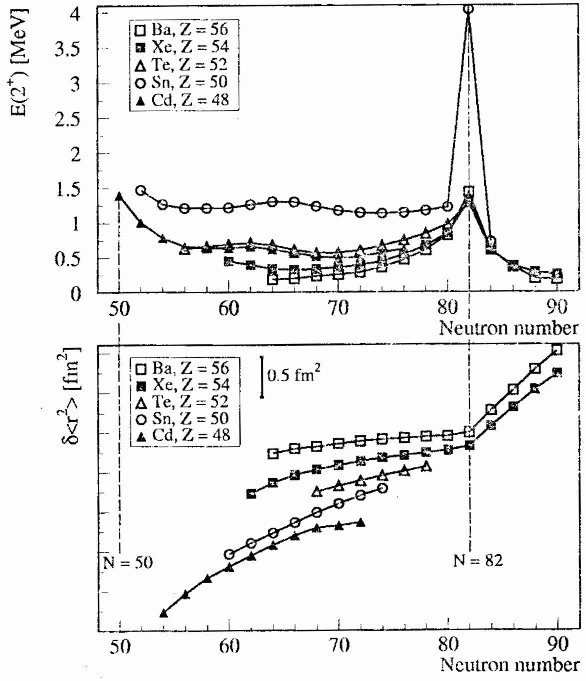

Figure 1: Energy of the first excited 2^+ states and $\delta <r_c^2>$ in some isotopic series near Z = 50.

in the N = 82 magic nuclei of the neighbouring isotopic series. The sharp increase of the 2^+ energy at N = 82 shows the strong stiffness of the doubly magic nucleus ^{132}Sn.
As regards now the behaviour of the $\delta <r_c^2>$ in these isotopic series, one can note that in Ba and Xe, the crossing of the N = 82 closed neutron shell results in a $\delta <r_c^2>$ slope change, indicating that the magic nuclei are spherical and that the deformation is increasing when the neutron number moves away from the N = 82 magic number. Moreover, from Ba to Sn, when Z decreases down to the proton magic number Z = 50, the slope of the $\delta <r_c^2>$ curve increases indicating a decrease of the deformation change. Thus one expects that, in the spherical Sn isotopes, no slope change will occur in the $\delta <r_c^2>$ curve at N = 82. However, as a kink has been observed at N = 128 (neutron closed shell) in the magic Pb nuclei (Z = 82), it remains to be seen whether there is a kink at N = 82 in the proton magic Sn nuclei.

3. Experimental procedure

3.1. Yields of the neutron rich Sn nuclei

The neutron rich tin nuclei have been obtained at ISOLDE by fission reactions, in an uranium carbide target, induced by the 1 GeV proton beam delivered by the CERN-PS-Booster. This target is associated either with the MK5 hot plasma ion source designed for the ionization of low volatility elements or with a laser ion source tuned for tin. Figure 2 shows the very similar tin yields obtained with both types of ion source. It is worth noting that, with the hot plasma source, many other elements are ionized like In, Cd, Sb, Te, I,and Cs, and for instance at A = 132 tin represents only 0.24% of the observed nuclei. With the laser ion source, Cs is also ionized, probably by the surface ionization mechanism. The Cs yields are high: for instance at A = 130, Cs production is 50 times that of tin, and even higher than that observed with the hot plasma ion source. These various isobaric contaminations have to be taken into account to determine which ion source has to be used depending on the setup chosen to perform laser spectroscopy measurements. Indeed three setups are available at ISOLDE: COLLAPS, COMPLIS and the laser ion source. The laser ion source [3] has an excellent efficiency due to its high laser repetition rate (10 kHz); the optical resolution (some GHz) gives elemental selectivity for most elements but it is not high enough to perform isotope shift measurements in the tin nuclei. COLLAPS [4], designed to perform collinear laser spectroscopy on fast atomic beams, has an excellent frequency resolution (~ 65 MHz) but works best with isobar-free beams, which excludes the use of the hot plasma ion source. But even with the laser ion source, the great amount of Cs isobars could give rise to a fluorescent light and thus to a continuous background noise reducing the detector sensitivity. COMPLIS, designed originally for high resolution studies on refractory or daughter elements, was not an obvious choice for experiments on tin. However, it is in fact competitive, since the hot plasma ion source, whose Cs yield is lower than that of the laser ion source, can be used. Up to now, the only experimental data from laser spectroscopy on the neutron rich Sn isotopes have been obtained using COMPLIS.

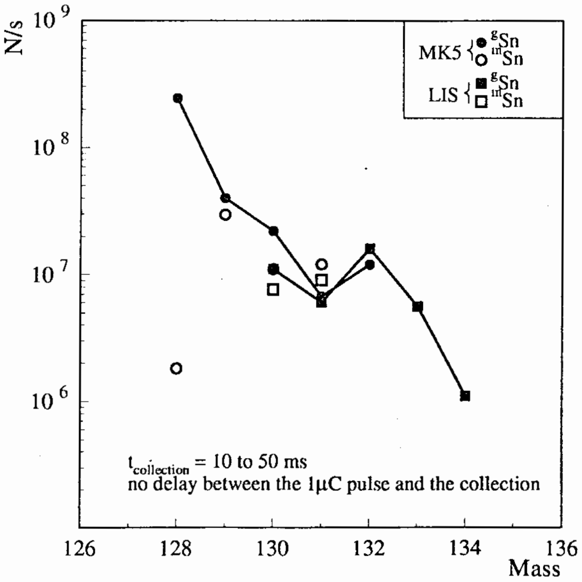

Figure 2: Yields of tin obtained with the hot plasma and laser ion sources.

3.2. Laser spectroscopy measurements

The COMPLIS experimental setup has been described elsewhere in detail [5]. The tin ions delivered at 60 kV by ISOLDE enter the COMPLIS incident beam line, are decelerated to 1 kV and implanted in the first atomic layers of a graphite disk. The collected atoms are desorbed by a pulsed Nd:YAG laser focused beam at 532 nm. Some microseconds later, two synchronized lasers are fired to selectively ionize the tin atoms by two resonant laser excitations into the continuum. Spectroscopic information is obtained by scanning the first laser excitation step at 286.4 nm ($5p^2\ ^3P_0 \rightarrow 5p6s\ ^3P_1$ transition) supplied by a single mode continuously tunable pulsed dye laser [6]. The frequency of this laser is monitored using a Fabry-Perot interferometer, an iodine absorption cell and a lambdameter to have precise relative and absolute frequency calibration. The second excitation is into a broad auto-ionizing level at a wavelength of 410 nm. When the frequency of the first excitation step corresponds to a resonant transition, the tin atoms are excited and ionized. Then the ions are accelerated, deflected to the COMPLIS emergent line by a magnet and finally detected by microchannel plates with a time of flight mass-analysis. The frequency spectrum of the isotope under study is recorded simultaneously with that of a stable or long-lived tin isotope previously collected on the graphite disk and used as a reference for the optical isotope shift determination. The stable tin ions, provided by a stable-beam injector linked to the COMPLIS incident beam line, are also used to determine the optimal conditions for the desorption and ionization before the experiment. The tin isotopes studied in our experiments range from A = 125 up to 132.

3.2.1. The COMPLIS running modes

Two running modes are available with COMPLIS: the collection-desorption mode and the step-by-step mode.
In the collection-desorption mode, the measurement starts by the collection of the isotope under study. During about a quarter of an hour, the ions delivered by ISOLDE are collected on the slowly rotating graphite disk. Then the disk turns back to its initial

position and starts rotating again with the same velocity as during the collection while the Nd:YAG pulses desorb the surface-implanted ions and the frequency scan is performed. Thus there is a waiting time, equal to the collection time, between the collection of the ions and the laser measurement. This running mode is suitable for the long-lived isotopes ($T_{\frac{1}{2}} \gtrsim 5$ m).

In the step-by-step mode, the ion collection is performed at a fixed position of the graphite disk during some ten seconds (one or several PS-Booster macrocycles). Then, in order to optimize the overlap between the collection spot (width ~ 1 mm) and the desorption spot (width $\sim 50\ \mu$m), the disk turns around this position to explore the whole implanted spot during the measurement, i.e., the desorption and the ionization at a given frequency of the excitation step. After the frequency of the excitation step is changed, the cycle collection-measurement is repeated to scan the whole chosen frequency range. This second running mode is used for the short-lived isotopes or those with low yield since it allows the accumulation of the isotopes under study before the laser measurement.

The comparison of the hyperfine spectra obtained using both running modes allows us to distinguish between the hyperfine transitions corresponding to the ground and isomeric states provided their half-lives are different. In the spectrum obtained in the collection-desorption mode shown in fig. 3a, the transitions corresponding to the ground state of ^{125}Sn have high intensity whereas those corresponding to the isomeric state of shorter half-life are weak. On the contrary, in the spectrum obtained in the step-by-step running mode (fig. 3b), all the hyperfine transitions have roughly the same intensity, because in this running mode there is no waiting time between the collection and the measurement, thus the shorter half-life isomer has not yet decayed.

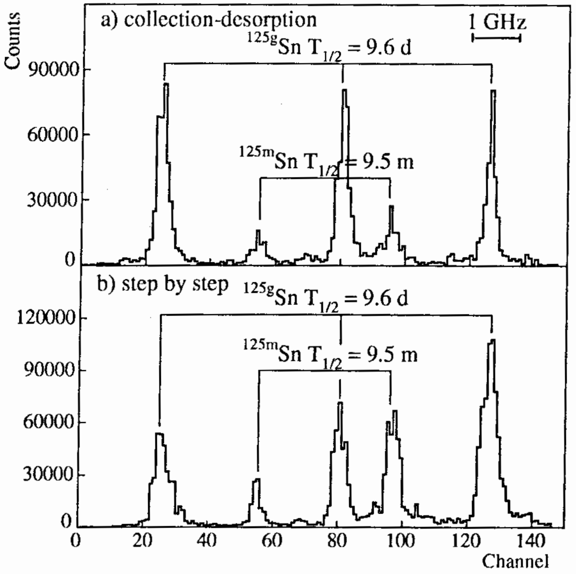

Figure 3: Hyperfine spectra of the two isomers of ^{125}Sn obtained with the collection-desorption (a) and step-by-step (b) running modes.

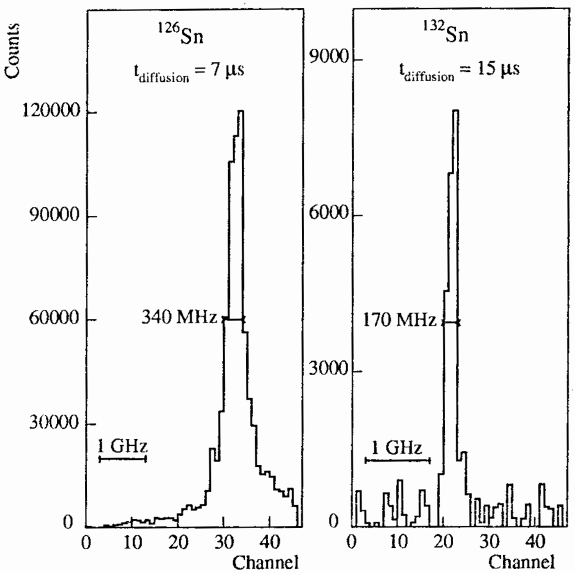

Figure 4: Influence of the diffusion time on the frequency resolution.

3.2.2. The frequency resolution

The frequency resolution obtained with COMPLIS is limited mainly by the Doppler broadening related to the dispersion in the desorbed atom velocity component parallel to the direction of the laser beam used for the excitation step. If we define x, y and z, a system of three orthogonal axes, x being the direction orthogonal to the graphite disk, y the direction of the ionization laser beam and z the direction of the excitation step laser beam, one can show [7] that the frequency resolution can be written as: $\frac{\Delta\nu}{\nu} = \frac{a}{c \times t_d}$, where a is the width of the ionization beam along z, c the speed of light in vacuum and t_d the diffusion time, i.e., the time between the desorption and the ionization.

Figure 4 shows the frequency spectra obtained for ^{126}Sn and ^{132}Sn when the diffusion time was fixed to 7 μs in the first case and to 15 μs in the second case. Increasing the diffusion time by a factor of 2 results in an improvement of the frequency resolution by a factor of 2. It is worth noting that the resolution obtained for ^{132}Sn is the best that we have ever obtained and it is excellent for such a kind of experimental setup. Indeed, we have to make a compromise between resolution and efficiency since, for a given experimental condition defined by a the width of the ionization beam and d the distance along x between the collection disk and the excitation and ionization laser beam crossing, an increase of the diffusion time results in a gain in frequency resolution but also in a loss in efficiency.

4. Experimental results and discussion

The isotope shift contains three contributions: the normal mass shift (NMS), the specific mass shift (SMS) and the field shift (FS). The field shift arises when the transition involves an electron s or $p_{\frac{1}{2}}$, i.e., an electron with a non-vanishing probability to be inside the nucleus. The field shift can be written as : $\Delta\nu_{FS} = F \times \lambda$, with F an electronic

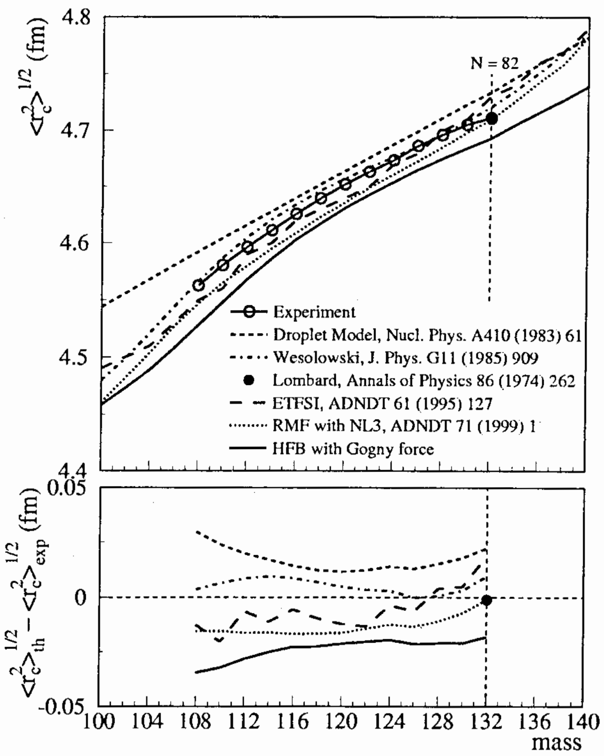

Figure 5: Comparison of the experimental charge radius in tin isotopes with predictions of various models.

factor and λ a nuclear factor related to $\delta <r_c^2>$, $\lambda = K \times \delta <r_c^2>$ [8]. The normal mass shift is easy to calculate, and in order to evaluate the specific mass shift and the F factor, we have made a King plot using the precise results available for the numerous stable tin isotopes : the $\delta\nu^{AA'}$ obtained by laser spectroscopy for the 286.4 nm transition [1] and the $\delta <r_c^2>$ obtained from muonic atom experiments [2]. This analysis led to F = 3.29±0.30 GHz/fm^2 and $\Delta\nu_{SMS}^{AA'} = -2.28\times\Delta\nu_{NMS}^{AA'}$. Moreover, since the muonic atom experiments give access to the nuclear charge radius of the stable tin isotopes, we have extracted from the $\delta <r_c^2>$ measurements the radius of all the neutron rich tin isotopes up to ^{132}Sn.

Figure 5 shows the charge radius of the even-even tin isotopes from A = 108 up to 132. Theoretical values obtained using macroscopic or microscopic approaches are also indicated in this figure. Concerning the macroscopic approaches, the well known spherical droplet model [9] gives radius values systematically higher than the experimental ones. The Wesolowski formula [10] takes into account neutron shell effects related to the neutron occupation number between the N = 50 and N = 82 closed shells. These neutron shell effects give rise to a parabolic behaviour of the radius which is in quite good agreement with the experiment. Concerning now the microscopic calculations, the first value has been given by Beiner and Lombard [11] for ^{132}Sn. It has been obtained in the frame of an extension of the Brueckner formulation of the energy density formalism taking into account shell structure effects. It is in perfect agreement with the experimental value. It would be interesting to extend this calculation to the other tin isotopes in order to know if this excellent theory-experiment agreement is obtained all along the isotopic series. The next microscopic approach is the Extended Thomas Fermi plus Strutinsky Integral (ETFSI) method [12] that is a semi-classical approximation of the Hartree-Fock method using the Skyrme SkSC4 effective interaction and including Strutinsky shell corrections. The agreement with the experimental values is quite good. The values obtained by the relativistic mean-field theory with the NL3 effective interaction [13] are also in good agreement with the experiment. The last theoretical values reported in fig. 5 have been obtained by the Hartree-Fock Bogolyubov static calculations using the Gogny force; in this case, the calculated radii are systematically below the experimental values, the general trend, however, is quite well reproduced. One can wonder whether this systematic difference between the theoretical and experimental $<r_c^2>$ values is reduced when dynamic calculations are performed.

The differences between these various theoretical values and the experimental charge radii are also reported in fig. 5. In all cases, they are smaller than 0.8%. It is worth noting that the microscopic approaches give a theory-experiment agreement as good as the macroscopic approaches. However, the behaviour of the charge radius beyond A = 132 remains an open question.

5. Future prospects

5.1. Measurements beyond ^{132}Sn

Improvements and optimization of the COMPLIS setup are needed and under way for isotope shift measurement beyond ^{132}Sn. For example, the ^{134}Sn yield is ~ 10^6 atoms/s, the Cs isotopes are ~ 100 times more produced and the half-life of ^{134}Sn is very short ($T_{\frac{1}{2}}$ = 1.1 s). Under these conditions, no accumulation of ^{134}Sn is possible and the step-by-step running mode cannot be used. Therefore the laser measurement has to be performed simultaneously with the collection. This requires a maximum overlap between the collection spot and the YAG desorption spot. The present overlap is poor since the widths of the collection and YAG desorption spots are ~ 1 mm and ~ 50 μm, respectively. To increase this overlap, we plan to use a multiple slit transmission grating, placed near the lens focusing the desorption laser beam, in order to diffract this laser beam and obtain several desorption spots on the focal plane. The first test has been done using slits of 0.3 mm width at 1.4 mm intervals, giving five desorption spots of approximately equal intensity in the collection zone. Figure 6 shows two hyperfine spectra recorded, for ^{131}Sn, with and without the slits. One can note that with the slits, the statistics is better indicating that the efficiency has been improved, with slight loss in frequency resolution due to the increased desorption zone increasing the Doppler broadening.

The other major improvement that we want to bring to the COMPLIS setup is to add a pulsed high voltage deflector in the emergent line in order to prevent the ions having a mass around A = 130 and created in the desorption process (and thus some 10 μs before the ions under study) to reach the detector. We hope, in that way, to improve the detector efficiency for the ions of interest, to reduce the parasitic noise and to obtain an improved transmission in the COMPLIS emergent beam line.

5.2. The hyperfine spectra of the odd tin isotopes

The hyperfine spectra of the odd tin isotopes exhibit only five lines instead of the six

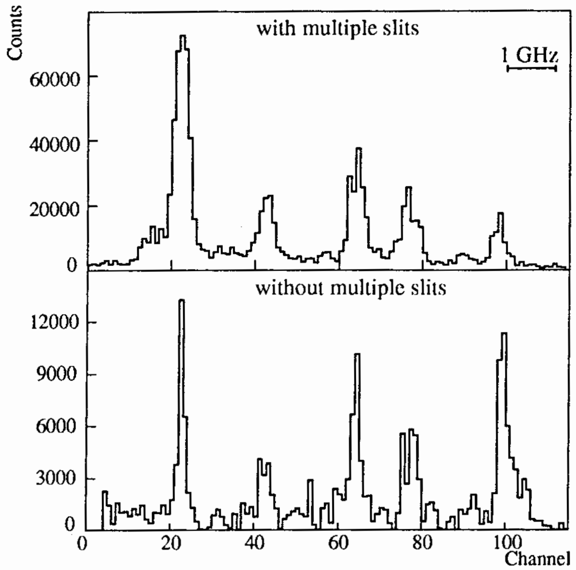

Figure 6: Hyperfine spectra of ^{131}Sn.

expected from both spin values $I^\pi = \frac{11}{2}^-$ and $\frac{3}{2}^+$ attributed to the ground and isomeric states (see figs. 3 and 6). Either one of the hyperfine transition corresponding to the isomeric state is merged into a transition belonging to the ground state, or the spin of one of these states is not $\frac{3}{2}$ but $\frac{1}{2}$ giving rise to two hyperfine transitions only. The analysis of the spectra is in progress and at the moment seems to confirm the first hypothesis. Direct experimental answers could be obtained by either performing measurements with COLLAPS which has an excellent frequency resolution and thus could separate the mixed resonant transitions, or using SIINODE (Séparation Isomérique et Isobarique des NOyaux DEscendants) which is an upgrading, presently under construction, to use COMPLIS as an isomeric separator.

The chamber located at the end of the COMPLIS emergent line and containing the microchannel plate detector will be replaced by a set of chambers that allows either the detection of the ions with a microchannel plate detector or, when removed, the collection of the ions on a tape. This tape can be moved in front of a Ge detector to perform γ-spectroscopy measurements. Using SIINODE for the odd tin isotopes, we will set the excitation step laser to a frequency corresponding to a given resonant transition and we will be able to attribute firmly this hyperfine transition to one of the ground or isomeric states or to both states, depending on the emitted γ-rays observed.

References

[1] M. Anselment *et al.*, Phys. Rev. **C34**, 1052 (1986).
[2] C. Piller *et al.*, Phys. Rev. **C42**, 182 (1990).
[3] J. Lettry *et al.*, Rev. Sci. Instr. **69**, 761 (1998).
[4] R. Neugart, Inst. Phys. Conf. Ser. **132**, 133 (1992).
[5] J. Sauvage *et al.*, Hyperfine Interactions **129**, 303 (2000).
[6] J. Pinard and S. Liberman, Opt. Comm. **20**, 334 (1977).

[7] J. Pinard *et al.*, Proceedings of the 3rd International Workshop on Hyperfine Structure and Nuclear Moments of Exotic Nuclei by Laser Spectroscopy, Poznań, Poland, February 3-5, 1997.
[8] G. Torbhom *et al.*, Phys. Rev. **A31**, 2038 (1985).
[9] W.D. Myers and K.H. Schmidt, Nucl. Phys. **A410**, 61 (1983).
[10] E. Wesołowski, J. Phys. **G11**, 909 (1985).
[11] M. Beiner and R.J. Lombard, Annals of Physics **86**, 262 (1974).
[12] Y. Aboussir *et al.*, Atomic Data and Nuclear Data Tables **61**, 127 (1995).
[13] G.A. Lalazissis *et al.*, Atomic Data and Nuclear Data Tables **71**, 1 (1999).

PREPARATION OF THE CHARGE RADII MEASUREMENTS OF ^{8,9,11}Li

W.Nörtershäuser, A. Dax, H. Wang, R. Kirchner, H.-J. Kluge, T. Kühl
GSI Darmstadt, Germany

I. Tannihata, M. Wakasugi
RIKEN, Saitama, Japan

C. Zimmermann
University of Tübingen, Germany

INTRODUCTION

The investigation of the so-called "halo nuclei", *e.g.*, ^{11}Li, ^{6}He has become a hot topic in nuclear physics since the discovery by Tannihata *et al.* [1]. However, the correlation between proton and neutron distributions in these exotic nuclei is still an open question, since nuclear collision studies are mainly sensitive to the matter distributions and do not allow a model-independent determination of charge radii. On the other hand, on-line laser spectroscopic measurements of hyperfine structure and isotope shifts have long been used to investigate charge radii of stable and unstable isotopes [2]. Combined with recent progress in the atomic theory of lithium [3], such a measurement will allow a model-independent determination of the charge radius of ^{8,9,11}Li. Therefore we prepare a precise measurement of isotope shifts for stable and short-lived isotopes of lithium at GSI in Darmstadt (Germany). Due to the low production rates of these exotic atoms (~ 10^4/s for ^{11}Li) a very sensitive technique must be developed that still allows an accurate determination of the differences in transition energies (relative accuracy ~10^{-5}). Resonance Ionization Spectroscopy (RIS) with cw-lasers has been used for the efficient detection of short-lived isotopes [4, 5] for many years and was found to be the most promising technique for our purpose. Results of test experiments in order to find the best excitation and ionization scheme were presented previously, together with a determination of the release efficiency for an on-line source of thermal lithium atoms [6]. In this report, we will give a short summary of the experimental approach and then focus on recent progress in the preparation of the laser-stabilization system and the characterization of the quadrupole mass spectrometer that will be used to detect the ions created by the laser resonance ionization process.

THEORY

The isotope shift (IS) in an optical transition can be divided into two parts: the mass shift (MS), caused by the difference in nuclear mass between the isotopes, and the field shift (FS), which has its origin in the change of the distribution of electrical charge inside the finite sized nucleus. The FS is directly related to the difference in the root-mean-square (rms) charge radius between two isotopes having masses *A* and *A'*:

$$\Delta E_{\mathrm{FS}} = -\frac{2\pi}{3} Ze^2 \, \Delta|\psi(0)|^2 \, \delta\langle r^2\rangle^{AA'},$$

where $\Delta|\psi(0)|^2$ is the change of electron charge density at the nucleus between lower and upper state of the optical transition. A determination of the field shift can thus provide accurate values for the rms charge radius. However, the mass- and field shift contributions to the isotope shift cannot be separated easily, therefore additional information from muonic atoms and electron scattering is usually combined with optical isotope shift data to extract charge radii [7]. If it is possible, however, to calculate the mass shift in a transition to a sufficiently high accuracy, the field shift can be directly extracted without any additional information. But mass shift evaluations are difficult since electron-electron correlations must be included and many-body problems are hard to attack. It has nevertheless been used to determine rms charge radii for ^{3}He and ^{6}Li from ^{3}He-^{4}He and ^{6}Li^{+}- ^{7}Li^{+} isotope shift measurements [8].

Table 1. Calculated mass shifts in the 2 ^2S - 2 ^2P transition of lithium [3]. All values in MHz

^{7}Li - ^{6}Li	^{8}Li - ^{6}Li	^{9}Li - ^{6}Li	^{11}Li - ^{6}Li
11453.07 (6)	20088.23 (10)	26785.18 (13)	36555.34 (21)

Recent advances in high-precision variational calculations for lithium and lithiumlike ions using multiple basis sets in Hylleraas coordinates [9], allowed mass-shift calculations for the 2*S*-3*S* and 2*S*-2*P* transitions in Li with an accuracy of approximately 200 kHz [3]. Yan and Drake provided a formula for the nuclear charge radius of any Li isotopes as a function of the measured isotope shift between the isotope ^{A}Li and ^{6}Li:

$$R^2_{\mathrm{rms}}\left({}^{A}\mathrm{Li}\right) = R^2_{\mathrm{rms}}\left({}^{6}\mathrm{Li}\right) + \frac{E^A_{\mathrm{meas}} - E^A_0}{C},$$

where E^A_{meas} is the measured isotope shift and E^A_0 contains all calculated contributions to the isotope shift except for the nuclear size contribution. The calculated mass shifts E^A_0 for all lithium isotopes are listed in Table 1 and the constant *C* for the 2s-3s transition was calculated to be $C = -1.5661$ MHz/fm^2.

EXPERIMENTAL

The lithium isotopes of interest have lifetimes of 838 (6) ms (^{8}Li), 178.3 (4) ms (^{9}Li), and 8.59 (14) ms (^{11}Li), respectively, thus IS measurements can only be performed on-line. It is planned to produce ^{8,9}Li in a ^{12}C (^{12}C , X) ^{8,9}Li reaction at the GSI UNILAC accelerator and ^{11}Li at ISOLDE/CERN, where 1 GeV protons induce spallation and fragmentation inside a tantalum target. In both cases the Li ions produced are released from the hot target, accelerated to 60 keV and mass separated in a sector magnet. Ion yields of approximately 10^5/s (^{8,9}Li,GSI) and 10^4/s (^{11}Li,CERN) are available. Ions are implanted into a graphite catcher foil (~ 80 µg/mm^2), where they recombine with electrons. The catcher foil is heated by a CO_2 laser beam to release the Li atoms with thermal velocities. Laser beams for resonance ionization are located close to the graphite surface to ensure a good overlap with the released atomic ensemble.

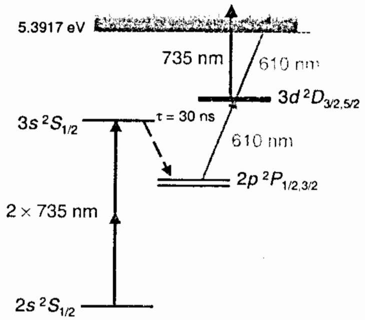

Figure 1. Excitation scheme for the resonance ionization of lithium

The excitation scheme for resonance ionization is shown in Fig. 1. After excitation to the 3*S* state in a two-photon transition, the atom undergoes spontaneous emission into the 2*P* state and is subsequently ionized through the 3*D* levels. The double-resonance four-photon ionization pathway has the following advantages:

- the 2*S*-3S two-photon excitation provides efficient excitation independent of the Doppler shift.
- the ionization step is decoupled from the 2*S*-3*S* transition, where high accuracy is needed, and the ionization step – ionization directly out of the 3*S* state would cause AC Stark shift and broadening and thus reduce accuracy.
- resonance enhancement for the ionization due to the intermediate 3*D* states, the 2*P*-3*D* transition is the strongest transition in lithium and can easily be saturated, thus, providing high efficiency for the ionization.

This ionization scheme was tested previously [6] and narrow lines with a FWHM of ~ 7 MHz were observed. Resonance ionization with single-ion detection was compared to fluorescence detection and was found to be ~ 20 times more efficient and to provide a higher signal to noise ratio even at moderate laser powers for the ionization step.

In Fig. 2 the experimental setup for the laser system (left) and resonance ionization mass spectrometry (right) is shown. The atoms released from the graphite catcher transverse the laser beams and the laser-ionized particles are collected with the ion optics of a commercial quadrupole mass spectrometer, mass analyzed and detected with a conversion dynode electron multiplier (CDEM).

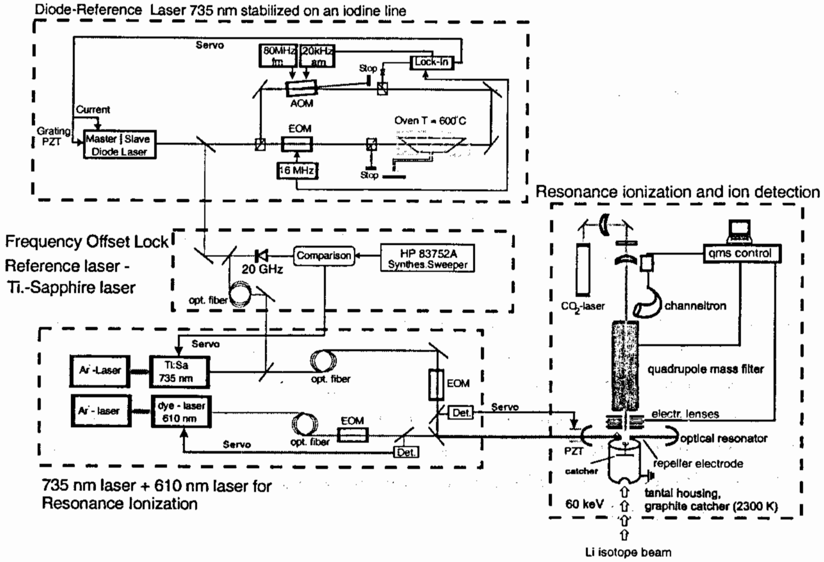

Figure 2. Experimental setup for the resonance ionization of lithium

Resonant laser radiation is provided by a titanium-sapphire laser (Ti:Sa) (735 nm) and a dye laser (610 nm), which are both pumped by argon-ion lasers. To obtain intensities that are sufficient to saturate the two-photon resonance transition and to provide high ionization efficiency, an optical resonator is mounted into the vacuum system around the interaction region. The cavity must provide resonance enhancement for both laser beams at the same time. Thus, the cavity length is locked to the frequency of the Ti:Sa laser, while the dye laser frequency, which is less critical due to strong saturation broadening in the 2*P*-3*D* transition, is locked to the optical resonator.

Accurate frequency tuning and stabilization is obtained by frequency-offset-locking of the Ti:Sa to a master-slave diode-laser system, which is locked to an molecular-iodine transition to provide a reliable frequency reference point for consecutive measurements. To realize this frequency-offset locking, the iodine transition frequency must be close to half the resonance frequencies for all lithium isotopes of interest. The difference should be less than ~ 20 GHz in order to allow counting of the beat signal between the diode laser and the Ti:Sa beam by means of a standard radiofrequency counter. A hot-band transition at 13603.22 cm^{-1} fulfills this criteria, but the hyperfine spectrum and saturation intensities of this line have not been investigated previously.

RESULTS

Due to the low production rates for the short-lived ^{11}Li isotope an overall detection efficiency of ~ 10^{-4} is required. The overall efficiency can be divided into the following parts: ion-to-atom-conversion efficiency of the graphite catcher, geometrical overlap between the atomic and laser beams, resonance ionization efficiency, transmission through the QMS and detection efficiency of the CDEM. The estimated or measured efficiencies for the different processes are listed in Tab. 2. The conversion efficiency in the graphite catcher as a function of temperature has been measured in previous experiments [6], and the geometrical overlap was calculated assuming a cosine-square distribution for the atomic beam and a 0.5 mm diameter laser beam spot in a distance of 1.5 mm. The ionization efficiency was estimated to be the product of an excitation efficiency to the 3*S* state of 20% (calculated on a basis of perturbation theory and verified experimentally), ionization efficiency of 3%, and a signal reduction of 65% due to the hyperfine splitting of the ground- and excited state. The product of the given efficiencies is slightly larger than 10^{-4} and should thus be sufficient to obtain an on-resonance count rate of ~1 Hz. The dark count rate of the CDEM was measured to be ~ 15 mHz and is thus considerably smaller than the expected signal rate.

Table 2. Expected efficiencies for processes involved in the ^{11}Li isotope shift measurement

release efficiency of the catcher	20 %
overlap with laser beams	20 %
excitation and ionization efficiency	0.5 %
quadrupole mass filter transmission	90 %
CDEM detector efficiency	80 %
overall detection efficiency	~10^{-4}

The QMS works as an additional mass filter for background suppression of ions that are either created in the ionization region by processes other than resonance ionization or have enough energy to penetrate into the ionization region. Peak shapes for the stable lithium isotopes have been recorded using a surface ionization ion source and are shown in Fig. 3 on a logarithmic scale. Due to the nearly flat-topped peaks, the transmission through the QMS is almost independent on the exact mass setting within a range of ~ 0.4 amu, but to the higher-mass side the signal drops sharply by more than 7 orders of magnitude. On the rising side the profiles are not as steep and exhibit a dip, which is caused by non-linear resonances [10] and leads to a kind of precursor peak. However, 0.5 amu below the mass of interest the signal intensity has decreased by a factor of ~10^7 and background contributions to the lithium signal should be small.

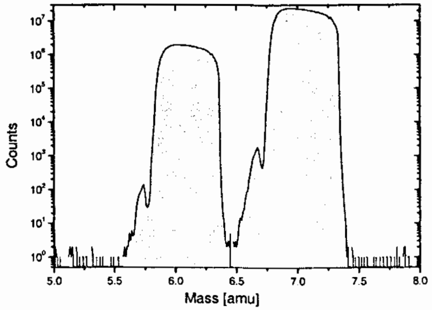

Figure 3. QMS mass spectrum of ^{6,7}Li ions produced by surface ionization

To obtain the isotope shift values with the required accuracy, an appropriate frequency reference point must be chosen for the frequency-offset locking of the resonance lasers to provide a relocking accuracy of better than a few 10 kHz. We performed FM-saturation spectroscopy on the iodine transition at 13603.22 cm^{-1} to test whether it could be used to obtain a saturation spectroscopy signal appropriate for laser-locking within the required accuracy. The experimental setup was similar to that shown in the rectangle on Fig. 2, marked as "Diode reference laser 735 nm" with the main difference that we used a Ti:Sa laser to obtain the saturation signal. The iodine cell was heated to ~ 600°C to provide sufficient population of the lower level of the hot-band transition. A saturation signal recorded with laser powers of 20 mW in the pump and 1 mW in the probe beam (Ø 1 mm, FWHM) is shown in Fig. 4. Three groups of unresolved and three single hyperfine lines were observed. The strongest isolated line (a_1) is well separated from all others and will be used for locking the diode laser. Signal-to-noise ratios of about 600 were achieved for this line and it shows a peak-to-peak distance of ~ 10 MHz, thus an accuracy of about 20 kHz for locking to the reference point can be expected.

The signal intensity of the chosen reference line was measured as a function of laser power in the pump beam. Saturation was clearly observed and a saturation intensity of 20 mW/mm^2 has been calculated. Such intensities should be available with the diode-laser master-slave system, which will be used as the reference laser for frequency offset locking.

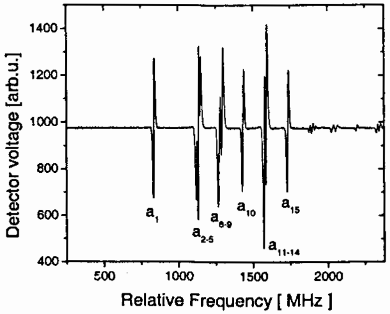

Figure 4. Hyperfine spectrum of the iodine $B0_u^+ \rightarrow X^1\Sigma_g^+ R(114)2\text{-}11$ transition at 600°C

SUMMARY AND OUTLOOK

The experimental setup for isotope shift measurements of ^{8,9,11}Li is in progress. The vacuum chamber has been assembled and the QMS was characterized in terms of mass peak shape and detector dark count rate. Saturation spectroscopy of the hot-band iodine transition chosen as a frequency reference point was performed and its suitability for frequency locking of the reference laser was demonstrated. After set-up of the enhancement cavity, which is underway, and all necessary frequency-locking electronics, we will first test the whole setup in off-line measurements with the stable isotopes ^{6,7}Li. Afterwards ^{8,9}Li measurements are planned at GSI, before transporting the whole setup to CERN to finally perform the measurements on ^{11}Li.

ACKNOWLEDGMENT

This work is supported by BMBF contract No. 06TU886/TP3

REFERENCES

1. Tanihata, I., et al., *Measurements of interaction cross sections and nuclear radii in the light p-shell region.* Physical Review Letters, 1985. **55**: p. 2676-2679.
2. Otten, E.W., *Nuclear radii and moments of unstable isotopes*, in *Treatise on heavy-ion science*, D.A. Bromley, Editor. 1989. p. 517-638.
3. Yan, Z.-C. and G.W.F. Drake, *Lithium isotope shifts as a measure of nuclear size.* Physical Review A, 2000. **61**: p. 022504.
4. Wendt, K., et al., *Recent developments in and applications of resonance ionization mass spectrometry.* Fresenius Journal of Analytical Chemistry, 1999. **364**: p. 471-477.
5. Bushaw, B.A., *High-resolution laser-induced ionization spectroscopy.* Prog. Analyt. Spectrosc., 1989. **12**: p. 247-276.
6. Schmitt, F., et al., *Towards the determination of the charge radius of ^{11}Li by laser spectroscopy.* Hyperfine Interactions, 2000. **127**: p. 111-115.
7. Fricke, G., et al., *Nuclear ground state charge radii from electromagnetic interactions.* Atomic Data Nuclear Data Tables, 1995. **60**: p. 177-285.
8. Riis, E., et al., *Lamb shifts and hyperfine structure in $^6Li^+$ and $^7Li^+$: Theory and experiment.* Physical Review A, 1994. **49**: p. 207-220.
9. Drake, G.W.F. and Z.-C. Yan, *Energies and relativistic corrections for the Rydberg states of helium: Variational results and asymptotic analysis.* Physical Review A, 1992. **46**: p. 2378–2409.
10. Blaum, K., et al., *Peak shape for a quadrupole mass spectrometer: comparison of computer simulation and experiment.* International Journal of Mass Spectrometry, 2000. **202**: p. 81-89.

MEASUREMENTS OF CHARGE RADII AND ELECTROMAGNETIC MOMENTS OF NUCLEI FAR FROM STABILITY BY PHOTOIONIZATION SPECTROSCOPY IN A LASER ION SOURCE

M.D. Seliverstov, A.E. Barzakh, D.V. Fedorov, V.N. Panteleev and Yu.M. Volkov

St. Petersburg Nuclear Physics Institute, 188350, Gatchina, Leningrad district, Russia

E-mail: mseliver@rec03.pnpi.spb.ru

The study of nuclei far from stability requires high sensitivity of the experimental technique. The method of Resonance Ionization Spectroscopy in a Laser Ion Source (RIS/LIS) enables one to carry out measurements of isotope shifts and hyperfine splittings for isotopes at the production rate about 10^3 atoms per second. The sensitivity of the method is determined by the high efficiency of the laser ion source and the low background of the detection system afforded by α-particle registration. The isotope shifts and hyperfine structures of ^{153,155}Yb, ^{154}Tm (I=9 and I=2) and ^{153}Tm (I=11/2) have been measured and isotopic changes of mean square charge radii and nuclear electromagnetic moments have been determined.

The further development of this experimental method – enhanced Target-Ion Source system aimed to suppress thermionic background – widens considerably the range of the applicability of the RIS/LIS method.

1. Introduction

During the last decades many nuclei far from stability have been investigated using laser based spectroscopic techniques. The study of atomic isotope shifts and hyperfine structures provides evaluation of nuclear spins, electromagnetic moments and changes in the mean square charge radii $\delta\langle r^2\rangle$. Investigations of long isotopic chains require highly sensitive experimental technique in view of a short lifetime and a small production rate of the isotopes far from the β-stability line.

At the IRIS mass-separator at the PNPI synchrocyclotron investigations of long isotopic chains of the rare-earth elements have previously been performed using resonance photoionization spectroscopy in an atomic beam [1,2]. This experimental technique enables successful experiments with the isotopes at a production rate down to 10^4 atoms per second. To extend the investigations to the more neutron deficient isotopes (first of all to the region of neutron deficient Yb and Tm isotopes near magic neutron number N = 82) photoionization spectroscopy in a laser ion source has been applied at the IRIS facility.

In this region a deviation from the established systematic behaviour of the isotope shift for the Yb isotopes with N = 82 - 84 has been recently reported [3]. The measurements indicate that the charge radii of Yb isotopes, between N = 82 and N = 84, increase far more rapidly than those observed in the other isotopic chains in this region. A strong deformation jump at N = 84 (^{154}Yb) was supposed to cause this surprising effect. It is of interest to measure the isotope shifts and hyperfine structures of the adjacent odd isotopes, ^{153,155}Yb, in order to estimate the deformation value of the Yb isotopes with N = 82 – 86. Similarly, it is of importance to investigate the isotopes of the neighbouring element with the same neutron number, i.e., thulium (Z = 69).

2. Experimental method

In this work we have used one of the most promising methods for on-line study of radioactive nuclides – photoionization spectroscopy in a laser ion source [4]. This method is based on the application of the laser ion source technique to the study of isotope shifts and hyperfine structures.

Atoms are ionized by step-by-step resonant laser excitation to autoionizing states. The following ionization schemes were used:

– for Yb atoms:

$$6s^2\,{}^1S_0 \xrightarrow{555.6\text{ nm}} 6s6p\,{}^3P_1 \xrightarrow{581.1\text{ nm}} 4f^{13}({}^2F_{7/2})6s^26p_{3/2} \xrightarrow{581.1\text{ nm}} \textit{autoionizing state (or continuum)},$$

– for Tm atoms:

$$4f^{13}6s^2\,{}^2F_0 \xrightarrow{597.1\text{ nm}} 4f^{13}6s6p\,(7/2,0)_{7/2} \xrightarrow{600.3\text{ nm}} 4f^{13}5d6s \xrightarrow{552.4\text{ nm}} \textit{autoionizing state.}$$

The experimental set-up is presented in fig. 1. Nuclides under study were produced in the tantalum target (12 g/cm^2) of the mass-separator by spallation reactions induced by 1 GeV protons. The atoms were thermally released from the target to the ionizer tube (1.5 – 2.5 mm in diameter, 60 mm in length) made of Nb or W, where they were ionized by the beams of three pulsed dye lasers merged into a single beam and directed into the tube. The dye lasers (of average power ~300 mW) were pumped by three copper vapour lasers at a repetition rate of 9 kHz. The frequencies of the dye lasers were tuned to the resonance transitions of the chosen excitation scheme. The radiation frequency of the two broadband lasers (bandwidth 30 GHz) were fixed on the second and the third step frequencies. In the experiments with ^{153}Yb the radiation of the broadband laser (used at the second and third steps of excitation) was amplified in a dye cell amplifier pumped by copper vapour laser. Average power of the laser+amplifier system was 900 mW. The wavelength of the narrow band laser (bandwidth 1 GHz) was scanned through the first transition frequency. On resonance,the photoion current in the mass-separator collector increases. Thus, the experimental spectra represent the dependence of ion current on the scanned laser frequency.

The high efficiency of the method provided by following factors. Multiple intersection of the laser beam by the atoms in the laser ion source cavity considerably increases the probability of photoionization. At the same time electron emission from the heated tube wall creates an electric potential near the wall, which traps photoions near the central axis and prevents their recombination on the wall surface. The electric field created by the heating DC drives photoions towards the extraction electrode of the mass-separator.

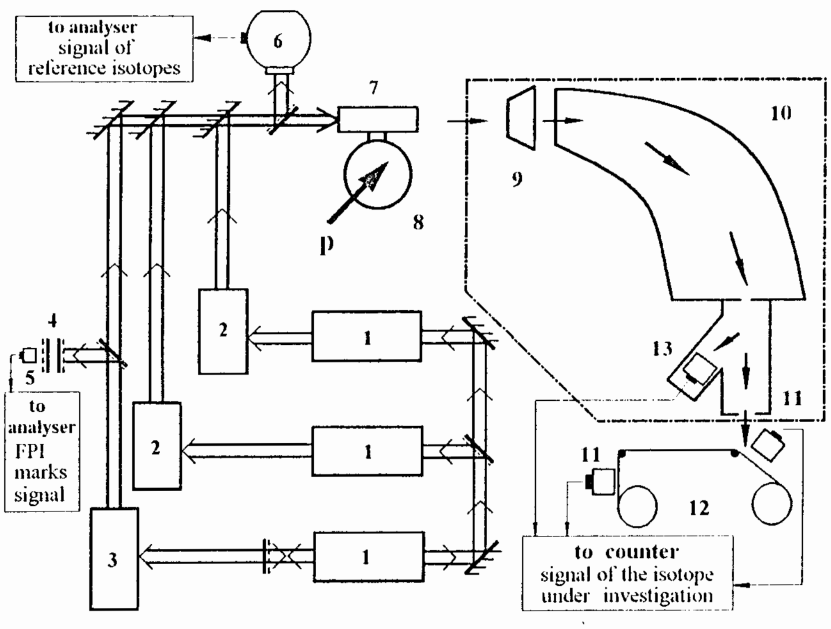

Fig. 1. Experimental setup

1 – Cu-vapour lasers; 2 –broadband dye laser; 3 – narrowband scanning dye laser; 4 – Fabry-Perot interferometer; 5 – photodiode; 6 – reference chamber; 7 – laser ion source; 8 – target; 9 – extraction electrode; 10 – mass-separator; 11 – α-detector, 12 – tape-driving device; 13 – channel electron multiplier.

A portion of the scanning laser radiation was directed to the Fabry-Perot interferometer (free spectral range 5 GHz) to produce the frequency marks for frequency scale calibration. Another part of the laser beam was used in a reference chamber to provide a reference spectrum from the sample of stable isotopes. Two modes of photoion detection have been used:

(1) direct registration of the ion current by the channel electron multiplier (when selectivity was high enough), and

(2) registration of the α-particles from the decay of the isotopes under investigation.

The photoionization efficiency in the laser ion source may reach some tens of percent [5]. The main obstacle for the successful spectroscopic measurements is high background ion current. Background ions are produced by the surface ionization inside the ion source and the target as well. If the production rate of isobars is significantly higher than that of isotope under study, the background ion current can make the direct ion counting by the electron multiplier impossible. In such case an isotope selective method of registration is required and this can, for example, be achieved with the counting of characteristic α-decays.

In our experiments a high temperature target ($T \geq 2500°C$) has been used in order to increase production yield of short-lived isotopes. In this case the main contribution to background comes from the target itself. In order to extend the applicability of the RIS/LIS technique a new method of isobar suppression has been developed [6] and applied. In this method,suppression is provided by the locking of the background thermoions inside the high temperature target by a potential of the heating direct current flowing through the target container. The background current was reduced by a factor of 20 using this technique. The application of this method of background suppression has provided an opportunity to perform measurements of isotope shifts and hyperfine structures for radioactive Tm isotopes when isobaric Yb and Ho contamination is severe.

3. Experimental results

In isotope shift measurements with $^{158-163}$Tm and $^{158-164}$Yb, photoions were detected with the channel electron multiplier. The experimental spectra obtained in this experiments are shown in Fig. 2 and Fig. 3. The measured IS are presented in Table 1 and Table 2 and compared with reference data. In the experiments with ^{153,155,156}Yb and ^{153,154}Tm, an isotope selective photoion detection by registration of the α-particles from the decay of the isotopes under study was applied. In case of ^{153}Yb, the registration of the α-particles from the decay of its daughter nucleus (^{153}Tm) was applied.

The experimental spectra obtained in this experiments are shown in Fig. 4 and. Fig. 5. The measured values of the isotope shifts and the hyperfine structure constants and the corresponding values of $\delta\langle r^2\rangle$ (calculated with an electronic factor $F = 11.9$ GHz/fm^2 and mass shift constant $M = 296$ GHz [7]), μ, and Q_S, are given in table 3. The measured value of isotope shift of ^{156}Yb ($\Delta\nu_{174,156} = 17610(120)$ MHz) is in agreement with that measured by Sprouse *et al.*[7] ($\Delta\nu_{174,156} =$ 17514(21) MHz)).

The total ionization efficiency calculated as the ratio of the experimentally observed ion beam intensity and calculated production rate of ^{156}Yb is about 10%. Correspondingly the production rate of ^{153}Yb can be estimated as (2 3)$\cdot 10^3$ atoms per second.

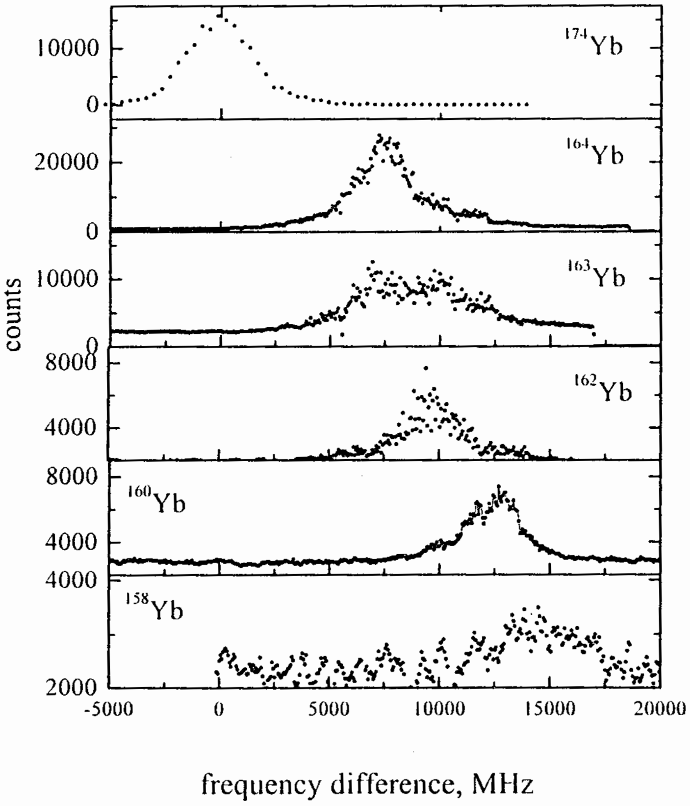

Fig. 2. Experimental spectra of $^{158\text{-}164}$Yb.

Table 1: Isotope shifts of Yb isotopes, measured with the direct registration of the ion current by the electron multiplier

Isotope	**$\Delta\nu_{174,A}$, MHz**	**$\Delta\nu^{ref}_{174,A}$, MHz [8]**
^{166}Yb	5327(100)	5290(4)
^{164}Yb	7368(100)	7331(6)
^{162}Yb	9703(100)	9710(8)
^{160}Yb	12278(100)	12257(10)

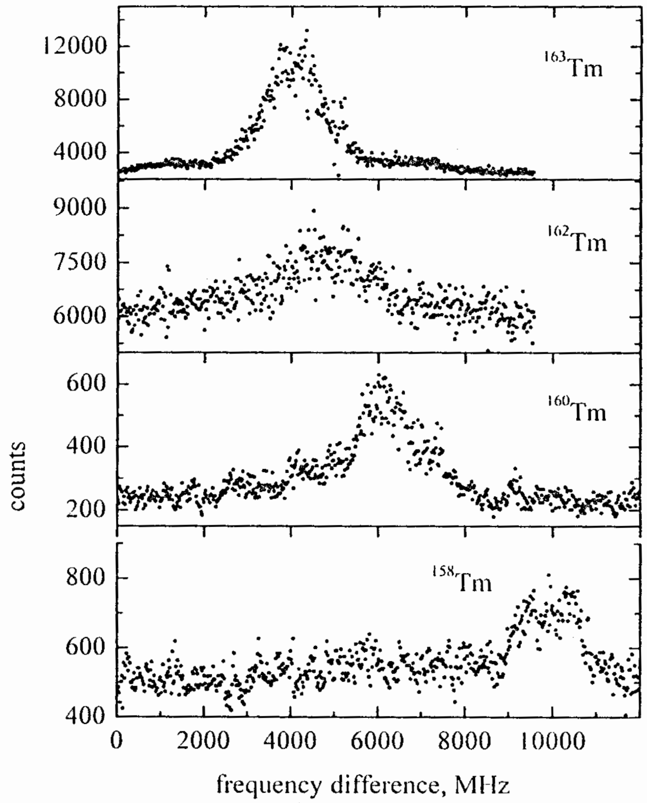

Fig. 3. Experimental spectra of $^{158\text{-}163}$Tm.

Table 2: Isotope shifts of Tm isotopes, measured with the direct registration of the ion current by the electron multiplier

Isotope	**$\Delta\nu_{169,A}$**	**$\Delta\nu^{ref}_{169,A}$, [9]**
^{163}Tm	4140(80)	4101(20)
^{162}Tm	5425(100)	5460(50)
^{160}Tm	7590(190)	7538(40)
^{158}Tm	10145(180)	10205(80)

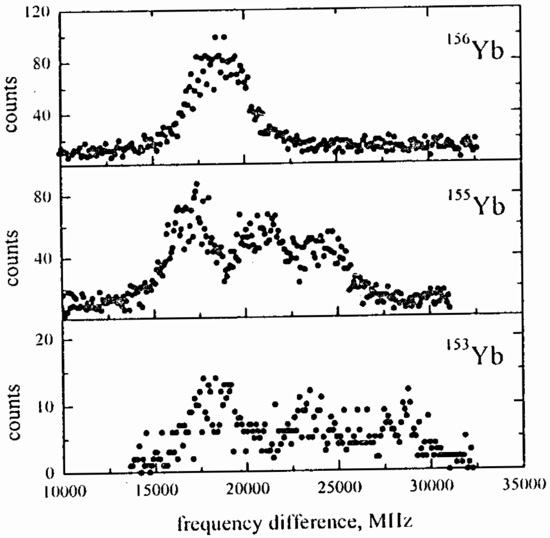

Fig. 4. Experimental spectra of ^{153,155,156}Yb

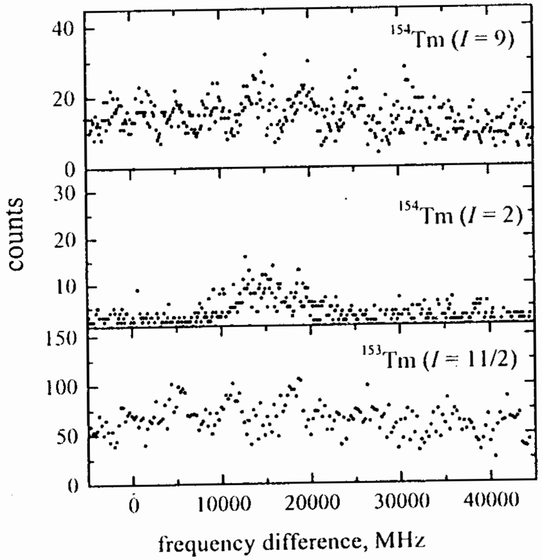

Fig. 5. Experimental spectra of ^{153,154}Tm

Table 3: Ground state characteristics of ^{153}Yb, ^{155}Yb, ^{153}Tm (I=11/2), ^{154}Tm (I=2) and ^{154}Tm (I=9).

Isotope	$\delta\nu_{174,A}$, **MHz**	A, **MHz**	B, **MHz**	$\delta\langle r^2\rangle_{174,A}$, **fm^2**	μ, **n.m.**	Q_S, **b**
^{155}Yb	19115(80)	-1050(25)	160(80)	–1.623(8)	-0.913(22)	-0.5(3)
^{153}Yb	21695(150)	-1210(30)	490(20)	–1.843(12)	-1.052(25)	-1.5(6)

Isotope	$\delta\nu_{169,A}$, **MHz**	A, **MHz**	B, **MHz**	$\delta\langle r^2\rangle_{169,A}$, **fm^2**	μ, **n.m.**	Q_S, **b**
$^{154,I=9}$Tm.	15520(150)	532(3)	200(500)	–1.522(15)	5.91(5)	-0.2(4)
$^{154,I=2}$Tm	15150(200)	-460(10)	-600(1200)	–1.486(19)	-1.14(2)	0.4(9)
$^{153\ I=11/2}$Tm	16470(320)	1020(16)	-700(1300)	–1.615(31)	6.93(11)	0.5(10)

The errors shown in Table 3 are purely experimental. Systematic uncertainty for $\delta\langle r^2\rangle$ is determined by the uncertainty in the semiempirical calculation of the F and M values. It is supposed to be about 5% [10].

The data for the Tm isotopes can be compared with the analogous data for the Ho isotopes with the same neutron numbers and spins [10]. The magnetic moments of the Tm isotopes are very close to corresponding single particle values and practically coincide with the magnetic moments of the isotonic isotopes with the same spin: $\mu_{sp}(11/2)$ = 6.9 n.m., $\mu(^{151}$Ho, I = 11/2) = 6.93(2) n.m., $\mu(^{152}$Ho, I = 9) = 5.92(2) n.m., $\mu(^{152}$Ho, I=2) = –1.02(2) n.m. The slope for the isotopic dependency of $\delta\langle r^2\rangle$ is very close to the corresponding values for Ho and Er. Thus the characteristics of the Tm isotopes with N = 84 – 86 do not noticeably deviate from the systematic trends in this region of the nuclide chart.

The isotopic changes of mean square charge radii for Yb isotopes with N = 82 – 86 are presented in Fig. 6. Corresponding data [10] for Dy (Z = 66) and Sm (Z = 62) isotopes are also shown for comparison. The IS data for $^{152-154}$Yb point to the inverse odd-even staggering effect (see Fig. 6). Usually this effect corresponds to the development of static octupole deformation (Ra, Fr isotopes [10]). In the case of near magic Yb isotopes the similar description seems to be doubtful. The small negative values of the spectroscopic quadrupole moment of ^{153,155}Yb make also doubtful the explanation of the unusual $\delta\langle r^2\rangle$ behaviour by static quadrupole deformation.

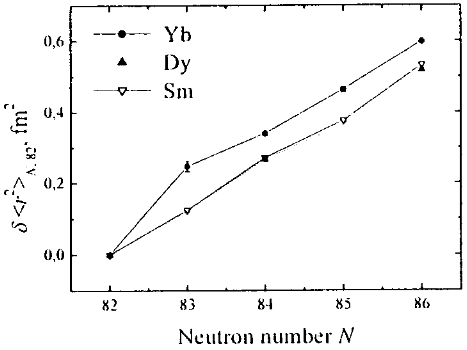

Fig. 6. Change in mean square charge radii of Yb, Dy and Sm isotopes relative to $N = 82$.

4. Conclusion and outlook

The on-line experiments with neutron deficient Yb and Tm isotopes have shown a high sensitivity of the method of resonant photoionization in a laser ion source. The further development of this experimental method – enhanced Target-Ion Source system aimed to suppress thermionic background – essentially widens the range of the applicability of the RIS/LIS method. Application of the other modes of registration, for example, by X-ray or γ-detection enables the further extension of the region of applicability of this method of laser spectroscopy.

5. Reference

1. G.D. Alkhazov et al., *Pis'ma Zh. Teor. Fiz.* **37** (1983) 231
2. V.S. Letokhov et al., *J.Phys.G.* **18** (1992) 1177
3. G.D. Sprouse et al., *Phys. Rev. Lett.* **63** (1989) 1463
4. G.D. Alkhazov et al., *Nucl. Instr. Meth.* **B69** (1992) 517
5 A.E. Barzakh et al., *Nucl. Instr. Meth.* **B126** (1997) 85
6. V.N. Panteleev et al., *Hyp. Int.* **127** (2000) 421
7. G.D. Sprouse et al., *Hyp. Int.* **59** (1990) 91
8. F. Buchinger et al, *Nucl. Instr. Meth* **202** (1982) 159.
9. G.D. Alkhazov et al., *Nucl. Phys.* **A477** (1988) 37
10. E.W. Otten, in *Treatise on heavy-ion science*, Vol. 8, ed. D.A. Bromley, (Plenum, New York, 1989)

PROSPECTS WITH COOLED AND BUNCHED BEAMS AT THE JYFL LASER-IGISOL FACILITY

P. Campbell[a], A. Nieminen[b], J. Billowes[a], P. Dendooven[b],
K.T. Flanagan[a], D.H. Forest[c], J.A.R. Griffith[c], J. Huikari[b],
A. Jokinen[b], I.D. Moore[a], R. Moore[a], H.L. Thayer[c], G. Tungate[c],
S.G. Zemlyanoi[a,d] and J. Äystö[b]

[a]Schuster Laboratory, University of Manchester, Manchester M13 9PL, England
[b]Accelerator Laboratory, University of Jyväskylä, Jyväskylä SF–403 51, Finland
[c]Department of Physics and Space Research, University of Birmingham, Birmingham B15 2TT, England
[d]Flerov Laboratory of Nuclear Reactions, JINR, 141980 Dubna, Moscow Region, Russia

Abstract

A new RFQ ion-beam cooler and buncher, installed in the mass-separated beamline of the ion guide isotope separator, IGISOL, JYFL, has dramatically increased the scope and efficiency of collinear laser spectroscopy at the JYFL facility. In this paper we review the new prospects, aside from standard collinear spectroscopy, that are now also provided by the device. In particular, new opportunities for on-line stable isotope production, collinear resonance ionisation spectroscopy and the spectroscopy of ultra-low lying isomers are discussed.

Introduction

The laser spectroscopic station at the JYFL IGISOL (ion guide isotope separator) has now been enhanced by the addition of an on-line ion-beam cooler [1]. When used in a continuous mode, access to low emittance, low energy spread ion beams can be achieved irrespective of the original beam properties and, importantly, without compromising the short release time (~ 1 ms) of the IGISOL production platform. The improvement in the ion beam properties alone greatly enhances the prospects for on-line laser spectroscopy at the facility [2]. The device however also permits the temporary trapping (~ 200ms) and bunching of radioactive ions; allows energy selection windows to be placed on the original beam; and opens a variety of non-fluorescence based spectroscopic techniques.

New measurements of the nuclear structural changes in the Ti, Zr and Hf isotope chains have been made using the device in an ion-bunching mode. The results of these investigations appear elsewhere in these proceedings [3]. In this contribution the new prospects offered by the cooler, and the results of initial investigations, are presented.

1 The JYFL cooler

The JYFL cooler consists of two gas-filled radiofrequency quadrupoles (RFQ) mounted on a differentially pumped, high voltage platform. The platform voltage of the cooler is precisely maintained at a level 100 - 200 V beneath the IGISOL accelerating voltage. Beams entering the device are focussed into a large gas-filled quadrupole as they decelerate and a high proportion, ~ 80%, are captured onto contained trajectories. Within the RFQ the buffer gas acts to damp the radial motion and the ions are cooled onto the axis of the device. A weak axial field (~ 10 V/m) guides the ions along the axis of the quadrupole and the cooled ensemble is injected into a miniature, low pressure, RFQ at the end of the device. Extraction and re-acceleration of ions from the low-pressure miniature quadrupole can be achieved without the re-introduction of a large energy spread in the ensemble. A switchable voltage on the mounting plate of the miniature quadrupole allows the entire cooler to be operated as a linear Paul trap and injected ions can be cooled and collected before being moved into the miniature RFQ (see next section).

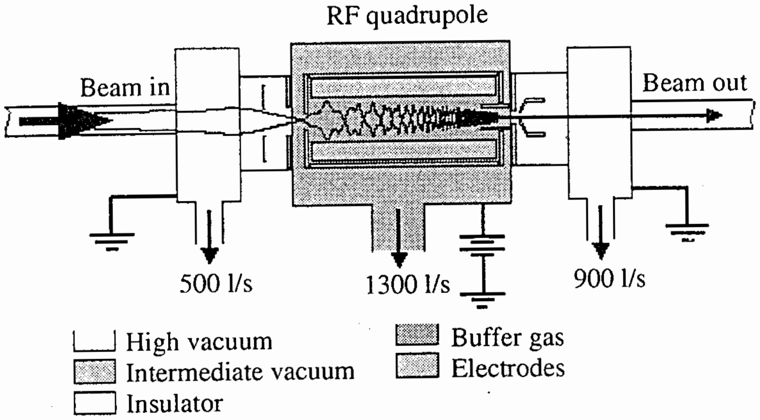

Figure 1: The JYFL beam cooler.

The action of the gas-filled RFQs provide an efficient, on-line, improvement of the emittance of IGISOL-produced ion beams and the compression of the space and phase-space occupied by the beam greatly improves the efficiency of collinear laser spectroscopy [1, 2]. The device is especially valuable at IGISOL facilities where substantial beam energy spreads (~ 100 eV) are encountered at standard separator conditions. Figure 1 shows a schematic of the JYFL cooler.

2 Bunched-beam spectroscopy

Efficient ion beam bunching can, for sufficiently long-lived species, enable collinear ion laser beam spectroscopy to be performed with an experimental sensitivity that compares to, or exceeds, all present forms of fast beam spectroscopy [3]. The technique, at the IGISOL, has been realised by applying a switchable axial containment field to the cooler (in order to form a temporary trapping potential in the device). Ions delivered by the IGISOL may be trapped for up to 200ms and, upon removing the containment field, can be subsequently released in a 10 - 20 μs bunch. A photomultiplier viewing an 18mm region of the overlap of the re-accelerated ensemble and a counter-propagating laser beam can then be gated to register photons only as the ion bunch traverses the interaction region. The photon background in the fluorescent photon signal is then reduced in the ratio of the bunch-width to accumulation time (10^{-4}) and collinear spectroscopy has been successfully performed on samples produced at rates of less than 100 ions per second [3].

3 On-line stable beam production

Prior to the installation of the cooler it was only possible to perform collinear laser spectroscopy at the IGISOL by operating the ion-guide in a natural low energy-spread mode. In this mode the skimmer electrode, which facilitates the collection of ions and the removal of the helium catcher gas, was operated at very low voltages (<20V) and the efficiency of the ion guide was compromised [4].

The cooler-buncher has removed the requirement for low energy-spread in the primary IGISOL beam and high skimmer voltages and maximum efficiency are now accessible. During the initial on-line commissioning of the cooler a new feature at high skimmer voltages was recognised. On-line, at sufficiently high voltage, a corona discharge is formed on the skimmer electrode. The discharge results from the breakdown of He buffer gas ionised by the cyclotron beam. Immediately prior to the on-line commissioning run the IGISOL had been run with an off-line discharge source and the skimmer plate had been left lightly coated with stable metallic hafnium. On-line it was discovered that weak ion beams, ~ 10,000 ions per second, of stable hafnium were released, during the discharge, at an energy corresponding to the potential of the skimmer electrode. The conditions resulted in two beams of different average energy and different origin being produced on-line: one of radioactive recoils and the other ions of the stable skimmer coating. The finite energy acceptance window of the cooler can be adjusted to select only one of these beams for trapping and subsequent re-acceleration. Figure 2 shows the ion yield as a function of skimmer voltage and total energy. The acceptance window of the cooler is 100 - 150 eV and may be held at any voltage relative to the IGISOL. In order to preserve electrostatic beam steering parameters experimentally, the IGISOL voltage is adjusted relative to a fixed cooler potential. Fine tuning the separator potential thus enables a movement between radioactive measurements and stable calibrations *on-line* with great speed and no disruption to the experiment. Great reductions in systematic measurement uncertainties have been achieved using such stable calibrations.

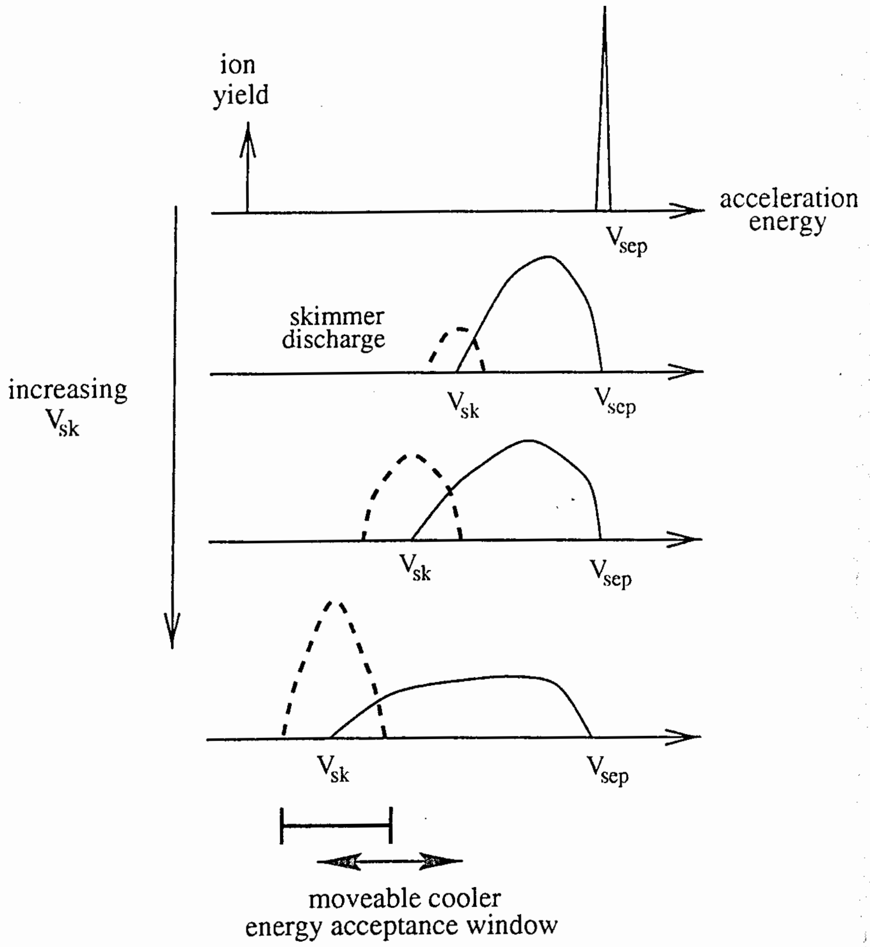

Figure 2: IGISOL ion yield as a function of total energy and skimmer voltage.

4 Collinear resonance ionisation spectroscopy

Collinear resonance ionisation is an extremely sensitive spectroscopic tool [5]. The spectroscopy however cannot realise its full efficiency if performed on continuous fast ion beams due to the low duty cycle of the required high-power ionising lasers. For even a high-repetition laser, such as 10kHz Cu-vapour based system, a maximum duty cycle of only a few percent has been achieved [5]. The efficient delivery of bunched ion beams from the JYFL cooler will enable high-efficiency, 100% duty cycle, collinear RIS using a 50Hz Nd:YAG-based laser system if sufficiently short bunch lengths can be produced.

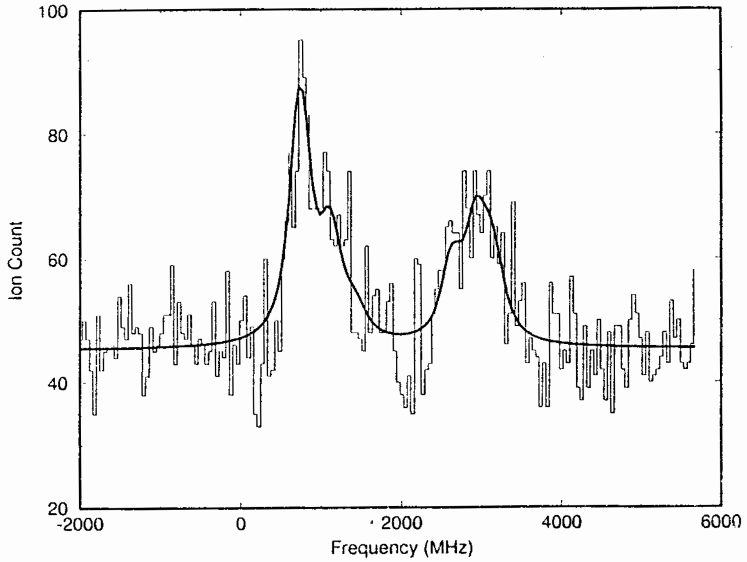

Figure 3: Resonant ion spectrum of ^{27}Al.

Figure 3 shows a resonant ion spectrum for ^{27}Al taken during initial collinear RIS tests at the IGISOL. The ion count is shown as a function of laser frequency in the region of the $s^2p\ ^2P_{1/2}$ – $s^2d\ ^2D_{3/2}$ 308.2nm transition. For the tests fast Al^+ ions (at $\sim$ 38keV) were neutralised via non-resonant charge exchange reactions with Na vapour. Residual charged ions were deflected out of the path of the the neutral component which was then overlapped for $\sim$ 1m with two laser beams. A two-step resonance ionisation was then performed using the amplified and doubled output of a Spectra Physics 380D dye laser (308nm) and a brute-force ionisation using $\sim$10mJ of 532nm Nd:YAG second harmonic. Resonantly produced ions were deflected after the interaction region and counted on a double-stack of micro-channel plates.

Ion bunches of 20μs minimum duration, corresponding to $\sim$ 10 metres bunch length, were used during the tests. Of this $\sim$ 1m could be overlapped between charge exchange and ion detection, and consequently of the 20,000 fast atoms per second used during the accumulation only 2,000 per second were accessible for laser ionisation. The total accumulation time for the spectrum in figure 3 was 10 minutes. On the largest of the

^{27}Al hyperfine components one photo-ion was counted per 40 neutral atoms (of the fluoresced sample). An increase in spectroscopic efficiency of more than two orders of magnitude compared to photon detection was thus achieved at the cost of a larger, 300MHz, linewidth.

Substantial improvements in signal and background can be readily achieved from the shortening of the bunch width and the use of a pulsed charge exchanged medium. At present the permanent presence of the charge exchange vapour causes a poor vacuum in the interaction region and results in a high probability for collisional ionisation ($\sim$ 1 in 100). A pulsed charge exchange process using YAG ablated plumes is presently under investigation at JYFL. The production of shorter bunches from the cooler-buncher will be attempted by removing the miniature quadrupole from the device. During a future on-line experiment faster counting of the produced photo-ions must be achieved (up to 10 ions per microsecond) and fast ion avalanche counters will be installed for this purpose.

5 Spectroscopy of ultra-low lying isomers

The existence of an ultra-low lying isomer is well established in the case of ^{235m}U (76.8 eV) but is only poorly established in the case of ^{229m}Th ($\sim$ 3.5 eV) [6]. The ^{229m}Th case has attracted great interest, as it exists on the atomic-nuclear boundary, but no direct observation of the isomer has been achieved [7]. The laser-IGISOL facility provides an excellent platform for the investigation of such isomers. Both the ^{235m}U and ^{229m}Th isomers are expected, or known, to be populated by alpha decay feeding (from ^{239}Pu and ^{233}U parents respectively). The decay branches strongly in the case of uranium, 73.3%, but only weakly in the case of thorium, where the feeding is estimated to be at the few percent level. Alpha-recoil production of the isomeric nuclei is thus feasible from thin samples of the parent and standard IGISOL ion guides provide ideal gas stoppers for the low-energy recoils.

Two experimental approaches for studying such isomers are under investigation at JYFL. The first, collinear spectroscopy of bunched ions, will require the efficient production of singly charged species (as opposed to the 2^+ production expected from thermalizing in pure, plasma-free, helium). An alternative, resonance ionisation spectroscopy within the ion guide, requires a substantial neutral fraction to be formed. Ionic charge state and neutral fraction are both known to critically depend on impurities and diffusion time in the buffer gas. The ion guide parameters required to achieve conditions suitable for either spectroscopic approach are under investigation in studies using mixed alpha sources (to provide a range of chemical species and associated ionisation potentials). Presently the production of ^{219}Rn, from a ^{213}Ra source, has been achieved with singly-charged ion production efficiencies of 5 – 10% using standard IGISOL ion-guide constructions.

6 Summary

The JYFL on-line cooler provides many new possibilities for laser spectroscopic studies of exotic nuclear systems. Efficient bunching of continuous ion beam is also possible with the device and all produced beams have ion-optical qualities that compare to, or exceed, those obtained from thermal, hot-cavity, ion sources. Techniques such as bunched-beam spectroscopy and collinear resonance ionisation spectroscopy have been performed and extremely high experimental sensitivities have been achieved. A full programme of development of these techniques is underway at the facility.

References

[1] Nieminen A. et al. *Hyp. Int.* **127** 507 (2000).

[2] Campbell P. et al. *Hyp. Int.* **127** 83 (2000).

[3] Forest D.H. et al. *these proceedings.*

[4] Levins J.M.G. et al. *Phys. Rev. Lett.* **82** 2476 (1999).

[5] Ch. Schulz et al. *J. Phys. B.* **24** 4831 (1991).

[6] Helmer R.G. and Reich C.W. *Phys. Rev. C* **49** 1845 (1994).

[7] Pachucki et al. *Phys. Rev. C* **64** 064301 (2001) *and references therein.*

FIRST OBSERVATION OF OPTICAL TRANSITIONS IN FERMIUM (Z = 100)

M. Sewtz [1], *H. Backe* [1], *A. Dretzke* [1], *K. Eberhardt*[3], *St. Fritzsche*[5], *C. Grüning* [3],
G. Gwinner [4], *R. G. Haire* [6], *G. Huber* [2], *J.V. Kratz* [3], *G. Kube* [1], *P. Kunz* [2], *J. Lassen* [2],
W. Lauth [1], *G. Passler* [2], *R. Repnow* [4], *D. Schwalm* [4], *P. Schwamb* [1], *P. Thörle* [3],
N. Trautmann [3]
[1]Institut für Kernphysik, [2]Institut für Physik and [3]Institut für Kernchemie der
Universität Mainz, D-55099 Mainz, Germany
[4]Max-Planck-Institut für Kernphysik, D-69029 Heidelberg, Germany
[5]Fachbereich Physik, Univerisät Kassel, D-34132 Kassel, Germany
[6]ORNL, Oak Ridge, TN 37831, USA

Laser spectroscopical studies have been performed for the first time at the element fermium (Z=100). A fraction of $2.7 \cdot 10^{10}$ *atoms was electrodeposited on a Ta filament and covered with 1* μm *Ti. From the filament the Fm atoms were evaporated at a temperature of about 1000 °C in the buffer gas of an optical cell and resonantly ionized with two beams of an excimer-dye-laser combination running with XeF. The resulting ions were identified by mass selective detection. Two resonant transitions were found at energies of 25100* cm^{-1} *and 25112* cm^{-1}.

1 Introduction

Fermium (Z=100) is the first heavy element for which no atomic data at all are presently known. An ultra sensitive laser spectroscopic method has been developed for the investigation of the atomic structure of such elements. The method is based on Resonance Ionization Spectroscopy (RIS) in a buffer gas cell with detection of the ionization process by the Ion-Guide-Quadrupole-Mass-Separation (IGQMS) technique [1]. The experimental set up, as installed at the tandem accelerator facility of the Max-Planck-Institut für Kernphysik in Heidelberg, Germany, has been described in a previous report [2].

About 1 ng ^{255}Fm with a half-life of 20.1 h was prepared by milking from ^{255}Es produced in the high flux reactor at ORNL, Oak Ridge, USA and shipped to Mainz. At the Institut für Kernchemie der Universität Mainz a fraction of $2.7 \cdot 10^{10}$ atoms was deposited electrochemically on a tantalum filament and covered with a 1 μm titanium layer. At a temperature of about 1000 °C the Fm atoms were evaporated into the buffer gas of an optical cell. At an argon pressure of 35 mbar the atoms are stored for typically 40 ms before they diffuse out of the laser illuminated region. Therefore, pulsed lasers with a repetition rate of 200 Hz can be employed for resonance ionization. Since no atomic spectroscopic data were known a two step excitation scheme was chosen using an excimer laser (XeF, 351/353 nm) pumped tunable dye laser. A fraction of the UV pump laser light was used for the ionization step while the dye laser was tuned over a wave number range from 24.390 cm^{-1} to 25.990 cm^{-1} for the ground state excitation. The fermium ions were extracted out of the buffer gas cell for the detection of the ionization process. After mass analysis in a quadrupole mass filter the ions were detected with a channeltron detector.

2 Results

In a first step the evaporation temperature t_e had to be determined. Outside the buffer gas cell, two semiconductor detectors were placed monitoring the activity of the filament through thin (1.8 mg/cm2) Ti windows, see Figure 1.

Observing a decrease of the activity as function of the temperature, t_e was determined employing a color pyrometer. During the course of the experiment (25 h) t_e was increased from (960 ± 10)°C to (1184 ± 10)°C.

With no atomic spectroscopic data available for Fm, a two step ionization scheme was chosen for the search of a resonant atomic relay level. The dye laser was tuned over the wave number range from 24390 cm^{-1} to 25990 cm^{-1} for the ground state excitation. The split UV light from the excimer pump laser was used for the non-resonant ionization. Two resonant transitions in ^{255}Fm were found at energies of 25099.8 cm^{-1} and 25111.8 cm^{-1}, see Figure 2.

Relativistic Multiconfiguration Dirac-Fock calculations [3] yield the configuration $5f^{12}7s^2$ $^3H_6$ for the ground state and $5f^{12}7s7p$, $J^P = 6^-, 5^-, 7^-$ at 27394 cm^{-1}, 27633 cm^{-1} and 27802 cm^{-1}, respectively, for the first excited levels with sufficient transition probabilities for laser excitation. Within the uncertainty of these calculations of 3000 cm^{-1}, the two observed level energies are in accord with the predictions. The third line may be outside the limited experimental search range.

With this information on excited states in fermium and with the same amount of ^{255}Fm, we should have a good chance to determine the ionization potential of fermium in a follow-up experiment.

In the time distribution spectra of the ions, as detected with the channeltron detector behind the quadrupole mass filter, shifts in the distribution of different atomic and molecular ions become apparent, see Fig.3.

The time delay $T = \int_S ds/v_D(s) = \frac{1}{K}\int_S ds/E(s)$ allows the determination of the ion mobility K. Here $v_D(s)=K \cdot E(s)$ is the Ion drift velocity which is connected to the electric field E(s) on the trajectories. The latter essentially coincides with the field lines. In a preliminary analysis to determine the mobility K the value $\int_S ds/E(s)$ has been determined by a numerical simulation of the electric field. In our experiment the mean field strength $\bar{E} = \frac{S}{\int_S ds/E(s)}$ amounts typically to $\bar{E}$=25.6 V/cm, and the path length S from the point of ionization to the nozzle S= 3.9 cm. The transport time from the nozzle to the channeltron detector amounts to less than 100 μs and has been neglected.

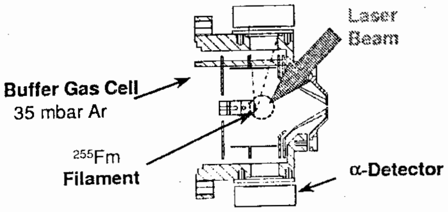

Figure 1: *Section of the optical cell.*

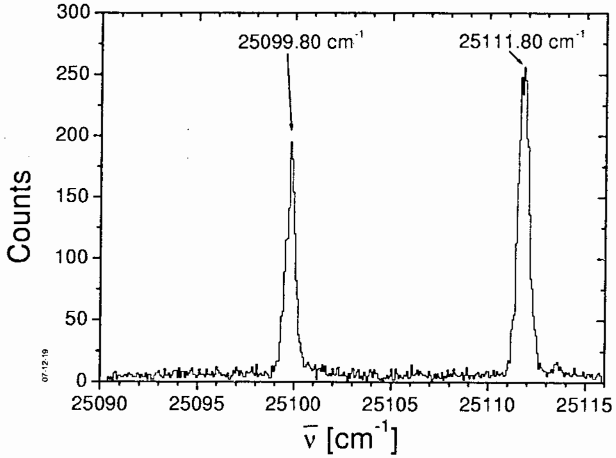

Figure 2: *Wave number scan of the dye laser at mass number A=255 with a 255Fm sample.*

With the known ion mobility K the momentum transfer cross section $\bar{\Omega}^{(1,1)}(T_{eff})$ can be calculated from the expression [4]

$$K = \frac{3}{16}\frac{e}{N}\sqrt{\frac{2\pi}{\mu k_B T_{eff}}}\,\frac{1+\alpha}{\bar{\Omega}^{(1,1)}(T_{eff})} \qquad (1)$$

with N : number density of buffer gas atoms, e : electric charge of the ion, m : reduced mass, k : Boltzmann constant, T_{eff} : effective temperature and α : higher order corrections.

In the rigid sphere model, the momentum transfer cross section can be written as

$$\bar{\Omega}^{(1,1)}(T_{eff}) = \pi d^2 = \pi(r_{Ar} + r_{Ion})^2 \qquad (2)$$

and the ionic radius r_{Ion} can be deduced if the radius r_{Ar} of argon is known. With $r_{Ar} = 1.44$ Å and $T_{eff} = 80$ °C the preliminary radii of Fm^+ and Cf^+ are $r_{Fm^+,Cf^+} = (1.8 \pm 1.0)$ Å and of UO^+ $r_{UO^+} = (2.1 \pm 1.0)$ Å. The errors are essentially based on the uncertainty in the location of the ionization process.

Relative changes of ion radii $\Delta r^{A,B}/r^B = (r^A - r^B)/r^B$ can be determined more precisely from the relative drift time differences $\Delta T^{A,B}/\Delta T^B$ by the expression

$$\frac{\Delta r^{A,B}}{r^B} \approx \frac{1}{2}\frac{\Delta T^{A,B}}{T^B}\left(1 + \frac{r_{Ar}}{r^B}\right) \quad . \qquad (3)$$

The results are $\Delta r^{UO^+,Cf^+}/r^{Cf^+} \approx 20\%$ and $\Delta r^{Fm^+,Cf^+}/r^{Cf^+} \approx -2\%$. The latter value is close to the prediction of relativistic calulations [5] yielding −3%.

In colnclusion, drift time measurements in the region of short lived actinides and transactinides may present an access to determine the increasing relativistic effects on ionic radii and bond lengths of simple molecular ions. These effects have been investigated theoretically [6] [7] but were up to now not accessible by experimental methods.

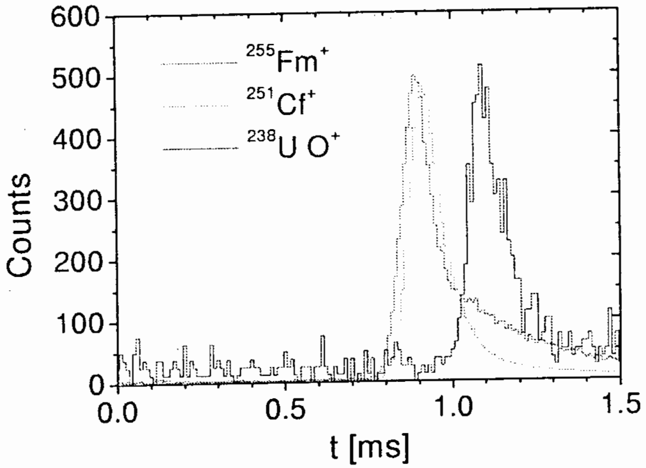

Figure 3: *Time distribution of mass selected ions as indicated. The start signal is the laser trigger at t = 0 ms. The time delay is essentially due to the transport of the ions in the buffer gas by electric fields towards the nozzle.*

Acknowledgement

Work supported by BMBF under contract 06 MZ 959I.

We are indebted to the Division of Chemical Sciences, Office of Basic Energy Research, U.S. Department of Energy, for making the ^{255}Fm material available through the transplutonium element production program at the Oak Ridge National Laboratory.

References

[1] H. Backe *et al.*, Nucl. Inst. Meth. Phys. Res. **B 126**, 406 (1997)

[2] H. Backe *et al.*, Proceeding of the 4th International Workshop, *Laser Spectroscopy on Beams of Radioactive Nuclei*, Dubna, (2000)

[3] S. Fritzsche, private communication

[4] E.A. Mason, *Transport Properties of Ions in Gases*, John Wiley & Sons, New York, (1988)

[5] J.P. Desclaux, At. Data Nucl. Data Tables **12**, 311 (1973)

[6] P. Pyykkö *et al.*, Acc. Chem. Res. **12**, 276 (1979)

[7] P. Pyykkö, Phys. Scr. **20**, 647 (1979)

ISOTOPE SHIFT IN CHROMIUM ATOM

B.Furmann, A.Jarosz, D.Stefańska, A.Krzykowski, J.Dembczyński

Chair of Atomic Physics, Faculty of Technical Physics,
Poznań University of Technology,
Piotrowo 3, 60-965 Poznań, Poland
furman@phys.put.poznan.pl

Introduction

Chromium is an element on the border of the light and the medium-heavy ones (Z=24). For this group of elements the field component in isotope shift is small but measurable with the use of a precise method of LIF on an atomic beam [7],[9]. The mass number of chromium isotope 52 is a magic number. Changes in mean square nuclear charge distribution in the vicinity of magic numbers are still not described satisfactorily from the theoretical point of view. Precise measurements of $\delta\langle r^2\rangle$ in chromium may prove useful for improvement of theoretical description of $\delta\langle r^2\rangle$ in the vicinity of closed nuclear shells.

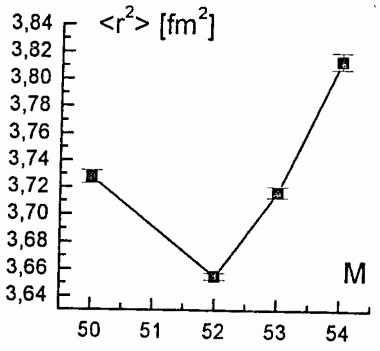

Fig.1. Mean-square nuclear charge radii of stable chromium isotopes

Positions of the metastable levels in chromium allow studies of pure s→p type transitions, as well as transitions involving the change of d-electrons. Analysis of the hfs of the only stable odd isotope ^{53}Cr allows estimation of the 4s electron probability at the nucleus $|\psi(0)|^2_{4s}$ and thus evaluation of the screening factors for s→p type transitions. In this work the results of the isotope shifts in stable chromium isotopes are presented.

Experimental setup

Method of the laser induced fluorescence (LIF) on an atomic beam has been used for measurements of the positions of all chromium stable isotopes. Apparatus for atomic beam generation is presented in fig. 2. Chromium, placed in a graphite or tantalum crucible, is heated and evaporated by the electron beam bombardment. An auxiliary discharge is applied for better population of the high lying metastable levels. Laser beam is generated by stabilized single-mode ring dye laser operated on stilbene 3 and pumped by an argon laser; it crosses perpendicularly the atomic beam. Fluorescence signal is recorded by a photomultiplier positioned perpendicularly to both the laser and the atomic beam directions.

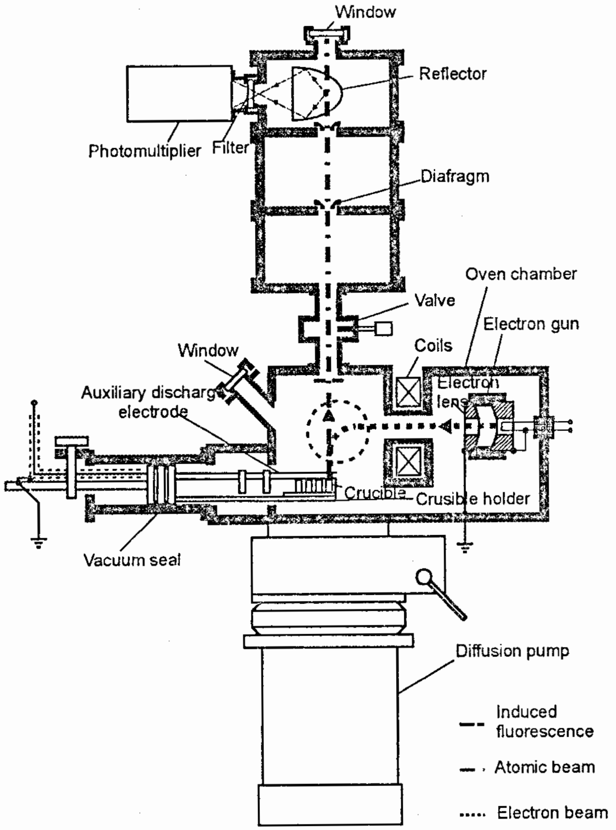

Fig.2.Atomic beam apparatus

Experimental determination of isotope shifts and hyperfine structure from the optical spectra

For every investigated optical transition on the average 10 scans with the use of a LIF method on an atomic beam have been recorded. Initially the recorded spectra have been calibrated with an approximate value of the *FSR* of the marker – 150 MHz. For each scan the positions of all the isotopes as well as the hfs parameters for the odd isotope ^{53}Cr have been fitted simultaneously (fig 3a and 3b). The final values for this stage have been the mean values of those obtained in individual scans, and the errors have been the mean standard deviations. The procedure described has been applied also to the lines involving levels measured very accurately with ABMR method by Childs and Goodman [7]. Intervals, known with high accuracy from [7], have been evaluated from our measurements and compared with the former ones. *FSR* value of the marker has been corrected until a least mean difference in the values of intervals has been obtained. The corrected *FSR* amounts to 149.98 MHz. The final values quoted are calibrated with the corrected *FSR* value of the marker.

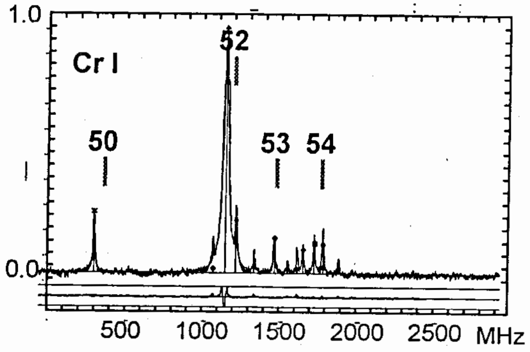

Fig.3a. Experimental HFS and IS data with fit curve and fit deviations for transition with positive specific isotope shift

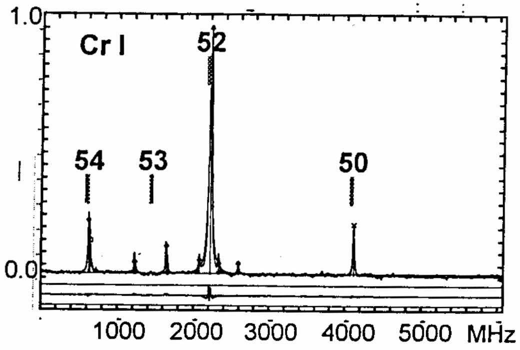

Fig.3b. Experimental HFS and IS data with fit curve and fit deviations for transition with negative specific isotope shift

Tab.1. Transitions in chromium investigated from the point of view of the isotope shifts.

Lower level		k[cm^{-1}] (in vacum)	λ[nm] (in air)		Upper level
Term	J			J	Term
$3d^5(^6S)4s\ a^5S$	2	21827,74	458,0043	1	$3d^4(^5D)4s4p(^3P^o)\ y^5P^o$
	2	21991,46	454,5945	2	
$3d^44s^2\ a^5D$	0	23036,52	433,9713	1	$3d^4(^5D)4s4p(^3P^o)\ z^5F^o$
	1	22976,48	435,1054	1	
	1	23048,00	433,7552	2	
	2	23037,99	433,9436	3	
	3	22870,25	437,1264	3	
	3	23011,16	434,4496	4	
	4	22798,80	438,4964	4	
	4	22972,78	435,1755	5	
$3d^44s^2\ a^5D$	0	21670,12	461,3357	1	$3d^4(^5D)4s4p(^3P^o)\ y^5P^o$
	1	21610,08	462,6174	1	
	1	21773,80	459,1389	2	
	2	21493,43	465,1282	1	
	2	21657,15	461,6120	2	
	2	21897,28	456,5498	3	
	3	21489,41	465,2152	2	
	4	21517,18	464,6148	3	
$3d^5(^4G)4s\ a^5G$	2	21997,95	454,4604	2	$3d^5(^4G)4p\ z^5G^o$
	6	22086,21	452,6443	6	
	3	22017,89	454,0488	3	
	4	22041,16	453,5695	4	
	5	22065,31	453,0730	5	
	4	22065,56	453,0679	5	
	6	22069,65	452,9839	5	
	5	22081,87	452,7332	6	
$3d^5(^4P)4s\ a^5P$	3	23034,35	434,0122	2	$3d^4(a^3P)4s4p(^3P^o)\ v^5P^o$
	2	22818,86	438,1109	1	
	2	23265,34	429,7031	3	
	1	23018,25	434,3158	2	

Tab.2. Isotope shifts (IS) measured in the investigated transitions.

Lower level		$IS^{52,50}$[MHz]	$IS^{53,50}$[MHz]	$IS^{54,50}$[MHz]		Upper level
Term	J				J	Term
$3d^{5}(^{6}S)4s\ a^{5}S$	2	-1898.2(0.7)	-2722.7(0.9)	-3480.4(5.7)	1	$3d^{4}(^{5}D)4s4p(^{3}P^{o})\ y^{5}P^{o}$
	2	-1893.6(0.7)	-2724.1(0.9)	-3474.3(0.9)	2	
$3d^{4}4s^{2}\ a^{5}D$	0	852.8(1.6)	1171.5(1.9)	1436.9(2.6)	1	$3d^{4}(^{5}D)4s4p(^{3}P^{o})\ z^{5}F^{o}$
	1	846.1(1.5)	1163.9(1.6)	1428.8(2.0)	1	
	1	851.2(0.6)	1166.8(1.3)	1431.7(0.8)	2	
	2	860.6(1.2)	1168.8(1.1)	1442.8(1.8)	3	
	3	850.0(0.2)	1167.3(0.5)	1432.7(0.6)	3	
	3	848.7(1.8)	1168.0(1.8)	1433.1(0.7)	4	
	4	847.1(3.4)	1166.2(1.9)	1430.0(2.1)	4	
	4	852.1(0.3)	1170.5(0.3)	1437.8(0.2)	5	
$3d^{4}4s^{2}\ a^{5}D$	0	787.3(0.3)	1071.7(1.4)	1315.9(0.8)	1	$3d^{4}(^{5}D)4s4p(^{3}P^{o})\ y^{5}P^{o}$
	1	782.3(0.6)	1068.1(2.5)	1309.6(2.6)	1	
	1	784.4(0.6)	1071.5(1.0)	1311.3(1.2)	2	
	2	784.0(1.0)	1072.0(0.8)	1309.8(1.2)	1	
	2	792.1(2.3)	1069.6(2.4)	1308.4(1.4)	2	
	2	783.8(0.6)	1070.9(1.4)	1310.3(0.6)	3	
	3	767.7(3.0)	1065.1(0.8)	1306.2(1.5)	2	
	4	788.0(0.6)	1069.7(1.1)	1303.6(0.5)	3	
$3d^{5}(^{4}G)4s\ a^{5}G$	2	-152.4(1.5)	-256.8(1.4)	-372.8(0.8)	2	$3d^{5}(^{4}G)4p\ z^{5}G^{o}$
	6	-170.2(0.4)	-281.7(0.8)	-403.7(1.7)	6	
	3	-152.5(0.6)	-269.2(2.3)	-386.9(3.6)	3	
	4	-167.8(1.1)	-276.4(0.8)	-399.1(1.5)	4	
	5	-166.0(4.1)	-298.7(5.5)	-408.1(1.0)	5	
	4	-172.0(1.7)	-285.1(1.0)	-412.1(1.8)	5	
	6	-176.2(3.1)	-292.3(3.5)	-415.1(1.2)	5	
	5	-173.9(2.1)	-293.1(2.5)	-415.6(2.0)	6	
$3d^{5}(^{4}P)4s\ a^{5}P$	3	-1177.5(0.9)	-1707.6(0.6)	-2202.0(1.3)	2	$3d^{4}(a^{3}P)4s4p(^{3}P^{o})\ v^{5}P^{o}$
	2	-1153.7(3.8)	-1686.0(7.7)	-2132.3(9.5)	1	
	2	-1125,8(5.5)	-1658.6(8.5)	-2140.8(7.0)	3	
	1	-1177.0(0.7)	-1707.4(0.9)	-2202.9(1.2)	2	

Analysis of the results

Isotope shift in a transition:

$$IS^{AA'} = \nu^{A} - \nu^{A'}$$

may be splitted in two terms:

$$IS^{AA'} = MS^{AA'} + FS^{AA'},$$

where: $MS^{AA'}$ - mass shift $FS^{AA'}$ - field shift.

Mass shift consists of two contributions:

$$MS^{AA'} = NMS^{AA'} + SMS^{AA'},$$

$$NMS^{AA'} = \frac{m_e}{m_p}\frac{A-A'}{A\cdot A'}\nu_i \qquad \text{- \textit{normal} mass shift,}$$

$$SMS^{AA'} = M_i^{SMS}\,\frac{A-A'}{A\cdot A'} \qquad \text{- \textit{specific} mass shift,}$$

where M_i^{SMS} is an electronic factor for the transition. Field shift can be expressed as:

$$FS^{AA'} = F_i\,\lambda^{AA'} \cong F_i\,\delta\langle r^2\rangle^{AA'},$$

where F_i is an electronic factor for the transition, and $\delta\langle r^2\rangle^{AA'}$ - change of the mean square charge radius of the nucleus (a nuclear factor).
Normal mass shift can easily be calculated and is often subtracted from the total isotope shift to give the *residual* isotope shift $RIS^{AA'}$

$$RIS^{AA'} \equiv IS^{AA'} - NMS^{AA'} = SMS^{AA'} + FS^{AA'} = M_i^{SMS}\,\frac{A-A'}{A\cdot A'} + F_i\,\delta\langle r^2\rangle^{AA'}.$$

Separation of $SMS^{AA'}$ and $FS^{AA'}$ can be performed with the use of a King plot: *modified* optical $RIS^{AA'}$ vs *modified* $\delta\langle r^2\rangle^{AA'}$ (for chromium model independent $\delta\langle r^2\rangle^{AA'}$ are known from muonic x-ray spectroscopy and electron scattering [3]). *Modified* $RIS^{AA'}$ is defined as follows:

$$\mu\cdot RIS^{AA'} = \frac{A\cdot A'}{A-A'}\cdot\frac{52-50}{52\cdot 50}RIS^{AA'}$$

(the isotopes ^{52}Cr and ^{50}Cr have been chosen a pair of reference isotopes) and $\delta\langle r^2\rangle^{AA'}$ have been *modified* in the same way.

Theoretical description of the electronic factors M_i^{SMS} and F_i is satisfactory only for the simplest cases. For all the M_i^{SMS} involved *ab initio* calculations available so far predict neither the magnitude nor the sign correctly; thus it is possible neither to compare the obtained experimental results with theoretical predictions, nor to draw any further conclusions concerning this effect.

For the transitions considered F_i can be evaluated as follows:

$$F_i = \gamma\,F_{4s}$$

where

- $$\gamma = \frac{|\Psi(0)|^2_{core(lower)} + |\Psi(0)|^2_{4s} - |\Psi(0)|^2_{core(upper)}}{|\Psi(0)|^2_{4s}}$$ - screening factor

  ($|\Psi(0)|^2$ - electron density at the nucleus),

- $F_{4s} = D\,Z\,A_{4s}\,/\,g_I$ - electronic factor for $4s$ electron [4].
  The values to be introduced into the above formula are as follows:
  $D = 6.16381\cdot10^{-3}$ fm^{-2} (details in [4])
  A_{4s} - magnetic dipole *hfs* constant for $4s$ electron (values from [5]).

Procedure described above has been applied for all measured transitions. Exemplary obtained King plots for all types of transitions are presented in fig.4. Obtained values of M_i^{SMS} and F_i electronic factors are listed in Table 3. Since the differences between the factors for all lines involving one term are small, mean values for M_i^{SMS}/M_i^{NMS} and γ have been evaluated (Tab.4 and 5).

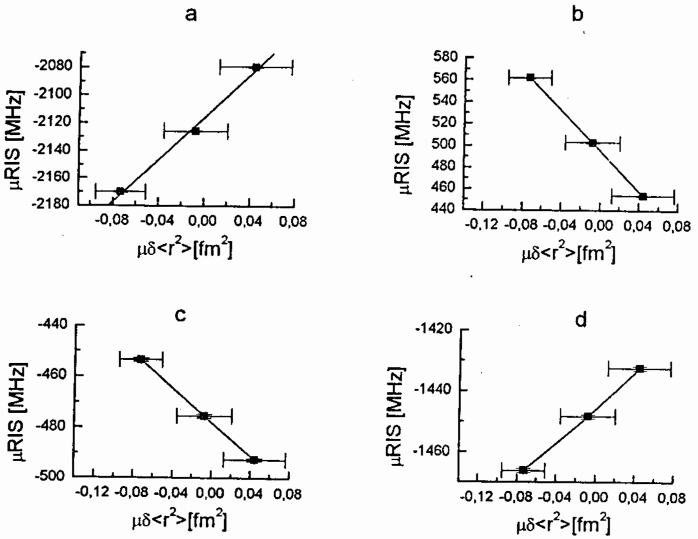

Fig.4. King plots (modified RIS against modified δ<r²>) for all types of measured transitions:

a) $3d^5(^6S)4s\ a^5S_2 \rightarrow 3d^4(^5D)4s4p(^3P^o)\ y^5P^o_2$
b) $3d^44s^2\ a^5D_1 \rightarrow 3d^4(^5D)4s4p(^3P^o)\ z^5F^o_2$
c) $3d^5(^4G)4s\ a^5G_6 \rightarrow 3d^5(^4G)4p\ z^5G^o_5$
d) $3d^5(^4P)4s\ a^5P_1 \rightarrow 3d^4(a^3P)4s4p(^3P^o)\ v^5P^o_2$

Tab.3. Electronic factors F_i and M_i^{SMS} for the studied transitions.

Lower level		M_i^{SMS}[GHz]	F_i[MHz/fm^2]		Upper level
Term	J			J	Term
$3d^5(^6S)4s\ a^5S$	2	-2115.0(3.5)	782(20)	1	$3d^4(^5D)4s4p(^3P^o)\ y^5P^o$
	2	-2115.0(4.0)	769(15	2	
$3d^44s^2\ a^5D$	0	497.8(1.1)	-907(23)	1	$3d^4(^5D)4s4p(^3P^o)\ z^5F^o$
	1	493.4(1.2)	-886(25)	1	
	1	495.0(0.7)	-917(14)	2	
	2	500.2(2.2)	-952(45)	3	
	3	497.3(1.0)	-902(20)	3	
	3	495.5(1.4)	-889(29)	4	
	4	496.6(1.6)	-890(33)	4	
	4	498.4(0.9)	-898(18)	5	
$3d^44s^2\ a^5D$	0	449.8(0.7)	-887(13)	1	$3d^4(^5D)4s4p(^3P^o)\ y^5P^o$
	1	447.2(0.1)	-871(2)	1	
	1	446.8(0.6)	-881(11)	2	
	2	450.0(1.0)	-884(19)	1	
	2	448.9(1.3)	-962(26)	2	
	2	444.7(0.6)	-880(12)	3	
	3	443.9(2.7)	-759(55)	2	
	4	448.7(0.3)	-946(5)	3	
$3d^5(^4G)4s\ a^5G$	2	-454.0(0.5)	-348(10)	2	$3d^5(^4G)4p\ z^5G^o$
	6	-471.8(0.5)	-333(10)	6	
	3	-460.2(1.6)	-412(32)	3	
	4	-468.4(1.0)	-332(21)	4	
	5	-475.5(5.4)	-396(90)	5	
	4	-474.6(0.9)	-354(18)	5	
	6	-477.9(0.1)	-333(2)	5	
	5	-477.9(0.8)	-356(16)	6	
$3d^5(^4P)4s\ a^5P$	3	-1445.8(0.6)	295(12)	2	$3d^4(a^3P)4s4p(^3P^o)\ v^5P^o$
	2	-1417.1(8.3)	390(168)	1	
	2	-1411.9(4.1)	120(83)	3	
	1	-1445.6(0.5)	287(9)	2	

Tab.4. Ratio M_i^{SMS}/M_i^{NMS} for various types of transitions.

Lower term → Upper term	M_i^{SMS}/M_i^{NMS}
$3d^5(^6S)4s\ a^5S \rightarrow 3d^4(^5D)4s4p(^3P^o)\ y^5P^o$	-7.71
$3d^44s^2\ a^5D \rightarrow 3d^4(^5D)4s4p(^3P^o)\ z^5F^o$	1.83
$3d^44s^2\ a^5D \rightarrow 3d^4(^5D)4s4p(^3P^o)\ y^5P^o$	1.65
$3d^5(^4P)4s\ a^5P \rightarrow 3d^4(a^3P)4s4p(^3P^o)\ v^5P^o$	-4.93
$3d^5(^4G)4s\ a^5G \rightarrow 3d^5(^4G)4p\ z^5G^o$	-1.70

Tab.5. Experimentally evaluated screening factors γ for pure s→p type transitions.

Lower term → Upper term	γ
$3d^44s^2\ a^5D \rightarrow 3d^4(^5D)4s4p(^3P^o)\ z^5F^o$	3.06(4)
$3d^44s^2\ a^5D \rightarrow 3d^4(^5D)4s4p(^3P^o)\ y^5P^o$	2.96(6)
$3d^5(^4G)4s\ a^5G \rightarrow 3d^5(^4G)4p\ z^5G^o$	1.20(7)

The results of more detailed studies of F_i and M_i^{SMS} are presented in fig. 5, where J dependence of the above factors within the terms for three terms is plotted.

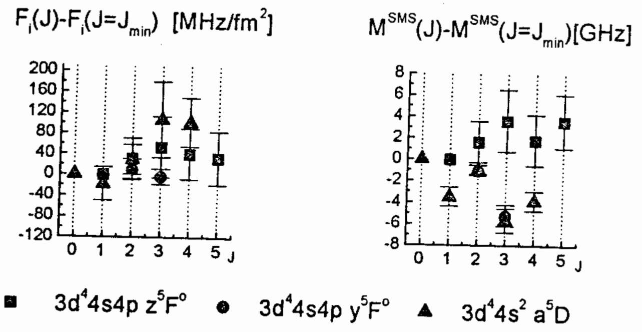

Fig.5. CSO effect (J-dependence) in field shift (F_i) and specific mass shift (M_i^{SMS}) for three terms in chromium

Conclusions:

Isotope shifts for all the investigated transitions apart from NMS include also SMS and FS. Field shifts are of the order of some tens of MHz. For transitions of the type $d^N \rightarrow d^{N-1}$, SMS is negative and 5-7 times larger than NMS. For transitions of the type s→p, SMS is positive or negative and amounts to ca. 1.7 NMS. Screening factor for the transitions $3d^54s \rightarrow 3d^54p$ amounts to 1.2 and agrees with the theoretical estimate of Aufmuth [6]. Screening factor for the transitions $3d^44s^2 \rightarrow 3d^44s4p$ amounts to ca. 3.0. There are no theoretical predictions, but the large screening is probably due to a larger number of valence electrons [2]. A surprise may be relatively large field shifts in transition type $d^N \rightarrow d^{N-1}$. In previous investigation field components in such type of transition in chromium were not observed [2]. Estimate of the second order effect (J-dependence) in three terms: $3d^44s4p\ z^5F^o$, $3d^44s4p\ z^5P^o$ and $3d^44s^2\ a^5D$ shows first an increase of F_i with an increase of J quantum number (largest F_i for J=3) and then a decrease. M_i^{SMS} increases with J for the term $3d^44s4p\ z^5F^o$ and decreases for terms $3d^44s4p\ z^5P^o$ and $3d^44s^2\ a^5D$. All these differences are on the border of experimental accuracy. Corrected value $\langle r^2 \rangle$ for the isotope ^{53}Cr is 0.003 fm^2 smaller than the muonic [3] value. Because values of corrections for other isotopes are negligible, odd-even staggering effect in chromium may prove to be more significant, than it appeared from previous results.

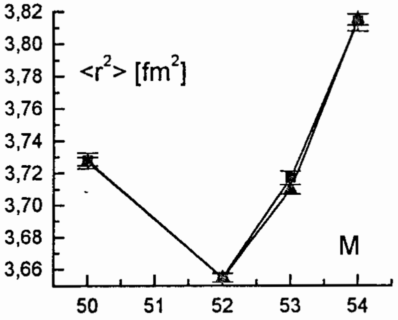

Fig.6. "Corrected" mean-square nuclear charge radii stable chromium isotopes.

Acknowledgments

We would like to thank Prof. W. Ertmer from University of Hannover for presentation us with the apparatus for atomic beam generation. We also wish to thank Dr G. Szawioła for helpful discussions. This work was supported by the Polish State Committee for Scientific Research (KBN) under project No. BW 63-018/2001.

References:

[1]. King W.H.: *„Isotope Shifts in Atomic Spectra"* (New York, London: Plenum 1984)
[2]. Heilig K and Steudel A.: *At. Data Nucl. Data Tables* <u>14</u> (1974) 613-38
[3]. Wohlfahrt. H.D., Shera E.B., Hoehn M.V., Yamazaki Y., Steffen R.M.: *Phys. Rev.* **2 3**, (1981) 533
[4]. Mårtensson-Pendrill A.M., Pendrill L., Salomonson S., Ynnerman A., Warston H.: *J. Phys. B: At. Mol. Opt. Phys.* <u>3</u> (1990) 1749-1761
[5]. Jarosz A., *PhD Thesis* Poznan 2001
[6]. Aufmuth P., *J. Phys. B: At. Mol. Opt. Phys.* <u>15</u> (1982) 3127-3140
[7]. Childs W.J.,Goodman L.S., von Ehrenstein D.: *Phys. Rev.* 132 (1963) 2128
[8]. Krzykowski A., Furmann B., Stefanska D., Jarosz A. and Kajoch A.: *Optics Communications* <u>140</u> (1997) 216
[9]. Furmann B., Stefańska D.,Krzykowski A., Jarosz A., Kajoch A.: *Z. Phys. D* <u>37</u> (1996) 289

HYPERFINE MAGNETIC ANOMALY IN THE ATOMIC SPECTRA OF RARE EARTH ELEMENTS

Yu.P. Gangrsky, D.V. Karaivanov, K.P. Marinova, B.N. Markov and S.G. Zemlyanoi

Laboratory of Nuclear Reactions, JINR, Dubna, Russia

INTRODUCTION

One of the effects responsible for hyperfine splitting (HFS) of atomic or ionic spectral optical lines is that the magnetic moment of the nucleus is spatially distributed over its volume (the Bohr-Weisskopf effect) [1]. This effect causes the HFS magnetic dipole constant to decrease, and that decrease may vary in value for isotopes of the same element:

$$A = A_0(1-\varepsilon), \qquad (1)$$

where A and A_0 are the magnetic dipole constants for the real and the point nucleus; ε is the Bohr-Weisskopf effect (see the diagram). This difference in the values of ε results in the fact that the ratio of constant A and giromagnetic factor g = μ/I (μ and I are the magnetic moment and the spin of the nucleus) will differ in value for isotopes of the same element, which brings about hyperfine anomaly (HFA) in their spectra. For the small values of ε, HFA is expressible as

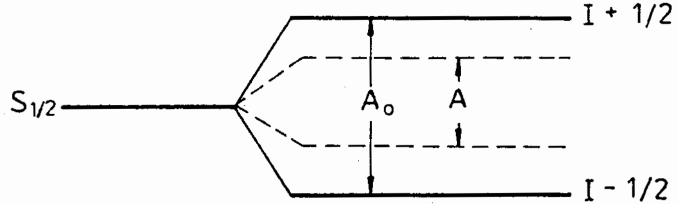

$$ {}^{1}\Delta^{2} = \varepsilon_1 - \varepsilon_2 \approx \frac{A_1}{A_2}\cdot\frac{g_2}{g_1} - 1, \qquad (2)$$

where subscripts 1 and 2 refer to the isotopes that are being compared (subscript 1 conventionally refers to the smaller mass number isotope).

Measured HFA values enable one to judge a number of important nuclear parameters. Among them are: the average radius of the distribution in the nucleus of valence electrons, which define the value of the magnetic moment; the spin to orbital component ratio of the magnetic moment. Those nuclear parameters are, by and large, decisive criteria in testing various nuclear structure models. They have grown in importance owing to recent research on nucleon drip-line nuclei. In such nuclei, which have a large excess of protons or neutrons, the binding energy of the outer nucleons is extremely low (typically below 1 MeV). This may result in their spatial distribution being unusually wide (proton and neutron halos) [2].

The aim of this work is to measure the HFA in the atomic spectra of rare earth elements (REEs) (Nd, Eu, Gd and Lu) by high resolution resonance laser spectroscopy. The choice of REEs has been motivated by a number of their peculiarities. The electron shell levels in atoms of those elements are nearly the same in structure. The ground state term is of the $4f^n6s^2$ configuration (it is $4f^n5d6s^2$ in the case of La, Gd and Lu). The presence of paired electrons considerably decreases the contribution of the magnetic moment spatial distribution effect to HFS. So REE ground state atoms are likely to have extremely small HFA values. This consideration is supported by the data of Table 1. Presented there are the ratios of ground state constants A, measured to a high accuracy by radio frequency spectroscopy [3-5], and the ratios of giromagnetic factors, measured independently [6,7]. It can be seen that the values of the HFAs, derived from the A and g ratios by expression (2), are extremely small (as a rule, less than 10^{-3}). Finite HFA values can appear due to unpaired s-electron configurations being admixed with ground state configurations. This means that the ratios of ground state constants A can be used instead of the ratios of the giromagnetic factors to derive HFA for REEs:

Table 1. Ratio of giromagnetic factors, magnetic dipole constants A and electric quadrupole constants B of HFS for the ground states of REE atoms.

Isotopes	Term and configuration	A_1/A_2	B_1/B_2	g_1/g_2	$^1\Delta^2$, %
^{143,145}Nd	$^5I_4 4f^4 6s^2$	1,60861(2)	1,8968(5)	1,60883(4)	-0,014(3)
^{147,149}Sm	$^7F_0 4f^6 6s^2$	1,21305(2)	-3,4598(7)	1,213(1)	0,004(82)
^{151,153}Eu	$^8S^0_{7/2} 4f^7 6s^2$	2,26498(8)	0,3928(4)	2,2646(12)	0,017(53)
^{155,157}Gd	$^9D_2 4f^7 5d6s^2$	0,76253(12)	0,9383(1)	0,7625(20)	0,004(263)
^{161,163}Dy	$^5I_8 4f^{10} 6s^2$	-0,71416(1)	0,9468(1)	- 0,714(7)	0,02(98)
^{171,173}Yb	$^1S_0 4f^{14} 6s^2$	-3,6305(2)		-3 ,63051(18)	-0,0003(10)
^{171,176}Lu	$^2D_{3/2} 4f^{14} 5d6s^2$	1,409011(1)	0,708812(1)	1,4087(21)	-0,014(3)

$$^1\Delta^2 = \frac{A_1(ex)}{A_2(ex)} \cdot \frac{A_2(gr)}{A_1(gr)} - 1, \tag{3}$$

where the symbols (gr) and (ex) refer to the ground and excited states. This consideration is of great importance especially for radioactive isotopes, whose magnetic moments (and thus g-factors) are unknown or measured with an inadequate degree of accuracy.

At the same time REEs differ widely in nuclear properties. The light elements (La – Sm), situated in the vicinity of the N=82 close neutron shell, are spherical in shape. As on passes from Nd to Gd at N=90, the nucleus, changing drastically in shape, becomes deformed [8]. Nuclei of the heavy REEs (Dy – Lu) are strongly deformed. Such a change in the structure of the nucleus is undeniably to affect the way in which the nuclear magnetism is distributed in it. Therefore HFA values should be expected to differ markedly for different REEs. The elements being investigated in this work are just ones different in nuclear structure.

EXPERIMENTAL TECHNIQUE

The basic requirement for the experimental technique to meet is that it should ensure a high frequency resolution. This would enable hyperfine structure (HFS) constants to be established with a minimum error and the HFAs to be derived from them. Therefore we used the resonance laser fluorescence method and parallel atomic beams (Fig. 1). The experimental setup is described in detail in our previous works [9,10]. The samples under study were atomised by evaporating in an electrically heated crucible [9] or by irradiating with infrared radiation from a high-powered pulsed Q-switched laser (its pulse power was 5 MW [10]. The atomic beam was collimated with a set of diaphragms, its divergence in the laser radiation zone being 0.015 rad. The atomic beam, laser beam and resonant scattered fluorescence radiation were directed in mutually perpendicular directions. This geometry allowed the Doppler widening of the optic lines to be minimised (it was 25 and 80 MHz respectively for thermal and laser evaporation). The samples were either metals (Nd, Gd) or their oxides (Eu_2O_3, Lu_2O_3) of natural isotope composition.

To register resonance scattered fluorescence radiation, use was made of a photomultiplier operated in the single-photons counting mode. The intensity of that radiation was measured as a function of laser radiation frequency, which was scanned up to 30 GHz. This allowed a spectrum that included all the HFS components associated with the isotope under study to be obtained in one scan. To carry out frequency calibration of the spectra, a Fabry-Perot confocal interferometer with a constant of 150 MHz was used. Frequency markers from the interferometer were registered simultaneously with the measured spectrum. Data on the spectra were collected and processed with a personal computer, which also enabled the spectra to be visualised during experiment.

MEASURED RESULTS

On the above setup, the resonance laser fluorescence spectra of the following REE elements: ^{143}Nd, ^{145}Nd, ^{151}Eu, ^{153}Eu, ^{155}Eu, ^{155}Gd, ^{157}Gd, ^{175}Lu and ^{176}Lu were measured in atomic beams. In all the cases (except for the radioactive isotope ^{155}Eu), samples of natural isotope composition were used. The setup frequency resolution was high enough for the HFS components of the isotopes under study to be distinguished in the complex spectrum. The ^{155}Eu isotope was produced by irradiating a ^{154}Sm-enriched sample with thermal neutrons in a reactor and then isolated chemically. The production reaction was $^{154}\text{Sm}\,(n, \gamma)\,^{155}\text{Sm} \xrightarrow{\beta} {}^{155}\text{Eu}$. In this way, 10^{14} atoms of ^{155}Eu were produced. The sample contained admixed ^{151}Eu and ^{153}Eu, 10^{16} atoms each. The resonance fluorescence spectrum of that sample as well as the spectra of Nd and Gd is presented in Fig. 2. The spectrum has clearly defined intense lines due to the HFS components associated with ^{151}Eu and ^{153}Eu as well as weak lines associated with ^{155}Eu. The spacing between the lines, which is due to the transitions between one of the lower (upper) HFS level components and the two or three neighbouring upper (lower) level components, allows the values of the constants (magnetic dipole constant A and electric quadrupole constant B) for both levels to be determined. These constants are related to the frequency spacing between the HFS components, which, in turn, are related to total moments F and F-I (equal to the vector sum of the nuclear spin I and the electronic shell spin J) by the expression [11]:

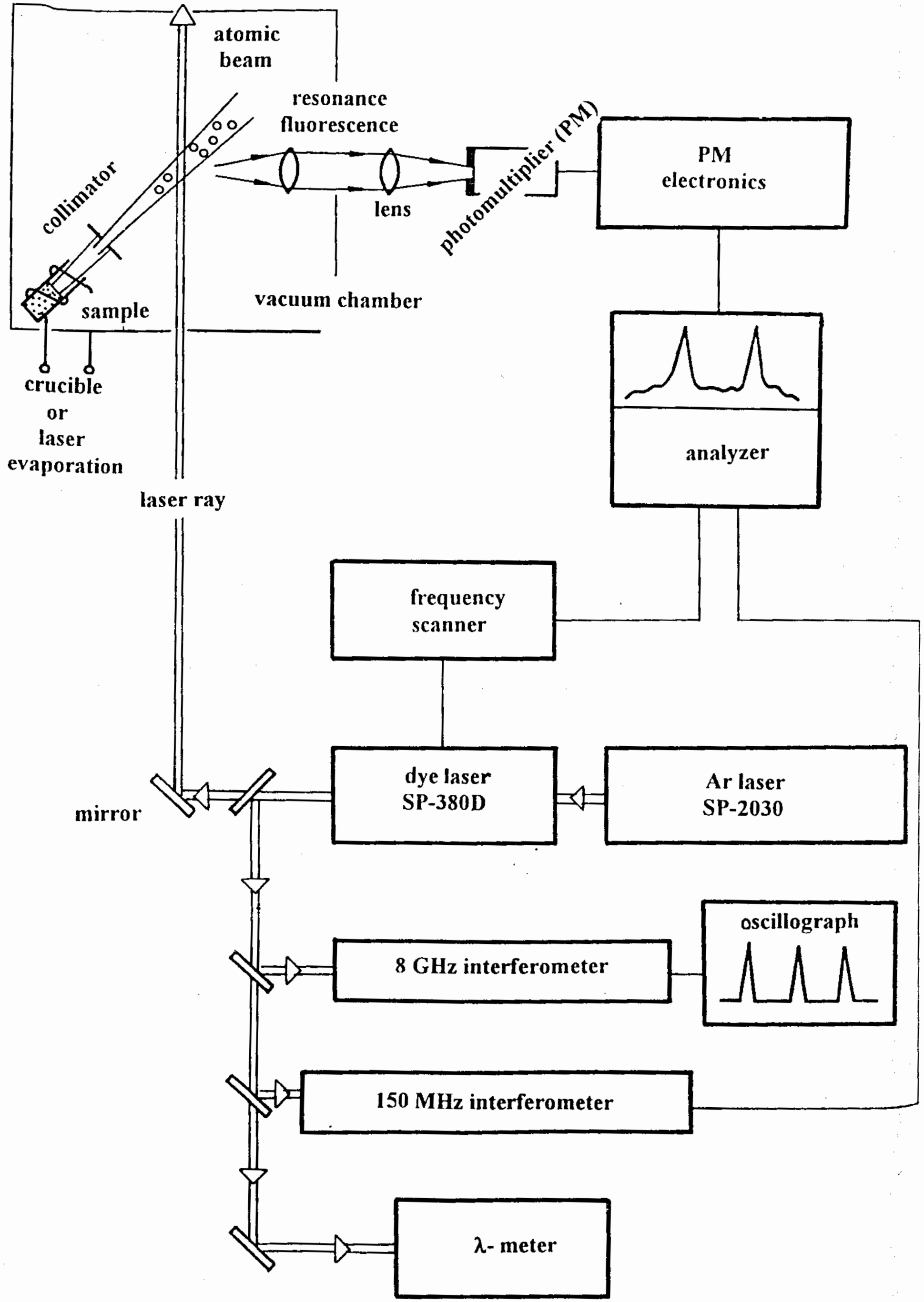

Fig.1. The block-scheme of the experimental laser setup

$$\Delta\nu(F,F-1)=AF+B\frac{3F\left[F^2+\frac{1}{2}-I(I+1)-J(J+1)\right]}{2IJ(2I-1)(2J-1)}. \qquad (4)$$

In this expression, the terms of higher orders, due to the magnetic octupole and hexadecapole moments are neglected. From reported data, it follows that their contribution, as a rule, is less than 10^{-4}, which is beyond the accuracy of the measurement discussed.

To determine the exact position of the centres of gravity of the identified HFS components, each of them was approximated with a Feugt profile of a specified width corresponding to the experimental resolution (the latter was found in special experiments). Then the positions of the peaks and the frequency spacing between the HFS components were determined with the help of the special-purpose EXHYSPFI program [12]. This processing technique allowed the spacing to be found with an accuracy of up to a few megaherzs or a fraction of a percent. Constants A and B were calculated on the basis of expression (4) by the least-squares method, every frequency spacing being taken care of and the χ^2 criterion being used. The thus obtained values of constants A and B for the excited levels of the isotopes considered are presented in Table 2. It also contains the terms and configurations of the upper levels (those characteristics for the lower levels are presented in Table 1) and the transition wave lengths.

Table 2. Measured values of the magnetic dipole constants and electric quadrupole constants of HFS for some excited states of REE atoms.

Isotope	I^π	Term and configuration	E, cm^{-1}	A, MHz	B, MHz
^{143}Nd	$7/2^-$	$z^5H_5^o4f^75d^26s$	19816	-122,35(5)	25,2(4,2)
^{145}Nd	$7/2$			-76,23(11)	13,8(4,5)
^{151}Eu	$5/2^+$	$z^6P_{3/2}4f^76s6p$	17707	591,16(9)	-354,58(97)
^{153}Eu	$5/2^+$			-262,94(11)	-922,07(79)
^{155}Eu	$5/2^+$			-261,48(11)	-950,4(1,0)
^{155}Gd	$3/2$	$z^9F_14f^75d6s6p$	17381	266,67(24)	76,2(6)
^{157}Gd	$3/2$			350,03(23)	78,6(6)
^{175}Lu	$7/2^+$	$^4F_{3/2}4f^{14}5d6s6p$	17432	-926,49(35)	1771,9(3,4)
^{176}Lu	7^-			-652,10(36)	2492,9(6,2)

The values of constants A and B for the lower levels are in good agreement with reported more accurate values obtained by the radio-frequency technique [3-5]. This points to the fact that the obtained values have no methodical error and that the data processing technique used was adequate. The values of upper level constants A and B are known for the isotopes ^{151}Eu, ^{153}Eu [13], ^{175}Lu and ^{176}Lu [14] (they were measured by laser techniques similar to the technique used in our work). There is good agreement for both Eu isotopes. As for the Lu isotopes, the discrepancy exceeds the combined error. However the ratios of constants A and B for the Lu isotopes, which are necessary for the HFA to be found, are practically the same. The values of

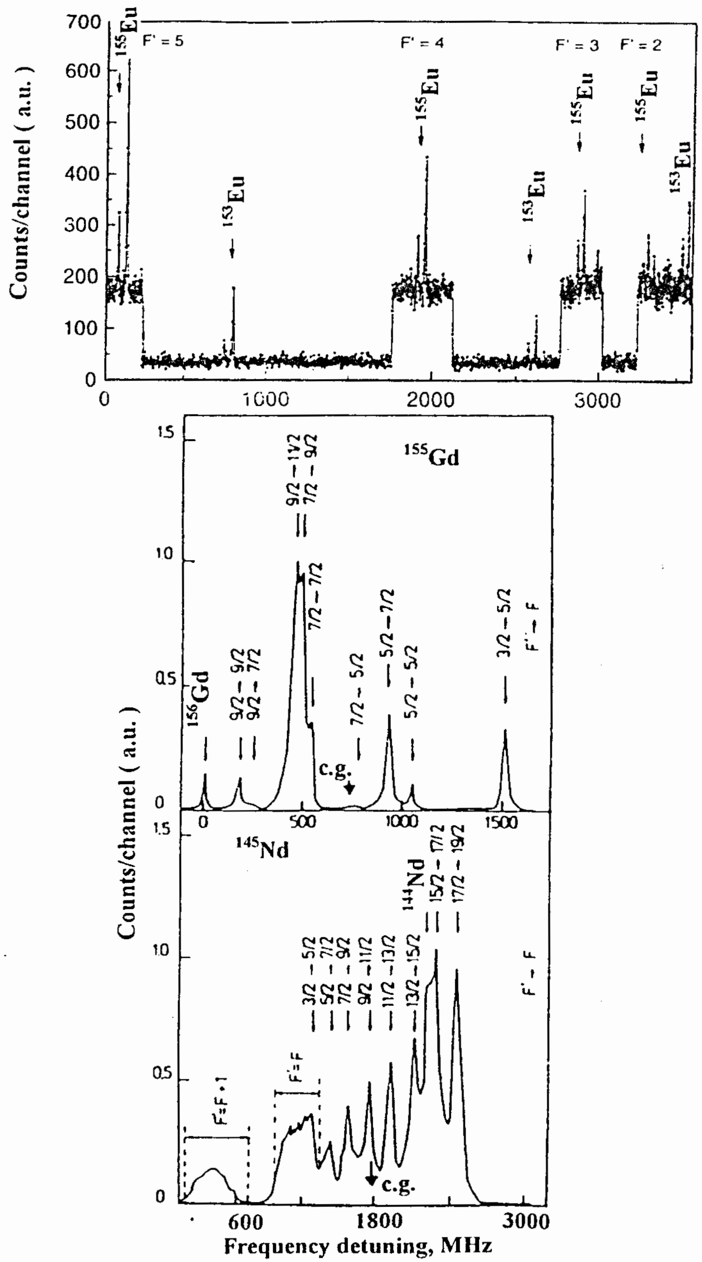

Fig.2. The resonance laser-induced fluorescence spectra of Nd, Eu, and Gd are presented. In the case of ^{155}Eu the scan velocity for recording the peaks was about ten times lower then the one of the ^{153}Eu peaks in order to obtain higher statistics. The flag-pattern groups of ^{155}Eu are indicated by the total quantum number F′ of the upper level.

constants A and B for the upper levels of the Nd and Gd isotopes as well as for both levels of ^{155}Eu have been determined for the first time.

Presented in Table 3 are the values of the HFA for all the pairs of odd REE isotopes that were studied. They were derived by comparing constants A for the upper and lower levels. To make the picture complete, the HFA values are also presented for the Nd [15] and Gd [16] isotopes. Those values were obtained on the basis of metastable state constants A measured by the radio-frequency method (the configuration of metastable states is characterised by an unpaired electron, therefore they are sensitive to spatial distribution of nuclear magnetism).

Table 3. HFA values for some excited states of REE atoms.

Isotopes	Term	A_1/A_2 (ex)	B_1/B_2 (ex)	$^1\Delta^2$, %
^{143,145}Nd	Z $^5H_5$	1,6050(24)	1,83(60)	-0,22(15)
[15]	$^7L_{6-11}$	1,60975(2)	1,8957(7)	0,07(1)
^{151,153}Eu	Z $^6P_{5/2}$	2,2483(8)	0,3845(9)	-0,74(4)
^{153,155}Eu	Z $^6P_{5/2}$	1,0056(5)	0,969(9)	-0,26(38)
^{155,157}Gd	Z $^9F_2$	0,7618(8)	0,966(12)	0,090(12)
[16]	$^{11}F_{3-8}$	0,76180(4)	0,9387(1)	0,090(21)
^{175,176}Lu	$^4F_{3/2}$	1,4208(9)	0,7107(25)	0,84(7)

For Gd isotopes, the HFA values are in good agreement with our data, whereas for Nd isotopes, they exceed the combined error. The discrepancy seems to be due either to the neglected contribution of the effects of higher orders or to excited states having different fractions of admixed $s_{1/2}$ or $p_{1/2}$ electrons.

TAKING ACCOUNT OF THE EFFECTS OF HIGHER ORDERS

Before deriving the HFA values from measured constants A, it is necessary to take account of the other effects that influence the HFS magnetic dipole constants and thus contribute to experimental HFA values (those effects are dealt with in work [17]). In REE atoms, the most essential effect is non-diagonal hyperfine interaction between the levels. This interaction results in repulsion of their HFS components of the same value of total moment F [11]. The components are shifted by

$$\Delta\nu = \sum_i \frac{\left|\langle\Psi(JIF)H_{HFS}\Psi'(J'IF)\rangle\right|^2}{\nu(JIF)-\nu(J'IF)}, \tag{5}$$

where the numerator is the square of the atomic level radiation transition matrix element; and the denominator, the interlevel distance. Expression (5) indicates that the neighbouring levels make the largest contribution to causing the HFS components to shift. In the case of the ground state, the largest contribution is due to the other levels of the same term with the known components of the wave function. This allows one to correctly calculate the matrix elements for the radiation transitions of different multipolity between the HFS components of the different levels of a term. Such calculations, done for M1 and E2 transitions, showed that for all the elements studied, the HFS components of the ground term levels are shifted due to non-diagonal hyperfine interaction by no more than 10 kHz (the similar result was obtained in work [4] for the odd isotopes of Nd). That the HFS of the ground term levels are weakly affected by this effect can be judged by the HFA values presented in Table 1. As indicated above, those levels are affected by spatial distribution of nuclear magnetism to a essentially smaller degree due to the presence of paired s-electrons, and the low values of HFA ($<10^{-4}$) are indicative of the other effects of higher orders being small.

In the case of excited states, the picture is not so evident owing to a number of levels of different terms being likely to reside in the immediate vicinity of the state being considered. Therefore the contributions of the non-diagonal interactions due to all the neighbouring levels should be calculated. For the majority of them, the components of the wave function are unknown, and unlike the case of the ground term levels, the radiation transition matrix elements can be calculated with great uncertainty. Therefore an approach was applied that uses the single-electron matrix elements for electrons in pure states $4f_{7/2}$, $4f_{5/2}$, $5d_{5/2}$, $5d_{3/2}$ and $6s_{1/2}$ (a mixture of those states does determine the wave function of each of the levels) and the formulae proposed in work [18]. To this end, the relativistic wave functions for electrons in the indicated states were found by solving Dirac's equation in the middle field pre-calculated by the Hartry-Fok-Sleter method. The wave functions thus obtained allowed the non-diagonal matrix elements to be calculated. To do this, the known expression was used [11]

$$M(\lambda)=\int_0^\infty (f_1 g_2 + f_2 g_1)\frac{dr}{r^3}, \qquad (6)$$

where f and g are the radial wave functions. Those calculations showed that for any pure states and their mixtures at an interlevel distance of more than 100 cm^{-1}, the components are shifted by no more than 1 kHz. Hence the corrections for constants A don't exceed that magnitude, which is distinctly less than the error of our measurement, and they were not taken account of.

How great the contribution of those corrections can also be judged on the ratios of constants B for excited (Table 3) and ground (Table 1) states. Constants B are known to be more sensitive to effects of higher orders than constants A. Those ratios are seen to differ practically in all the cases by less than 2%, i.e.,the correction to constants B is no more than that magnitude and the correction to constants A is even much less. In all the elements studied, this consideration remains valid for the excited states chosen to determine the HFA. Therefore the corrections to constants A for the effects of higher orders can be neglected.

CONCLUSIONS

An analysis of the HFA values presented in Table 3 shows that the HFAs obviously are of a nuclear nature and reflect the distribution of the magnetic moments in the nucleus. Indeed, isotopes similar in nuclear structure (equal spins, close magnetic moments and quadrupole deformation parameters), ^{143,145}Nd, ^{153,155}Eu, ^{155,157}Gd, show minimum HFA values. At the same time, a change in nuclear deformation (^{151,153}Eu) or the adding of an odd neutron, which changes the ratio between the spin and orbital components of the nuclear magnetic moment (^{175,176}Lu), results in markedly greater HFA values.

The measurements carried out have showed that the laser based technique of spectral measurement can be successfully used in precision measurement of HFS magnetic dipole constants, which enable the HFA values to be determined. The obtained HFA values, corrected for the other effects of second order, allow one to judge the way in which the distribution of magnetism in the nucleus changes as the number of neutrons increases. For this purpose, it is necessary to take the $s_{1/2}$-related part of constant A and do calculations, using the nuclear model suitable to the region of interest.

The authors would like to express their gratitude to Prof. Yu.Ts. Oganessian and Prof. M.G. Itkis for supporting the work, to Prof. Yu.E. Penionzhkevich and Prof. T.T. Inamura for the helpful discussions.

The work was supported by the Russian Fund of Fundamental Research (Grant No. 00-02-16674) and the Alexander von Humbold Fund.

REFERENCES

1. Bohr A., Weisskopf V.W. // Phys. Rev., 1950, V.**77**, P.94-98
2. Tanihata I., Hamagaki H., Hashimoto O. et. al. // Phys. Rev. Lett., 1985, V.**55**, P.2276-2280.
3. Childs W., Goodman L.S. // Phys. Rev. A, 1972, V.6, P.1772-1778.
4. Childs W., Goodman L.S. // Phys. Rev. A, 1972, V.6, P.2011-2017.
5. Sandars P.G.H., Woodgate G.K. // Proc. Roy. Soc. A, 1960, V.**257**, P.269-281.
6. Fuller G.H., Cohen V.W. // NDT, 1969, V.**A5**, P.433-612.
7. Raghavan P. // ADNDT,1989, V.**42**, P.189-310.
8. Borisov S.K., Gangrsky Yu.P., Gradecny C. et. al. // Phys. JETF, 1987, V.**66**, P.882.
9. Gangrsky Yu.P., Marinova K.P., Markov B.N. et. al . // Izv. Akad. Nauk USSR, ser. Fiz., 1985, V.**49**, P.2261-2268.
10. Gangrsky Yu.P., Zemlyanoi S.G., Izosimov I.N. et. al. // PTE, 1990, № **1**, P.168.
11. Kopfermann H. // Nuclear Moments, 1958, Academic Press, New York.
12. Anastassov A., Gangrsky Yu.P., Genova B. et. al. // Optica and Spectroscopy, 1996, V.**81**, P.191-196.
13. Eliel E.R., van Leeuwen K.A.H., Hogervorst W. // Phys. Rev. A, 1980, V.**22**, P.1491-1499.
14. Brennner T., Büttgenbach S., Ruppercht W., Träber F. // Nucl. Phys A, 1985, V.**440**, P. 407-423.
15. Childs W. // Phys. Rev. A, 1991, V.**44**, P.760-769.
16. Childs W. // Phys. Rev. A, 1989, V.**39**, P.4956-4966
17. Atomic Energy Levels, the Rare-Earth Elements, Natl. Bur. Stand (US), Circ. № **60**, Edited by W.C.Martin, R.Zalubas, L.Hagen (Washington, D.C. 1978).
18. Schwartz C. // Phys. Rev., 1955, V.**97**, P.380-391.

HYPERFINE ANOMALY IN THE LANTHANIDES

J. R. Persson
Kristianstad University
SE-291 88 Kristianstad, Sweden
jonas.persson@mna.hkr.se

July 30, 2001

Abstract

The hyperfine anomaly has been obtained for a number of elements, however there does not exist any systematic studies of the isotopic effects other than in a few cases. In this contribution a summary of hyperfine anomaly studies in the lanthanides is presented together with a prospect for systematic studies.

1 Introduction

The influence on the hyperfine structure (hfs) of the finite size of the nucleus was first considered by Bohr and Weisskopf [1]. They calculated the hyperfine interaction of $s_{1/2}$ and $p_{1/2}$ electrons in the field of an extended nucleus, and showed that the magnetic dipole hyperfine interaction constant a for an extended nucleus is generally smaller than that expected for a point nucleus. Isotopic variations of magnetic moments become larger than those in the point dipole interaction when there are different contributions to the hfs from the orbital and spin parts of the magnetisation in the case of extended nuclei. The fractional difference between the point nucleus magnetic dipole hyperfine interaction constant and the constant obtained for the extended nuclear magnetisation is commonly referred to as the Bohr-Weisskopf (BW) effect [2]. The magnetic dipole hyperfine interaction constant a can therefore be written as

$$a = a_{point}(1 + \epsilon_{BW}) \tag{1}$$

where ϵ_{BW} is the BW-effect; and a_{point},the a constant for a point nucleus. Because electronic wavefunctions cannot be calculated with high accuracy in complex atoms it is not always possible to determine ϵ_{BW} directly. In the case of hydrogen-like ions and muonic atoms it is possible to extract the BW-effect directly. The BW-effect is,as the isotope shift, dependent on both a nuclear part as well as an atomic part. The atomic part is essentially the electron density within the nucleus. The nuclear part, i. e., the distribution of nuclear magnetisation, can be calculated using different nuclear models [2, 3]. However, it is impossible to experimentally determine the BW-effect direct, only the difference of the BW-effect in two isotopes, the so-called hyperfine anomaly, can be determined experimentally. Therefore one compares the ratio of the measured hfs constants for two isotopes (or isomers) of the same element with the independently measured ratio of the nuclear magnetic dipole moments to extract the hyperfine anomaly, ${}^1\Delta^2$, for the isotopes 1 and 2, and a given atomic state:

$$1 + {}^1\Delta^2 = \frac{a^{(1)}}{a^{(2)}} \frac{\mu_I^{(2)}/I^{(2)}}{\mu_I^{(1)}/I^{(1)}} \approx 1 + \epsilon_{BW}^{(1)} - \epsilon_{BW}^{(2)} \tag{2}$$

For electrons with a total angular momentum $j > 1/2$ the anomalies may be disregarded as the corresponding wavefunctions (electron-densities) vanish at the nucleus. If we study the hyperfine anomaly for different atomic states we find a variation of the values. We have a state dependent hyperfine anomaly, the differences in values in different states can be large .The reason for these differences is due to that the hyperfine interaction consists of three parts[4, 5], orbital, spin-orbit and contact (spin) interaction. Only the contact interaction contributes to the hyperfine anomaly. Thus we can rewrite the general magnetic dipole hyperfine interaction constant as

$$a = a_{nc} + a_c , \tag{3}$$

where a_c is the contribution due to the contact interaction of s and $p_{1/2}$ electrons, respectively, and a_{nc} is the contribution due to non-contact interactions. The experimentally determined hyperfine anomaly, which is defined with the total magnetic dipole hyperfine anomaly constant a, should then be rewritten to obtain the relative contribution to the hyperfine anomaly:

$${}^1\Delta^2_{exp} = {}^1\Delta^2_c \frac{a_c}{a} , \tag{4}$$

where ${}^1\Delta^2_c$ is the hyperfine anomaly due to the contact interaction, that is, for an s- or p-electron. One can show that a_c is proportional to $g_J - 1$ which gives an indication on the magnitude of $\frac{a_c}{a}$. So far we have only considered direct interactions between the electron and the nucleus, in order to get a complete picture we should include electron- electron interactions. One interaction, which can influence the hyperfine interaction constant, is the polarisation of the electron core [4], which may give a substantial contribution to the experimental hyperfine anomaly [2]. Core polarisation can be seen as an excitation of a d-electron, which does not give any contribution to the anomaly, to an s-electron, which gives a large hyperfine anomaly. Since the hyperfine anomaly (${}^1\Delta^2_s$), is independent of n, it is possible to use the hyperfine anomaly to obtain values of the core-polarisation [2, 6].

2 Determination of the hyperfine anomaly

From the discussion above one is led to the conclusion that one need independent measurements of the nuclear magnetic moment in order to obtain the hyperfine anomaly, this is , however, not true. As has been shown by Persson [7], it is possible to extract the anomaly solely from hyperfine interaction constants, by comparing the hyperfine interaction constant ratio, for two isotopes, in at least two different atomic levels. That is:

$$\frac{a_A^{(1)}/a_A^{(2)}}{a_B^{(1)}/a_B^{(2)}} \approx 1 + {}^1\Delta_s^2\left(\frac{a_s^A}{a^A} - \frac{a_s^B}{a^B}\right), \tag{5}$$

where A and B denote different atomic levels and 1 and 2 denote different isotopes. The ratio between the two magnetic dipole hyperfine interaction constant ratios for the two isotopes will be dependent only on the difference of the contact contributions of the two atomic states and the hyperfine anomaly for the s-electron. It should be noted that the ratio a_s/a is isotope independent. Once it has been determined for one isotopic pair, the ratio can be used for all isotopic pairs, which is very useful in the study of hyperfine anomaly in radioactive isotopes. The ratio can be determined in two ways; either by making an analysis of the hyperfine interaction and deducing a_s/a from the analysis, or by using a known hyperfine anomaly.

In order to determine the hyperfine anomaly one needs to know either the nuclear magnetic dipole moment and one a-constant or two a-constants[2, 7]. Since the hyperfine anomaly is normally very small (1% or less) it is necessary to have high accuracy of the values use, as a rule better than 10^{-4}[2]. In the case of stable isotopes there is no major problem to measure the nuclear magnetic dipole moment, with NMR or ABMR, while unstable isotopes are more difficult to measure, a review of different methods can be found in [8, 2]. In most cases there do not exist any high precision measurements of the nuclear magnetic dipole moment. However, there might exist measurements of two a-constants, especially if the unstable isotopes nuclear charge radius has been measured by means of laser spectroscopy [8]. In order to obtain the hyperfine anomaly one needs to measure the a-constants with an accuracy better than 10^{-4}. This can be done by laserspectroscopy when the a-constant is larger than 1000 MHz. The use of radiofrequency spectroscopy, in beams or traps, is an alternative since the accuracy is at least 2 orders of magnitude better.

3 Hyperfine anomaly in the lanthanides

The lanthanides have been an area of interest from an atomic as well as a nuclear physics view. Even if there has been done systematic studies of the atomic structure as well as for the isotope shift, the BW-effect and hyperfine anomaly have not been well studied. This is despite the fact that one of the largest state dependent hyperfine anomalies has been observed in Eu [9, 10]. One reason for this might be that the nuclear magnetic moments are not known with high accuracy, another being the rather complicated atomic structure. The status of the BW-effect investigations in the lanthanides is summarised in table 1. It is interesting to note that the BW-effect has been deduced from muonic atoms in three of the lanthanides, giving a possibility to extract the BW-effect for a series of isotopes and making a direct comparison with calculations. The BW-effect for muonic atoms is given in table 2 [2].

Table 1: Status of BW investigations in the lanthanides.

La	Muonic
Pr	Muonic
Nd	Anomaly extracted from a-factors
Sm	Under analysis
Eu	Muonic,Standard method, Anomaly extracted from a-factors
Gd	Anomaly extracted from a-factors
Dy	State dependent anomaly extracted from a-factors,
Yb	Standard method
Lu	Standard method, state dependent anomaly

Table 2: BW-effect from muonic atoms.

Isotope	ϵ_{BW}
^{139}La	-0.156(46)%
^{141}Pr	-0.383(23)%
^{151}Eu	-0.63(13)%

The hyperfine anomaly has been extracted in four elements and isotope pairs. As we are only considering the s-electron anomaly here, we exclude the state dependent hyperfine anomaly that has been obtained in some of the elements. The values of the s-electron anomaly are given in table 3[2, 6].

We observe that Eu is a special case. We know the BW-effect from muonic atoms as well as the hyperfine anomaly. In addition, there have been done measurements of the hyperfine structure in a long chain of isotopes[11, 12, 13], making it possible to use the method of Persson [7]to extract the hyperfine anomaly. Concentrating on the odd isotopes we find that the hyperfine anomaly can be deduced for all odd isotopes from A=145 to A=155, the result is given in table 4.

One can clearly see the shape transition between ^{151}Eu and ^{153}Eu as the anomaly changes drastically. The hyperfine anomaly for the lighter isotopes seems to be fairly constant, an indication that the magnetization does not change much from the spherical ^{145}Eu nucleus to ^{151}Eu. A bit

Table 3: Hyperfine anomaly in the lanthanides.

Isotopes	${}^1\Delta_s^2$
$^{143,145}Nd$	0.2034(63)%
$^{151,153}Eu$	-0.64(3)%
$^{155,157}Gd$	0.106(24)%
$^{171,173}Yb$	-0.386(5)%

Table 4: Hyperfine anomalies for odd Eu isotopes.

Isotope	${}^{A}\Delta_s^{151}(\%)$
145	-0.08(15)
147	-0.12(17)
149	-0.19(16)
151	0
153	-0.64(3)
155	-0.91(37)(exp)

Table 5: BW-effect in Eu, experimental and calculations.

Isotope	$\epsilon_{BW,exp}(\%)$	$\epsilon_{BW,calc}$ Particle-Rotor	$\epsilon_{BW,calc}$[14] Core-excitations	
			I	II
${}^{151}Eu$	-0.63(13)	-1.489	-1.046	-1.036
${}^{153}Eu$	0.01(16)	-0.056	-0.919	-1.039
${}^{155}Eu$	0.28(50)	-0.052	-0.919	-1.035

surprising is the difference between ${}^{153}Eu$ and ${}^{155}Eu$,as these nuclei are almost identical, with respect to the nuclear moments and energy levels, still the error is large enough allowing for an anomaly close to zero. With these experimental results we can make comparisons with theoretical calculations. Since we know the BW-effect for ${}^{151}Eu$, can we make a direct comparison between experimental and theoretical values. The experimental results of A=151-155 are compared with the results of Asaga et al. [14], who use core-excitations to calculate the BW-effect. A comparison with results from a particle-rotor calculation is also done. The results are given in table 5. As can be seen both methods reproduce the trend. However, it seems like the particle-rotor calculations are a bit better, although the BW-effect is a factor 2.4 too large. Both methods indicate the lighter isotopes have the same BW-effect as ${}^{151}Eu$. The conclusion would be that the particle-rotor formalism works reasonably well for Eu, making it interesting to extend the investigations to neighbouring elements.

4 Future projects

As has been shown in the case of Eu, it is possible to obtain a lot of information on the hyperfine anomaly without knowing the nuclear magnetic moment of the isotopes under study. In this section a discussion on the possibilities of obtaining the BW-effect in the lanthanides will be performed.

The lanthanides are characterised by a vast number of low-lying energy states [15], due to three open shells. A general feature found is the small values of the hyperfine interaction constants in the low lying levels of the $4f^n6s^2$ and $4f^{n-1}5d6s^2$ configurations, where neither free s-electron nor core-polarisation contribute to the hyperfine interaction [16]. In other words we have a number of states where the hyperfine anomaly will be practically zero. These states are therefore suitable in determining the ratio of the nuclear magnetic dipole moment. However, the a-constants in these states are in most cases small ($\leq$ 100 MHz) so the accuracy obtained by laserspectroscopy is normally not sufficient for determining the hyperfine anomaly. The use of rf-spectroscopy is, therefore, preferred. If we can not make use of the zero-anomaly states, we need to find at least 2 states where the factor a_s/a or a_c/a differ substantially. Since a_s/a is proportional to $g_J - 1$, we can easily find suitable candidates. The best choice is the lowest J-value and one or two of the higher J-values within a multiplet. One caveat is that the multiplet, and the states, should be close to pure LS-coupling. This has been found to be the case in many of the lowest lying multiplets in both atoms and ions of the lanthanides.

As the number of states with excitation energy $\leq$10000 cm^{-1} is high in most of the lanthanides there are plenty of suitable transitions that can be studied with simple atomic beam sources. However, in order to populate other states than the ground state, one can easily loose signal. An alternative would be to combine rf-measurements of the atomic ground state, which normally has a small a-constant, with measurements of the ground state a-constant in the ion. The ground states of singly charged lanthanide ions belong normally to a configuration with an un-paired s-electron. One might also consider doing ion-trap experiments using both singly- and doubly- charged ions, again in order to have one state with an unpaired s-electron.

As the prospect for systematic measurements of the hyperfine anomaly in the lanthanides probably involves more than one experimental technique, it seems like an international collaboration would be preferable.

5 Conclusion

There exist very little data on the hyperfine anomaly in the lanthanides, but it has been shown here that it is possible to gain more data with rather simple means. However, a systematic study of the hyperfine anomaly can be rather difficult and would therefore involve several techniques and laboratories. The conclusion would be to form a network of the laboratories, in order to promote the study of hyperfine anomaly. It seems feasible that , within a not too distant future, the hyperfine anomaly is well known and, hopefully, well understood in the lanthanides.

References

[1] A. Bohr and V.F. Weisskopf, Phys. Rev. **77**, 94 (1950)

[2] S. Büttgenbach, Hyperfine Int. **20**, 1 (1984)

[3] T. Fujita and A. Arima, Nucl. Phys. **A254**, (1975) 513

[4] I. Lindgren and J. Morrison, *Atomic Many-Body Theory*

NUCLEAR ANAPOLE MOMENTS. YESTERDAY, TODAY, TOMORROW

V.F. Dmitriev[1] and I.B. Khriplovich[2]

Budker Institute of Nuclear Physics, 630090 Novosibirsk, Russia

Abstract

We discuss the present state of the problem of nuclear anapole moments. Both experimental and theoretical results are presented. A new possibility is pointed out

1. Forty-five years ago it was pointed out [1] that in a system which has no definite parity a special distribution of magnetic field may arise. It cannot be reduced to common electromagnetic multipoles, such as dipole or quadrupole moments, but looks like the magnetic field created by a current in toroidal winding. This special source of electromagnetic field was called (by A.S. Kompaneets) "anapole".

For many years the anapole remained a theoretical curiosity only. The situation has changed due to the investigation of parity nonconservation (PNC) in atoms. Since these tiny effects increase with the nuclear charge Z, all the experiments are carried out with heavy atoms. The main contribution to the effect is independent of nuclear spin and caused by the parity-violating weak interaction of electron and nucleon neutral currents. This interaction is proportional to the so-called weak nuclear charge Q which is numerically close (up to the sign) to the neutron number N. Thus, in heavy atoms the nuclear-spin-independent weak interaction is additionally enhanced by about two orders of magnitude. Meanwhile, the nuclear-spin-dependent effects due to neutral currents not only lack the mentioned coherent enhancement, but are also strongly suppressed numerically in the electroweak theory. Therefore, the observation of PNC nuclear-spin-dependent effects in atoms looked absolutely unrealistic.

However, it was demonstrated [2, 3] that these effects in atoms are dominated not by the weak interaction of neutral currents, but by the electromagnetic interaction of atomic electrons with nuclear anapole moment (AM). It should be mentioned first of all that the magnetic field of an anapole is contained within it, in the same way as the magnetic field of a toroidal winding is completely confined inside the winding. It means that the electromagnetic interaction of an electron with the nuclear AM occurs only as long as the electron wave function penetrates the nucleus. In other words, this electromagnetic interaction is as local as the weak interaction, and they cannot be distinguished by this interaction. The nuclear AM is induced by PNC nuclear forces and is therefore proportional to the same Fermi constant $G = 1.027 \times 10^{-5} m^{-2}$ (we use the units $\hbar = 1, c = 1$; m is the proton mass), which determines the magnitude of the weak interactions in general and that of neutral currents in particular. The electron interaction with the AM, being of the electromagnetic nature, introduces an extra small factor into the effect discussed, the fine-structure constant $\alpha = 1/137$. Then, how it comes that this effect is dominating? The answer follows from the same picture of a toroidal winding. It is only natural that the interaction discussed is proportional to the magnetic flux through such a winding, and hence in our case to the cross-section of the nucleus, i.e., to $A^{2/3}$ where A is the atomic number. In heavy nuclei this enhancement factor is close to 30 and compensates essentially for the smallness of the fine-structure constant α. As a result, the dimensionless effective constant κ which characterizes the anapole interaction in the units of G is not so small in heavy atoms, but is numerically close to 0.3 (we use the same definition of the effective constant κ as in [2, 3]).

Nevertheless, the interaction discussed constitutes only about one percent of the main atomic PNC effect independent of the nuclear spin, which is due to the "weak" charge Q and is enhanced therefore as N. To single out the anapole interaction one should compare the PNC effects for different hyperfine components of an optical transition. The main effect, independent of the nuclear spin, will obviously be the same for all components. But the anapole contribution depends on the mutual orientation of the nuclear spin and the electron total angular momentum, and thus changes from one hyperfine component to another. The observation of this tiny effect is an extremely difficult problem, and it is no accident that the searches for the nuclear AM demanded many years of hard work by several groups [4 – 8].

At last, the nuclear anapole moment was experimentally discovered [9]. This result for the total effective constant of the PNC nuclear-spin-dependent interaction in ^{137}Cs is

$$\kappa_{tot} = 0.44(6). \tag{1}$$

To extract this number from experimental data, the results of atomic calculations [10, 11] were used; these calculations performed using different approaches are in excellent agreement, and there are good reasons to believe that their accuracy is no worth than 2-3%. If one excludes the neutral current nuclear-spin-dependent contribution from the above number, as well as the result of the combined action of the "weak" charge Q and the usual hyperfine interaction, the answer for the anapole constant will be

$$\kappa = 0.37(6). \tag{2}$$

Thus, the existence of an AM of the ^{137}Cs nucleus is reliably established. A beautiful new physical phenomenon, a peculiar electromagnetic multipole has been discovered.

2. But the discussed result does not reduce to only this. It brings valuable information on PNC nuclear forces. Of course, to this end it should be combined with reliable nuclear calculations. However, it is instructive to start, as it was done in [3]), with a rather crude approximation. Not only one assumes here that the nuclear spin **I** coincides with the total angular momentum of an odd valence nucleon, while the other nucleons form a core with the zero angular momentum. The next assumption is that the core density $\rho(r)$ is constant throughout the space and coincides with the mean nuclear density ρ_0. The last assumption, ascending to [12], is reasonable if the wave function of the external nucleon is mainly localized in the region of the core. Then simple calculations give the following result for the anapole constant [3]:

$$\kappa = \frac{9}{10} g \frac{\alpha\mu}{m r_0} A^{2/3}. \tag{3}$$

---

[1] e-mail address: dmitriev@inp.nsk.su

[2] e-mail address: khriplovich@inp.nsk.su

Here g is the effective constant of the P-odd interaction of the outer nucleon with the nuclear core, μ is the magnetic moment of the outer nucleon, $r_0 = 1.2$ fm. The A-dependence of this constant is very natural. Indeed, since the anapole corresponds to the magnetic field configuration induced by a toroidal winding, the AM value should be proportional to the magnetic flux, i.e., to the cross-section area of the nucleus, hence to $A^{2/3}$.

The so-called "best values" for the parameters of P-odd nuclear forces [13] result in $g_p = 4.5$ for an outer proton [3, 14, 15]. Thus obtained values for the nuclear AMs, which were investigated experimentally in [4 – 9], are presented in the first column of Table.

	[3]$^{a)}$	[3]$^{b)}$	[16]$^{c)}$	[17, 18]$^{d)}$	[19]$^{e)}$	[19]$^{f)}$	[20]$^{g)}$	[21]	[22]	[23]
^{133}Cs	0.37	0.28	0.14 (0.28)	0.27	0.33	0.26	0.22	—	0.15	0.21
^{203,205}Tl	0.49	0.43	—	0.27	0.42	0.40	0.37	0.24	0.24	0.10
^{209}Bi	0.51	0.35	—	0.27	0.45	0.29	0.30	—	0.15	—

Table

a)Calculation with formula (3). b)Woods-Saxon potential including spin-orbit interaction. c)Only the P-odd π-meson-exchange was calculated in [16]; we indicate in brackets what to our guess would be the result of [16] if the P-odd short-range were included. d)Our extrapolation of the results of [17, 18], from their values of g_p to $g_p = 4.5$. e)Oscillator potential, contribution of contact current included. f)Woods-Saxon potential, contributions of contact and spin-orbit currents included. g)Many-body corrections calculated in the constant-density approximation.

Various calculations of the nuclear AMs, going beyond simple analytical formula (3), (see the results in Table) can be roughly divided into two groups: the calculations within the independent particle model (IPM) using Woods-Saxon and oscillator potentials [3, 17 – 19], and the calculations including many-body effects [16, 20 – 23]. In fact, some of the many-body contributions were discussed in [17, 18] as well.

The analytical estimate (3) produces smooth $A^{2/3}$ behaviour, but certainly exaggerates the effect due to the assumption that the P-odd contact interaction with the nuclear core extends throughout the whole localization region of the unpaired nucleon. Indeed, the IPM calculations reveal certain shell effects quite pronounced in the values of κ for Tl and Bi (see Table). Both these nuclei are close to the doubly-magic ^{208}Pb. However, while the anapole moment of Tl nucleus in IPM is close to its analytical estimate, the anapole moment of Bi in IPM differs significantly both from the analytical formula and from the anapole moment of Tl. This difference can be attributed to the difference in the single-particle orbitals for the unpaired proton in Tl and Bi. The $3s_{1/2}$ wave function in Tl is concentrated essentially inside the nuclear core, while the $1h_{9/2}$ wave function in Bi is pushed strongly outside of it. By this reason the unpaired proton in Bi "feels" in fact much smaller part of the P-odd weak potential. An analogous suppression of the PNC interaction takes place for the outer $1g_{7/2}$ proton in Cs.

Various approaches were used as well in the many-body calculations [16, 20 – 23]. In one of them [20, 22] the random-phase approximation (RPA) with effective forces was employed to calculate the effects of the core polarization. In another approach [16, 23] large basis shell-model calculations were performed. However, in the last case there is a serious problem: the basis necessary to describe simultaneously the effects of both regular nuclear forces and P-odd ones is in fact too large. Therefore, some additional approximations were made in [16, 23] in order to reduce the size of the basis space.

Fortunately, the Tl nucleus is a rather special case in the many-body approach as well. Not only is it close to the doubly-magic ^{208}Pb, but its unpaired proton is $3s_{1/2}$, but not $1h_{9/2}$ as in Bi. This makes the effects of the core polarization here relatively small. Thus the density of states in Tl is reduced, and an effective Hamiltonian suitable for shell-model calculations can be constructed [24]. This Hamiltonian was used in [21] to calculate the anapole moment of Tl nucleus. The result of [21] and the RPA result of [22] for the thallium coincide, in spite of completely different descriptions of nuclear forces used in these works to calculate the core polarization. These results of [21, 22] differ essentially from the value obtained in [23] under extra assumptions: the closure approximation and further reduction of a three-body matrix element to the two-body one. It is also worth mentioning perhaps that in [21, 22] and [23] different parameterizations of the parity violating nuclear forces have been used.

Thus we believe that the theoretical predictions for the AMs of nuclei of the present experimental interest, can be reasonably summarized now, at "best values" of P-odd constants, as follows:

$$\kappa(^{133}\mathrm{Cs}) = 0.15 - 0.21, \quad \kappa(^{203,205}\mathrm{Tl}) = 0.24, \quad \kappa(^{209}\mathrm{Bi}) = 0.15. \tag{4}$$

We believe also that there are good reasons to consider these predictions as sufficiently reliable, at the accepted values of the P-odd nuclear constants.

The comparison of the value (4) for the cesium AM with the experimental result (2) indicates that the "best values" of [13] somewhat underestimate the magnitude of P-odd nuclear forces. In no way is this conclusion trivial. The point is that the magnitude of parity-nonconserving effects found in some nuclear experiments is much smaller than that following from the "best values" (see review [25]). In all these experiments, however, either the experimental accuracy is not high enough, or the theoretical interpretation is not sufficiently convincing. The experiment [9] looks much more reliable in both respects. Therefore, in line with its general physics interest, the investigation of nuclear AMs in atomic experiments is first-rate, almost table-top nuclear physics.

3. But what next? Here first of all one should point out perhaps a problem we still have not mentioned. The point is that the experimental result for the thallium AM, $\kappa = -0.22 \pm 0.30$ [7], does not comply with the theoretical prediction for it presented in (4) (the disagreement will be even more serious if one assumes that the nuclear P-odd constants are larger than the "best values" of [13] as indicated by the measurement of the cesium AM). Obviously, it is highly desirable for this problem to be cleared up.

As mentioned already, the performed experiments aimed at the detection and measurement of nuclear AMs are extremely difficult. This is why experimentalists are looking for new approaches to the problem. Few directions are pursued here (see, for instance, review [26]). We will describe below one of them, which looks at the moment most promising. It is a proposal to measure PNC in the strongly forbidden $6s^2\ ^1S_0 \rightarrow 6s5d\ ^3D_1$ transition in ytterbium [27]. The advantage of this transition is that the PNC effect in it is more than 100 times larger than in cesium. The enhancement is due to the fact that the $^3D_1$ state is close ($\Delta E \simeq 600$ cm^{-1}) to a level of opposite parity $^1P_1$ which composition is $6s6p$ with a strong admixture of $5d6p$. Due to this $5d6p$ component, there is large PNC mixing between $^3D_1$ and $^1P_1$. The relatively simple atomic spectrum of Yb allows one to perform atomic calculations of the PNC effect with an accuracy about 20% [27 – 29].

Ytterbium has seven stable isotopes between A=168 and A=176, two of them, ^{171}Yb, I=1/2 and ^{173}Yb, I=5/2, with non-zero nuclear spin can be used to measure the AMs. With a valence neutron in these nuclei, such measurements will be a valuable complement to the cesium anapole result in the determination of the PNC nuclear constants.

Moreover, one more transition in Yb, $6s^2\ ^1S_0 \rightarrow 6s5d\ ^3D_2$, is of a special interest for the anapole measurements [30]. PNC mixing between $^3D_2$ and $^1P_1$ states (their separation is $\Delta E \simeq 300$ cm^{-1}) is only due to the P-odd interaction electrons with nuclear spin, $\delta J = 1$. Thus, in this transition the anapole interaction will be the main source of P-odd effects, rather than a small correction to the dominant nuclear-spin-independent interaction as it is the case with $^1S_0 \rightarrow ^3 D_1$.

Some preliminary spectroscopic measurements in ytterbium, related to the discussed experiments, have been performed. They resulted in the lifetime of the $^3D_1$ state, 380(30) ns [31], as well as in the values of the E2 amplitude of the $^1S_0 \rightarrow ^3 D_2$ transition, 0.65(3) ea_0^2 [32], and of the strongly forbidden M1 amplitude of the $^1S_0 \rightarrow ^3 D_1$ transition, $1.33(26) \times 10^{-4}\,\mu_B$ [33].

***

Seventy-five years ago studies of atomic hyperfine structure gave the first clue to the existence of nuclear magnetic moments. Since then atomic and molecular spectroscopy have served as a source of valuable information on nuclear properties, such as multipole moments and the radii of nuclei. Now a new chapter in this story has opened: optical spectroscopy brings data on parity-nonconserving nuclear forces.

Acknowledgements We are grateful to Yu.P. Gangrsky and B.N. Markov for their interest to the problem and the suggestion to write this note. The work was supported in part by the Grant No. 00-15-96811 for Leading Scientific Schools, and by the Federal Program Integration-2001.

References

[1] Ya.B. Zel'dovich, Zh. Eksp. Teor. Fiz. **33** (1957) 1531 [Sov. Phys. JETP **6** (1957) 1184] (the paper contains also the mention of the analogous results obtained by V.G. Vaks.)

[2] V.V. Flambaum, I.B. Khriplovich, Zh. Eksp. Teor. Fiz. **79** (1980) 1656 [Sov. Phys. JETP **52** (1980) 835]

[3] V.V. Flambaum, I.B. Khriplovich, O.P. Sushkov, Phys. Lett. **B146** (1984) 367

[4] M.S. Noecker, B.P. Masterson, C.E. Wieman, Phys. Rev. Lett. **61** (1988) 310

[5] M.J.D. Macpherson et al., Phys. Rev. Lett. **67** (1991) 2784

[6] D.M. Meekhof et al., Phys. Rev. Lett. **71** (1993) 3442

[7] P.A. Vetter et al., Phys. Rev. Lett. **74** (1995) 2658

[8] N.H. Edwards et al., Phys. Rev. Lett. **74** (1995) 2654

[9] C.S. Woods et al., Science **275** (1997) 1759

[10] P.A. Frantsuzov, I.B. Khriplovich, Z. Phys. **D7** (1988) 297

[11] A.Ya. Kraftmakher, Phys. Lett. **A132** (1988) 167

[12] F. Curtis Michel, Phys. Rev. **B133** (1964) 329

[13] B. Desplanques, J.F. Donoghue, B.R. Holstein, Ann. Phys. **124** (1980) 449

[14] V.F. Dmitriev et al., Phys. Lett. **B125** (1983) 1

[15] V.V. Flambaum, V.B. Telitsin, O.P. Sushkov, Nucl. Phys. **A444** (1985) 611

[16] W.C. Haxton, E.M. Henley, M.J. Musolf, Phys. Rev. Lett. **63** (1989) 949

[17] C. Bouchiat, C.A. Piketty, Z. Phys. **C49** (1991) 91

[18] C. Bouchiat, C.A. Piketty, Phys. Lett. **B269** (1991) 195; erratum **B274** (1992) 526

[19] V.F. Dmitriev, I.B. Khriplovich, V.B. Telitsin, Nucl. Phys. **A577** (1994) 691

[20] V.F. Dmitriev, V.B. Telitsin, Nucl. Phys. **A613** (1997) 237

[21] N. Auerbach, B.A. Brown, Phys. Rev. **C60** (1999) 025501

[22] V.F. Dmitriev, V.B. Telitsin, Nucl. Phys. **A674** (2000) 168

[23] W.C. Haxton, C.-P. Liu, M.J. Ramsey-Musolf, nucl-th/0109014

[24] L. Rydstrom et al., Nucl. Phys. **A512** (1990) 217

[25] E.G. Adelberger, W.C. Haxton, Ann.Rev.Nucl.Part.Sci. **35** (1985) 501

[26] D. Budker, in Proceedings of the Fifth International WEIN Symposium, p.418 (World Scientific, Singapore, 1999)

[27] D. DeMille, Phys. Rev. Lett. **74** (1995) 4165

[28] S. Porsev, Yu. Rakhlina, and M.Kozlov, Pis'ma Zh. Eksp. Teor. Fiz. **61** (1995) 449 [Sov. Phys. JETP Pis'ma **61** (1995) 459]

[29] B.P. Das, Phys. Rev. **A56** (1997) 1635

[30] I.B. Khriplovich, unpublished (1995)

[31] C.J. Bowers et al., Phys.Rev. **A53** (1996) 3103

[32] C.J. Bowers et al., Phys.Rev. **A59** (1999) 3513

[33] J.E. Stalnaker et al., physics/0201026

THE COHERENT REPOPULATION OF HYPERFINE STRUCTURE BY BICHROMATIC RESONANCE WAVE. NUCLEAR SPECTROSCOPY AND QUANTUM COMPUTING

D.F.Zaretsky, S.B. Sazonov

Russian Scientific Center "Kurchatov Institute", 123182 Moscow, Russia

The effect of coherent repopulation of atomic levels by bichromatic laser wave was investigated by different authors. [1,2] The coherent level repopulation occurs in the case of resonant interaction of Zeeman hyperfine structure components with a bichromatic radiofrequency wave also.[3] This repopulation is real due to the coherence of transition amplitudes on the common levels.

In this work the repopulation was shown to be quite prononced even in the case of equal initial population. But there should be fulfiled several conditions: 1) the electromagnetic field has to be pulsed; 2) the pulse time and Rabi-period have to be much less than all relaxation times of hyperfine states in a medium. Thus we assume that the resonant interaction of a system with bichromatic field should be sufficienty stronger than the interaction with the thermostate, and the Rabi period is shorter than the time of the pulse of the field.

The bichromatic field is:

$$E(t)=E_1\cos(\omega_1 t+\varphi)+E_2\cos(\omega_2 t). \qquad (1)$$

We have considered the interaction of the bichromatic wave and the three level quantum system (Fig.1). We suppose that one componet is in resonance with transition between the level number one and another component is in resonance with transition between the level number two and the common level number three:

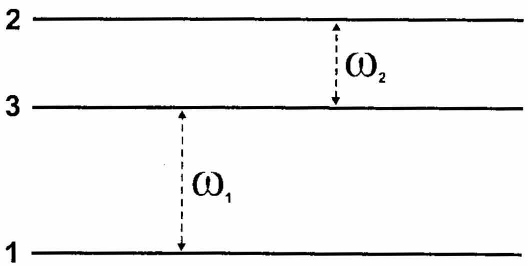

FIGURE 1. Three level quantum system

The hamiltonian of the atom+rf field system has the form $H(t)=H_0+V(t)$, where H_0 is the hamiltonian of a system of quantum levels with the characteristic wave functions F_i,and $V(t)$ is the interaction operator for this system with the rf-field.

Since the time duration for this system to interact with the field is shorter than all relaxation times,it is possible to examine the process assuming that the system is in a state described by a wave function which can be represented as a superposition of the functions F_i:

$$\Psi(t)=\sum_i b_i(t)F_i \,. \qquad (2)$$

The amplitudes $b_i(t)$ are the population amplitudes of the *i*th levels, which satisfy the following initial conditions: $b_i(0)=A_i\exp(i\alpha_i)$, where A_i is the initial amplitude of population of the level *i*, with $A_i^2=|b_i(0)|^2$, and α_i is the initial phase of its population amplitude.

Since the interaction time is shorter than any of the relaxation times, there are essentially no stochastic pertubations of the system during the interaction process. Thus, the amplitude $b_i(t)$ at any time is proportional to the constant phase factor $\exp(i\alpha_i)$ and can be represented in the form $b_i(t)=a_i(t)\exp(i\alpha_i)$, where at any time the functions $a_i(t)$ are independent of the α_i and at $t=0$ they are given by $a_i(0)=A_i$.

The eigenfunctions F_i of the hamiltonian H_0 have an orbitrary constant phases but we are choosing this functions in the form $F_i=F_i'\exp(-i\alpha_i)$, where the F_i' are independent of the phases α_i. Than the formula (2) takes the form:

$$\Psi(t)=\sum_i a_i(t)F_i' \,. \qquad (3)$$

This means that the result of coherent repopulation of the levels is independent of the initial phases of the level population

The amplitudes $a_i(t)$ should be obtained by the solution of the time-dependent Schrödinger equation. In addition, we assume that the phases of the components of the bichromatic wave and their difference φ also remain constant during the interaction of the system with the field. As a result we have for the amplitude of level "3" population:

$$a_3(t)=-A_3\cos(\Omega t)-i[A_2V_2\exp(-i\varphi)+A_1V_1]*\sin(\Omega t)/\Omega, \quad (4)$$

where V_1, V_2 are the matrix elements for the transitions 1<—>3 and 2<—>3 respectively. $\Omega=(V_1^2+V_2^2)^{1/2}$ is the Rabi frequency.

There are two interesting cases $\Omega t=\pi/2$ and $\Omega t>>1$. Let all $A_i=1$, $V_1=V_2$. Then in the first case for $\varphi=\pi$ the second term of $a_3(t)$ is zero, and we have $a_3(t)=0$!!!

In the second case we may average the population over time (over many periods). For the same parameters as before we have: $\overline{a_{33}}=1/2$; $\overline{a_{11}}=\overline{a_{22}}=5/4$. $(a_{ii}=|a_i(t)|^2)$.

The interesting case is when the levels are equdistant and the frequensies of the components of the field are equel and the difference of its phases is not equal to zero. In this case the transition matrix element is the sum of two components:

$$W=V_1+V_2\exp(i\varphi), \text{ or } W=\Omega_0\exp(i\alpha/2), \qquad (5)$$

$$\Omega_0=(V_1^2+V_2^2+2V_1V_2\cos\varphi)^{1\,2}; \ \alpha=2\mathrm{arctg}[V_1\sin\varphi/(V_1+V_2\cos\varphi)].$$

Then the solution of Schrödinger equation for the population of the third level is

$|a_3(t)|^2=[1+\sin^2(\Omega t)\cos\alpha)]$, where $\Omega=\sqrt{2}\,\Omega_0$ is the Rabi frequency. In this case this frequency depends on the relative phase of two waves. The same problem was solved also for 4-level Zeeman structure (spin 3/2).

The populations for case of spin 1 and for case of spin 3/2 are displayed on Fig.2 and Fig.3 as a functions of α and $\Omega t=\pi/2$:

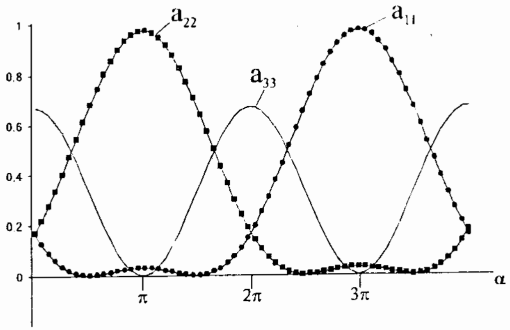

FIGURE 2

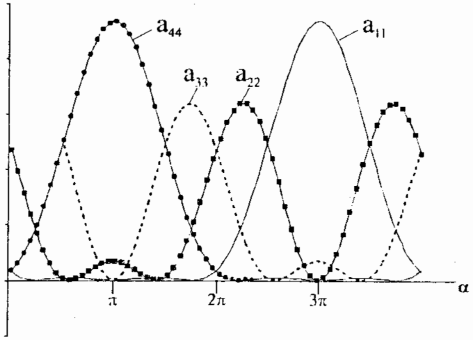

FIGURE 3

It appears to us that the suggested method of polarization can find use in quantum computer design. The most important problems in this respect are a search for a quantum system suitable for use as an information medium in quantum computations and the problem of initiating the initial state of this system. As known, a particle with spin 1/2 in a solid matrix is one of most important examples of such physical system - qubit. Qubit is a base for quantum computing. But the procedure of initiating the initial state of this quantum computer needs a very low temperature $(\sim 1\mu K^0)$. It is demonstrated above how can the initially uniformly populated levels be polarized by our method. In our case we do not need very low temperatures!!! Let us consider the nonequidistant three level system (fig.4):

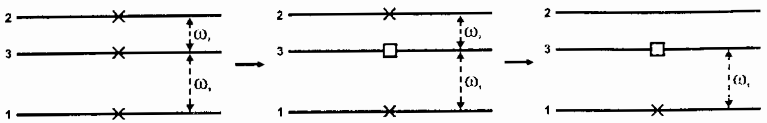

1) 2) 3)

FIGURE 4

The symbol × mean that the level is populated; the symbol □,that the level is empty. We are going from position 1) to 2) by π/2 pulse of bichromatic wave. In position 3) we may work with monochromatic wave with frequency ω_2.

The effect considered might be important for investigations associated with EPR and NMR problems for Zeeman hyperfine levels of an impurity in a solid matrix.

REFERENCES

1.Orriols, G., *Nuovo Chimento B* **53**, 1 (1979)

2.Agap'ev, B.D., Gorny,M.B., Matisov, B.G. and Rozhdestvenski, Yu.V., *Usp.Fiz.Nauk* **163**, 1 (1993) [Phys.Usp., **36**, 763 (1993)]

3.Zaretsky,D.F., and Sazonov, S.B., *Zh.Eksp.Teor.Fiz.* **113**, 1181 (1998) [JETP **86**, 644 (1998)]

DETERMINATION OF ^{55}Mn ELECTRIC QUADRUPOLE MOMENT ALMOST FREE OF STERNHEIMER CORRECTIONS

A. Jarosz, E. Stachowska, J. Ruczkowski, B. Furmann, J. Dembczyński

Poznań University of Technology, Chair of Atomic Physics
ul. Piotrowo 3, 60-965 Poznań, POLAND

1. Introduction

Hyperfine splittings of atomic spectral lines, arising from interaction between finite-size, non-spherical nucleus and electrons, give possibility to derive some information about nucleus from optical investigations. Analysis of hyperfine structure (HFS) leads to determination of nuclear moments. Contemporary spectroscopic techniques like Doppler-reduced or Doppler-free laser spectroscopy as well as even more precise laser-rf double resonance method together with theoretical analysis of hyperfine interaction, including higher order effects like configuration interaction, allow to considerably reduce the screening effects distorting values of nuclear moments. Because of complexity of *ab initio* theoretical calculations taking into account configuration interaction effects, an effective way of hyperfine interactions analysis are semi-empirical methods, where values of chosen parameters are determined by least squares fitting of evaluated quantities to their experimental values.

2. The method of simultaneous parametrization of one- and two-body interactions in atomic hyperfine structure

Interaction between non-spherical, finite-size nucleus and electrons in an N-electron atom can be described with the use of the following Hamiltonian, written in the multipole expansion form [1]:

$$\hat{H}^{Eff}_{HFS} = \sum_{K=1}^{\infty} \hat{T}_n^{(K)} \cdot \sum_{i=1}^{N} \left(\hat{T}_e^{(K)Eff}\right)_i ,$$

where $\hat{T}_n^{(K)}$ is the nuclear multipole moment operator – electrostatic $\hat{F}^{(K)}$ for K=0,2,4,... or magnetic $\hat{N}^{(K)}$ for K=1,3,5,... . $\hat{T}_e^{(K)Eff}$ is Sandars and Beck's effective electronic operator. K denotes successive multipole interactions: K = 1 – magnetic dipole, K = 2 – electric quadrupole, K = 3 – magnetic octupole,etc. To obtain precise information about nuclear moments it is necessary to take into account perturbation theory second-order contribution to hyperfine interactions energies. Dembczyński *et al.* [2,3] proposed a method of simultaneous parametrization of one- and two-body interactions in atomic hyperfine structure.

The second-order energy shift to the first order matrix element $\langle\psi|\hat{H}|\psi'\rangle$ is given by:

$$S(\psi,\psi') = -\sum_{\psi_1\neq\psi,\psi'} \frac{\langle\psi|\hat{H}|\psi_1\rangle\langle\psi_1|\hat{H}|\psi'\rangle}{\Delta E},$$

where $\hat{H} = \hat{H}_{EL} + \hat{H}_{SO} + \hat{H}_{HFS}$ is a sum of three terms corresponding to Coulomb interactions, spin-dependent interactions and hyperfine interactions, respectively. ΔE is the energy separation between the centre of gravity of the model space under study and the perturbing levels. ψ and ψ' are states of the model space whereas ψ_1 is a state of a perturbing distant configuration. The main contribution to relative energy shifts is due to the electrostatically correlated hyperfine interaction (EL-HFS):

$$S_{EL-HFS}(\psi,\psi') = -\sum_{\psi_1\neq\psi,\psi'} \frac{\langle\psi|\hat{H}_{EL}|\psi_1\rangle\langle\psi_1|\hat{H}_{HFS}|\psi'\rangle}{\Delta E} - \sum_{\psi_1\neq\psi,\psi'} \frac{\langle\psi|\hat{H}_{HFS}|\psi_1\rangle\langle\psi_1|\hat{H}_{EL}|\psi'\rangle}{\Delta E}.$$

This correction can be written as a matrix element of the following effective Hamiltonian:

$$\hat{H}_{EL-HFS} = \sum_{K} \hat{T}_N^K \cdot \sum_{\kappa k} \hat{X}_{EL-HFS}^{(\kappa k)K},$$

where $\kappa k = 01,\ 12,\ 10$ or 02 are tensor ranks in spin and orbit space, respectively. Restriction to K=1,2 (magnetic dipole and electric quadrupole interactions) leads to expressions for HFS A and B constants for the model space $(3d+4s)^{N+2}$:

$$A(\psi) = \sum_{\kappa k,nl} \alpha_{nl}^{\kappa k}(\psi)\, a_{nl}^{\kappa k} + \sum_{i=1}^{11} \alpha_i(\psi)\, a_i, \qquad \kappa k=01,\ 12,\ 10, \qquad nl=3d,\ 4s,$$

$$B(\psi) = \sum_{\kappa k,nl} \beta_{nl}^{\kappa k}(\psi)\, b_{nl}^{\kappa k} + \sum_{i=1}^{8} \beta_i(\psi)\, b_i, \qquad \kappa k=02,\ 13,\ 11, \qquad nl=3d,$$

where:
$\psi \equiv (SLJ)$ – real fine-structure states written in SL-basis (intermediate coupling scheme),
$a_{nl}^{\kappa k}$ and $b_{nl}^{\kappa k}$ – one-body radial parameters (originating from first-order HFS operator),
$\alpha_{nl}^{\kappa k}(\psi)$ and $\beta_{nl}^{\kappa k}(\psi)$ – angular coefficients of first-order contributions,
a_i and b_i – two–body radial parameters (originating from second-order HFS operator),
$\alpha_i(\psi)$ and $\beta_i(\psi)$ – angular coefficients of second-order contributions.

Index i denotes different kinds of two-body radial parameters corresponding to appropriate types of excitations. One-body parameters are common to all configurations composing the model space. The angular parts of one-body and two-body contributions to HFS constants (and therefore to hyperfine splittings) can be calculated exactly. Mentioned parametrization method gives possibility to separate second-order from the first-order contributions. This separation results, however, in parameters number increase. Additionally the second-order contributions exhibit SL-dependence. This means that sufficient number of experimental data (A and B HFS constants) is required to determine values of one- and two-body parameters, mentioned above, in the procedure of fitting of the evaluated A and B constants to their experimental values with the use of least squares method:

$$\sum_{SLJ} \left(A_{eval.}(SLJ) - A_{\exp.}(SLJ)\right)^2 = \min.$$

$$\sum_{SLJ} \left(B_{eval.}(SLJ) - B_{\exp.}(SLJ)\right)^2 = \min.$$

3. Measurements

Presented evaluation of electric quadrupole moment of ^{55}Mn nucleus was based mainly on experimental data available in publications. However, some measurements were carried out to complete HFS data concerning the $3d^6(^5D)4s\ a^4D$ term. Measurements were made with the use of laser-induced fluorescence on an atomic beam method. Atomic beam was generated by the evaporation of manganese sample from the graphite crucible heated with the use of electron beam from the electron gun. Additional electric discharge in metal vapours was applied to increase population of high lying metastable states. Apparatus for atomic beam generation was described in more detail in [4]. As a source of exciting light a cw tunable single-mode ring dye laser with active frequency stabilization was used. Induced fluorescence was detected by photomultiplier. Signal from photomultiplier was amplified with the use of lock-in amplifier. PC-compatible computer controlled laser scan and data acquisition process. Signal proportional to the transmission of stable Fabry-Perot interferometer, recorded simultaneously with the induced fluorescence signal, provided HFS spectra with frequency scale. For the investigations mentioned above hyperfine splittings of following spectral lines were measured:
449.0090 nm (in air) $3d^6(^5D)4s\ a^4D_{1/2} \rightarrow 3d^6(^5D)4p\ z^4D^o_{3/2}$,
428.4085 nm (in air) $3d^6(^5D)4s\ a^4D_{1/2} \rightarrow 3d^6(^5D)4p\ y^4P^o_{3/2}$,
425.7669 nm (in air) $3d^6(^5D)4s\ a^4D_{1/2} \rightarrow 3d^6(^5D)4p\ y^4P^o_{1/2}$.

4. Determination of one- and two-body HFS parameters for Mn I

In the applied parametrization method hyperfine structure of levels belonging to the $(3d+4s)^{N+2}$ model space can be parametrized with the use of sixteen adjustable radial parameters for the magnetic dipole interaction and twelve radial parameters for the electric quadrupole interaction. The number of fully free parameters in fitting procedure depends on the number of available A and B values derived from the experiment. Fitting procedure for radial parameters was performed with the use of computer program package developed in Chair of Atomic Physics [5]. The package consists of several programs performing different kinds of calculations necessary for final fitting procedure. The main tasks performed by these programs are: calculation of energy matrix elements, fine structure analysis (in particular

– determination of eigenvectors amplitudes in SL-basis), evaluation of angular coefficients for one- and two-body contributions to hyperfine interaction energy, and determination of one- and two-body radial parameters values in the fitting procedure.

For the analysis of Mn I HFS model space *(3d+4s)*^{7} consisting of $3d^7$, $3d^64s$ and $3d^54s^2$ configurations was chosen. The analysis of fine structure of terms belonging to the model space configurations was performed with the use of experimental data on Mn I fine structure [6] and results of earlier analysis [7]. The experimental *A* and *B* values used in fitting procedure are listed in Tab.I., while values of one- and two-body parameters obtained in HFS fit are presented in Tab.II. Because amount of experimental data was not sufficient to assume all parameters as free adjustable ones, values of several parameters were fixed.

Tab.I. A and B constants used in HFS fit

Configuration	Term	J	Energy [cm^{-1}]	A [MHz]	B [MHz]	Ref.
$3d^54s^2$	a^6S	5/2	0.00	-72,420836(15)	-0,019031(17)	[8]
$3d^6(^5D)4s$	a^6D	9/2	17052.29	510,308(8) *	132,200(120) *	[9]
		7/2	17282.00	458,930(3) *	21,701(40) *	[9]
		5/2	17451.52	436,715(3) *	-46,769(30) *	[9]
		3/2	17568.48	469,391(7) *	-65,091(50)*	[9]
		1/2	17637.15	882,056(12) *		[9]
$3d^6(^5D)4s$	a^4D	7/2	23296.67	-159,0184(3)	127,113(4)	[10]
				-159,0504 *	125,752 *	[10]
		5/2	23549.20	-138,0574(6)	47,385(4)	[10]
				-138,1724 *	45,144 *	[10]
		3/2	23719.52	42,6592(1)	4,922(1)	[10]
				42,2322 *	0,467 *	[10]
		1/2	23818.87	**1512,06(52)**		
$3d^54s^2$	a^4G	11/2	25265.74	405,3674(12)	0,890(25)	[10]
				405,265(6) *	-6,75 *	[10,11]
		5/2	25281.04	595,598(32)	8,247(3)	[10]
				596,183(30) *	-0.833 *	[10,11]
		9/2	25285.43	396,588(1)	70,156(30)	[10]
				395,201(3) *	0,196 *	[10,11]
		7/2	25287.74	438,242(13)	-62,859(2)	[10]
				437,074(15) *	0,671 *	[10,11]

*) corrected values

Tab.II. Values of one- and two-body radial parameters obtained in HFS-fitting procedure for Mn I

Parameter	Value in MHz	Parameter	Value in MHz
a_{3d}^{01}	948,2(2,7)	b_{3d}^{02}	587,11(26)
a_{3d}^{12}	953,5(3,2)	b_{3d}^{13}	9,71(76)
a_{3d}^{10}	-72,39(86)	b_{3d}^{11}	-4,92(37)
a_{4s}^{10}	2831,8(8,3)		
a_{CI}^{12}	= 0 *)	b_{CI}^{02}	18,5(2,8)
a_1'	283,2(1,6)	b_1	173,196(75)
a_2	46,61(27)	b_2	28,533(13)
a_3	31,07(18)	b_3	19,022(9)
a_4	= 0	b_4	= 0
a_5	= 0	b_5	= 0
a_6	= 0	b_6	16,4(2,7)
a_7	-50,13(28)	b_7	-20,255(9)
a_8	-12,460(71)	b_8	-7,632(4)
a_9' **)	671(15)		
a_{10}	= 0		
a_{11}	-982(408)		

*) fixed parameters

**) $a_9' = a_9 - a_{10}$ [12]

5. Determination of ^{55}Mn nuclear quadrupole moment almost free of Sternheimer corrections

Value of nuclear quadrupole moment obtained from measured HFS *B* constant may be distorted as a result of quadrupole shielding effects called Sternheimer effects. This shielding is a result of non-zero quadrupole moment of inner electronic shells induced by the nuclear quadrupole moment and influence of non-spherical charge distribution in valence shell, which can be characterized, in the first approximation, also by the quadrupole moment. Method of simultaneous parametrization of one- and two-body interactions in atomic hyperfine structure gives the set of one- and two-body radial parameters from which nuclear quadrupole moment almost free of Sternheimer corrections can be evaluated [2]:

$$Q_1 = \frac{2\mu_B g_I}{e^2} \frac{b_{nl}^{\kappa k}}{a_{nl}^{\kappa k}} \frac{(1+\Delta_{ll'}^{(\kappa k)1})F^{\kappa k}}{(1+\Delta_{ll'}^{(\kappa k)2})R^{\kappa k}},$$

$$Q_2 = \frac{2\mu_B g_I}{e^2}\frac{b_i}{a_i} \qquad i = 1,\dots,8,$$

where $F^{\kappa k}$, $R^{\kappa k}$ are the relativistic correction factors [1] and $\Delta_{ll'}^{(\kappa k)}$ are the contributions of one-body excitations of full shell to empty shell. Value of quadrupole moment Q_I of ^{55}Mn nucleus was obtained from parameters a_{3d}^{01} and b_{3d}^{02} while value of Q_2 was obtained from parameters a_1 and b_1:

$$Q_1 = 0{,}349(2)\ \mathrm{b}$$
$$Q_2 = 0{,}345(3)\ \mathrm{b}$$

The difference between values of Q_I and Q_2 is within the error limits. Value obtained in this work is bigger than value previously reported Q(^{55}Mn) = 0,33(1) b [9].

Acknowledgments

We would like to thank Prof. W. Ertmer from University of Hannover for presentation us with the apparatus for atomic beam generation. We also wish to thank dr. D. Stefańska and Dr G. Szawioła for helpful discussions. This work was supported by the Polish State Committee for Scientific Research (KBN) under project No. BW 63-018/2001.

References

[1] I. Lindgren, A. Rosén, *Case Stud. At. Phys.* **4**, 93 (1974).
[2] J. Dembczyński, W. Ertmer, U. Johann and P. Unkel, *Z. Phys.* A **321**, 1 (1985).
[3] J. Dembczyński, *Physica Scripta* **T65**, 88 (1996).
[4] B. Furmann, A. Jarosz, D. Stefańska, A. Krzykowski, J. Dembczyński, *Isotope shift in chromium atom* - contributed to this Conference.
[5] J. Dembczyński, J. Ruczkowski, E. Stachowska, A. Stachowska, *Comp. Meth. in Sci. and Techn.* **4**, 79 (1998).
[6] *Atomic Spectra Database*, National Institute of Standards and Technology, http://physics.nist.gov.
[7] J. Dembczyński, *Physica* **100C**, 105 (1980).
[8] S.J. Davis, J.J. Wright, L.C. Balling, *Phys. Rev.* A **3**, 1220 (1971).
[9] J. Dembczyński, W. Ertmer, U. Johann, S. Penselin, P. Stinner, *Z.Phys.* A **291**, 207 (1979).
[10] U. Johann, PhD thesis, Universitaät Bonn, Bonn 1981 (unpublished)
[11] U. Johann, J. Dembczyński, W. Ertmer, *Z. Phys.* A **303**, 7 (1981).
[12] J. Dembczyński, G.H. Guthöhrlein, E. Stachowska, *Phys. Rev.* A **48**, 2752 (1993)

DETERMINATION OF g_I -FACTOR OF Eu$^+$ FROM THE MEASUREMENTS IN PENNING TRAP

E.Stachowska*, S.Trapp, G.Szawioła*, G.Tommaseo, T.Pfeil, G.Werth
J.Dembczyński*

Institut für Physik, Universität Mainz, Germany

---

* Katedra Fizyki Atomowej, Politechnika Poznańska, Poland

HFS constants in the found data $4f^76s\ ^9S_4$ uncorrected and corrected for the second order HFS interactions;

Version I $\Delta E = f(\Psi,J)$

Version II $\Delta E = f(\Psi,J,F)$

HFS constant	^{151}Eu^{+} (Hz)	^{153}Eu^{+} (Hz)
	uncorrected	
A	1 540 476 486(12)	*684 601 369(5)*
B	*8 910 554(231)*	*137 400(86)*
C	*466(22)*	*66(8)*
D	*-6(5)*	*-5(2)*
	after correction	*version I and II*
A	*1 540 297 161(12)*	*684 565 948(5)*
B	*-653 445(231)*	*-1 751 726(86)*
C	*466(23)*	*66(8)*
D	*-6(5)*	*-5(2)*
A	*1 540 297 394(13)*	*684 565 993(9)*
B	*-660 862(231)*	*-1 752 868(84)*
C	*26(23)*	*3(7)*
D	*-6(5)*	*-5(2)*

Isotope	HFS constant	Uncorrected	Corrected
^{148}Eu^{+}	*A*	517 302 217(5)	517 281 950(150)
	B	4 579 440(85)	-292 630(1000)
^{149}Eu^{+}	*A*	1 585 640 944(10)	1 585 450 570(250)
	B	9 637 340(240)	-534 850(1900)
^{150}Eu^{+}	*A*	599 037 743(12)	599 010 680(200)
	B	5 698 770(430)	-839 730(3000)

Discrepancies in A-ratios for the isotopes ^{151,153}Eu^{+} observed in the ground and excited states

ground state

$4f^76s$

A(^{151}Eu^{+} $^9S_4$) / A(^{153}Eu^{+} $^9S_4$)= 2.25003493(4) [1]

A(^{151}Eu^{+} $^9S_4$) / A(^{153}Eu^{+} $^9S_4$)= 2.2500338(3) [2]

excited states

$4f^76s$

A(^{151}Eu^{+} $^7S_3$) / A(^{153}Eu^{+} $^7S_3$)= 2.2503957(4) [3]

$4f^75d$

A(^{151}Eu^{+} $^9D_2$) / A(^{153}Eu^{+} $^9D_2$)= 2.2565(1) [4]

A(^{151}Eu^{+} $^9D_3$) / A(^{153}Eu^{+} $^9D_3$)= 2.2520(1) [4]

A(^{151}Eu^{+} $^9D_4$) / A(^{153}Eu^{+} $^9D_4$)= 2.2445(1) [4]

A(^{151}Eu^{+} $^9D_5$) / A(^{153}Eu^{+} $^9D_5$)= 2.2365(1) [4]

A(^{151}Eu^{+} $^9D_6$) / A(^{153}Eu^{+} $^9D_6$)= 2.2641(60) [5]

A(^{151}Eu^{+} ^9D_J) / A(^{153}Eu^{+} ^9D_J)= 2.2507(1)

[1] O.Becker, K.Enders and G.Werth; Phys.Rev. A **48**, 3546-3554 (1993)
[2] K.Enders; doctor thesis, Mainz 1996
[3] K.Enders, E.Stachowska, G.Marx, Ch.Zölch, G.Revalde, J.Dembczyński, G.Werth; Z.Phys. D **42**, 171-175 (1997)
[4] A.Sen, W.J.Childs; Phys. Rev. A **36**, 1983-1993 (1987)
[5] A.Bergweger, G.Guthöhrlein; private communication

hyperfine anomaly

in the ground state

4f⁷6s

$^{151}\Delta^{153}\ (^9S_4) = -\,0.006\underline{63}(18)$ [1]

$^{151}\Delta^{153}\ (^9S_4) = -\,0.006\underline{63}(18)$

in the excited states

4f⁷6s

$^{151}\Delta^{153}\ (^7S_3) = -.0.006\underline{29}(54)$ [2,3]

$^{151}\Delta^{153}\ (^7S_3) = -.0.006\underline{47}(18)$

4f⁷5d

$^{151}\Delta^{153}\ (^9D_2) = -.0.00377(19)$

$^{151}\Delta^{153}\ (^9D_3) = -.0.00576(21)$

$^{151}\Delta^{153}\ (^9D_4) = -.0.00907(19)$

$^{151}\Delta^{153}\ (^9D_5) = -.0.01260(21)$

$^{151}\Delta^{153}\ (^9D_6) = -.0.00042(20)$

$^{151}\Delta^{153}\ (^9D_J) = -.0.006\underline{34}(5)$

[1] O.Becker, K.Enders and G.Werth; Phys.Rev. A **48**, 3546-3554 (1993)
[2] K.Enders; doctor thesis, Mainz 1996
[3] K.Enders, E.Stachowska, G.Marx, Ch.Zölch, G.Revalde, J.Dembczyński, G.Werth; Z.Phys. D **42**, 171-175 (1997)
[4] A.Sen, W.J.Childs; Phys. Rev. A **36**, 1983-1993 (1987)
[5] A.Bergweger, G.Guthöhrlein; private communication

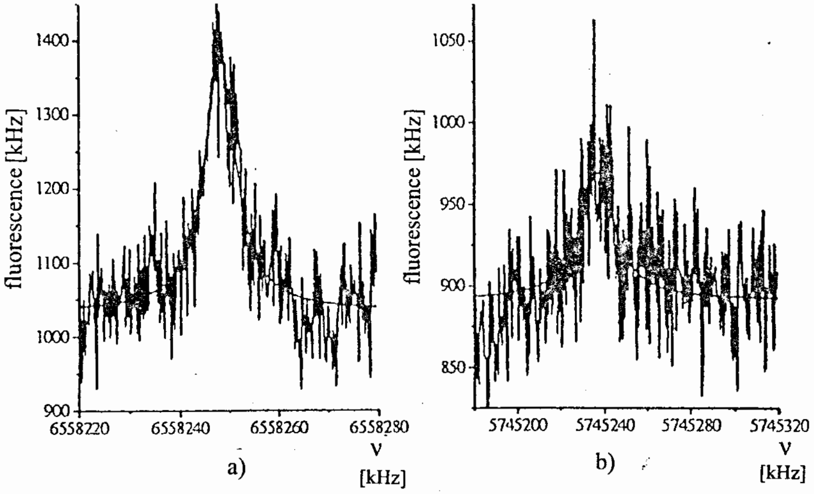

a) b)

$\Delta m_J = 0$ Übergang $\Delta m_I = 1$	ν[kHz]	$\Delta\nu$[kHz]	FWHM[kHz]	$\frac{\Delta\nu}{\nu}$
$m_J = -4; m_I = +\frac{3}{2} \to +\frac{5}{2}$	a) 6 558 248.1	0.37	7.68	$5.6 \cdot 10^{-8}$
$m_J = -4; m_I = +\frac{1}{2} \to +\frac{3}{2}$	6 241 411.5	1.02	11.02	$1.6 \cdot 10^{-7}$
$m_J = -4; m_I = -\frac{1}{2} \to +\frac{1}{2}$	5 975 525.7	0.84	11.94	$1.3 \cdot 10^{-7}$
$m_J = -4; m_I = -\frac{3}{2} \to -\frac{1}{2}$	b) 5 745 237.0	0.94	16.74	$1.5 \cdot 10^{-7}$
$m_J = -3; m_I = +\frac{3}{2} \to +\frac{5}{2}$	5 642 485.1	0.65	11.09	$1.2 \cdot 10^{-7}$

$$H_{ZEEMAN} = -\vec{\mu}\cdot\vec{B}$$

- Two successive approximations:

$$\vec{\mu} = -\frac{\mu_B}{\hbar}\left(g_l\,\vec{J} + g_I'\,\vec{I}\right) \qquad \vec{\mu} = -\frac{\mu_B}{\hbar}\left(g_l\,\vec{L} + g_s\,\vec{S} + g_I'\,\vec{I}\right),$$

where

$$g_I' = g_I\,\frac{\mu_N}{\mu_B}\,.$$

- In the pure SL coupling the matrix elements vanish:

$$\left\langle \alpha\ {}^9S_4\ M_J, I\ M_I \middle| H_{ZEEMAN} \middle| \alpha\ {}^7S_3\ M_J', I\ M_I' \right\rangle = 0\,.$$

- In the intermediate coupling the matrix elements have nonzero value

$$\left\langle REAL\ {}^9S_4\ M_J, I\ M_I \middle| H_{ZEEMAN} \middle| REAL\ {}^7S_3\ M_J', I\ M_I' \right\rangle \neq 0,$$

thus

$$\Delta E_2 = \\ = \sum_{M'_J, M'_I} \frac{\left|\left\langle REAL\ {}^9S_4\ M_J, I\ M_I \middle| H_{ZEEMAN} \middle| REAL\ {}^7S_3\ M_J', I\ M_I' \right\rangle\right|^2}{E\left({}^9S_4\right) - E\left({}^7S_3\right)},$$

$$\begin{aligned} |4f^7({}^8S)6s;{}^9S_4\rangle = {} & 0.982\,641|4f^7({}^8S)6s;{}^9S_4\rangle + 0.183\,122|4f^7({}^6P)6s;{}^7P_4\rangle \\ & -0.003\,995|4f^7({}^6D)6s;{}^5D_4\rangle - 0.014\,654|4f^7({}^6D)6s;{}^7D_4\rangle \\ & +0.000\,576|4f^7({}^6F)6s;{}^5F_4\rangle + 0.001\,258|4f^7({}^6F)6s;{}^7F_4\rangle + \cdots\ , \\ |4f^7({}^8S)6s;{}^7S_3\rangle = {} & 0.982\,013|4f^7({}^8S)6s;{}^7S_3\rangle + 0.181\,359|4f^7({}^6P)6s;{}^5P_3\rangle \\ & -0.042\,496|4f^7({}^6P)6s;{}^7P_3\rangle - 0.014\,466|4f^7({}^6D)6s;{}^5D_3\rangle \\ & +0.006\,310|4f^7({}^6D)6s;{}^7D_3\rangle + 0.001\,216|4f^7({}^6F)6s;{}^5F_3\rangle + \cdots\,. \end{aligned}$$

Zeeman second order corrections originating from perturbation of $^9S_4$ by $^7S_3$ vs. measured Zeeman intervals

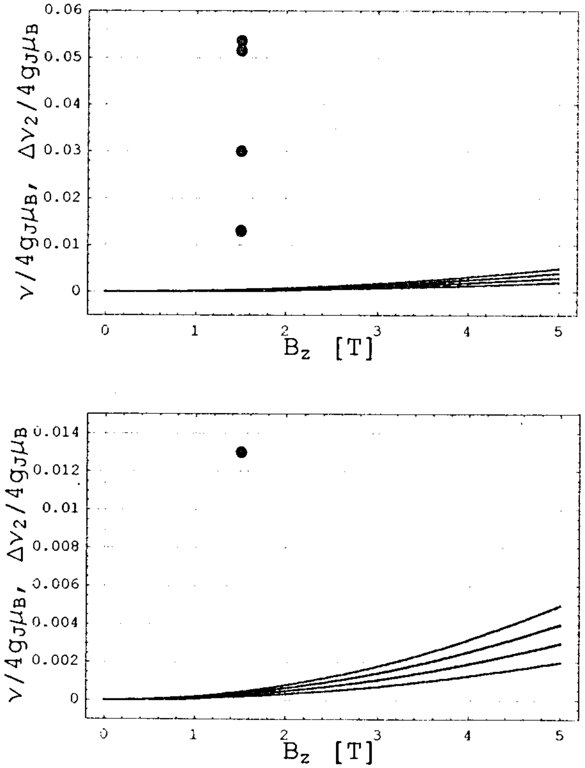

$^{151}g_I = 1.37734(6)$

$^9S_4$

$g_J = 1.99116951$

(exp) $g_J = 1.984$

^{156}Eu $(I=0)$

PROPERTIES OF LASER ION SOURCE FOR LASER SPECTROSCOPY OF NUCLIDES FAR FROM STABILITY: CALCULATION AND EXPERIMENT

M.D. Seliverstov, A.E. Barzakh, D.V. Fedorov and V.N. Panteleev

St. Petersburg Nuclear Physics Institute, 188350 Gatchina, Russia

E-mail: mseliver@rec03.pnpi.spb.ru

The study of nuclei far from stability requires high sensitivity of the experimental technique. The method of Resonance Ionization Spectroscopy in a Laser Ion Source (RIS/LIS) allows one to perform measurements of isotope shifts and hyperfine splitting for isotopes at the production rate about 10^3 atoms per second. A series of experiments with Yb and Tm isotopes far from stability (^{153,155}Yb, ^{153,154}Tm) has been carried out at the IRIS facility (PNPI). The sensitivity of this method is determined by the high efficiency (~10% for Yb isotopes) and selectivity of the laser ion source.

The basic properties of this type of laser ion source have been discussed. The results of Monte Carlo calculation of the basic properties (efficiency, selectivity, time structure of the ion beam and Doppler width and shift of the optical line) together with corresponding experimental data have been presented.

Introduction

A resonant ionization laser ion source (RILIS) is a powerful tool for producing isotopically pure ion beams of exotic nuclei [1]. The use of narrow-bandwidth laser allows one to resolve a small difference in the transition energy due to hyperfine interaction of the atomic electrons with the nucleus. Thus the RILIS can be used as a sensitive tool for atomic spectroscopy of short-lived isotopes. The isotope shifts and hyperfine structure can be measured and isotopic changes in mean square charge radii and nuclear electromagnetic moments can be evaluated. A series of the experiments with Yb and Tm neutron deficient isotopes has been carried out at IRIS facility [2,3].

The schematic view of the target-ion source unit of IRIS facility mass separator is presented in Fig. 1.

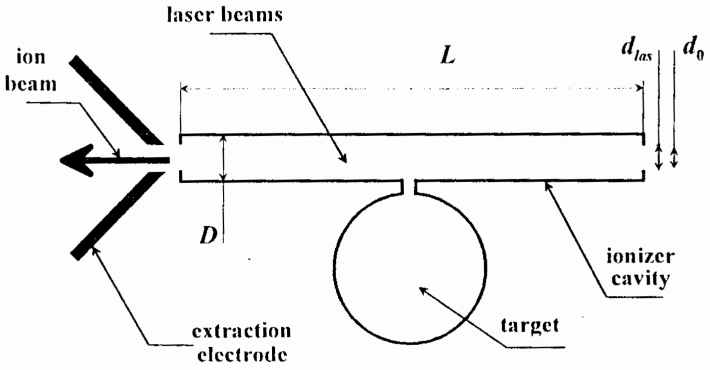

Fig. 1. Schematic view of the target-ion source unit used at IRIS on-line mass-separator.

The nuclides under study are produced in a high temperature target of the mass-separator. Then the atoms are thermally released from the target to the ionizer cavity, where they are resonantly photoionized by the beams of three pulsed dye lasers merged into single beam and directed into the cavity. Multiple intersection of the laser beam by the atoms in the laser ion source cavity considerably increases the probability of the photoionization. The high temperature of the cavity prevents atoms from attaching to the walls for a too long time (condensation), at the same time electron emission from the heated cavity wall creates an electrical potential near the wall, which traps photoions near the central axis and prevents recombination and adhesion to the wall. The electric field created by the DC heating drives photoions towards the extraction electrode of the mass-separator. The ionizer can be also a tubular one, in that case $D = d_0 = d$.

The basic properties of this type of laser ion source can be summarized as follows:

- Efficiency η_{ion}: The total efficiency is defined as the ratio of the rate of ions of investigated isotope measured in the mass-separator collector and the rate of atoms of the same isotope produced in the target. A high value of total ionization efficiency is of great importance for the investigation of the exotic nuclei with very low production rate.

  Selectivity S: The selectivity is defined as the ratio of the ion current after mass-separator while the lasers are on resonance and the ion current while the lasers are off resonance. Due to high efficiency of the resonant photoionization the selectivity of the laser ion source can be very high. However, as the nuclear reaction is often non-selective, isobaric contamination of elements with a low ionization potential can be severe.

For the optical spectroscopy the spectral width and shift of the light absorption line are also of great importance.

For the estimation of the pointed out parameters the computer program for Monte Carlo simulations of the processes in the RILIS has been developed. Here some results are presented.

Laser ion source efficiency

The total ionization efficiency can be presented as:

$$\eta_{ion} = \eta_{photo}\,\eta_{irr}\,\eta_{extr}. \tag{1}$$

where η_{photo} is the probability of photoionization of the single atom per laser pulse, η_{irr} is the probability for the atoms to be irradiated by the laser light, η_{extr} is the ion extraction efficiency.

The value of η_{photo} depends on the thermal population of the atomic ground state (in the case of application of the laser ion source for spectroscopic measurements on the relative population of the hfs components), the transition cross-sections, the laser beam intensities as well as the spontaneous decay times of excited states.

In order to obtain high value of η_{photo} process of resonant ionization must be saturated. To reach this goal the excitation and ionization steps should be subsequently saturated. In our experiments the following ionization schemes were used:

- for Yb atoms:

$$6s^2\,{}^1S_0 \xrightarrow{555.6\text{ nm}} 6s6p\,{}^3P_1 \xrightarrow{581.1\text{ nm}} 4f^{13}({}^2F_{7/2})6s^26p_{3/2} \xrightarrow{581.1\text{ nm}} \textit{autoionizing state (or continuum)},$$

- for Tm atoms:

$$4f^{13}6s^2\,{}^2F_0 \xrightarrow{597.1\text{ nm}} 4f^{13}6s6p\,(7/2,0)_{7/2} \xrightarrow{600.3\text{ nm}} 4f^{13}5d6s \xrightarrow{552.4\text{ nm}} \textit{autoionizing state.}$$

The obtained saturation curves for excitation and ionization steps are shown in Fig. 2 and Fig. 3.

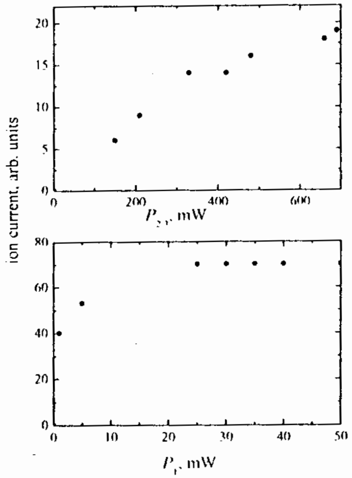

Fig. 2. Number of laser produced and mass separated Yb ions as a function of the laser power for the first (bottom) and for the second and ionization steps (top).

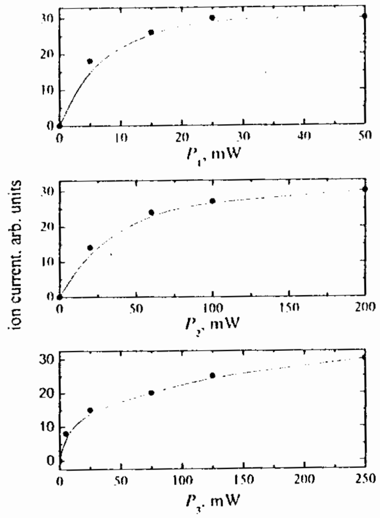

Fig. 3. Number of laser produced and mass separated Tm ions as a function of the laser power for the first (bottom), second (middle) and ionization steps (top).

The value of η_{irr} depends on the time which the atoms spend in the zone of the interaction with the laser radiation before they left the ionizer cavity and on the laser pulse duration and the pulse repetition rate. The calculated distribution of atomic residential time in an inner volume of the ion source cavity is presented in Fig. 4. As the time between laser pulses is 100 μs (corresponding to a repetition rate of 10 kHz), some atoms can be irradiated more than once and it will cause nonlinear dependence of η_{ion} on η_{photo} (see Fig. 5).

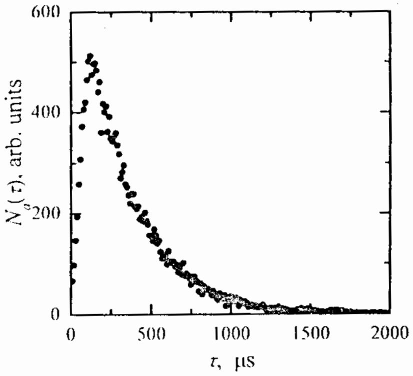

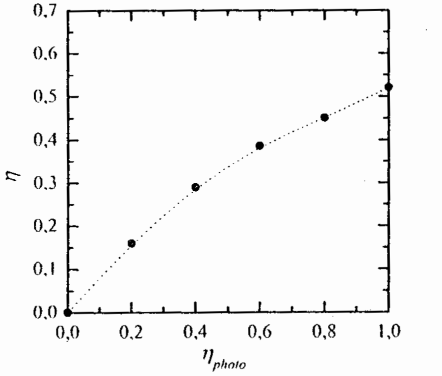

Fig. 4. The calculated distribution of the atomic residential time in an inner volume of the ion source cavity (d = 1.5 mm, L = 50 mm, T = 2200 K).

Fig. 5. The calculated dependence of η_{ion} on η_{photo} for the ionizer with d = 1.5 mm, L = 50 mm and d_{las} = 0.7 mm.

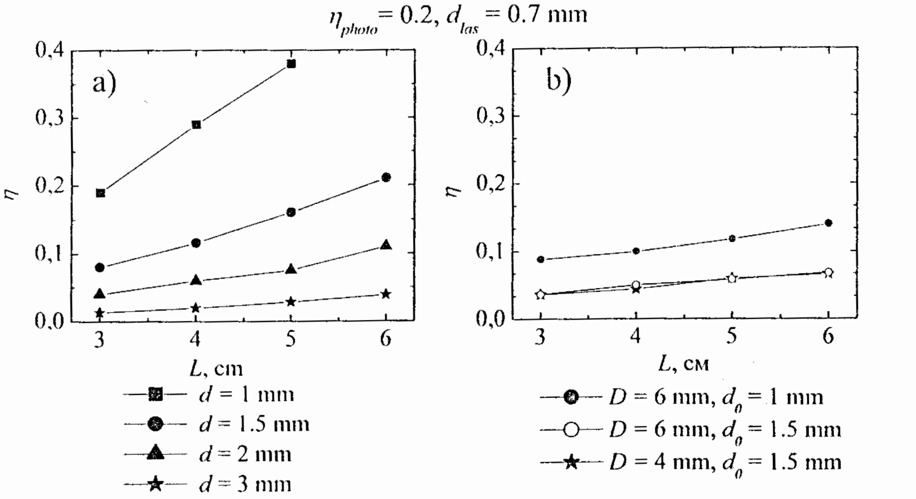

Fig. 6. The calculated ionization efficiency dependence on the ion source geometrical parameters.

The calculated ionization efficiency dependence on the ion source geometrical parameters is presented in Fig. 6. In this calculation the extraction efficiency was $\eta_{extr} = 1$. The experimental data for Yb ionization efficiency values obtained at IRIS (η_{ion} = 0.3 for the niobium ionizer with $d = 1$ mm, $L = 45$ mm and η_{ion} = 0.15 for ionizer with $d = 1.6$ mm, L = 45 mm [4]) is in good agreement with the results of the Monte Carlo simulation (see Fig. 6 a). The value of η_{photo} is selected according to the parameters of the lasers used during the tests and the saturation curves given above. As it is seen in Fig. 6 b, the ionization efficiency for cavity-like ionizers with small orifices does not depend on the cavity diameter D.

The calculated atomic density distribution along the ionizer at different values of η_{photo} is shown in Fig. 7. In the absence of photoionization the atomic density decreases linearly along the tube (z axis) from the entrance hole ($z_{entr} = L/2$) to the exit holes ($z_{ex1} = 0$, $z_{ex2} = L$) according to the Fick law:

$$J_{at} = -D'\frac{dn_{at}}{dz} = \text{const}, \qquad (2)$$

where J_{at} is the atomic flux density, n_{at} is the atomic density and D' is the diffusion coefficient. If $\eta_{photo} > 0$ the atomic flux is not constant along the tube due to photoionization and the atomic density depends on z non-linearly. The dependency of the photoionic density in the interaction zone $n_{ion}(z)$, $t = t_{las}$, for the ionizers with different geometrical parameters is shown in Fig. 7.

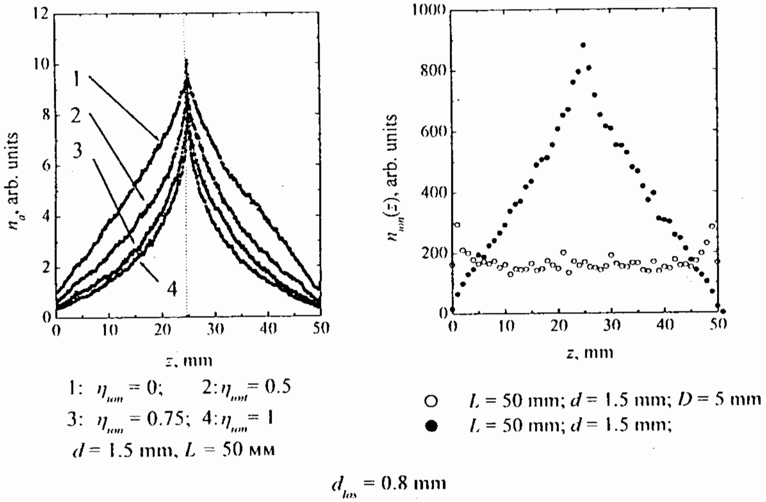

Fig. 7. The calculated atomic and ionic density distributions.

Since photoions are produced by pulsed lasers, the obtained photoion beam is pulsed with the laser repetition frequency. Ion current time structure is consequently determined by the initial density and velocity distribution of the photoions created in the cavity as well as by extraction time and extraction efficiency of the photoions. The time structure of the photoion current from the laser ion source ($d = 1.5$ mm, $d_{las} = 0.7$ mm, $L = 50$ mm) with different heating voltage applied are shown in Fig. 8 as well as the calculated curves.

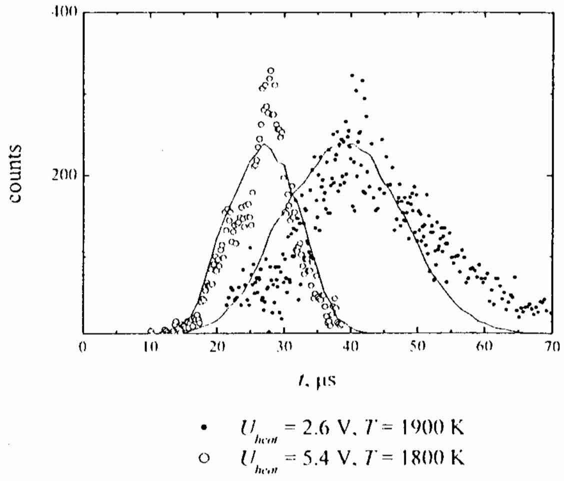

Fig. 8. The time structure of the photoion current of laser ion source.

High extraction efficiency η_{extr} caused by the ion confinement by the potential barrier near the cavity wall. The value and the sign of the potential well are given by [5]:

$$\phi = \frac{kT}{2e}\ln\left(\frac{n_i}{n_e}\right); \qquad (3)$$

where n_i and n_e are the density of ions and electrons in the volume of the ionizer, respectively. According to [5] the value of ϕ for Ta and W ionizers at T = 2300 – 2700 K is about 2.5 V. This potential prevents photoions to stick the wall and recombine to neutral atoms.

To evaluate the single ion extraction efficiency one should take into account all the wall collisions which the ion suffers before leaving the cavity. The number of ion-wall collisions depends on a geometrical parameters of the ionizer and on the axial electric field inside the cavity U_{heat}.

The influence of the ion density on the extraction efficiency is illustrated in Fig. 9 a. In this picture time structure of the ion current from the laser ion source observed during the off-line tests is presented. The temperature of the ionizer (T = 2000 K) and the voltage of ohmic heating (U_{heat} = 5.4 V) are the same for both curves, but the atomic flux of Tm tracer from the oven was changed, consequently the ions density in the ionizer was changed as well. The large relative contribution to the total ion current of the ions with the lower extraction time is determined by the dependence of the extraction efficiency for each ion on the distance from the exit hole. It can be caused by the dependence of ionic density and consequently ϕ on z and (or) by the dependence of the total extraction efficiency on the number of the ion-wall collisions: the ions created near the exit hole have in average lower value of N_{coll}. In Fig. 9 a. the calculated ions' extraction time distributions are also shown.

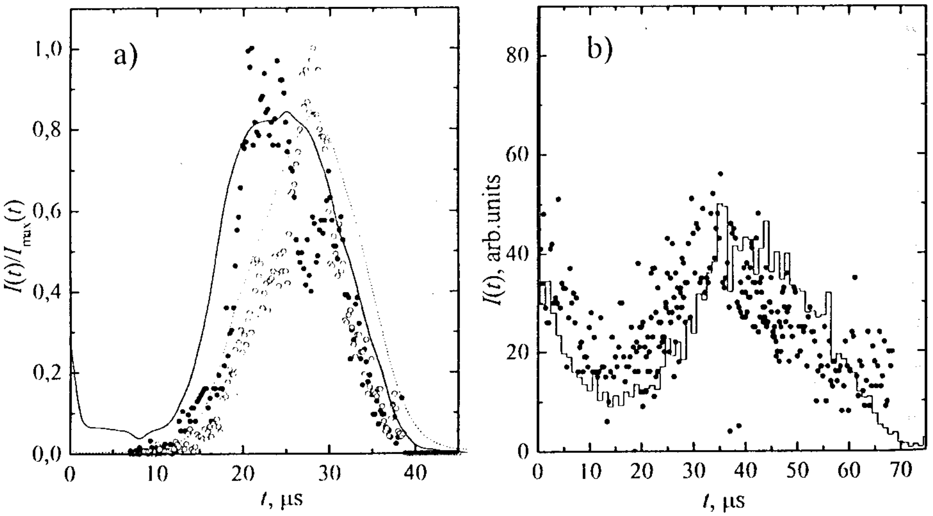

Fig. 9. Ions delay time distribution at different values of η_{extr} .

The time structure of the photoion current can be used for the η_{extr} estimation. The extraction efficiency of ions with short extraction time shows only weak dependence on the probability of the recombination on the cavity wall because these ions are created near the exit hole and leave the cavity without the striking the wall or suffer only few wall collisions before leaving the cavity. An example of the ion current time structure observed during on-line experiment with $^{160\text{-}164}$Yb is shown in Fig. 9 b. As is seen in Fig. 9 b the amplitude of first peak (t_{extr} < 10 μs) is comparable with the main peak's amplitude, it can be explained by low extraction efficiency. The ionization efficiency calculated as the ratio of experimentally observed ion beam intensity and calculated production rate is about 0.5%, and the total ionization efficiency calculated with η_{extr} = 1 is about 5%. The calculated photoion current structure with η_{extr} = 0.1 is also shown in Fig. 9 b.

Laser ion source selectivity

The temperature of the laser ion source cavity should be kept high enough to prevent atoms from the condensation on the ionizer walls and to provide the ion confinement. Consequently, thermal ionization of atoms takes place on the hot surface, particularly, if the ionization potential of the atom is low. The value of thermoionization efficiency at single atom-wall collision is given by [5]:

$$\beta_{therm} = \frac{\alpha}{1+\alpha}, \quad \alpha = \left(\frac{\sigma_i}{\sigma_0}\right)\exp\left[(\varphi - W_i)kT\right], \tag{4}$$

σ_i and σ_0 are the statistical weights of the ionic and atomic ground states, W_i is the ionization potential of the atoms, φ is the work function of the cavity material.

The total thermoionization efficiency is [5]:

$$\eta_{therm} = \beta_{therm}\eta_{extr}^{therm}N_{coll}^{at}, \tag{5}$$

where N_{coll}^{at} is the mean number of atom-wall collision, η_{extr}^{therm} is the thermoions' extraction efficiency. Extraction efficiency of thermoions can be lower than that of photoions since the thermoion created at the ionizer surface acquires additional energy $e\phi$ passing through the potential barrier near the ionizer surface and has enough energy to hit the wall again. The thermoionization efficiency depends strongly on the temperature of the cavity and, as the result, the selectivity decreases with the temperature. As the thermoionization efficiency depends on work function of the cavity material, materials with low work functions seems to be preferable.

As the total thermoionization efficiency depends on mean number of the atom-wall collisions, the selectivity of laser ion source can be characterized by the ratio of the total photoionization efficiency and mean number of atom-wall collisions. The calculations shows that the value of $\gamma = \eta_{ion}/N_{coll}^{at}$ does not depend on the ionizer length (L was varied from 30 to 60 mm). For tubular ionizers with d_{las} = 0.8 mm and d_1 = 1 mm, d_2 = 1.5 mm, d_3 = 2 mm and d_4 = 3 mm the calculated values of the parameter γ are: $\gamma_1 = 1.4\cdot10^{-3}$, $\gamma_2 = 8\cdot10^{-4}$, $\gamma_3 = 6.5\cdot10^{-4}$ and $\gamma_4 = 4\cdot10^{-4}$, respectively. For cavity-like ionizers:

$D = 4$ mm, $d = 1.5$ mm: $\gamma = 3\cdot10^{-4}$;

$D = 6$ mm, $d = 1.5$ mm: $\gamma = 2\cdot10^{-4}$;

$D = 6$ mm, $d = 1$ mm: $\gamma = 1\cdot10^{-4}$;

So the option of the tubular ionizer seems to be preferable.

Background ions are produced by the surface ionization in the ion source and target. In our experiments, a high temperature target ($T \geq 2700$ K) has been used in order to increase production yield of short-lived isotopes. In this case the main contribution to background current comes from the target itself. In Fig. 10 the dependence of the selectivity of the Yb photoionization on the target temperature is shown.

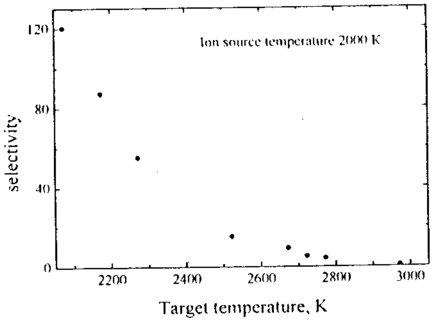

Fig. 10. Dependence of the target-ion source selectivity on the target temperature.

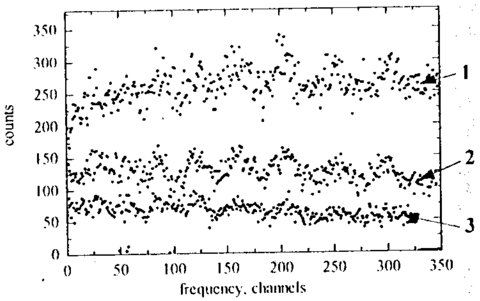

Fig. 11. Experimental ^{154}Tm spectra recorded at different ionizer temperatures: 1 – 2300 K; 2 – 2100 K; 3 – 2000 K.

In Fig. 11 experimental spectra of ^{154}Tm obtained at different ionizer temperatures are shown. To increase the selectivity of the target-laser ion source unit the locking of the background thermoions in the high temperature target by the potential of the heating current flowing through the target container was applied [6]. The background current was reduced by a factor of 20 using this technique. To increase selectivity further, time structure of the photoion current can be used. By introducing time gates in the detection system the selectivity can be increased by a factor of five (see Fig. 8).

Experiments

As was shown above the total ionization efficiency depends on the geometrical parameters of the ionizer. The preferable option is the tubular ionizer with the diameter close to the laser beam size. As the ions' extraction time and efficiency depends on voltage applied, the wall thickness should be small enough to obtain a high ohmic resistance and, consequently, the relatively high corresponding electric field. On the other hand, the ionizer should be mechanically stable at high temperature which is needed to obtain low wall sticking time and high ion extraction efficiency. Initially ionizers made of Nb were used because of its low work function. The Nb ionizer with acceptable mechanical stability had a diameter of 2.5 mm, a length of 55 mm and a wall thickness of 0.5 mm. A typical value of U_{heat} was 1.5 V. The temperature regimes of the target-ion source unit were selected during the experiments by stepwise changing of the target and ionizer temperature to obtain high ion current of the isotopes under study with acceptable selectivity. The ^{155}Yb photoion current was increased by the factor of 1.5 with the target temperature rising from 2500 to 2800 K, correspondingly the selectivity value decreased from $S = 7$ to $S = 4$, and the optimal ionizer temperature was $T_{ion} = (2100 \quad 2200)$ K. Due to high isobaric contamination in the experiments with ^{153,156}Yb and ^{153,154}Tm the isotope selective photoion detection by counting of α-particles from the decay of isotopes under study was applied. In that case the selectivity was determined by the background thermal ion current of the isotope under investigation. The estimations based on the calculated production rate, known ion beam line transmittance and detection efficiency gave a value of photoionization efficiency: $\eta_{ion} \approx 3\%$. As the high temperature target-ion source unit selectivity is determined by the background thermal ion current from the target (see Fig. 10), for experiments with ^{153}Yb we used ionizer made of W, which had a higher work function but provided a better mechanical stability at the high temperatures. In that case ionizer had a diameter of 1.5 mm and a wall thickness of 0.2 mm. The optimal temperatures of the target and ionizer were $T_{targ} = 2800$ K and $T_{ion} = 2100$ K. The estimated ionization efficiency was about 10%. The selectivity was about 5. The typical value of U_{heat} was 2.5 V. The photoions from each laser pulse were bunched with duration of 15 μs and delay of 35 μs.

Spectral width and shift of the absorption line

The resolution of the RIS/LIS method is Doppler-limited and this technique can only be used for medium to heavy elements with relatively large isotope shifts and hyperfine splittings. For medium mass elements ($A \approx 150$) the Doppler broadening is about 1 GHz. To avoid additional power broadening the first transition of the chosen ionization scheme should not be deeply saturated.

As was shown above, in the case of high ion density in the inner volume of the ionizer the extraction efficiency may depend on the ion-wall collision number and thus on the ion initial velocity, the absorption line (here absorption means the photon absorption followed by ionization and successful ion extraction from the ionizer cavity) may be Doppler shifted. The comparison [7] of the measured isotope shifts with those measured by other techniques shows that the absorption lines were unshifted within the error bars determined by the uncertainty of frequency scale calibration.

The Doppler shift of the absorption line was observed only in the case of very low extraction efficiency when only the ions which do not suffer ion-wall collision came out from the ionizer cavity. In contrast with the normal experimental conditions only one sharp peak ($\Delta t < 1$ μs) with very short delay time was observed. In that case the observed Doppler shift ($\Delta\nu_D \approx 700$ MHz) is in agreement with the calculated value (~500 MHz).

The possible shifts should be checked in the course of the experiment and taken into account in the data proccessing.

Reference

1. V. Fedoseyev et al., *Hyperfine Interaction* **127** (2000) 409
2. A.E. Barzakh et al., *European Phys. J.*, **A 1** (1998) 3
3. M. Seliverstov et al., *Hyperfine Interaction* **127** (2000) 430
4. A.E. Barzakh et al., *Nucl. Instrum. and Meth.* **B 126** (1997) 85
5. R. Kirenher,. *Nucl. Instrum. and Meth.* **186** (1981) 275
6. V.N. Panteleev et al., *Hyperfine Interaction* **127** (2000) 421
7. M.D. Seliverstov, these proceedings

LASER SPECTROSCOPY OF ATOMIC CLUSTERS

V.O. NESTERENKO[1] and W. KLEINIG[1,2]

[1] Bogoliubov Laboratory of Theoretical Physics, Joint Institute for Nuclear Research, 141980 Dubna, Moscow region, Russia

[2] Institut für Analysis, Technische Universität Dresden, D-01062 Dresden, Germany

Abstract

Laser spectroscopy of atomic clusters is briefly reviewed. The main attention is paid to problems connected with the dipole giant resonance. Numerous practical applications of atomic clusters and other mesoscopic systems are listed to emphasize their crucial role in modern hi-tech.

1 Introduction

During last two decades new kinds of finite Fermi systems have been fabricated. They involve atomic clusters [1]-[7], fullerenes as the particular case of carbon clusters [8], quantum dots [9], trapped dilute gas of Fermion atoms [10], nanotubes and nanowires [11], nanoarchitectures on surfaces [12], etc. These systems are of the scale of nanometer and so are called as nanoparticles (nanosystems). Since they demonstrate both quantum peculiarities of small particles and properties of the bulk, they are treated as mesoscopic systems. Present techniques allow to produce nanoparticles from about any element of the periodic table. Moreover, the number of fermions in such systems can be controlled with high accuracy. Investigation of nanosystems have led to a remarkable progress in understanding both fundamental properties of Fermi systems and their amazing variety. Moreover, nanosystems result in numerous striking applications. They promise fantastic progress in many areas, from medicine to computering and modern electronics.

In this review atomic clusters will be mainly considered. Certain kind of them, metal clusters, demonstrate a remarkable similarity with atomic nuclei [1]-[6]. Laser spectroscopy is widely used in both cluster and nuclear physics but in cluster physics it plays much more important role. Indeed, while nuclear physics exploits a wide collection of different reactions and probes, the tools of clusters physics are mainly limited to reaction with a light (photoabsorption, photofragmentation, Raman scattering, ...) [2, 7]. Inelastic electron scattering [13, 14] and Coulomb interaction with ions [15] are also used but in a less extent. The laser spectroscopy is really overwhelming experimental tool in cluster physics.

This review provides a simple guide for nuclear specialists on using laser techniques in cluster physics. Some hot examples are demonstrated. The review is organized by the following way. In Sec. 2 the basic information on atomic clusters and their giant resonances (GR) is given. In Sec. 3 main properties of E1-GR are considered and several remarkable laser-used experiments with E1-GR are described. In Sec. 3 examples of practical applications of nanosystems are listed.

2 Atomic clusters: basic aspects

Atomic cluster is a bound system consisting (mainly or completely) of identical atoms. If the atoms belong to a certain metal, we have a metal cluster (MC). The amount of atoms can vary from a few to millions and more. Some MC, mainly of alkali (Li, K, Na, ...) and noble (Ag, Au, ...) metals, demonstrate a striking similarity to atomic nuclei (see reviews [1]-[6]). In these clusters the valence electrons are *weakly* coupled to the ions and, like nucleons in nuclei, are not strongly localized. The mean free path of valence electrons is of the same order of magnitude as the size of the cluster and so their motion can be quantized. This favors forming a mean field for valence electrons, which is of the same kind as in nuclei (with similar shell structure and magic numbers). In addition to the mean field, MC demonstrate other similarities with atomic nuclei: deformation of clusters with open shells, variety of giant resonances, fission, etc. As a result, many ideas and methods of nuclear physics can, after a certain modification, be applied to MC [1, 3, 5].

This review mainly covers collective oscillations of valence electrons in MC. Valence electrons can be considered as the counterparts of nucleons in nuclei, and their oscillations as the counterparts of nuclear GR. Investigation of GR in MC is interesting in two aspects: it allows both to deepen our knowledge on general properties of collective modes in finite Fermi systems and to study peculiarities of MC. GR in clusters and atomic nuclei are well overlapped and, at the same time, have considerable differences. In clusters, for example: i) the Coulomb interaction and the "spill-out" effect provide a specific dependence of GR properties on the mass number; ii) the negligible character of the spin-orbital interaction leads to the decoupling of spin and orbital magnetic modes; iii) clusters can have much more particles (atoms) than nuclei, which favors very strong orbital magnetic resonances; iv) for most of the clusters the role of the ionic subsystem is important; v) at different temperatures MC can be in solid, liquid and even "boiling" phases which influence GR properties; vi) characteristics of GR vary considerably whether the clusters are charged or neutral, free or embedded to a substrate, pure or with impurities, etc.

Our consideration will be limited by certain physical conditions.

i) The modern techniques allow to fabricate atomic clusters from atoms of about any element of the periodic table. However, the conception of the mean field for valence electrons is realized only for a minority, mainly for clusters of alkali and noble metals, and, in a less extent, for neighboring elements.

ii) In some alkali metals (Na and K) the ionic lattice can, to good accuracy, be replaced by a uniform distribution of the positive charge over cluster's volume. This so-called jellium approximation greatly simplifies the calculations and is sufficiently accurate for the description of many properties of alkali MC. However, it often fails beyond Na and K and then more explicit treatment of the ionic structure is necessary [3, 4].

iii) The ionic subsystem is supposed to be "frozen", i.e., without any ionic phonon excitations.

iv) Validity of the jellium approximation is justified by temperature fluctuations of ions, smoothing ion positions. The approximation fails at low temperature, $T < 100$ K, where the explicit treatment of the ionic structure is important. At too high temperature, $T > 1000$ K, the quantum shells of the mean field are washed out, what establishes an upper limit for our considerations. We will consider GR in a temperature interval between these two extreme cases.

Lasers are actively exploited, mainly in the region of the visible light, in about all the areas of cluster physics [2] including production and transformation of clusters, investigation of their ground state and excitations, etc.

In particular, lasers provide very effective and universal method of cluster fabrication by vaporization. The first recorded observation of the fullerenes was made just by this method, see for review [16]. Namely, a pulsed laser beam (the green second harmonic of a Nd:YAG laser, 532 nm) was directed onto the surface of a rotating graphite disk. Only a few tens of millijoules were deposited onto a 1-mm-diameter spot of the surface of the disk but that was done in an extremely short time of 5 ns. The prompt heat was sufficient to generate a superhot plasma of carbon vapor which was then cooled by a burst of helium gas to start the process of clustering. Finally, a supersonic cluster jet was formed to be used for laser spectroscopy or (after ionization of clusters by a laser beam) for time-of-flight mass spectroscopy.

There are also other techniques to produce clusters, with using lasers at different stages [2]. For example, in JINR (Dubna) lasers were applied to fabricate heavy clusters of fissile elements [17]

Lasers are used to study E1-GR (dipole plasmon) in clusters by means of depletion spectroscopy (see [18] as a typical example). For this aim, the cluster beam is illuminated by a chopped laser beam. Photoabsorption by a cluster excites E1-GR (dipole oscillations of valence electrons) which quickly damps to a heat. The heated cluster rapidly evaporates one or more atoms and its subsequent transverse recoil prevents the cluster from entering the detector. Photoabsorption cross section is obtained by comparing the detected counting rate before and after irradiation of the cluster beam.

As was mentioned above, lasers are applied to ionize clusters. Multiple ionization results in fission of clusters[19].

3 Experiments with dipole plasmon

While in atomic nuclei investigations cover different multipole GR, the studies of GR in clusters are mainly limited to electric dipole resonance (dipole plasmon). E1-GR has been observed (mainly in photoabsorption) in a variety of clusters: small and large, spherical and deformed, neutral and charged, hot and cooled, free and supported, in linear and nonlinear regimes (see reviews [6, 7]). For other GR there are only theoretical predictions [6, 20, 21] since, as a rule, they cannot be observed in simple reactions with light. At

the same time, other reactions in cluster physics are still in their infancy.

Physical interpretations of E1-GR in clusters and nuclei are very similar: in nuclei it is caused by translations of neutrons against protons, while in clusters it is a result of translations of valence electrons against ions [22]. Such treatment reflects the fact that in principle E1-GR can exist in any finite two-component Fermi system. Indeed, this resonance has been observed in all nanosystems listed in the introduction. Some clusters have several kinds of valence electrons and so demonstrate more than one E1-GR. For example, in the fullerene C_{60}, two E1-GR are known as determined by weakly bonded π electrons and strongly bonded σ electrons (see, e.g., Ref. [23]). At the same time, noble gas clusters, being one-component Fermi system consisting only of Fermi-atoms (without separation to valence electrons and ionic background), have no any E1-GR [24].

Unlike to the case of atomic nuclei, E1-GR in clusters is determined by Coulomb interaction and is very influenced by an environment. As a result, it exhibits many interesting peculiarities. i) Most of clusters demonstrate the "spill-out" effect when some fraction of valence electrons lies beyond the ionic subsystem (like neutron fur-coat in some light atomic nuclei). In alkali metal clusters this leads to increasing E1-GR energy with the cluster size. Vice versa, in Ag clusters some electrons inside ions are also involved to the dipole oscillations. Interplay of latter effect with the "spill-out" one leads to the opposite trend: like in atomic nuclei, E1-GR energy decreases with the particle number. ii) Fragmentation (Landau damping) of the dipole strength strongly depends on a cluster charge: being strongest in negatively charged clusters, the fragmentation reduces in neutral and even more in positively charged clusters [25]. iii) In most of clusters jellium approximation is not valid and ionic subsystem drastically influences E1-GR properties. Besides, characteristics of E1-GR vary whether the clusters are free or embedded to a substrate, pure or with impurities, coated or not, etc. As compared with other Fermi systems, atomic clusters seem to demonstrate the richest collection of different kinds of E1-GR. Vice versa, E1-GR serves as one of the main physical probes of the cluster's features.

In particular, the resonance provides a single direct observation of cluster quadrupole deformation. In atomic nuclei, the deformation is directly indicated by rotational bands. This is impossible in clusters where big inertia moments result in rotational energies being too low to be observed at the background of thermal effects. Only deformation splitting of E1-GR can

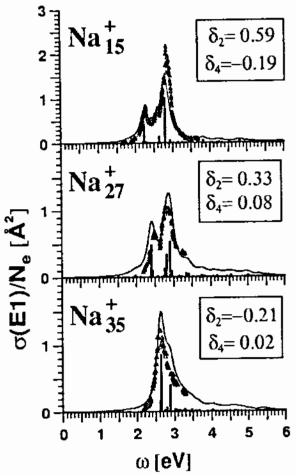

Figure 1: Photoabsorption cross section for dipole plasmon in deformed sodium clusters: prolate Na_{15}^+ and Na_{27}^+ and prolate Na_{35}^+. Parameters of quadrupole and hexadecapole deformations are given in boxes. The experimental data [26](triangles) are compared with the calculations [27] (bars for every state and curves for the averaged strength function). The bars are given in $eV a_0$.

serve as a direct evidence of cluster quadrupole deformation. Fig. 1 shows that the deformation splitting in axial clusters is of the same character as in nuclei. Namely, the resonance is split into short and high peaks corresponding to $\mu = 0$ and $\mu = \pm 1$ modes, respectively. Like in nuclei, the mutual position of the peaks reflects prolate (Na_{15}^+ and Na_{15}^+) or oblate (Na_{35}^+) shape. Experimental data [26] presented in Fig. 1 have been obtained in photoabsorption reaction where the cluster beam was illuminated by a pulsed dye laser.

Dependence of E1-GR energy on the number of atoms in clusters can be used to fabricate clusters of a desirable size and shape. The corresponding

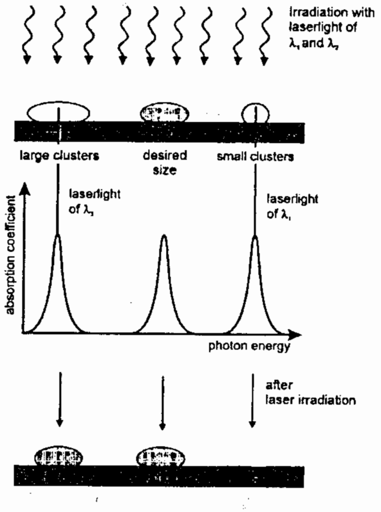

Figure 2: Scheme of the method to narrow the size distribution of supported clusters by laser irradiation [28].

laser-based method has been recently proposed for clusters on substrate surfaces [28] (see Fig. 2). The clusters were prepared by deposition of atoms and subsequent growth. These clusters are characterized by a wide size distribution. The distribution is narrowed by irradiation of clusters with a pulsed laser light whose frequency is chosen such that only clusters of a certain size interval absorb light efficiently. The absorbed photon energy is rapidly converted into heat, the cluster evaporates atoms and thus shrinks in size. Change in the size leads to the shift of E1-GR energy and the absorption process overs automatically when the cluster leaves the resonance energy region. If to use two frequencies specially adjusted for too big and too small clusters, then big clusters are shrank to a desirable size and small clusters are mainly deleted. As a result, size distribution of the clusters narrows dramatically.

The same technique can be used to control shape of the clusters. Shape of supported clusters, being driven by the interplay between cluster surface tension and interaction of clusters with the surface, varies from spherical to oblate form. In oblate clusters, E1-GR is split into two peaks whose energies depend on the deformation. This dependence is again exploited to fabricate clusters of a desirable shape by the same laser-based method. Moreover, the method can be used for simultaneous control of the size and shape.

During last decade, femtosecond lasers are widely used in cluster physics and chemistry. They provide fantastic possibilities to investigate different stages of chemical reactions. In cluster physics ultrashort laser pulses with a moderate laser fluency have been recently applied to study multiple dipole resonances in sodium clusters [29]. This problem is similar to one with double GR in atomic nuclei. The main trouble was to provide a sequential absorption of several laser photons for a time shorter than the plasmon life time. For this aim a femtosecond titanium-sapphire laser system was used. Finally, the multiple excitation involving up to 8 dipole plasmons has been detected! This study has also allowed to estimate the plasmon life time as 15-20 fs.

Much effort has gone into understanding of the interaction of short (≤ 1 ps) and intense ($\geq 10^{15} W/cm^2$) laser pulses with matter [30]. The motivation was to generate in the matter photons and particles with energies far above the energy of a single laser photon. X-rays and particles with energies up to the keV and even MeV range have been produced. As compared with other targets (gas, solid, etc.), the solids coated by a layer of clusters seem to be especially promising. Indeed, the interaction of the light pulses with clusters can be so intense that the absorption reaches nearly 100% [31]. This takes place when the photon energy matches the dipole resonance in clusters. Strong femtosecond laser fields can be also used for plasmon-enhanced multi-ionization of clusters [32].

4 Applications of nanosystems

Nanosystems have found wide applications in different areas. Only part of the applications is connected with using lasers. However, we find useful to list most exciting applications, irrespective of using or not the lasers, to demonstrate a great influence of nanosystems on modern technologies. Even if lasers are not directly used in the applications, they, as was demonstrated

above, are actively exploited in investigation of fundamental properties of nanosystems. These investigations in turn provide a basis for practical applications.

A tentative list of applications includes:

- Cluster ion beams are used to fabricate new materials by depositing clusters onto a surface (layer by layer) [33]. Such method is more effective than using atomic or molecular beams since, changing cluster's size and charge, we obtain more freedom to get a projectile with a desirable properties and thus to provide an optimal regime of the deposition (hard, soft, ...) [34].
- Irradiation of super-hard surfaces (diamond, silicon and silicon compounds, hard metal oxides, ...) by noble gas clusters can provide precise machining of these surfaces. Roughness of the surfaces can be decreased by an order of magnitude, thus forming atomically smooth surfaces [34].
- Cluster projectiles can create extremely large energy densities in a matter, which can be used, for example, to heat plasma. The cluster C_{60} accelerated to the energy 10 MeV induces larger energy density along its trajectory in material than 1 GeV ^{238}U projectile [34]!
- Changing number of atoms in clusters can result in dramatic modification of their properties. As compared with the bulk, some clusters change their behavior from metal to nonmetal, non-magnetic to ferromagnetic, antiferromagnetic to ferro- and ferri-magnetic, etc. [33]. Interaction with the surface additionally changes the properties. Such modifications can be useful for production of new materials.
- Sodium and some other metals, being widely applied to the catalysis, demonstrate new interesting catalytic possibilities while being used in a cluster form. The possibilities vary with a cluster size. Partial coating the cluster by other atoms additionally changes the catalytic activity [33].
- Modern electronics deals with objects of nanometer scale. The nanolithography allows to create different nanoscale structures and architectures on a surface for the aims of nanoeletronics and nanocomputering [33].
- Numerous nanoscale circuits, switches, devices are developed. The cluster C_{60} can serve as an amplifier [36]. Thermometers can be fabricated by nanolithographic techniques. Nanoscale microcoolers can serve for cooling X-ray and sub-mm wave detectors in astronomy. Nanoscale ultra-high-density magnetic recording disks are designed.
- Much effort is done to construct molecular nanocomputer with defect-tolerant architecture [33]. Discrete molecular devices are developed within

molecular and intramolecular approaches [35].

- Carbon nanotubes have found widest applications [37]. They have been recently proposed to be used as a transistor [38].
- Fullerene-potassium structures demonstrate high-temperature superconductivity.
- Cluster beams are applied to treat the cancer. Nanoparticles can be used for non-viral gene therapy. Fullerenes and fullerene derivatives doped with radioactive atoms (for example, $C_{60}+^{11}C$, $C_{60}+^{7}Be$) are of considerable use in radiochemical techniques in medicine (see, e.g., [39] and references therein).

Acknowledgments

The work was partly supported (V.O.N) by RFBR (grant 00-02-17194).

References

[1] V.O. Nesterenko, *Sov. J. Part. Nucl.* **23**, 1665 (1992).

[2] W.A. de Heer, *Rev. Mod. Phys.* **65**, 611 (1993).

[3] M. Brack, *Rev. Mod. Phys.* **65**, 677 (1993).

[4] C. Brechignac and J.P. Connerade, *J. Phys.* B**27**, 3795 (1994).

[5] V.O. Nesterenko, W. Kleinig, and V.V. Gudkov, in Proc. Intern. Conf. *Nuclear Structure and Related topics*, ed. S.N. Ershov, R.V. Jolos and V.V. Voronov (JINR, Dubna, 1997) p. 322.

[6] V.O. Nesterenko, W. Kleinig, and F.F. de Souza Cruz, in Proc. of Intern. Workshop *Collective Excitations in Fermi and Bose Systems*, Serra Negra, San Paulo, Brazil, 1998, Eds. C.A. Bertulani, L.F. Canto and M.S. Hussein, World Scientific, Singapore, 1999, p. 205; arXiv: physics/9904017 19 Apr 1999.

[7] F. Calvayrac, P.-G. Reinhard, E. Suraud, and C.A. Ullrich, *Phys. Rev.* C**337**, 493 (2000).

[8] H.W. Kroto *et al*, *Nature* **318**, 162 (1985); W. Kratschmer *et al*, *Nature* **347**, 354 (1990); A.F. Hebard *et al*, *Nature* **350**, 600 (1991).

[9] R.C. Ashoori, *Nature* **379**, 413 (1996).

[10] E.R.I. Abraham *et al*, *Phys. Rev. Lett* **74**, 1315 (1995). M. Farine, P. Shuck, and X. Viñas, *Phys. Rev.* A**62**, 013608 (2000).

[11] T.W. Ebbesen, *Phys. Today* **49**, 26 (1996); A. Thess *et al*, *Science* **273**, 483 (1996).

[12] Proceed. of Intern. Symp. *Cluster and Nanostructure Interfaces*, (Richmond, Virginia, USA, 1999), Eds. P. Jena, S.N. Khanna, and B.K. Rao, World Scient. Publ. 2000.

[13] L.G. Gerchikov *et al*, *J. Phys.* B**31**, 3065 (1998).

[14] Y. Chen *et al*, *Phys. Rev. Lett* **83**, 2406 (1999).

[15] F. Chandezon *et al*, *Phys. Rev. Lett* **74**, 3784 (1995).

[16] R.E. Smalley, *Sciences (N.Y.)* **31**, 22 (1991).

[17] Yu.P. Gangrskii *et al*, *J. Exper. Theor. Phys.* **85**, 42 (1997).

[18] K. Selby *et al*, *Phys. Rev.* B**40**, 5417 (1989).

[19] U. Näher *et al*, *Phys. Rep.* **285**, 245 (1997).

[20] V.O. Nesterenko, W. Kleinig, F.F. de Souza Cruz, and N. Lo Iudice, *Phys. Rev. Lett.* **83**, 57 (1999).

[21] V.O. Nesterenko, J.R. Marinelli, F.F. de Souza Cruz, W. Kleinig and P.-G. Reinhard, *Phys. Rev. Lett.* **85**, 3141 (2000).

[22] C. Yannouleas and R.A. Broglia, *Phys. Rev.* A**44**, 5793 (1991).

[23] N. Van Giai and E. Lipparini, *Z. Phys.* D**27**, 193 (1993).

[24] S. Bjornholm, *Contemp. Phys.* **31**, 309 (1990).

[25] C. Yannouleas, *Chem. Phys. Lett.* **193**, 587 (1992).

[26] M. Schmidt and H. Haberland, *Eur. Phys. J* D6, 109 (1999).

[27] W. Kleinig, V.O. Nesterenko, and P.-G. Reinhard, to be published in *Ann. Phys. (NY)*.

[28] F. Stietz and F. Träger, *Philosoph. Magazin* **B79**, (1999) 1281; T. Wenzel, J. Bosbach, F. Stietz and F. Träger, *Surf. Sci.* **432**, 257 (1999).

[29] R. Schlipper et al, *Phys. Rev. Lett.* **80**, 1194 (1998).

[30] M.D. Perry and G. Mourou, *Science* **264**, 917 (1994).

[31] T. Dimitre et al, *Phys. Rev. Lett.* **78**, 3121 (1997).

[32] L. Köller et al, *Phys. Rev. Lett.* **82**, 3783 (1999).

[33] *Cluster and Nanostructure Interfaces*, Eds. P.Jena, S.N. Khanna, and B.K. Rao, World, Scientific Publ., Singapore, 2000.

[34] Proc. of Intern. Symposium "Similarities and Differences between Atomic Nuclei and Clusters", Tsukuba, Japan, 1997, Ed. Y. Abe, I. Arai, S.M. Lee, and K. Yabana, AIP Confer. Proceed., v.416 (1998).

[35] C. Joachim, *Superlattices and Microstructures* **28**, 305 (2000).

[36] C. Joachim and J.K. Gimzewski, *Chem. Phys. Lett.* **265**, 353 (1997).

[37] M.S. Dresselhaus, G. Dresselhaus, and P.C. Eklund, *Science of fullerenes and carbon nanotubes* , Academic Press, New York, 1996.

[38] S.J. Tans, R.M. Verscheren, and C. Dekker, *Nature* **393**, 49 (1998).

[39] T. Ohtsuki et al., *Phys. Rev. Lett.* **77**, 3522 (1996).

PRODUCTION OF METAL ATOMIC CLUSTERS IN THE INTERACTION OF PULSED LASER RADIATION WITH MATTER

Z. Blaszczak[1], Yu.P. Gangrsky[2], I.N. Izosimov[3] and B.N. Markov[2]

1) *Faculty of Physics, Adam Mickiewiecz University, Poznań, Poland*
2) *Joint Institute for Nuclear Research, Dubna, Russia*
3) *V.G. Khlopin Radium Institute, St. Petersburg, Russia*

ABSTRACT

The formation of heavy clusters of Sn, Pb, Th and U atoms has been studied in a wide range of mass numbers in the interaction of intense laser radiation with matter. A description is presented of a setup for measuring yields and mass distributions of clusters. The operation of the setup is based on various methods: the laser resonance fluorescence method, the time-of-flight method and the fission fragment track counting method. The dependence is discussed of the yield and mass spectrum of clusters on production conditions.

INTRODUCTION

The recent progress of experimental facilities and methods has brought about the rapid development of nanoparticle physics, which deals with microscopic systems of nanometric dimensions. The term nanoparticle is used in reference to a wide group of various objects like atomic clusters, fullerens of different types, nanotubes, varied nano-architectures and ensembles on backings and in matrices, etc. At present nanoparticles can in fact be produced of any element. The attractive aspect of nanoparticles is that owing to the strong surface effects their properties are essentially different from those of the respective solid. What is more, being not fully formed, the ion grid of nanoparticles of a relatively small number of atoms is different from a standard grid, which also affects their properties. Nanoparticles are of great interest both for fundamental science (studying the evolution of systems from an atom to a solid; the interrelation of microscopic and macroscopic effects) and for applications. For example, state of the art microelectronics and microcomputers employ nanometric objects and are in ever-growing part based on various nano-architectures. The tendencies in this field strongly suggest that nanotecnologies will occupy a prominent place in the 21st century. All those unusual properties of nanostructure manifest themselves when a new class of bonded systems, atomic clusters, are produced and used.

ATOMIC CLUSTERS

The study of atomic clusters is now a promising and rapidly evolving area of physics [1-6]. Clusters are known as consisting of a finite number of bonded atoms n and filling the place between isolated atoms and the solid. They in fact constitute a particular state of matter. There is a line of investigation that deals with metal clusters (MCs), which resemble atomic nuclei in most of their properties. Phenomena like a mean field and shell structure, deformation of various types, cluster fission and others are also typical of MCs. Therefore it is of great interest to study the formation mechanism of large MCs in various processes and manifestation of shell effects in them. It is expected that the number of atoms in a cluster of that type close to about a few tens of thousands is likely to cause its transformation from a micro to a macrosystem. Naturally, this number depends on the sort of the atoms, the temperature and some of the other characteristics of the cluster. However those relationships are rather poorly known. No data actually are available on large MCs of elements heavier than lead [1,7-11]. As for clusters of the actinides and the transuranium elements, information on them is practically lacking, which appears to be due to the difficulties associated with handling radioactive elements. Some elements situated in the middle of the periodic table, for example tin, are also little studied.

This work presents the results of a study of the formation of clusters of Sn, Pb, Th and U atoms in a wide range of the number of atoms in them. MCs were formed in interaction of intense pulsed laser radiation with the above metals.

The interaction of intense laser radiation with matter is studied quite thoroughly [12, 13]. Pulsed laser radiation of no more than 10^9 W/cm^2 gives rise to the three main processes: 1) heating without phase transition, 2) melting and evaporation and 3) ionisation and plasma formation. As a result of those processes, atoms, molecules, singly- and multicharged ions, clusters and macroscopic particles of matter are emitted. The relationship among the intensities of those components is a function both of the laser radiation characteristics and of the surface properties of the sample irradiated. This results in cluster formation occurring under essentially different conditions. The three main ways are differentiated of cluster formation: a) condensation from evaporated atoms at the initial moment of the flying apart of the matter, b) the breaking up of hot macroscopic grains and c) intense evaporation of atoms from them. Such a variety of processes may be expected to result in the formation of clusters characterised by wide mass and temperature ranges.

EXPERIMENTAL TECHNIGUE

To study cluster formation, three detection techniques were used. Single atoms and singly-charged ions were detected by their resonant fluorescent radiation induced by continuous radiation from a tuned laser. In the case of clusters of up to several hundreds of atoms, the time-of-flight method was used. Heaviest clusters of more than thousand atoms were identified by the number of fission fragments produced due to the fission of the MC nuclei.

The setup diagram is shown in Fig. 1. Radiation from a pulsed laser (15) was focused on the sample under study (1), which was situated in a vacuum chamber pumped out up to a pressure of 5×10^{-6} Torr. The laser radiation was focused with lenses of diameter 20 mm and focus 45 mm.

To produce MCs, a copper vapour pulsed laser of the LGI-201 type and an yttrium-aluminium pulsed laser of the LTIPCH-7 type were used. The parameters of those lasers are presented in Table 1. The parameters are seen to permit varying the irradiance in a wide range (from 10^6 to 3×10^9 W/cm^2), which makes it possible to study cluster formation in a wide temperature range.

Table 1. Parameters of the lasers used to produce clusters

Laser	λ, nm	ω, Hz	Δt, ns	E_{puls}, mJ	$\bar{p}$, W	q, W/cm^2
LGI-201	510 ; 570	10^4	20	0.5	5	$10^6 - 10^7$
LTIPCH-7	1064	25	10	50	0.12	$10^7 - 3\cdot10^9$
	532	25	10	20	0.6	$10^7 - 2\cdot10^9$

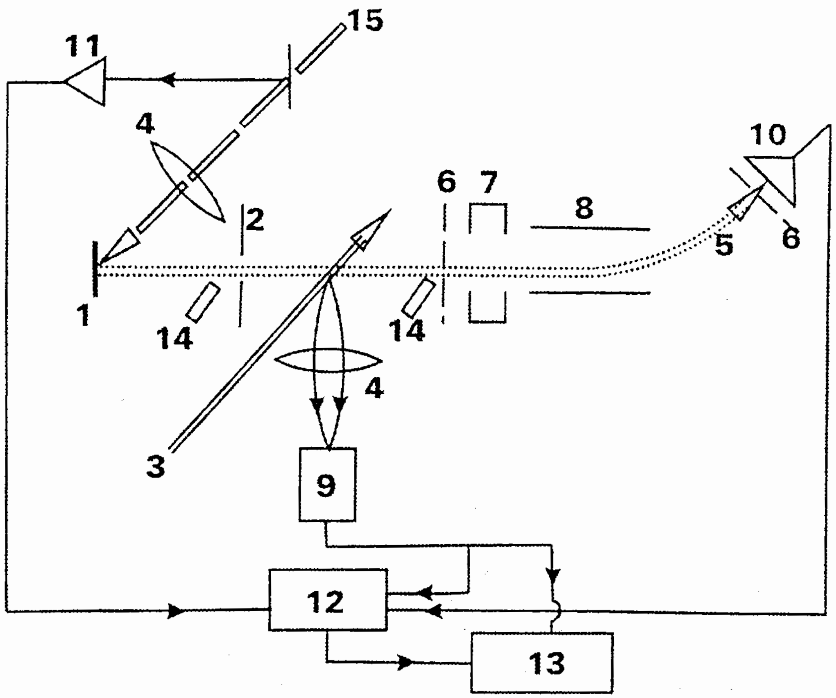

Fig. 1. Setup diagram. 1 – sample, 2 – collimator, 3 – beam of continuous-wave dye laser, 4 – optical lenses, 5 – beam of atoms and clusters, 6 – accelerating grid, 7 – electrostatic lens, 8 – deflectors, 9 – photomultiplier, 10 – ion detector, 11 – pulsed laser radiation detector, 12 – time analyzer, 13 – computer, 14 – dielectrical detectors, 15 – beam of pulsed laser

A collimator system (2) formed a beam of a prescribed angular divergence from the stream of atoms, ions and clusters (5) produced in interaction of pulsed laser radiation with the sample surface. This beam intersected the laser beam (3) at a right angle, laser beam 3 causing the resonant excitation of the flying atoms or ions. Laser beam 3 was emitted by a dye laser (the 380 D model, Spectra Physics), which was pumped by an ion argon continuous-wave laser (the 2030 SP model). The laser radiation frequency was automatically scanned in a given range up to 30 GHz in width. The laser line half-width did not exceed 29 MHz, which was essentially less than the Doppler frequency widening due to the energy and angular straggling of the atomic or ion beam. The light radiation emitted by the excited atoms or ions was focused on the cathode (9) of a FEU-136 photomultiplier, which was operated in the single-photon-counting mode [14]. The measured spectra of the resonant frequencies allow the intensity and average speed of the particles to be determined, which provides information about the MC formation conditions in the interaction of intense laser radiation with matter (about the plasma temperature and density on the sample surface). The spectrometric laser facility is diagrammed in Fig. 2.

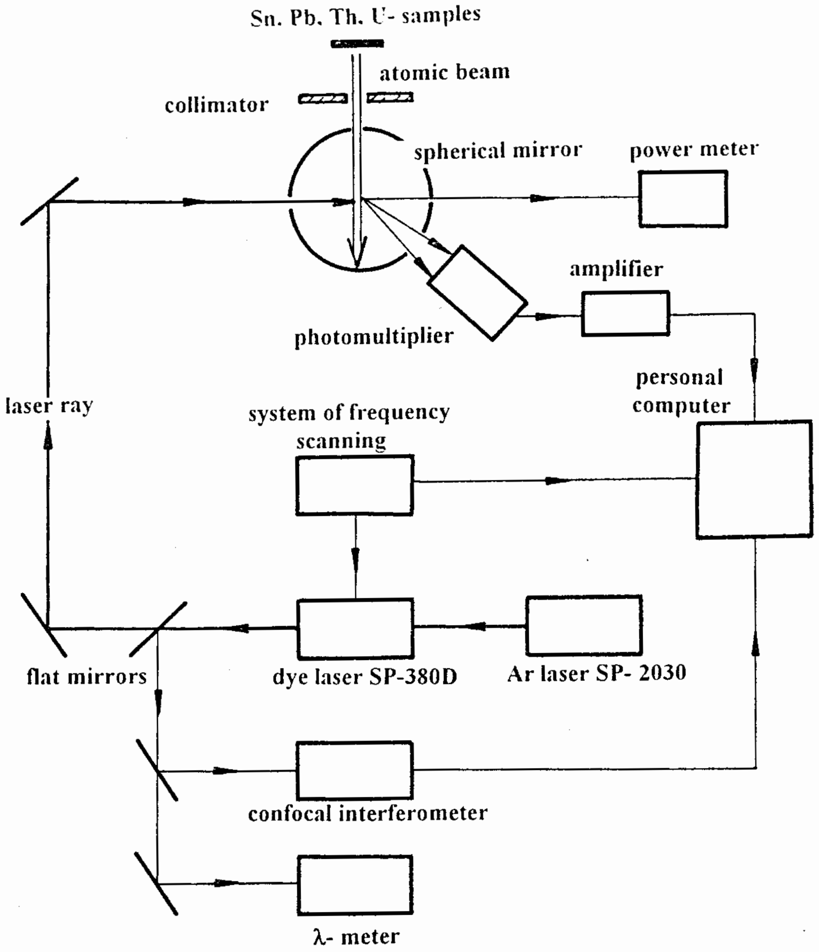

Fig. 2. Spectrometric laser facility

The characteristics of clusters (their mass spectra and speeds) were determined by measuring the time-of-flight of charged clusters for a given distance (from the sample surface to the detector) [15]. On passing forming collimator 2 (see Fig. 1), the charged clusters entered an area of an accelerating electric field created by a high voltage of up to 2.8 kV applied to grid 6. The accelerating distance was 30 mm. Then the beam of clusters of a specified energy was focused by an electrostatic lens (7) and entered a drifting zone 400 mm in length with a cluster detector (10) (a VEU-6 secondary electric multiplier) at its end. Deflectors 8, situated in the zone, served to separate charged clusters from neutral ones, for the latter not to hit the detector.

Pulses from that detector were stop signals for time analyzer 12, its start signals being pulses from photodiode 11, to which a portion of the pulsed laser radiation was diverted. The measured time-of-flight T is related to the cluster mass M (in mass units) by the relationship:

$$M = T^2 \left[\frac{7.25 \times 10^{-7} L_1}{E_0 + U} + \frac{1.44 \times 10^{-6} (E_0 + U)^{1/2} L_2 - E_0^{1/2}}{U} \right]^{-2}, \qquad (1)$$

where U is the accelerating potential (V); E_0 the initial cluster energy (eV); L_1 and L_2 the accelerating and drifting area lengths (mm).

By the same procedure, the speed distribution can also be measured for neutral atoms. In this case, a stop signal was a pulse from the FEU-136 photomultiplier (Fig. 2), which detected resonant scattered fluorescent radiation. This speed distribution also provided information on the sample surface temperature. As the mass of singly-charged clusters increases their kinetic energy (which is governed by the accelerating voltage) remains unchanged and the MC speed decreases.

The velocity of heavy clusters of more than 10^4 atoms is close to the thermal velocity (10^4-10^5 cm/s), and the ion detector signal does not exceed the noise level. Therefore such heavy clusters were detected and their mass was determined by another method. This method, only applicable in the case of clusters of atoms of fissionable elements (for example Th and U), is based on counting fission fragments from fission induced by an intense flow of neutrons or γ-quanta. The number of fission fragmens, number N,emitted from a cluster is defined by the expression:

$$N = 2A \int_0^{E_0} \sigma(E) Y(E,t) dE, \qquad (2)$$

where A is the number of atoms in the cluster; σ(E) and Y(E, t) the fission cross section and the integral flux of bombarding particles of an energy E in a time t respectively.

Fission fragments were detected with a dielectric film detector of 20 μm lavsan. Etching in a 20% NaOH solution for 15 min. made the tracks of the fragments become visible through an optical microscope (they were ~10 μm in length) [16]. The number of atoms of a fissionable element in a cluster can be found by counting the number of tracks issuing from one point, which are due to the fission of the atoms of the cluster.

These values are related by the expression:

$$A = \frac{N}{2\varepsilon \int_0^{E_0} \sigma(E) Y(E,t) dE}, \tag{3}$$

where ε is the dielectric detector fragment detection efficiency. In our experiments, in which clusters deposited on the detector surface, ε=0.5, i.e., the number of tracks observed corresponded to the number of the atoms in a cluster that underwent fission.

Expression (3) shows that the coefficient that links a number of tracks N with the number of atoms in a cluster A is defined by the fission cross section of the nuclei of the sample under study and by the integral flux of bombarding particles. For example, for ^{235}U sample and irradiation of the detector with thermal neutrons the fission cross section is $\sigma = 5 \times 10^{-22}$ cm^2 and the neutron intensity I(E) in the thermal column of a high power reactor can be as high as 10^{15} n/s · cm^2. Under such conditions, irradiating the detector for several hours (~2·10^4 s) results in:

$$\int_0^{E_0} \sigma(E) I(E) dE dt \approx 10^{-2}, \tag{4}$$

that is, each track observed corresponds to there being about a hundred of atoms in a cluster.

Cases in which each cluster has several tens (up to a hundred) of tracks issuing from it are most suitable for carrying out measurement. A large number of tracks will result in some of them being overlapped, which will bring about an error in determining their number. Since the number of events of nuclear fission in a cluster is a statistic process, the error in determining the number of tracks and hence the number of atoms in the cluster is expressed as:

$$\frac{\Delta N}{N} = \frac{1}{\sqrt{KN}}, \tag{5}$$

where K is the number of clusters observed. With N and K lying in the range 10 to 100, the accuracy of determining the number of atoms in a cluster, which is the mass resolution of the method, was 3÷10%. Though in some cases this resolution is not enough to obtain a detail picture of mass distribution, this method is highly sensitive and can be successfully employed for small yields of clusters.

Practically insensitive to other sorts of radiation: to plasma radiation, to atoms or ions, dielectric fission fragment detectors can be positioned in close proximity to the surface of a sample irradiated. In this way, with detectors positioned at different distances (10-400 mm) from the sample surface, a high measuring sensitivity is achievable. Comparing the cluster mass distributions from different detectors provides information on the break-up of clusters moving from the sample.

The setup outlined above, which is designed for studying MC formation, is characterised by the following parameters:

efficiency: ~0.01,
transportation time for laser-evaporated products: ~2 ms;
laser spectrometer frequency resolution: equal to or better than ~100 MHz;
time-of-flight selector time resolution: ~50 ns;
mass resolution by cluster tracks: 0.1.

MEASURED RESULTS

This setup was used to carry out experiments on measuring the mass spectrum of particles from single atoms and ions to microparticles produced under the action of pulsed laser radiation of power density lying in a wide range on samples of tin, lead, thorium and uranium (isotopes of ^{235}U and ^{238}U). Table 2 presents some of the characteristics of those elements and, for comparison purposes, Na, much used in cluster research [17]. Those characteristics define the thermodynamic and electric properties of the elements under study. In comparison with sodium, those elements are atomised at much higher temperatures and energies. At the same time, their relatively low conductivity is an indication of a smaller free electron concentration. In each experiment, the mass of the matter evaporated from the sample was determined by weighing the sample before and after the experiment as well as by measuring the crater produced on the sample surface (both methods gave close results).

Table 2. Characteristics of the element under study [17]

	Na	Sn (α)	Pb	Th	U
Density, g/cm^3 (t=20°C)	0.971	5.75	11.35	11.72	18.95
Boiling point, K	1156.1	2543	2013	5060	4018
Heat of evaporation, kJ/mol	89.04	290.4	179.4	543.9	422.6
Specific resistance, 10^{-6}·Ohm·cm (t=0°C)	4.2	11.0	20.6	13.0	30.8
Ionization potential, eV	5.14	7.34	7.41	6.08	6.05

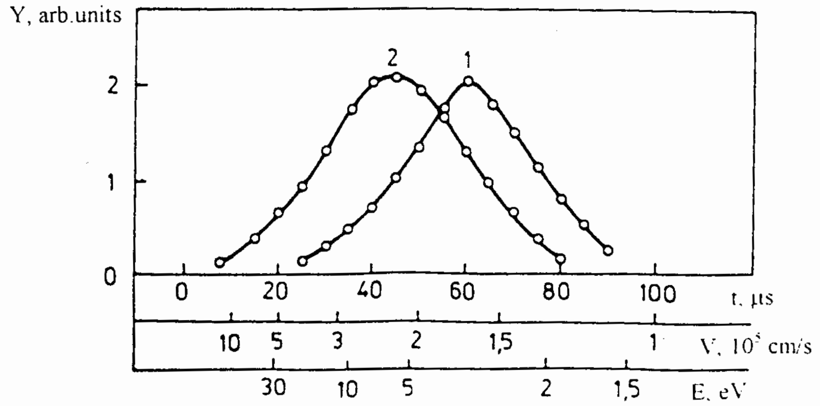

Fig. 3. Time-of-flight spectra for uranium atoms at various laser radiation power. 1- q=3x10^7 W/cm^2 ; 2- q=10^8 W/cm^2

Fig. 3 shows the measured time-of-flight spectrum for ^{235}U at two values of 1060 nm laser radiation power density (the irradiated area on the sample surface was ~1 mm^2). Those spectra permit calculating the velocity and energy spectra for a known flight distance (sample-to-laser beam distance) and atomic mass. In Fig. 3, each of those values has its own abscissa. The spectra obtained are consistent with the Maxwell velocity and energy distributions of atoms evaporated from the sample. They provide information on the temperature of the sample surface area irradiated by a laser beam. The temperature was evaluated taking account of there being an increase in the velocity of atoms due to the gas-dynamic flying apart of plasma [13, 18]. Table 3 presents the values of the average velocities and yields of atoms for Pb and U samples for various power densities and the diameters of laser-irradiated area.

Table 3. Velocities and yields of atoms for irradiation of Pb and U samples with laser radiation

λ, nm	q, W/cm^2	d, mm	V, 10^5 cm/s	Y, at/pulse	
				Pb	U
510;570	$3.0 \cdot 10^7$	0.3	$1.5 \cdot 10^5$	$3.5 \cdot 10^{12}$	$5.0 \cdot 10^{10}$
1064	$1.1 \cdot 10^8$	1.4	$2.0 \cdot 10^5$	$4 \cdot 10^{13}$	$1.5 \cdot 10^{12}$
1064	$2.5 \cdot 10^8$	1.0	$2.2 \cdot 10^5$	$1.5 \cdot 10^{14}$	$1.0 \cdot 10^{13}$
1064	$5.0 \cdot 10^8$	0.7	$2.5 \cdot 10^5$	$6 \cdot 10^{14}$	$4.0 \cdot 10^{13}$
1064	$3.0 \cdot 10^9$	0.3	$2.8 \cdot 10^5$	$2.5 \cdot 10^{14}$	$1,5 \cdot 10^{14}$

Fig. 4 presents the yield of single atoms of ^{238}U and the mass of the matter evaporated and condensed in the form of clusters and macroparticles (whose mass spectrum is considered below) as a function of laser radiation power density. The lower abscissa is the temperature of the sample surface. Both components are seen to show a maximum at some value of power density (or temperature), for clusters the maximum being at lower temperature.

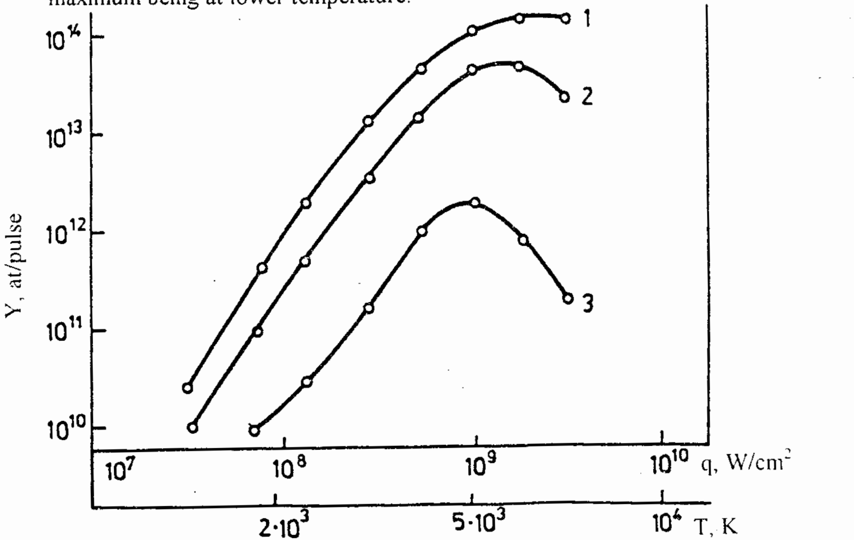

Fig. 4. Laser radiation power density dependence of the total yield of ^{238}U (1), the number of neutral atoms (2) and uranium clusters of N>1000 (3) evaporated from a sample by a laser pulse

Fig. 5 presents the mass distributions of the particles evaporated from Pb, Th and U samples under the action of 510 and 570 nm laser radiation of 3×10^7 W/cm^2, which were measured by the time-of-flight method. It is seen that in the case of Pb, singly-charged clusters of up to 10 atoms ($Pb^+_{n=1-10}$) are evaporated, whereas in the case of U, single ions are only observed. The similar mass distribution having a single peak for singly-charged single ions was also obtained for a Th sample (see the insert). That the yield of Pb_8^+ is smaller than that of Pb_7^+ is inconsistent with the shell model but seems to be understandable within the context of cluster valency [19]. It should be noted that for both elements the proportion of ionised clusters of 2 to 100 atoms did not exceed 1%. Other power densities (up to 10^7 W/cm^2) and another λ=1064 nm did not change the pattern. Under those conditions, no manifestation of shell structure was observed.

The mass distributions of Th and U clusters of more than 1000 atoms were measured by the track techniques of counting fission fragments on irradiation of dielectric detectors in a neutron stream. For example, in the case of the maximum neutron flux and a U sample, about 1000 atoms situated on the detector surface corresponded to one track. It should be noted that single tracks may be due both to single U atoms and to atoms grouped in a cluster of n<1000. Comparison of the number of tracks with the number of atoms measured by resonance fluorescence showed that no less than 95% of single tracks are due to single atoms whereas the proportion of clusters of n<1000 is less or equal to 5% of their number. At the same time, more-than-two-tracks events correspond to clusters (or macroparticles) of a number of atoms A (or n) more than 1000. Fig. 6 presents an example of one of the distributions. To decrease the statistical error in the number of clusters, they are grouped according to the number of atoms, the number of atoms in the clusters of one group ranging from A to 3A; where A is the minimum number of atoms which a cluster of that group can have. The error in the yields of clusters of each group is less than 5%. Fig. 6 shows that as with small numbers of atoms, the yield of clusters Y_{cl} decreases as A increases. The same is true for the whole range of laser radiation power density.

Table 4 presents the yields of different components – atoms, ions, small (A=2-100) and large (A>1000) Pb and U clusters for various laser radiation power densities. It is seen that in the case of Pb, the proportion of small clusters is ~10^{-2} of the number of single atoms whereas in the case of Th and U that proportion is less than 10^{-3}. The yield associated with the proportion of large clusters of a number of atoms A>1000 (the chosen reference value) is more noticeable owing to summing over the wider range of numbers of atoms in a cluster.

Table 4. Yields of the different components in irradiation of Pb and U samples with λ=1064 nm laser radiation

q, W/cm^2	Y_{at}, at/pulse		Y_{ion}, ion/pulse		Y_{cl}, cl/pulse A=2÷100		Y_{cl}, cl/pulse A>1000
	Pb	U	Pb	U	Pb	U	U
$1.1 \cdot 10^8$	$1.5 \cdot 10^{13}$	$5.3 \cdot 10^{11}$	$1.8 \cdot 10^{11}$	$1.0 \cdot 10^9$	$2.5 \cdot 10^{11}$	$<10^9$	$6.5 \cdot 10^{10}$
$2.5 \cdot 10^8$	$5.5 \cdot 10^{13}$	$2.5 \cdot 10^{12}$	$6.5 \cdot 10^{11}$	$2.3 \cdot 10^{10}$	$6.0 \cdot 10^{11}$	$<10^9$	$1.5 \cdot 10^{11}$
$5.0 \cdot 10^8$	$2.2 \cdot 10^{14}$	$1.2 \cdot 10^{13}$	$2.2 \cdot 10^{12}$	$1.2 \cdot 10^{11}$			$1.8 \cdot 10^{12}$
$3.0 \cdot 10^9$	$3.5 \cdot 10^{14}$	$1.8 \cdot 10^{13}$	$4.5 \cdot 10^{13}$	$2.5 \cdot 10^{12}$			$2.7 \cdot 10^{11}$

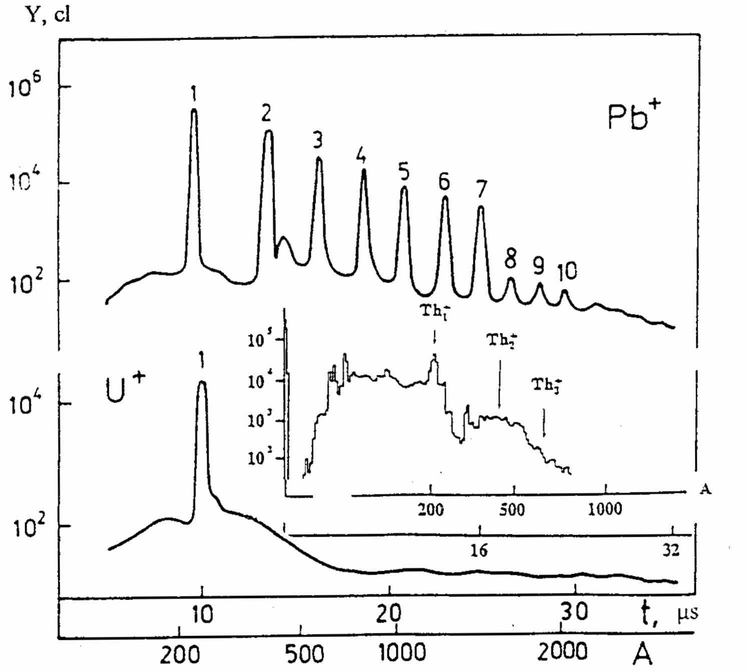

Fig. 5. Mass distribution of clusters of lead (at the top) and uranium (at the bottom) measured by the time-of-flight method at $q=3x10^7$ W/cm^2. The insert: data for Th$^+$ under the same conditions

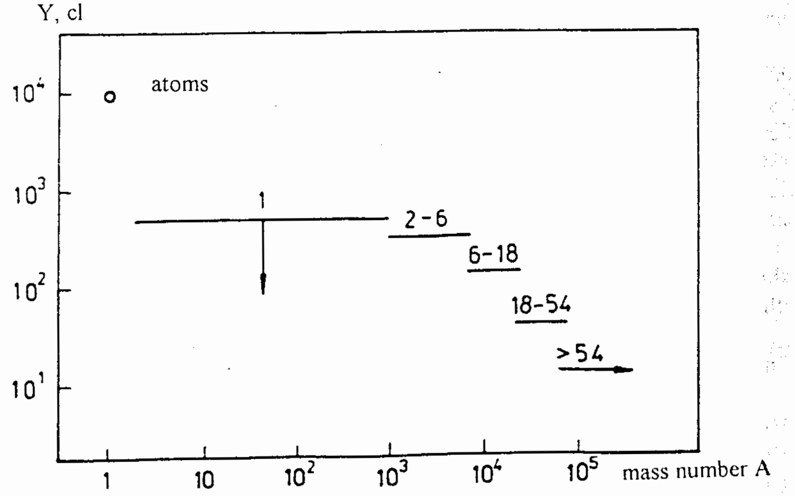

Fig. 6. Mass distribution for uranium clusters measured by the number of tracks of fission fragments, $q=3x10^7$ W/cm^2. The numbers above the lines are the numbers of observed tracks of fission fragments.

DISCUSSION

The experiments carried out showed that the yields of clusters produced under the action of intense laser radiation are essentially element dependent. Under the same radiation conditions, a marked yield of ionised Pb clusters (see Fig. 5) of 2-10 atoms and with noticeable shell structure was observed and no similar Th and U clusters were detected (whose yields were at least three orders of magnitude lower than those of similar clusters in the case of Pb).

For comparison purposes, experiments on MC formation were also carried out for tin, Sn, an element that, like Pb, belongs in group VI of the periodic table. Fig. 7 shows the mass distribution of the yields of Sn clusters, which was also measured by time-of-flight method at a laser radiation power density of $3x10^7$ W/cm^2. The yield of multi-atomic clusters of $Sn^+_{n=1-7}$ is noticeable, which suggests manifestation of shell structure in clusters of that sort. The experiments on Pb and Sn allow a tentative conclusion that the formation characteristics of multi-atomic clusters are similar for the elements of the same periodic table group and of close thermal properties. The importance of the discovery of shell effects in MCs lies in the fact that for the first time shell structure of non-geometrical character [13, 19] and close magic numbers manifests itself, as in atomic nuclei and atoms. Some difference in the numbers is accountable for by the fact that in MCs, spin-orbital interaction is negligibly small. In particular, super shells are likely to manifest themselves in clusters of a large enough n ($\geq$1000) [20]. In this connection, further studying the formation of heavy MCs in the region of Th, U and other elements is of great importance.

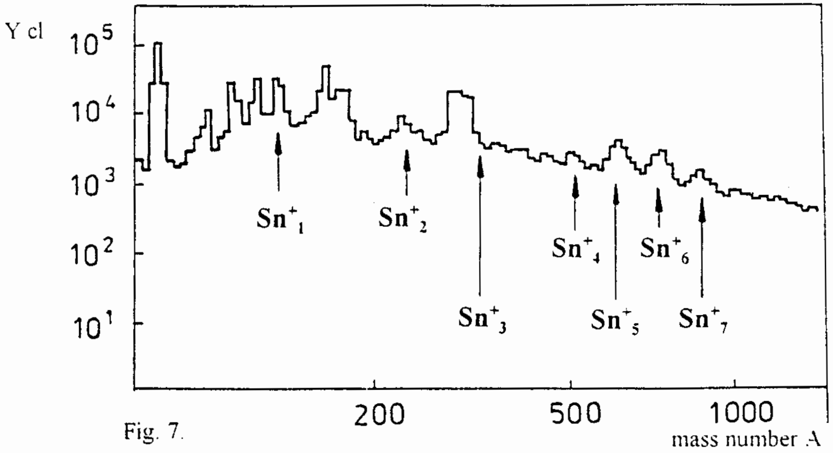

Fig. 7.

The measured velocity spectra of atoms of the elements under study (Fig. 3) permit making an estimate of the temperature of the plasma produced in the interaction of laser radiation with the sample surface. For radiation power densities lying in the range $3x10^7 \div 3x10^9$ W/cm^2, the temperature is $(2-6)x10^5$ K. So high plasma temperature is obviously not optimal for MC formation.

However at a smaller temperature (obtainable by decreasing the power of laser radiation) the yield of evaporated atoms decreases drastically, especially with high-melting elements like Th and U, which results in a decrease in the cluster yield The results of the work show that the probability of small Th and U clusters of the number of atoms n=2-100 being formed from macroscopic grains is very low. That plasma temperature does not seem to be enough for macroscopic grains to break up or for atoms to evaporate intensively from them, which could have result in small clusters being produced. Assessments of the time it takes a large amount of atoms (>1000) to evaporate, similar to those in work [21], showed that this time is great in value ($>10^{-3}$ s), which is noticeably greater than the time it takes grains to fly up to the fragment detector.

It was found that the yield of clusters produced in interaction of intense laser radiation with matter essentially depends on the temperature of the plasma produced. At the same time the temperature dependence of the distribution of clusters by the number of atoms in them is more indefinite. The probability of cluster formation differs noticeably for different elements.

The authors express their gratitude to Prof. Yu.Ts. Oganessian and Prof. Yu.E. Penionzhkevich (JINR, Dubna, Russia), Prof. A. Dobek and Prof. W. Nawrocik (AMU, Poznań, Poland) for their permanent interest in the work as well as to Prof. V.P. Perelygin (JINR) and to the members of his group for the help with gathering data from dielectric fission fragment detectors.

REFERENCES

1. A de Heer W., Knight W.D., Chou M.Y. et. al. // Solid-St. Phys. 1987, V.**40**, P.93.
2. Kresin V.V. // Phys. Rep., 1992, V.**220**, P.1.
3. Нестеренко В.О. // ЭЧАЯ, 1992, Т.**23**, С.1665.
4. A de Heer W. // Rev. Mod. Phys., 1993, V.**65**, P.611.
5. Brack m. // Rev. Mod. Phys., 1993, V.**65**, P.677.
6. Brechignac C., Connerade J.P. // J. Phys., 1994, V.**B27**, P.3795.
7. Muhlbach J., Satteler K., Pfau P., Recknagel E. // Phys. Rev. Lett., 1992, V.**87A**, P.415.
8. Satteler K. // Surf. Sci.,1985, V.**156**, P.292.
9. Lim H.S., Ong C.K., Ercolessi F. // Surf. Sci.,1992, V.**270**, P.1109.
10. Lim H.S., Ong C.K., Ercolessi F. // Z. Phys. D, 1993, V.**26**, P.45.
11. Siekmann H.R., Holubkrappe E., Wrenger B. et. al. // Z. Phys. B, 1993, V.**20**, P.201.
12. Рэди Д. // Действие мощного лазерного излучения на вещество,1974, М., Мир.
13. Быковский Ю.А., Сильнов С.М., Сотниченко Е.А., Шестаков Б.А. // ЖЭТФ, 1987, Т.**93**, С.500.
14. Ганрский Ю.П., Маринова К.П., Марков Б.Н. и др. // Изв. АН СССР, сер. физ., 1985, Т.**49**, С.2261.
15. Изосимов И.Н., Ворыхалов И.В., Римский-Корсаков А.А. // Изв.РАН, сер. физ., 1995, Т.**59**, С.21.
16. Флейшер Р.А., Прайс П.Б. // Треки заряженных частиц в твердых телах, 1981, М., Атомиздат.
17. Эмсли Дж. // Элементы, 1993, М., Мир.
18. Зельдович Я.Б., Райнер Ю.П. // Физика ударных волн и высокотемпературных гидродинамических явлений, 1966, М., Наука.
19. Ганрский Ю.П., Земляной С.Г., Марков Б.Н. и др. // ЖЭТФ, 1997, Т.**112**, С.78.
20. Pedersen J., Bjornholm S., Borggreen J. // Letters to Nature, 1991, V.**353**, P.733.
21. Смирнов Б.М. // ЖЭТФ, 1996, Т.**110**, С.47.

APPLICATION OF THE CHEMILUMINESCENCE EFFECTS AND PULSE LASER SPECTROSCOPY METHODS FOR U, Pu AND Np TRACE AMOUNT DETECTION IN SOLUTIONS

I.N.Izosimov, N.G.Gorshkov, L.G.Mashirov, N.G.Firsin, A.A.Kazimov,
S.V.Kolichev, N.A.Kudryshev, A.A.Rimski-Korsakov
V.G.Khlopin Radium Institute, 194021 St.Petersburg, Russia

Abstract

The applications of the laser spectroscopy methods for actinide trace amount detection in solutions are discussed. The special attention is devoted to the methods of chemiluminescence effects using and to its modifications. It is pointed out that the enlargement of the actinide elements number which can be detected with high sensitivity and selectivity may be obtain by using the combinations of the TRLIF method with other laser spectroscopy methods and chemiluminescence effects.

1. Introduction

Selective and sensitive direct actinide elements trace amounts detection in the different samples presents today major importance for ecology, radwaste handling and control, rehabilitation of contaminated areas and risk assessment. In recent years in the element and isotope analyses of environmental samples the laser radiation is used more and more widely [1-3]. The laser radiation can be tuned smoothly in the wide range of wavelength, has a high energy resolution and high power in comparison with usual light sources. These qualities of the laser radiation open new possibilities in determination of element and isotope composition of the environmental samples.

However the practical use of the laser spectroscopy methods in the analysis of different samples encounters one essential difficulty, namely it is necessary to get the investigated element from the sample to a zone of interaction with laser radiation. That is why the most attractive from practical point of view is to use the solutions of investigated samples. But in this case, as a rule, one cannot determine the isotopic composition of a sample.

The time-resolved technique (Time Resolved Laser Induced Fluorescence (TRLIF) method) allows to separate useful long-lived fluorescence from short-lived fluorescence impurity and from scattered light, that enables to increase considerably the sensitivity of a method in the application to long-lived fluorescence of lanthanides and actinides in solutions [4-6].

Now the following actinides : UO^{2+}, Cm^{3+}, Am^{3+}, Cf^{3+}, Es^{3+} *and* Bk^{3+} and some complexes of above-indicated actinides valence forms can be detected by TRLIF method [5-7]. The most progress achieved in UO^{2+}, Cm^{3+} *and* Am^{3+} TRLIF detection [5,8,9].

The observation of direct luminescence from Np, Pu and many molecules containing U in solutions is practically impossible in most cases because of very strong rate of radiationless deactivation [10].

We have found the possibility for Pu, Np and U detection in solutions with high sensitivity by using chemiluminescence effects. New approach to the problem, that uses high-resolution time resolved laser spectrometry in combination with chemiluminescence effects, makes it possible to improve the sensitivity and selectivity of actinides, including Pu, detection in solutions using simple automated procedures. The chemiluminescence effects using allows to essentially spread scope for trace amount detection of actinide in solutions, determination of the actinide valence states in solutions and determination of the molecule type containing actinide. Especially perspective is to use the chemiluminescence effects for detection of actinides and complexes containing actinides in solution in the cases when in such systems actinide does not give direct luminescence but can induce chemiluminescence. We have carried out the wide range of experiments on chemiluminescence study in solutions containing actinides excited by pulse laser radiation. Most of experiments were done with solutions containing uranium, plutonium and neptunium. The luminol chemiluminescence effects caused by pulse laser radiation and by actinides in excited states were studied.

2. Chemiluminescence in solutions induced by uranium excited by pulse laser radiation

In chemiluminescence, the energy is produced by a chemical reaction. We study the process in which excitation of actinides complex by pulse laser radiation led to the OH^* radical production. Than OH^* radical participates in chemical reaction with luminol and chemiluminescence takes place. The chemical reaction produces energy of about 300 kJ mol^{-1} induced chemiluminescence in the blue-light emission region, with 150 kJ mol^{-1} induced chemiluminescence in the red-light emission region [11]. In the case of OH^* radical reaction with luminol we have observed chemiluminescence in the blue-green light emission region.

Scheme of experimental set-up for luminescence charcteristics study is presented in fig.1. The nitrogen pulse laser (power in pulse 15kW, pulse repetition up to 500Hz, pulse duration 10 ns, λ=337.1nm) was used for solutions excitation. The power of laser radiation was controlled by photo-detector (P.Det.1) using capacitor for total charge collection during laser pulse. The start signal for kinetics study experiments was formed by photo-detector (P.Det.2) constructed from p-i-n diode connected with fast preamplifier. The time resolution of start detector was about 2ns.

Cuvette with solution was irradiated by laser radiation. Monochromator was used for luminescence registration in the range 400nm – 800nm. For the registration efficiency increasing the special light pipe was used. Luminescence was registered by photomultipliers (P.Det.3 and P.Det.4) operating in single photon counting mode. The background counting without laser radiation was not more than 300 pulses per second at 20° C. The registration and data acquisition systems for experiments have been realised in CAMAC standard. The data acquisition is controlled by personal computer connected to the CAMAC highway. The luminescence registration in experiments can be done after laser pulse with delay time tuning between 0.05μs ÷ 200ms and gate time tuning between 0.5μs ÷ 200ms. The gate and delay time parameters range may be changed if necessary.

Absorption spectra were measured at Shimadzu UVI 3101 spectrometer. ORION-611 pH-meter was used for pH solutions measurements.

We selected the experimental scheme in such way that the two uranyl complexes were formed in solutions both containing luminol and without luminol [12]. One of them is $UO_2F_5^{3-}$, the other one - $UO_2F_4OH^{3-}$. After excitation by laser radiation the $UO_2F_5^{3-}$ gives the direct luminescence. The $UO_2F_4OH^{3-}$ complex does not give the luminescence but the OH^* radicals were produced after uranyl excitation by laser radiation in this complex. After OH^* radical interaction with luminol the typical chemiluminescence took place. The absorption spectra measurements give us possibility to control the influence of pH on the of uranyl complexes concentrations in solution. In our experiments HF was used for pH regulation. The pH increasing led to the increasing of the $UO_2F_4OH^{3-}$ complex concentration and decreasing of $UO_2F_5^{3-}$ concentration (fig.2). As a consequences of these we observed the decreasing of uranyl direct luminescence and increasing of chemiluminescence intensity (fig.3 —fig.6). So studied the influence of pH on the luminescence intensity in solutions and its kinetics we could study the chemiluminescence induced by uranyl which was excited by laser radiation in $UO_2F_4OH^{3-}$ complex [12].

The luminescence spectra of $UO_2F_5^{3-}$ in solutions with luminol and without it are presented in fig.4. By the proper registration wavelength interval choosing one can discriminate the luminol luminescence from the uranyl

luminescence. The luminol luminescence kinetics at different pH for solutions containing uranium and without it are shown in figures 5, 6. Solutions were excited by pulse nitrogen laser radiation. From data presented in figs.5, 6 one can conclude that the luminol luminescence intensity increases for solutions containing uranium when pH increases. This experimental fact in combination with the absorption spectra analysis (fig.2) gives evidence about OH^* radicals production after excitation of uranium in $UO_2F_4OH^{3-}$ complex and chemiluminescence of luminol after interaction with these OH^* radicals [12]. By proper selection of uranium excitation scheme one can use this chemiluminescence for trace amount detection of non-luminescence uranium complexes in solutions using time resolved method (TRLIF). The most convenient medium for trace uranium detection may be one in which uranium is introduced into the luminol molecule [13]. The sensitivity of both luminescence and non-luminescence uranium molecules detection in solutions by using the chemiluminescence effects may be up to 10^{-11}M (mol/l) that is similar to the other elements and molecules detection by chemiluminescence methods [11,14]. Such sensitivity is not so high (10^{-12}M) as for the direct luminescence registration using time resolved technique (TRLIF) [5,8,9] but essentially higher than the sensitivity of non-luminescence uranium molecules detection in solutions by using photoacoustic spectroscopy methods. For example, the sensitivity of the Laser-Indused Photoacoustic Spectroscopy (LIPAS) method is about 10^{-7} M [15-19]. But the LIPAS method allows to determine the valence states of actinides and type of molecules containing actinides in solutions widely used. The methods use chemiluminescence effects, also as photoacoustic spectroscopy methods give us possibility to determine the valence states ant type of molecules containing actinides in solutions,and have more high sensitivity of detection than LIPAS. But the direct application of chemiluminescence methods can not give the high selectivity of detection. The detection selectivity problem for U, Pu and Np is solved by using the multi-step excitation of chemiluminescence in solutions.

3. Chemiluminescence in solutions induced by plutonium excited by pulse laser radiation

The luminol chemiluminescence in solutions induced by plutonyl excited by pulse laser radiation was observed in the similar way as for uranyl containing solutions. In our experiments were used solutions in which two types of molecules containing plutonium - $PuO_2F_5^{3-}$ and $PuO_2F_4OH^{3-}$ exist. The ratio between $PuO_2F_5^{3-}$ and $PuO_2F_4OH^{3-}$ concentrations changes when pH changing. We controlled concentrations of $PuO_2F_5^{3-}$ and $PuO_2F_4OH^{3-}$ molecules by absorption spectra measurements. In fig.7, fig.8 the absorption spectra typical for $PuO_2F_5^{3-}$ and $PuO_2F_4OH^{3-}$ at different pH values are presented at different pH. The intensity of characteristic $PuO_2F_4OH^{3-}$ absorption band with $\lambda=846.5$nm increases when pH increases and the intensity of characteristic $PuO_2F_5^{3-}$ absorption band with $\lambda=839$nm decreases when pH increases.From this experimental fact we conclude that only two main molecules containing plutonium exist in our solution - $PuO_2F_5^{3-}$ and $PuO_2F_4OH^{3-}$. The concentration of $PuO_2F_4OH^{3-}$ increases and of $PuO_2F_5^{3-}$ decreases when pH increases.In fig.9 the luminol luminescence spectra in solutions containing plutonium and without plutonium are presented. The pulse nitrogen laser was used for excitation. We observed more intensive luminol luminescence at the $\lambda > 500$nm (fig.9) for solutions containing plutonium compared to solutions without plutonium More intensive luminol luminescence in solutions containing plutonium than in solutions without plutonium was observed at pH›8.5. The differences of luminol luminescence intensity between solutions containing plutonium and without plutonium increase when pH rises. Such luminol luminescence intensity increasing in solutions containing plutonium when pH rises was explained by OH^* radicals formation after plutonium excitation by laser radiation in $PuO_2F_4OH^{3-}$ and chemiluminescence after OH^* radicals interaction with luminol [20]. The decreasing of luminol luminescence at $\lambda < 500$nm (fig.9) is connected with two main factors. One of them is the implantation of the plutonyl complexes into luminol molecules and the other one is the absorption of chemiluminescence by plutonyl (fig.8) in solution (inner filter effect).

The chemiluminescence effects may be used for plutonium and molecules containing plutonium detection in solutions. Our estimations show that after the optimal excitation and registration wavelength selection, the methods of chemiluminescence and time resolution effects using allow to detect different valence states of plutonium in solutions with sensitivity up to $10^{-9}M \div 10^{-11}M$.

4. Chemiluminescence in solutions induced by neptunium excited by pulse laser radiation

Solutions containing luminol and luminol with two types of neptunium molecules: $NpO_2F_5^{3-}$ and $NpO_2F_4OH^{3-}$ at different pH were irradiated by pulse laser radiation from nitrogen laser. The pH increasing led to $NpO_2F_4OH^{3-}$ concentration rise. After excitation of Np in $NpO_2F_4OH^{3-}$ complex OH^* radicals were produced. Interaction of the OH^* radicals with luminol led to chemiluminescence. The chemiluminescence was registered by the fact of luminol luminescence intensity increasing at $\lambda > 550$nm in solutions containing neptunium compared to the solutions without neptunium when pH rose [21]. Such type of chemiluminescence was observed (fig.10, fig.11) at pH›8. Decreasing of the luminol luminescence intensity at $\lambda < 550$nm in solution containing neptunium (fig.11) was explained both by luminol with neptunyl complexes formation and by inner filter effect [21].

5. Perspectives of the chemiluminescence method applications for actinides detection in solutions

It is very attractive to apply the Time Resolved Laser Induced Fluorescence (TRLIF) method for actinides trace amount detection in solutions because of its high sensitivity. But many actinides and their complexes (including Pu and Np) do not give the direct luminescence in solutions. For the detection of non-luminescent actinides and molecules containing actinides in solutions it is very perspective to use chemiluminescence methods in combination with time resolution method and chemiluminescence multi-step excitation. The chemiluminescence registration gives high sensitivity of actinides detection and multi-step chemiluminescence excitation gives high selectivity of actinides detection.

Diagram placing chemiluminescence among the most typical photophysical processes [11] is presented in fig.12. The response function of spectrometers using chemiluminescence for trace detaction have linear response reaching up to six orders of magnitude. The Limits Of Detection (LOD) for spectrometers using the registration of chemiluminescence are in the range from 10^{-6} mol/l to 10^{-12} mol/l depending on the type of solutions and type of detectable molecule [11,14]. Chemiluminescence is widely used as a base for detection methods in many fields, such as flow injection analysis, chromatography, biology, medicine, etc. [11]. We have observed and study the chemiluminescence effects in solutions containing U, Pu and Np. It's open possibility for chemiluminescence application in ***Nuclear Chemistry***. The sensitivity of the chemiluminescence methods is higher than sensitivity of other methods (LIPAS for example) which are used for non-luminescent actinides and molecules detection now. The combinations of the chemiluminescence effects with high sensitivity and high selectivity laser spectroscopy methods make it possible to carry out an effective detection both of luminescent and ***non-luminescent*** actinides and molecules containing actinides (especially U, Pu and Np) in different solutions.

6. Conclusion

The liquid systems are very attractive for actinides trace detection by using pulse laser radiation and laser spectroscopy methods.

The following results were obtained from the analysis of the experiments with solutions containing U, Pu, Np and luminol:

1. We have observed the chemiluminescence in solutions induced by the actinides which were excited by the laser radiation.
2. The experiments on chemiluminescence kinetic study have shown that the laser spectroscopy methods with time resolution can be applied for chemiluminescence detection in solutions containing actinides.
3. The chemiluminescence technique can be used for **non-luminescent** actinides (Pu and Np) and **non-luminescent** molecules containing actinides (U, Pu and Np) detection.
4. The chemiluminescence technique can be used for valence states of actinide and type of molecules containing actinide determination in solutions.

Acknowledgment

This work is supported by International Science and Technology Centre (ISTC), projects ISTC 616 and ISTC 2265.

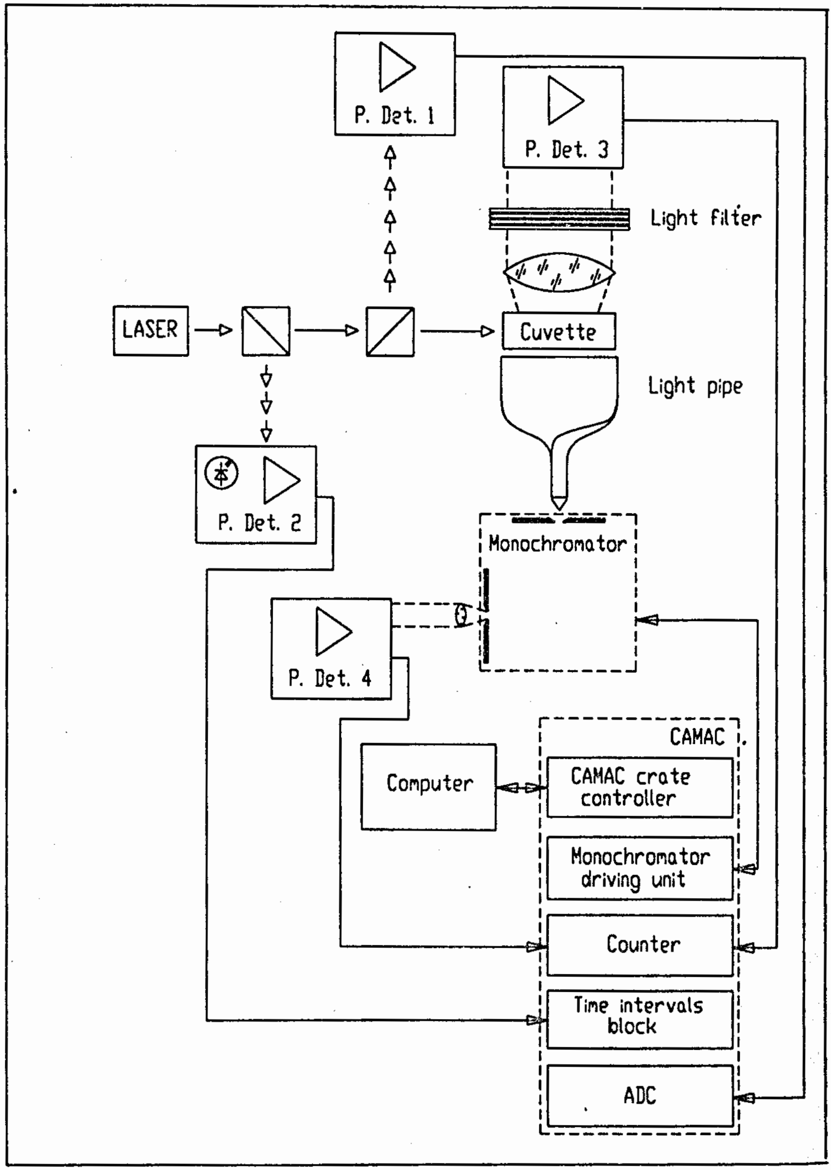

Fig.1. Scheme of experimental set-up for luminescence and chemiluminescence characteristics study.

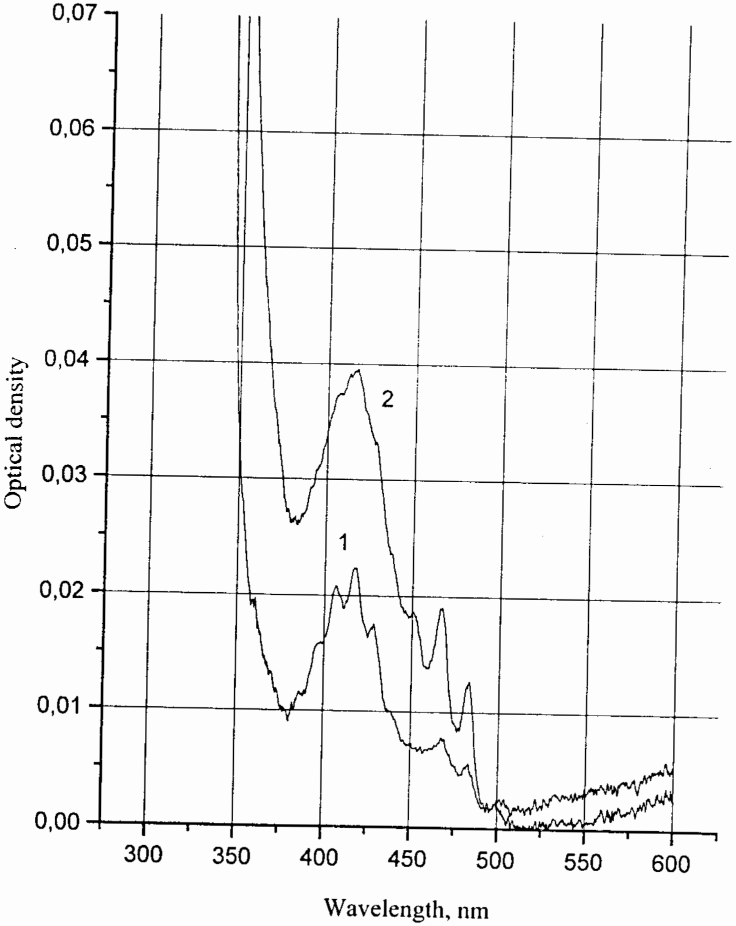

Fig.2. Absorption spectra of the uranyl complexes (0.005M UO_2^{2+}) in 42% CsF + 58% H_2O solution, pH=8.37 (1) and pH=10.8 (2). HF was used for pH correction.

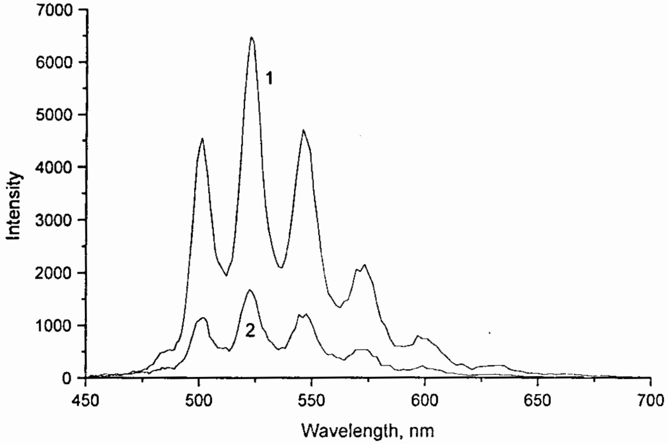

Fig.3. Luminescence spectra of uranyl complexes (0.005M UO_2^{2+}) in 42% CsF + H_2O solution for different pH values (1 – pH 8.37; 2 – pH 10.8).

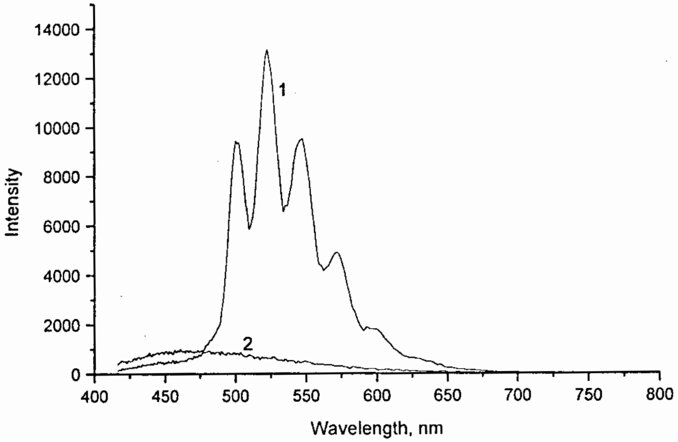

Fig.4. Luminescence spectra of $UO_2F_5^{3-}$ [0.005M] + luminol [10^{-3} M] in 42% CsF + H_2O solution (1) and luminol [10^{-3} M] in 42% CsF + H_2O solution (2) at pH = 8.37.

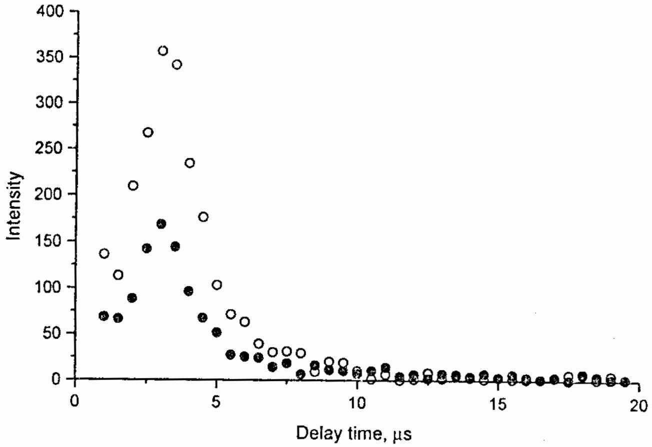

Fig.5. Luminol luminescence kinetics at λ=459nm in 42% CsF + H_2O, pH=8.19
○ - 10^{-3} M luminol without uranium
● - 10^{-3} M luminol + 0.009 M UO_2^{2+},
gate time 1 μs.

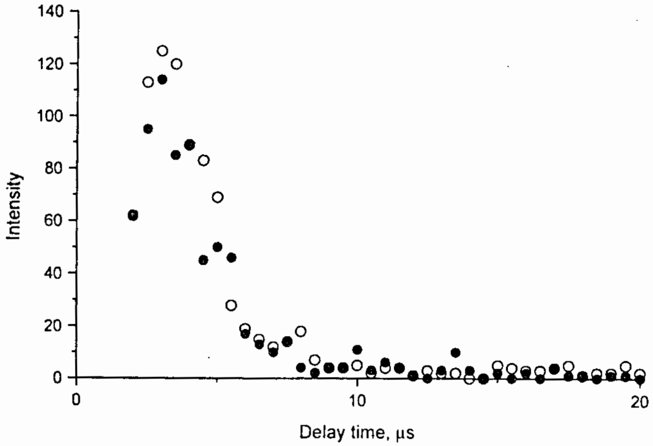

Fig.6. Luminol luminescence kinetics at λ=459nm in 42% CsF + H_2O, pH=11.85.
○ - 10^{-3} M luminol without uranium,
● - 10^{-3} M luminol + 0.009 M UO_2^{2+},
gate time 1 μs.

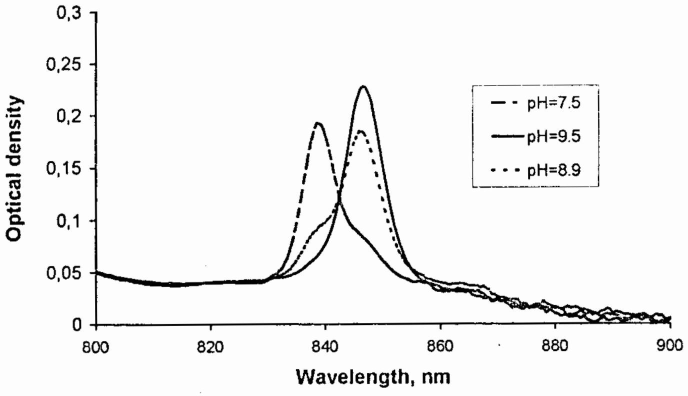

Fig.7. Absorption spectra of plutonyl complexes (PuO_2^{2+} 0.006 M) in 42 % CsF + H_2O solutions at different pH values.

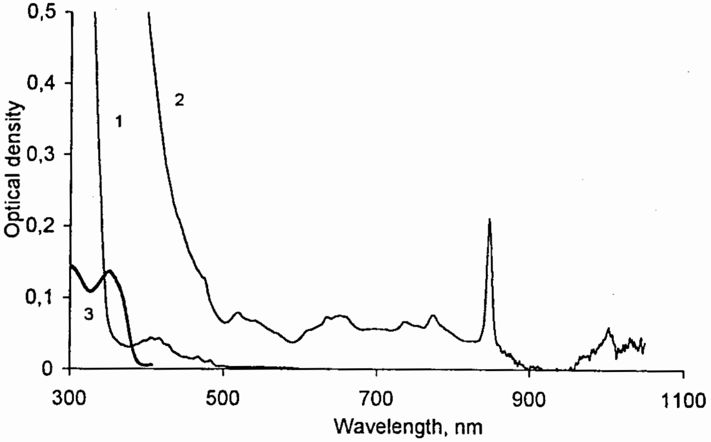

Fig.8. Absorption spectra: (1) - UO_2^{2+} (0.006 M), (2) - PuO_2^{2+}(0.006 M) and (3) – luminol at pH = 10.

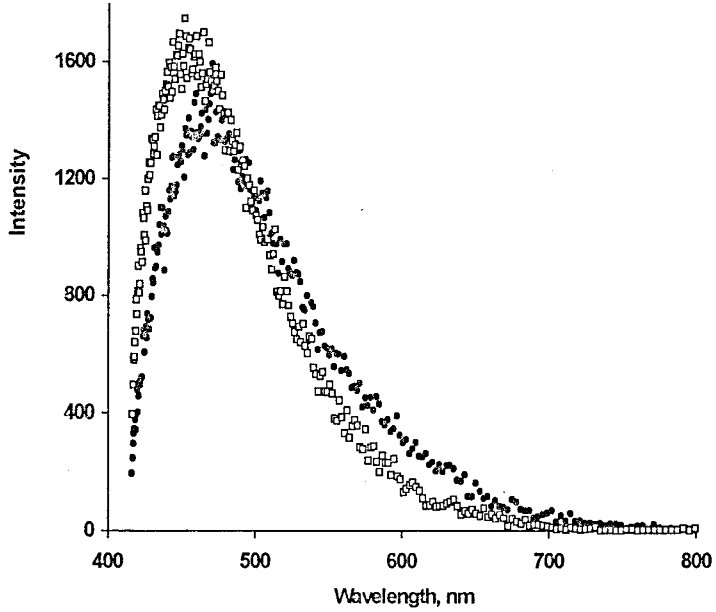

Fig.9. Photoluminescence in solution CsF (42%) + H_2O (pH = 8.5)

○ - plutonyl complexes (PuO_2^{2+} 0.001M) + luminol (10^{-3} M);

□ - luminol (10^{-3} M).

Excitation by pulsed (10ns) nitrogen laser radiation.

Delay time 2μs. Gate time 50 μs.

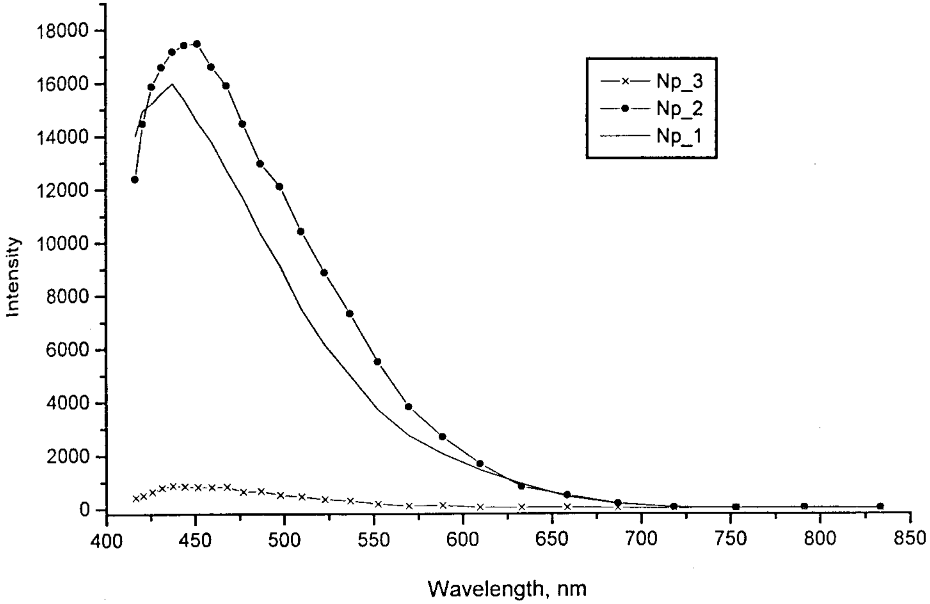

Fig.10. Photoluminescence :

Np_3 - luminol in solution CsF 42% in H_2O, **pH=8.0**; Delay time 200μs. Gate time 200μs.

Np_2 - luminol in solution CsF 42% in H_2O, **pH=8.0**; Delay time 1.5μs. Gate time 20μs.

Np_1 - neptunium complexes and luminol in solution CsF42% in H_2O, **pH=8.0**; Delay time 1.5μs. Gate time 20μs.

Excitation by pulse (10ns) nitrogen laser radiation.

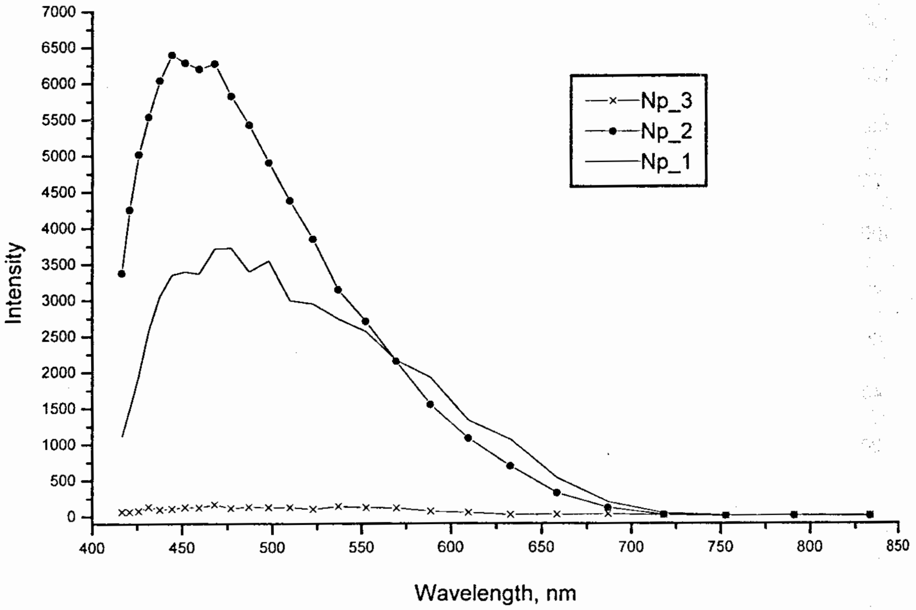

Fig.11. Photoluminescence :
Np_3 - luminol in solution CsF 42% in H_2O, **pH=9.6**; Delay time 200µs. Gate time 200µs.
Np_2 - luminol in solution CsF 42% in H_2O, **pH=9.6**; Delay time 1.5µs. Gate time 20µs.
Np_1 - neptunium complexes and luminol in solution CsF42% in H_2O, **pH=9.6**;
Delay time 1.5µs. Gate time 20µs.
Excitation by pulse (10ns) nitrogen laser radiation.

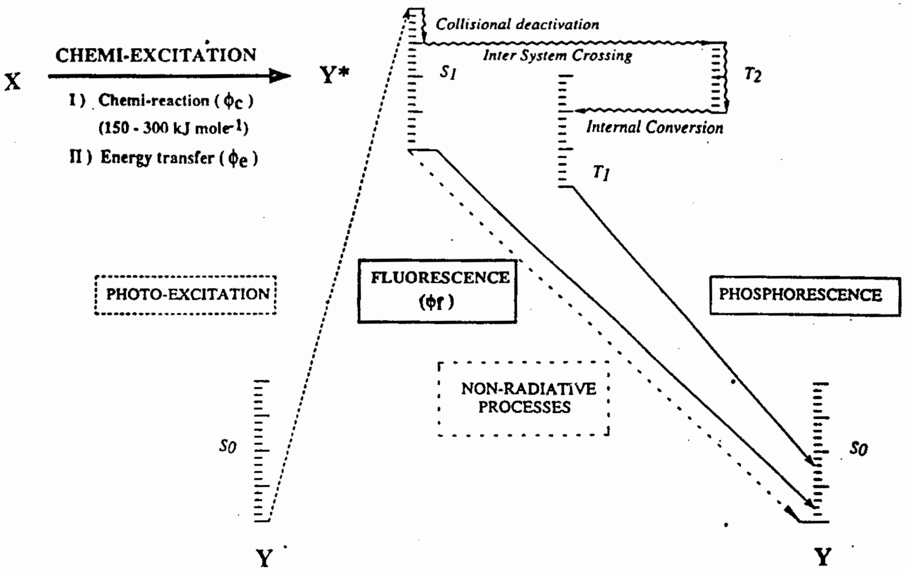

Fig.12. Diagram placing chemiluminescence among the typical photo-physical processes [11]. The chemiluminescence efficiency φ_{cl} (chemiluminescence quantum yield) is given by: $\varphi_{cl}=\varphi_c\cdot\varphi_e\cdot\varphi_f$, where φ_c is the fraction of reacting molecules giving an excitable molecule and accounts for the yield of the chemical reaction; φ_e is the fraction of such molecules in an electronically excited state and relates to the efficiency of the energy transfer and φ_f is the fraction of these excited molecules that return to the ground state by emitting a photon.

References

[1]. M.Nunnemann et.al., J. of Alloys and Compounds, 1998, v.271-273,p.45.

[2]. C.Moulin, et.al., Analytica Chimica Acta, 1990, v.238. p.291.

[3]. I.N.Izosimov, Proc. 4th International Workshop “Laser spectroscopy on beams of radioactive nuclei”, May 24-27, 1999, Poznan, Poland. p.169.

[4]. T.Berthoud, P.Decambox, B.Kirsch, et.al., Analytica Chimica Acta, 1989, v.220, p.235.

[5]. R.Klenze, J.I.Kim, H.Wimmer, Radiochim. Acta, 1991,v.52/53,p.97.

[6]. G.Bernhard, G.Geipel, V.Brendler, H.Nitsche, Radiochim. Acta, 1996, v.74, p.87.

[7]. C.Moulin, P.Decambox, P.Mauchien, Journal de Physique IV, 1991, v.C7, p.677.

[8]. C.Moulin, P.Decambox, P.Mauchien, Anal.Chem., 1996, v.68, p.3204.

[9]. P.Thouvenot, S.Hubert, C.Moulin, et.al., Radiochim.Acta, 1993, v.61, p.15.

[10]. C.P.Baird, T.J.Kemp, Progr. Reaction Kinetics, 1997, v.22, p.87.

[11]. C.Dodeigne, L.Thunus, R.Lejeune, Talanta 2000, v.51(3), p.415-439.

[12]. N.G.Gorshkov, I.N.Izosimov, A.A.Kazimov, S.V.Kolichev, et.al., Radiochemistry, 2001, V.43, No4, p.354.

[13]. N.G.Gorshkov, I.N.Izosimov, A.A.Kazimov, et.al., Optics and Spectroscopy, 2002, v.92, in print.

[14]. T.Schlederer, et.al. United States Patent 5,736,320 il 7,1998 “Method of detecting substances by chemiluminescence”.

[15]. M.P.Neu, D.C.Hoffman, K.E.Roberts, et.al., Radiochimica Acta, 1994, v.66/67, p.251.

[16]. G.Bidoglio, G.Tanet, P.Cavalli, et.al., Inorg.Chim.Acta, 1987, v.140, p.293.

[17]. S.Okajima, D.T.Reed, J.V.Beitz, et.al., Radiochim.Acta, 1991, v.52/53, p.111.

[18]. M.K.Richmann, D.T.Reed, Mat.Res.Soc.Symp.Proc., 1996, v.412, p.623.

[19]. G.R.Choppin, Analyt. Science, 1995, v.11,p.143.

[20]. N.G.Gorshkov, I.N.Izosimov, A.A.Kazimov, S.V.Kolichev, et.al., Radiochemistry, 2001, V.43, No4, p.360.

[21]. N.G.Gorshkov, I.N.Izosimov, A.A.Kazimov, S.V.Kolichev, et.al., Radiochemistry, 2002, in print.

TOPICAL APPLICATIONS OF BOUND INTERNAL CONVERSION

F.F. Karpeshin
V.A.Fock Institute of Physics and Physical Department,
St. Petersburg State University, Petrodvorets, RU-198904 St. Petersburg,
Russia

1 Introduction

It is tempting to use modern laser facilities to master nuclear processes in our purposes. Calculations show, however, that power of the available lasers in not enough, to produce a noticeable effect.

The action of laser field can be, however, enhanced by orders of magnitude, if a proper use is made of the resonance properties of the electron shell. This field, development of which was induced by paper [1], became a profound branch of contemporary investigation. The resonance, or discrete or bound internal conversion, introduced in paper [2] as early as in 1979, and experimentally discovered in heavy ions with joint efforts in an experiment carried out by Bordeaux group in 2000 [3,4], turned out an adequate means for description of the NEET (Nuclear Excitation by an Electron Transition) and its reverse, TEEN (Transfer of Energy by an Electron from the Nucleus) processes, which present a key to solution of the aforesaid problem. Application of TEEN offers a real tool of governing the rates of nuclear electromagnetic decays [5-7].

In the earlier our work we considered ways of producing the unique 3.5-eV isomer of ^{229}Th. Thorium atomic absorption and fluorescence spectra were studied experimentally, which forms a basis for practical realization of the proposed program. The 1-st Joint Workshop held in Saint-Petersburg in 2000 confirmed the right direction of the study [8]. Moreover, it gave an advanced picture of modern knowledge on Physics of Isomers, and formulated goals and prospects of future research in this direction.

The present proposal gives a plan of further development in this field, with use of the newest facilities and achievements of the contemporary investigation.

2 Study of NEET and TEEN in heavy ions

Use of modern facilities allows one to realize processes or conditions which cannot be created under usual conditions. Modern accelerators allow one to produce highly charged ions of heavy elements, up to one-electron ions of Th and heavier. Stripping of all the electrons but one allows one to use huge magnetic fields, which exist within atoms, but which impossible yet to create in laboratory. Such fields, together with use of resonance properties of the shell, are capable to fully change properties of the nuclei and modes of their transmutation. Thus, defect of the resonance in the case of ^{235m}U can be reduced to 0.3 eV, which is already within the domain of the hyperfine splitting. Moreover, resonance in H-like ions turns out to be much sharper than in neutral atoms [9]. Effect arising due to proceeding from neutral atoms to H-like ions is of the same magnitude as between radiative decay rate of bare nuclei and that in the case of resonance with the electron shell, that is many orders of magnitude.

Attenuation of the resonance in neutral atoms, e.g., for the K electrons, comes from the presence of the electrons in the 2p shell [3]. This causes too early filling the vacancies by the strong electric dipole transition of $2p \to 1s$. If all the upper electrons are removed, the vacancies can exist long enough that the converted electron can fill it again, transfering the energy back to the nucleus. Such a resonance exchange with the energy can occur several times running [9], which induces the resonance in the proper sense of the word.

The behavior of the electrons and their interaction with the nucleus in the field of an intense electromagnetic wave is described by the Quantum Electrodynamics (QED). Research into the processes with heavy ions brings us to the frontiers of the area where validity of QED is checked. Thus, there is a contradiction between experiment and theory concerning the hyperfine splitting in the H-like ions of ^{209}Bi [10,11]. The deviation is of approximately 0.3 eV, which is beyond the error bars of the experiment. The splitting has the same nature as internal conversion. It therefore is natural to apply the theory and experience acquired in studying the NEET and TEEN processes to calculation of the hyperfine splitting. Success will be a good test of both the QED and our description of the processes.

The results will find its application to producing isomers of ^{229m}Th. One can say that in H-like ions of Th 0.99999 of the work will be done by the natural hyperfine magnetic field [12], and only 10^{-5} of the work will remain to be done by man.

3 The role of NEET and TEEN in high-order multipole transitions

Resonance internal conversion can be considered as a glass helping in studying multipole transitions of higher orders. In first turn, this refers to isomers. Indeed, the probabilities of the radiative transitions drop quikly with the multipole order of the transition:

$$\Gamma_\gamma(\tau, L) \sim \frac{(\omega r)^{2L+1}}{[(2l+1)!!]^2} \quad . \tag{1}$$

where τ, L stand for the type and multipole order of the transition, r being a characteristic size of the system, and ω is the transition energy. The probability of the conversion transition can be conventionally represented as follows:

$$\Gamma_c = \alpha(\tau, L)\Gamma_\gamma(\tau, L) \quad , \tag{2}$$

where $\alpha(\tau, L)$ is by definition the internal conversion coefficient (ICC). In contrast with eq.(1), $\alpha(\tau, L)$ rapidly increases with the multipole order as follows [1]:

$$\alpha(\tau, L) \sim \frac{[(2l-1)!!]^2}{(\omega r)^{2L+1}} \quad . \tag{3}$$

It follows from eqs. (1) to (3) that the probability, or the width of the conversion transition weakly depends on the multipolarity:

$$\Gamma_c = \frac{1}{(2L+1)^2} \quad , \tag{4}$$

that converges slowly in the multipole order.

In turn, isomers usually arise as a consequence of a certain hindrance when the radiative transitions are considerably retarded. In principle, selection rules for conversion transitions are different from those for the radiative transitions. Therefore, the conversion transition can be non-prohibited at all, which results in the additionally increasing conversion probability. Therefore, the probability of internal conversion is especially high in the isomeric transition of large multipole order. Typical examples of such transitions are presented by the 75-keV E7 transition in ^{180}Ta.

It is of especial interest to perform calculations of the probabilities of deexcitation of these states through the TEEN process in ions of various degrees of ionization. This will allow to gain maximal resonance effect for a minimal energy difference of the electronic and nuclear levels.

4 The investigation of the processes occuring in laser-produced plasma

Research into processes which are induced by powerful femtosecond laser pulses is of great interest. As a result of interaction of the pulses with a surface of matter, the latter transforms into hot plasma. This consists of atoms with various degrees of ionization, and fast electrons. The electrons are accelerated in the tremendous electric and magnetic fields, arising in plasma due to nonlinear effects, up to energies of tens MeV. In the course of the acceleration, strong bremstrahlung hard radiation is produced, with the energy of the quanta up to tens MeV. Mechanism of all these processes is not quite understood yet.

Laser produced plasma can be used as a compact source of heavy ions. In experiments which are carried out in many laboratories heavy ions have been observed up to 46-fold stripped ions of Pb^{46+} [13].

Another important aspect consists in appearance of the huge magnetic fields. The tremendous magnetic fields arising in plasma make another important aspect of modern research. Characteristics of nuclei and nuclear transitions change very drastically under action of fields. The electron orbits are deformed, and squeezed into the nuclei. As a consequence, the nuclear decay rate of certain modes considerably increases. Among them is the electron capture by the nucleus, which occurs under normal conditions mainly with the K-shell electrons due to the weak interaction, and is accompanied by emitting of a neutrino. Another mode is internal conversion. With diminishing the electron orbit, a corresponding increase of the internal conversion probability is expected due to increasing Coulomb energy of the electron interaction with the nucleus. For this reason, these factors can serve as a trigger suddenly releasing the energy of the nuclear isomers.

5 Influence of the exclusion Pauli principle on the NEET and TEEN processes

The nuclear isomers typically have the transition energies of tens keV. For this reason, most often they can be in resonance with the electrons of the 1s shell. In such a situation, the converted electron which is lifted up to an excited state can fall on an occupied shell. At first sight, in this case realization of the resonance mechanism of NEET or TEEN becomes impossible. However, yet as early as in 1948 one of the founders of the QED R.Feynman showed that the exclusion principle is not needed to be taken explicitly into account. In a correct treatment of the principle, its influence on the unbound Feynman diagrams must also be taken into account. After dropping the unbound diagrams, the corresponding terms arise in usual bound diagrams, which exactly corresponds to as the Pauli principle would be disregarded from the very beginning. Therefore, there is no need to consider the exclusion principle in the intermediate state, which essentially extends the field of application of the NEET and TEEN for mastering the nuclear processes.

An example of treating the exclusion principle in a TEEN process in deexcitation of the 77-keV isomer of ^{197}Au was considered in paper [15]. It has been shown that the process of the two-quanta resonance conversion in the 1s-3s-2p-1s chain of the electron transition makes a negligible contribution to the nuclear deexcitation in a neutral atom. However, in the course of ionization a maximum in the conversion rate is achieved for the 42-fold ions. The maximum in the conversion rate corresponds to the minimum defect of the resonance, which arises due to change of the binding energies of the electron shells during ionization. For the 42-fold ions, the defect of the resonance decreases to the value of 1.2 eV as compared to 70 eV for the neutral atom.

Another isomer where this mechanism can be realized is a four-quasiparticle isomer of ^{178}Hf. This isomer is the only one where an acceleration of the decay induced by application of an X-ray beam has been reported [16]. It has been shown in the succeeding works induced by the publication [16] that it is impossible to explain the observed effect by a usual way of interaction of the isomer with the radiation. Incorporating the electron shell in the process will offer new ways of the interaction. Their discovery in experiment will be an outstanding success of the theory the resonance electron-nucleus interaction, a milestone in the development of the experimental technique. That shall affirm new horizons of applications of NEET and TEEN.

Experimental study of the resonance scattering of the photons and quanta is supposed to be an important issue of the proposal. From the experimental view point, this is a very difficult experiment because of a large background of various radiation arising in producing and scattering the radiation beams. A maximum in the scattering cross-section is observed when the energy of the incident photons approaches the energy of the intermediate state. If the intermediate state is occupied, the maximum might be suppressed by the exclusion principle. The suppression is however not expected to manifest itself because of the "violaton" of the Pauli principle in the intermediate state. The proposed experiment will give an exhausting answer on the given question.

6 Distinguishing features of NEET and TEEN induced by the electron scattering and radiation absorption

In many experiments on the NEET studies, excitation of atoms was performed by scattering of the electron beams and absorption of gamma radiation.

The electrons or gamma quanta are used for producing necessary vacancies. The Feynman graph of the corresponding process is presented in Fig. 1. Excitation of the nuclear level occurs in the electron transition, filling the vacancy. The energy of the transition is transferred to the nucleus. One can say that in the electron case, the excitation is also performed by photons, but by virtual ones. In spite of the similarities, both the ways have essential differences, which are considered bellow. Moreover, the electron cross-sections are important for understanding the dynamics of the processes in laser-produced plasma. In spite of considerable efforts, up to now no satisfactory agreement between theory and experiment has been achieved yet. The following circumstances can be pointed out as probable reason for the divergement.

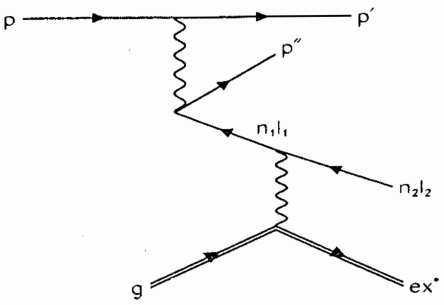

Figure 1: Feynman graph of the NEET. The necessary vacancies are produced by electron scattering.

1) Higher order effects in description of the electron interaction with the atoms are not taken into account.

2) The consequences of the “violaton” of the Pauli principle are not taken into account.

As a consequence of the “violation”, the resonance mechanism of the direct nuclear excitation by incoming electrons through the shell has to be taken into account. The corresponding Feynmann graph of the process is presented in Fig. 2. There is no ionization of the shell, and no vacancies are produced in this mechanism, contrary to what is conventionally believed to be necessary to induce NEET. Instead of this, a virtual process of the electron excitation to a resonant higher orbit takes place, with the succeeding transfer of the energy to the nucleus, as in a usual NEET process.

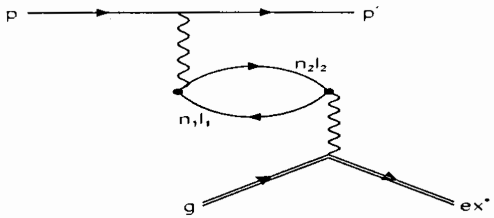

Figure 2: The Feynman graph of the direct resonance isomer pumping by electron scattering.

There is a way of direct experimental check of the second mechanism. For this purpose, one has to compare a cross-section of the nuclear excitation through NEET induced by monochromatic gamma quanta with that induced by electrons. If the energy of the quanta is enough for ionization of the atom, the second mechanism is absent in this case. If, however, the atoms are irradiated with gamma rays of continuum spectrum, the second mechanism arises again.

We note, however, that a possible mechanism of the atom excitation by photons through the Compton effect on the bound electrons has to be taken into account. The Feynmann graph of the process is presented in Fig. 3. In this mechanism, not the entire energy of the quantum is transferred to the electron, but only a fraction of it. In this sence, the Compton mechanism is again analogous to the second mechanism in the electron scattering. A difference is that in the electron case the transfer of a fraction of energy takes place already in the main, second order of

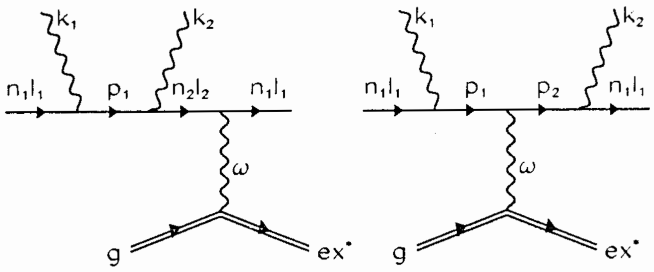

Figure 3: Feynman graphs of the NEET induced by Compton scattering of gamma rays: the resonance mechanism (left) and non-resonance one (right).

the perturbation series, whereas the Compton scattering of the gamma quanta occurs in the third order, which is two orders higher than in the conventional mechanism of producing vacancies through photoionization. Therefore. the relative role of these mechanisms is different. Note that research into the new mechanism of the Compton induced NEET. not discussed before, is of great interest by itself.

7 Study of the absorption and fluorescence spectra of thorium in various phases of matter

The following characteristic features of the atomic Th spectra were established in our experiments [20].

1) There are appropriate intense lines in the spectra, close to the energy of the $7s$ - $8p$ electron transition.

2) The absorption cross-section is in good agreement with the calculation [12] for the $7s$ - $8p$ transition.

3) An important part in the deexcitation of the atomic levels belongs to the. deexcitation via a quenching II kind processes of atom collisions, molecular excitation, etc.

The second kind dexcitation is a harmful effect, as this is a competing mode of the deexcitation, diminishing the NEET probability. In this sense, most effective way of producing the ^{229}Th isomer would be offered by optical pumping through NEET in an electron trap. when the density of the ions and therefore the quenching probability are minimum.

On the other hand, further study of the spectra in the targets corresponding to various phases of matter, such as solid, gaseous, liquid, or plasma ones, is of great interest from general viewpoint. It was shown in our previous papers that if a detuning is available between the frequencies of the atomic and nuclear transitions, then the probability of NEET increases with the increasing width of the resonant level. The nature and the value of the broadening are very different for various phases of the target matter. It also should be noted that the experiments aimed at studying ^{229}Th in the isomeric state dealt with very different sorts of the target materials. This also reasons further studies of the absorption and fluorescense spectra aimed at search for optimal ways of using NEET for pumping the nuclear isomers.

The author is grateful to M.B.Trzhaskovskaya for valuable help in preparing the manuscript and many discussions. He thanks Yu.P.Gangrsky for inducing discussions of the resonance internal conversion in the H-like heavy ions. This work has been supported by Defence Threat Reduction Agency (USA) under contract No. DTRA01-99-M-0514, and by Grant No. 99-02-17550 of the Russian Foundation for Basic Research.

References

[1] B.A.Zon, F.F. Karpeshin. Zh. Eksp. i Teor. Fiz., **97**, 401, 1990. (Engl. transl. Sov. Phys. JETP (USA), **70**, 224, 1990)

[2] D.F.Zaretsky, F.F. Karpeshin. Yad. Fiz., **29**, 306, 1979. (Engl. transl. Sov. J. Nucl. Phys., **29**, 151, 1979).

[3] F.F. Karpeshin, M.R.Harston et al., Phys. Rev. **C53**, 1640 (1996).

[4] M.R.Harston, T.Carreyre, J.F.Chemin. F.F.Karpeshin. and M.B.Trzhaskovskaya, Nucl.Phys. **A76**, 143 (2000)

[5] F.F. Karpeshin. I.M. Band, M.B. Trzaskovskaya. and M.A. Listengarten, Phys. Lett. **B372**, 1 (1996).

[6] F.F. Karpeshin, et al., Phys. Lett. **B282**, 267 (1992); Canad.J.Phys. **70**, 623 (1992).

[7] F.F. Karpeshin, I.M. Band. and M.B. Trzaskovskaya. Nucl.Phys. **A654**, 579 (1999).

[8] Physics of Isomers. Proceedings of the 1st Interbational Workshop, Saint-Petersburg, 18-21 June 2000. Editors: F.F.Karpeshin. S.N.Abramovich, Yu.P.Gangrsky. Sarov: RFNC - VNIIEF, 2001.

[9] F.F.Karpeshin. — In: ref. [5], p. 52.

[10] Klaft, S.Borneis et al. Phys. Rev. Lett., 73, (1994)

[11] V.M.Shabaev. J. Phys. **B27**, 5825 (1994).

[12] F.F. Karpeshin, S.Wysech, I.M. Band, M.B. Trzaskovskaya, M.Pfutzner, and J.Zylich, Phys. Rev. **C57**, 3085 (1998).

[13] E.L.Clark et al. Phys. Rev. Lett., **85**, 1654 (2000)

[14] V.S.Belyaev. — In ref. [5], p. 206.

[15] F.F.Karpeshin, M.B.Trzhaskovskaya, M.R.Harston, and J.F.Chemin. Phys.Rev. **C** (2001), in press.

[16] C.B.Collins et al. Phys. Rev. Lett., **82**, 695 (1999)

[17] S.Olariu and A.Olariu. Phys. Rev. Lett., **84**, 2541 (2000)

[18] D.P.McNabb, J.D.Anderson and J.A.Bocker. Phys. Rev. Lett., **84**, 2542 (2000)

[19] P. von Neumann-Cosel and A.Richter. Phys. Rev. Lett., **84**, 2543 (2000)

[20] A.E.Antropov et al. — In: ref. [5], p. 10.

DISCOVERY OF RESONANCE INTERNAL CONVERSION AND SOME OF ITS FURTHER APPLICATIONS

F.F.Karpeshin1), M.B.Trzhaskovskaya2), J.-F.Chemin3), and M.Harston3)

1)V.A.Fock Institute of Physics and Department of Physics. St.Petersburg University. Petrodvorets. RU-198904 St. Petersburg. Russia

2)Petersburg Institute of Physics. Gatchina. RU-188350 Gatchina. Russia

3) CENBG and IN2P3, Le Haut Vigneau, BP-120. F-33175 Gradignan Cedex. France

1 Introduction

Extending of well familiar old internal conversion beyond the usual sphere: off the mass shell and below threshold energies is a significant part of the contemporary investigation ([1]–[5] and refs.therein). Discrete, or resonance internal conversion plays a leading role in description of a resonance electron-nucleus interaction, which is of great interest for laser assistance of nuclear transitions [1]. Use of the resonance properties of the electron shell [3] allows one to drastically enhance the effect of externally applied radiation on the nucleus. This can be used as a tool for production of nuclear isomers, even allowing one to achieve inverse population of the nuclear levels, as shown by the example of the 3.5-eV isomer of ^{229m}Th [2]. Moreover, the hyperfine structure of H-like ions can be better understood in terms of discrete internal conversion, providing a test of QED. An illustrious example of using the hyperfine structure for producing the ^{229m}Th isomer is presented in [3].

In our theoretical study, we use modern methods in calculations of the atomic structure and of processes of interaction of electromagnetic radiation and a nucleus with the atomic electrons. We take into account configuration mixing, relativistic effects and higher-order QED corrections, like the Breit interaction between electrons, the electron self-energy, vacuum polarization, etc.

Presented below are several specific problems solved within the lines of such an investigation.

2 Internal conversion to bound final states in ^{125m}Te

In traditional internal conversion, the nucleus deexcites by ejection of a bound electron into continuum. If the nuclear excitation energy is less than the binding energy of the given electron, then the rate of conversion from this shell to continuum states had been expected to become zero. However, experiments on the deexcitation of highly-ionized ions of the ^{125m}Te nuclei showed a significant contribution from a subthreshold conversion process in which the nuclear deexcitation occurs via excitation of a bound electron to a higher-lying bound orbital. This process called BIC (Bound Internal Conversion) has been suggested to have a non-zero probability even when the nuclear deexcitation energy does not exactly match the electron excitation energy, due to the finite width of the atomic states, particularly the hole state produced by the electron excitation.

Investigations have focussed on the ^{125m}Te system. Its $1s$ binding energy is larger than the nuclear transition energy (35.491 keV) in ions with ionic charge $q \geq 45$. In such ions the nuclear transition energy may therefore lie close to the electron excitation energy of the $1s$ electron to a final Rydberg orbital just below the continuum threshold. The initial experiments performed by Attallah et al. (Phys.Rev.C **55**, 1665, 1997) have given indirect evidence for the BIC process based on the variation in the total half-life as a function of q. Direct evidence of the BIC decay by simultaneous measurements of both the X-rays following production of the $1s$ hole in Te and the γ-rays from the radiative nuclear decay has been obtained in recent experiments by Carreyre et al. in Bordeaux-Gradignan.

Most striking qualitative features of the BIC are as follows:

1) The conversion rate holds the same when the transition energy crosses the threshold energy, that is the energy goes under the ionization threshold for the K shell electrons.

2) The conversion rate strongly depends on the presence of electrons in the 2p shell. At first sight, they play a role of spectacles. However, their presence is main reason forming a sufficient width for the K-hole state formed as a result of BIC. For the 47-fold ions, when there are no electrons in the 2p shell, the BIC rate becomes zero for this reason.

We have performed the theoretical study of the decay rate of the isomeric nuclear state in ^{125m}Te for the ions Te^{45+} and Te^{46+} [6]. Calculations have been carried out in the framework of the multiconfiguration Dirac-Fock method (MCDF) with the allowance for the magnetic Breit interaction and for the QED corrections, including the electron self-energy, the vacuum polarization and so on. The correlation effects, the Breit interaction between electrons and the QED corrections have essential influence on the probability of BIC which is expected to be the main channel of the decay. The BIC probability and enhancement factors were computed having regard to the transitions from an each level of the initial state obtained in the MCDF calculations, to all levels of the final state, all possible populations of the valency $2p_{1/2}$ and $2p_{3/2}$ orbitals being considered.

The results of our calculations are in fair agreement with the experimental data obtained in Bordeaux-Gradignan. They give a convincing proof of manifestation of the BIC mechanism in the decay of the nucleus in Te^{45+} and Te^{46+}.

3 Producing the isomers

An idea of using an intense electromagnetic field of a laser in order to affect nuclear processes is of great interest from the scientific and practical viewpoint. However, application of even the strongest fields attainable nowadays leads to a negligible effect. Nevertheless, action of the field on the nucleus can be enhanced drastically, by several orders of magnitude, due to resonance properties of the electron shells. An efficient resonance occurs when the nuclear transition energy is close to that of the appropriate electron transition of the same multipolarity. This situation takes place for many nuclei: ^{197}Au, ^{229}Th, ^{179}Os, ^{237}Np, ^{235}U, etc. Employment of the resonance interaction allows one to exert control over nuclear processes.

A modern branch of such investigation is represented by the study of Nuclear Excitation during nonradiative Electron Transitions (NEET). Employment of the NEET processes for pumping of nuclear isomers, even allowing one to reach an inverse population of the ground and isomeric states, is of great interest for generation of coherent X-ray and gamma-ray radiation. Notice that the bound internal conversion may be considered as the reversal of NEET (so called the TEEN process).

In ^{229}Th, a uniquely low lying nuclear isomer level with spin and parity $3/2^+$ has been observed at the excitation energy of 3.5 ± 1.0 eV with respect to the ground state $5/2^+$. Investigation of the properties of the isomer requires practical methods of producing the source in enough quantities. In the α decay of ^{233}U, the isomeric yield of the Th nuclei is of the order of 10%. This way of getting the isomeric source has been used in a number of appropriate experiments. The isomeric nuclei, however, undergo the radiative transition to the ground state with the lifetime of 1 to 50 hours, which precludes collecting considerable amounts of the isomer.

A much more attractive way lies through use of pure ^{229}Th source. The lifetime of the ^{229}Th nuclei in the ground state is about 7000 years, which allows one to collect enough quantities of the nuclide. We have shown [3] that the isomeric state can be populated, e.g., by resonance laser radiation, the electron shell being a resonator. For this purpose, we have studied various mechanisms of the nuclear excitation. Their cross-sections σ have been calculated and compared to that for a bare nucleus σ_b.

i) The results obtained have shown that the most feasible for experimental study is the mechanism based on the NEET process including the $7s \rightarrow 8s$ electron transition. In this case, the enhancement factor $R = \sigma/\sigma_b$ achieves four orders of magnitude ($R = 8.96 \cdot 10^3$).

ii) We have also found new effective process for the excitation of the isomeric level, considering magnetic interaction of the electrons with the nuclei for excitation of the isomeric state. In collision of one-electron atom in the $1s$ state with a lead target nucleus, the electron produces a tremendous magnetic field in the vicinity of the nucleus. Prompt removing the electron in the collision induces related change of the potential, giving rise to the shake effects in the system. The effects can manifest themselves via excitation (shake-on) or disintegration of the system (shake-off).

iii) The effect has also been considered in muonic atoms. The shake arising in the decay of a muon in the $1s$ state, is marvelous. In this case, isomeric yield turns out to be practically 100%, that is an isomeric atom is obtained per every muon in the primary beam. This effect may become a most effective tool for pumping the 3.5-eV isomer in ^{229m}Th.

4 Enhancement of radiative transitions in a nucleus

We have also considered [4] the problem of enhancement of the radiative transitions between the ground and the 3.5 eV isomer states due to the hyperfine interaction in the hydrogen-like $^{229}\mathrm{Th}^{89+}$ ion. The extremely low energy of the M1 nuclear γ-transition results in the half-life of this excited state in a bare nucleus which is equal to several hours. In the hydrogen-like $^{229}\mathrm{Th}^{89+}$ ion, a single 1s electron produces an enormous magnetic field at the nucleus. For such a coupled nucleus-electron system, the hyperfine interaction may mix nuclear states of the same parity that differ by one unit of spin. The effect is enhanced by a small energy separation between the ground and isomeric states. Until now, such nuclear-spin mixing due to the magnetic interaction has only been observed in muonic atoms.

In collaboration with Polish scientists, we have shown that the spin mixing of the nuclear levels in $^{229}\mathrm{Th}^{89+}$ is expected to manifest itself via an impressive enhancement of the radiative transitions between the pairs of the hyperfine-structure components, relative to the nuclear γ transition. We have analyzed a possibility of experimental observation of these transitions at GSI (Darmstadt). This effect can be used for experimental discovering the isomer excitation in the NEET process via spin-flip transitions. Additionally, full spectroscopic information about the ground and isomer levels may be obtained, and a new effect of the nuclear-spin mixing may be discovered in such experiment.

5 Pauli exclusion principle in the NEET and TEEN processes

We have studied [7] the contribution to decay of the nucleus by an unexplored mode of the BIC process in which an excited nuclear state deexcites with excitation of an electron to an intermediate filled bound state that seemingly violates the Pauli exclusion principle. This contribution may be significant when very close matching of the atomic and nuclear transition energies is achieved. We have considered the M1 transition in ^{197}Au with the

energy 77.351 keV. The transition occurs by excitation of the $1s$ electron to the initially-occupied $3s$ orbital. We have shown that in this case, a proper treatment of the Pauli principle gives rise to a hindrance factor of the order of 500. The factor is proportional to the product of the lifetimes of the electron in intermediate states "forbidden" by the Pauli principle. Numerical calculations have been presented for the neutral atom of Au and for ions up to the ionic charge $q = 69$. This process has been found to have a maximum probability in the ion Au^{42+} due to close energy matching of the nuclear transition to the $1s \to 3s$ electron excitation. In this case the BIC decay mode contributes approximately 12% of the total decay rate of the nucleus ^{197}Au.

This work was supported by the Russian Foundation for Basic Research, project *No.* 99-02-17550, by Defence Threat Reduction Agency (USA) under contract *No.* DTRA 01-99-M-0514, by NATO Program of Portuguese Ministry of Science and Technology, and by Grant CNRS (France).

References

[1] F.F. Karpeshin, et al., Phys. Lett. B **282**, 267 (1992); Canad.J.Phys. **70**, 623 (1992).

[2] F.F. Karpeshin, I.M. Band, M.B. Trzaskovskaya, and M.A. Listengarten, Phys. Lett. B **372**, 1 (1996).

[3] F.F. Karpeshin, I.M. Band, and M.B. Trzaskovskaya, Nucl.Phys. A **654**, 579 (1999).

[4] F.F. Karpeshin, S.Wysech, I.M. Band, M.B. Trzaskovskaya, M.Pfutzner, and J.Zylich, Phys. Rev. C **57**, 3085 (1998).

[5] F.F. Karpeshin, M.R.Harston, et al., Phys. Rev. C **53**, 1640 (1996).

[6] M.R.Harston, T.Carreyre, J.F.Chemin, F.F.Karpeshin, and M.B.Trzhaskovskaya, Nucl.Phys. A **76**, 143 (2000).

[7] F.F.Karpeshin, M.B.Trzhaskovskaya, M.R.Harston, and J.F.Chemin, Phys.Rev.C (2001).

TUNABLE SEMICONDUCTOR WEAK POWER DIODE LASERS AND THEIR SECOND HARMONIC FOR ATOMIC ABSORPTION SPECTROSCOPY

Alfred Budziak and Tadeusz Pałasz

Institute of Physics
Jagiellonian University
30 059 Kraków, Reymonta 4
POLAND

Abstract

The construction of a single mode semiconductor diode laser spectrometer that can be tuned electronically by temperature as well as current is presented. The laser was tested by tuning to the rubidium resonant line (780.2 nm) : $5s^2S_{1/2}$ - $5p^2P_{3/2}$. By using a lithium iodate crystal the primary infrared light (830 nm) emitted by a Sharp LTO-15PT diode laser was successfully converted into the secondary light wave.

Keywords: lasers, second harmonic generation, absorption spectroscopy.

Introduction

Tunable lasers are an excellent source of light in basic research carried out in various branches of physics, chemistry and biology. In particular, they are extensively employed in atomic and molecular spectroscopy. In nuclear physics they are used to study the structure of the atomic nucleus and for separation of isotopes. Thanks to them the precise monitoring of air pollution was rendered possible (lidars). Nowadays we have at our disposal different dye and semiconductor lasers. Dye lasers allow for covering the whole visible spectrum of light and by means of second harmonic give us a chance to reach the corresponding ultraviolet region as well. However, a wider application of the dye lasers is tremendously limited by their large size, difficulties in handling and their relatively high price. The tunable semiconductor lasers are characterized as compared to the dye lasers by small size, easy and safety handling and low price. The presently produced laser diodes enable to cover the spectrum from the red to the infrared, and the range in the ultraviolet direction can be reached by their second harmonic.

In absorption spectroscopy the experiments are carried out by means of the following schematic system:

1. Source of light - Absorbent - Detection

The heart of that kind of a system is the source of light. At the present stage of technical development in that domain the specific requirements demanded of the sources of light are met only by lasers, especially by dye and semiconductor tunable lasers.

Unlike the classical sources of light such as arc discharge lamps the semiconductor lasers emit the light with a line width that is narrower by two orders of magnitude. They can be easily tuned by changing temperature or electric current strength, or by changing both parameters. As compared to the dye lasers the semiconductor lasers are characterized by a small size, low price, easy and safety handling, and exceptional durability. Inconvenience in their usage seems to be related to a relatively narrow range for altering their wavelength (for individual laser diodes) as well as the fact that they do not allow a user for continuous tuning because of a sudden mode switching. The above-mentioned limitations do not reduce the value of the semiconductor lasers since they can easily be eliminated. Usually to achieve this purpose several laser diodes are used to cover the range of wavelengths required in measurements and an optical resonator that is able to change the mode structure and to improve the continuity of tuning. The optical resonator plays one more role, it is able to decrease the laser line width below 10 kHz [1]. Due to these advantages the diode lasers have found in the last decade a wide scope of applications. Beside absorption spectroscopy their most important applications include: laser induced fluorescence, laser enhanced ionization, field ionization laser spectroscopy, resonance ionization spectroscopy, and resonance ionization mass spectroscopy [2-3].

In the present paper we present a simple construction of the thermally and electrically tunable semiconductor laser. We demonstrate its applicability in absorption spectroscopy and a possibility to extend its radiation to the ultraviolet region by means of generation of its second harmonic.

2. LASER CONSTRUCTION

In Fig. 1 the schematics of the mechanic construction of the tunable semiconductor laser is shown. A laser diode (1) is placed in a copper block with dimensions 20 x 60 x 70 mm adjacent to a plate (7) cooled by the Peltier thermoelements. A radiator (4) serves as a heat removing unit used in the course of the block cooling. The complete device is shielded from the outside by a thermal insulator. On the optical axis of the laser beam an Optima Precision antireflexive four-lens collimator (2) is located. The channel (3) is used for argon introduction and the argon flow protects the optics from wetting during the process of the laser diode cooling down to temperature *ca.* 0° C.

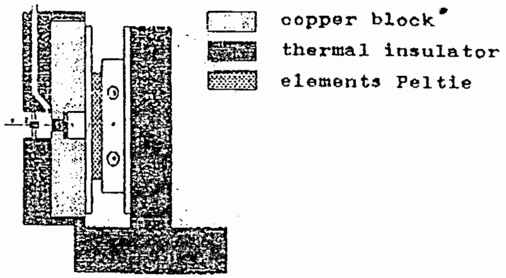

Fig. 1 Mechanic constructcion of the tunable semiconductor laser setup. 1 - diode laser, 2 - antireflexive four-lens collimator, 3 - channel, 5,6 - cooling3

This work has been financially supported by Polish Commitee for Scientific Research through the grant 2 P302 120 06 (PB 1104 / P3/ 94/06)

3. TUNING AND CONTROL OF WAVELENGTHS

In Fig. 2 the schematic chart of the elements used in tuning of the tunable diode laser is presented. The laser was tuned through the change of temperature or through the change of the strength of the laser diode electric current.

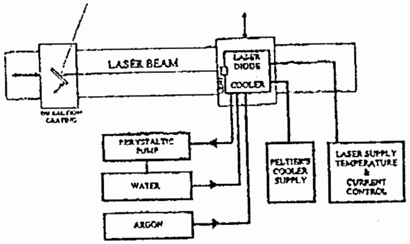

Fig. 2 Diode laser setup

The applied Peltier thermoelements with a overall power of 20 W enabled to decrease temperature to -2° C. The wavelength of the light emitted by the diode laser was measured by means of a Burleigh wavemeter (model WA-4500)

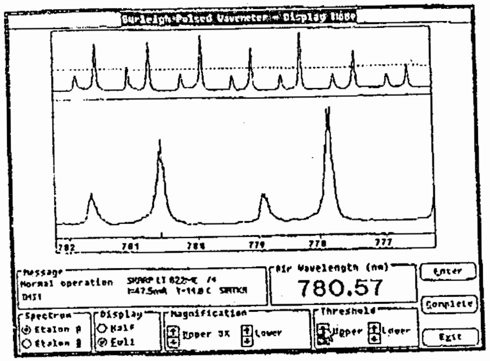

Message
Normal operation SHARP LT 022MC /4
I=47.5mA T=11.0 C
D4S1

Air Wavelength (nm)
780.57

Spectrum
● Etalon A
○ Etalon B

Display
○ Half
● Full

Magnification
Upper 3X
Lower

Threshold
Upper
Lower

Fig.3

In Fig. 3 a typical example of the laser line profile produced by a Sharp LT 022MC diode is shown, while Fig.4 illustrates two dependencies: the change of the wavelength as a function of temperature at constant strength of the diode feeding electric current (curve +++++), and the change of the wavelength as a function of the current strength at constant temperature of the diode (xxx)

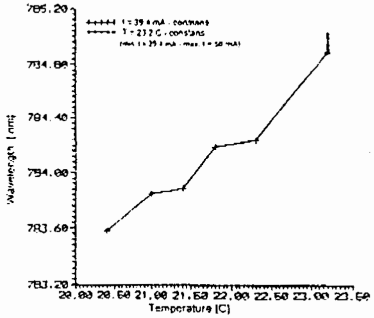

Fig.4 Change of the wavelength

4. LASER TUNING TO ABSORPTION LINE

The control over the precise tuning of the diode laser was maintained by making use of the absorption cell filled with rubidium vapors. In this case the diffraction grate playing the role of the optical resonator was not employed (see Fig. 2). The laser was tuned to the resonance line of rubidium (780.2 nm) by observing fluorescence of the rubidium vapors (Fig. 5).

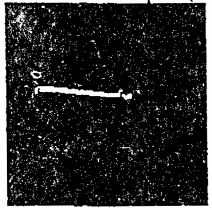

Fig.5 The fluorescence of rubidium vapour at room temperature upon tuning a diode laser (Sharp LT o22MC) to a rubidium resonance line (line D_2, - 780,2nm)

5. STABILITY OF LASER PERFORMANCE

The constructed system, upon tuning of the diode laser to the required wavelength, allows a stable performance within few minutes. This time has been extended to several minutes by correction of the electric current strength.

6. EXTENDING THE SPECTRAL RANGE OF THE SEMICONDUCTOR LASERS. SECOND HARMONIC GENERATION

The currently produced laser diodes emit the light spanning the range from red to deep infrared The region of the near ultraviolet towards the visual light spectrum can be reached by using the second harmonic.

The possibility of the light-to-light transformation of weak laser beams into second harmonic was demonstrated by Ashkin (1989) [4]. Kaczmarek and Jendrzejczak (1963) [5]. The progress in nonlinear optics allowed to produce new nonlinear crystals characterized by high efficiency of the light-to-light transformation. Budziak *et. al.* (1995) [6] have obtained a second harmonic of the semiconductor laser beam of 20 mW power and primary wavelength (830 nm).

In Fig. 6 the system employed for generation of the second harmonic is depicted. Unlike in the work [6] for the light wave transformation a nonlinear crystal of lithium iod ($LiIO_3$) was used.

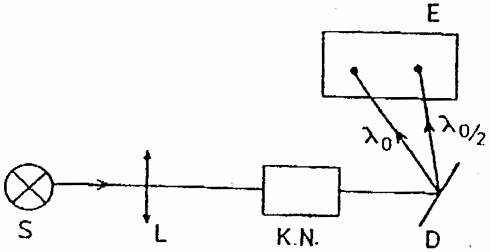

Fig. 6 The second harmonic generation set-up. S - Tunable diode laser KN - nonlinear crystal, D - reflecting diffraction grate

A laser beam having 25 mW of power (wavelength - 830 nm) was focused on a $LiIO_3$ crystal by means of a 3 cm focal-length lens (L). The crystal of $LiIO_3$ ensured that the transformation of light achieved almost 10% efficiency.

7. CONCLUSIONS

The described laser construction (more details can be found in [7]) allows for precise tuning of the laser diodes and guarantees a stable performance of the system upon tuning. In the experiments of absorption spectroscopy it may be applied in a simplified version, that is without the optical resonator, or the diffraction grate (see Fig. 2).

The possibility of transforming the weak laser beams into second harmonic will have a significant influence on the application of the tunable semiconductor lasers in absorption spectroscopy, spectrochemistry, and other fields of the scientific research. The single-mode semiconductor lasers have already been intensively used in holography [8].

8. ACKNOWLEDGEMENT

The authors wish to thank Professor W. Gawlik and Professor K.Niemax for the fruitful discussion and valuable remarks.

This work has been financially supported by the Polish Committee for Scientific Research through the grant 2 P302 120 06 (PB 1104/P3/94/06).

REFERENCES

1. K.C.Harvey, C.J. Myat, Opt.Lett. 16, 12 (1991)

2. V.S. Letokhov, Laser Photoionization Spectroscopy, Academic Press, Orlando, FL 91987)

3. R.Hergenroder and K.Niemax, Laser atomic absorption spectroscopy applying semiconductor diode lasers, Spectrochimica Acta, Vol.42B, 100, 1988, Printed in Great Britain

4.A.Ashkin, Boyd and Savage, Phys.Rev. Lett., 11 (1963) !4

5. F.Kaczmarek, A.Jendrzejczak, Optical and Quantum Electronics, 15 (1983) 187

6.A.Budziak, T.Pałasz, Tunable diod laser for atomic absorption spectroscopy, Proc. Int.Conf. PHOTONICS 95, Prague, Czech Republic, August 23-25, 1995

7. A.Budziak, A.Budziak, L. Pokora, Generation of second harmonic by means of diode laser, Proc. Int. Conf. PHOTONICS 95, Prague, Czech Republic, August, 23-25,1995

TRANSPORTATION OF PHOTOFISSION FRAGMENTS WITH AN AEROSOL-CONTAINING GAS FLOW

Yu.P. Gangrsky, V.P. Domanov, G.V. Mishinsky,
Yu.E. Penionzhkevich, Yu. Selesh, V.I. Zhemenik

Join Institute for Nuclear Research, Dubna, Russia

The experimental set-up described is intended for the transportation of the photofission fragments of heavy nuclei with an aerosol-containing inert gas flow. The operation of the set-up is as follows: the fission fragments that have escaped from the target are slowed down in an inert gas filled volume, adsorbed by aerosols and transported through a long and thin capillary to the radioactive radiation detectors. The results of tests of the set-up on a microtron bremsstrahlung beam with a ^{238}U target are presented in this paper. The set-up characteristics (efficiency of up to 70%, transportation times of 0.2 and 4 s for distances of 1 m and 30 m correspondingly) allow the set-up to be successfully employed in the studying of the nuclear fission process and the properties of the fragments produced.

Introduction

A wide variety of techniques are used for studying of the properties of nuclides far from the β-stability valley (neutron-deficient and neutron-rich nuclides). However no technique can do without a set-up for transportation of the fission fragments from a target of a fissionable substance to radioactive radiation detectors.

This work considers a technique for transportation fission fragments by a flow of an inert gas with aerosols added. Described is an experimental set-up tested on a microtron bremsstrahlung beam, making uranium nuclei fission. The results of those tests and the set-up characteristics obtained are presented. The fields of application of the set-up in nuclear research are discussed.

Experimental set-up

The set-up includes a reaction chamber with a target, a collecting chamber for collecting the fragments, a fogger, a vacuum pump for pumping out the gas, those parts of the set-up being connected with a long capillary (Fig. 1).

The reaction chamber was a cylinder with an inner diameter of 25 mm and depth of 30 mm; the entrance and exit windows, located at the butt-ends, were of 25 and 40 mm in diameter correspondingly. There were two holes in the reaction chamber, disposed opposite one another, for letting the buffer aerosol-containing gas in and out. Targets of fissionable substances were placed on the reaction chamber windows (0.1 mm aluminium foil), which isolate the inner volume of the reaction chamber from the atmosphere. During the set-up testing, the chambers of greater length and diameter, which allowed up to 10 targets to be used simultaneously, were also employed.

The chamber for collecting aerosol-adsorbed fission fragments was also a cylinder of 40 mm diameter and 80 mm height that had a hole in the butt-end (entrance hole) and the lateral surface (exit hole). The collector used was an aluminium disc of 15 mm diameter and 1 mm thick, which was situated opposite the entrance hole at the distance of 10 mm from the capillary end. This chamber was disposed directly on the damper of a 150 l/s Ruts pump.

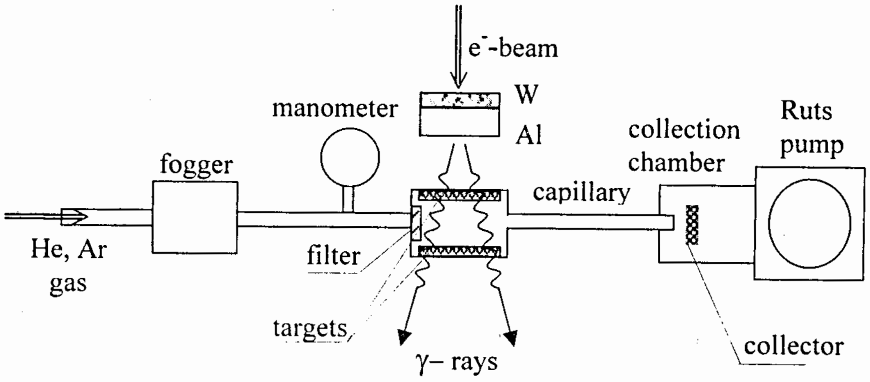

Fig. 1. The schematic view of the experimental set-up.

The fogger had a cylindrical quartz case (inner diameter of 14 mm, length of 55 mm) necked-down in the middle, where a limiter (a quartz plug with slits) was fixed. The limiter served to hold an quartz insert of 8 mm diameter within the cylinder. In the gap between the inner surface of the cylinder and the insert, fine-grained salt (its composition to be further discussed) for aerosols production was placed. The quartz cylinder was put into a two-section oven, the temperature in each section being adjustable and stabilised. The heating of the cylinder forced the salt to evaporate. The vapour produced was transported by an inert gas flow through the quartz plug to the lower part of the cylinder. Here, in less heated part of the cylinder, the vapour condensed to produce aerosols, which were carried out of the cylinder by the gas flow. A detailed description of the fogger and its operating modes can be found in [1].

The aerosols were transported into the reaction chamber through a 25 mm polyethylene capillary with inner diameter of 4 mm. A teflon capillary connected the reaction and collection chambers. Its inner diameter was of 2 mm, and length being variable from 1 to 30 m to regulate the fragment transportation time and hold the pressure in the collection chamber low enough for the good aerosols deposition.

Tests

To determine its characteristics, the set-up was tested on uranium photofission fragments produced in the bremsstrahlung-induced photofission of uranium. The bremsstrahlung cut-off energy being of 25 MeV. As a source of that radiation the Laboratory of Nuclear Reactions' MT-25 microtron was used (for its description see [2]). As an electron-beam-bremsstrahlung converter the running-water-cooled tungsten disc 4 mm thick was used. That disc was also an electron-beam current collector, the current being measured with an electric current integrator. Downstream of the collector, there was an aluminium cylinder 20 mm thick for the low energy electrons to be absorbed. The electron beam had the shape of an ellipse, its vertical and horizontal dimensions being 6 and 7 mm correspondingly.

To produce fission fragments, 1-14 mg/cm^2 targets of ^{238}U in the form of its oxide U_3O_8 were used. They were deposited on an aluminium backing of 20 mm thickness. The fragments that had escaped from the target were slowed down in a gas, adsorbed on aerosols and were transported through a long capillary to the collection chamber. As a carrier a high-purity inert gas – helium, nitrogen and argon (type M-60) was used. The gas pressure in the reaction chamber was such as for the fragment pathlength in the gas to be less than the chamber dimensions and all the fragments to be stopped within the gas volume. Into the chamber, aerosols, the 0.1-0.2 μm microparticles of various salts, were injected. Their concentration in the gas, governed by the fogger operating mode, was variable within tens of μg/l.

The collectors with collected fragments were brought to a Ge(Li) detector at different time intervals for their γ-radiation spectra to be measured, which allowed the fragments to be identified, i.e., their atomic number Z and mass number A to be determined. The identification of the fragments was carried out with the use of reported fission fragment γ-spectra and half-lives [3, 4]. Some of the identified nuclides were used in determining of the set-up characteristics – efficiency and transportation speed under different conditions (target thickness, aerosol concentration, capillary length).

The dependence of the fission fragments yield versus the target thickness was determined by comparing the γ-radiation intensity of the chosen fragments that escaped from the uranium layer and stopped in a collector and those that remained in the target or backing. To do this, a set of targets was used. The targets had an uranium oxide U_3O_8 layer of different thickness (from 1 to 14 mg/cm^2) deposited on an aluminium backing of 20 μm thickness (which exceeds the fragments pathlength in aluminium). The aluminium collectors of the same thickness covered the targets. On irradiation of the pile of targets and collectors, their γ-spectra were measured with a Ge(Li) detector. The measurement showed that up to 50% of the fragments escape from the targets of thickness of less than 1 mg/cm^2 (comparison was made for ^{97}Zr and ^{132}J fragments). The proportion of fragments that escaped decreases as the U_3O_8 layer thickness increases (for instance, it is 35% for the thickness of 3 mg/cm^2 and falls down to 15% for the thickness of 14 mg/cm^2). The dependencies obtained allow the optimum target thickness to be chosen, which ensures minimum matter consumption.

Set-up characteristics

Under the optimum conditions chosen in such a way, the main characteristics of the set-up were determined: transportation efficiency and target-to-collector transportation time for different fragments. Also was studied the dependence of those characteristics on the set-up parameters and transportation conditions: capillary length and diameter, chamber volume, gas pressure and composition, aerosol concentration and composition.

The transportation efficiency was determined using the same technique that was used to optimise the target thickness – by comparing the γ-radiation intensity of the chosen fragments in the irradiated target and on the collector in the collection chamber. In the majority of the experiments, the fragments were transported by argon; its pressure in the reaction chamber was chosen in such a way that all the fragments which had escaped from a 1 mg/cm^2 uranium target should be slowed down within the chamber volume and adsorbed on the aerosols. For the chamber depth of 30 mm, the pressure was of 1 atm. As aerosols, the NaCl particles, produced using the above described technique in the fogger, were used.

Analysis of the γ-spectra of the irradiated target and the collector allowed 11 nuclides – from ^{91}Sr to ^{153}Sm – to be identified among the fragments. In fact, the number of the transported nuclides is greater since each mass number corresponds to 2-3 elements (for example, A=91 corresponds to Rb and Sr, and A=97 corresponds to Y and Zr, etc). It was found that for a capillary of 10 m length and an aerosol concentration of more than 20 μg/l, the transportation efficiency is almost the same for all the fragments observed and has the value (70±10)%. Krypton and xenon are exceptions. For them, no γ-radiation was observed on the collector. Obviously those gases are not adsorbed on aerosols and do not deposit on the collector. The use of other gases instead of argon – helium and nitrogen – at appropriate pressure as well as the use of other aerosols (KCl, NaBr, KBr) gave the same values for the transportation efficiency.

The transportation efficiency was measured for capillaries of different lengths from 1 to 30 m at the fixed values of the argon pressure and NaCl aerosol concentration. The transportation efficiency proved to remain practically unchanged. What this means is that the major fragment losses appear to occur in entering the capillary and in transportation through its initial section (<1 m).

Under the same conditions, the transportation efficiency was measured as a function of a NaCl aerosol concentration. The latter was set by changing the fogger temperature and determined by the activity of the ^{34m}Cl isomer ($T_{1/2}$=32 m, E_γ=145 and 2127 keV) that was produced alongside the fragments in the ^{35}Cl(γ,n) reaction. The efficiency is seen to increase as the aerosol concentration increases from 0.02 to 20 μg/l but to remain unchanged for higher concentrations. It follows from this dependence that sufficiently high fragment transportation efficiency (~50%) is attainable with a comparatively low concentration of aerosols, which corresponds to a rate of NaCl deposition on the collector of ~ 0.1 mg/min. Such a low deposition rate allows one to have a very thin salt layer that enables spectroscopic measurement of the soft β and γ-radiation from fission fragments.

An important transportation characteristic is the target-to-collector fragment transportation time. Obviously it consists of two components: the drift time of aerosols with adsorbed fragments within the reaction chamber before entering the capillary, which is the ratio of the chamber volume to the gas flow rate, and the capillary transportation time. These components were determined by measuring the time dependence of the chamber pressure after cutting off the incoming gas flow. To carry out that measurement, chambers of different volume and capillaries of different length were used. From those dependencies, the transportation time components were deduced on the assumption that the concentration of aerosols with fragments captured is proportional to the chamber pressure. For this purpose, the chamber pumping rate for different pressures was determined by differentiating the curves obtained, which characterised the averaged duration of stay of aerosols with fragments in the reaction chamber T_{cham}. Comparison with the pumping rate calculated by reported formulae [4] for a capillary of specified length and diameter allowed the transportation time T_{cap} for that capillary to be obtained. It is seen that for the minimum volume (36 cm^2), the total transportation time for transportation of aerosols through capillaries 1 m and 10 m long is 0.22 and 1s correspondingly. Transportation times of such duration allow one to carry out experiments with the short-lived fission fragments (half-lives of fractions of a second).

The set-up was used in experiments on measuring the mass and charge distributions of ^{232}Th, ^{238}U and ^{244}Pu photofission fragments on a microtron bremsstrahlung beam. In those experiments, the γ-spectra were measured of fragments brought to the collector by a gas flow with NaCl aerosols. In the measured spectra, 16 fission products were identified, their yields being measured. The mass distributions of the cumulative yields of photofission fragments measured by that technique is in good agreement with reported data obtained using other techniques [5-7].

The set-up was also used for measuring the isotope distribution of Kr and Xe fragments. In those experiments, He, Ar flow without aerosols was used. A filter at the reaction chamber outlet retained the fragments of all the other elements, and only Kr and Xe entered the capillary. They were stopped in a cryostat, cooled by liquid nitrogen (its temperature (-210° C) is lower than that of the Kr and Xe condensation points). The experiments carried out showed that this set-up can be successfully employed in studying the fission mechanism of heavy nuclei and the fragments produced.

The authors would like to express their gratitude to Yu.Ts. Oganessian, M.G. Itkis, S.N. Dmitriev and J. Kliman for permanently supporting the work and the numerous helpful discussions and to A.G. Belov for assistance at the MT-25 microtron.

This work was supported by RFFR (grants 00-02-16674, 01-02-16455) and INTAS (grant 00-00243).

References

1. Zvara I., Domanov V.P., Shalaevsky M.P., Petrov D.V. // Preprint JINR, 12-80-48, Dubna, 1980.
2. Belov A.G. // Workshop on application of microtrons in nuclear physics, Plovdiv, 1992, D15-93-80, p.12
3. BlachotI., Fiche Ch. // ADNDT, 1977, v.20, p.241
4. Rozanov L.N. // Vacuum technology, Moscow, Visshay Shkola, 1990
5. Gangrsky Yu. P., Dalhsuren B., Markov B.N. // Fission fragments, Moscow, Energoatomizdat, 1986
6. Jacobs H., Thierens D., de Frenne D. et al // Phys.Rev. C, 1979, v.19, p.422
7. Thierens D., Jacobs H., de Clerc A. et al // Phys.Rev. C, 1983, v.27, p.1117

FINE STRUCTURE OF THE ^{147g}Tb (1.6h), ^{149}Tb (4.15h) AND ^{151}Tb (17.6h) β$^+$/EC DECAY STRENGTH FUNCTIONS

I. N. Izosimov[a], A. A. Kazimov[a], V. G. Kalinnikov[b], A. A. Solnyshkin[b], J. Suhonen[c]

[a] *V.G.Khlopin Radium Institute, 194021, St.Petersburg, Russia*
[b] *Joint Institute for Nuclear Research, 141980, Dubna, Russia*
[c] *Department of Physics, University of Jyväskylä, P.O.Box 35, FIN-40351 Jyväskylä, Finland*

Abstract

The fine structure of the resonances in ^{147g}Tb (1.6h), ^{149}Tb (4.15h) and ^{151}Tb (17.6h) β^+/EC decay strength functions has been identified and analyzed. The $M_T = +1$ Gamow-Teller resonance has been identified in ^{147g}Tb to ^{147}Gd β^+/EC decay. Qualitative agreement of the fine structure with the calculated β^+/EC strength function using the microscopic quasiparticle-phonon model is obtained.

PACS numbers: 23.40.Hc, 27.60+j

1. Introduction

The β-decay strength function $S_\beta(E)$ is one of the most important characteristics of atomic nucleus. It reflects the distribution of the squared β-decay type matrix elements with respect to the excitation energy E of the daughter-nucleus states [1]. The resonance structure of $S_\beta(E)$ depends on the structure of the atomic nucleus through the isovector component of the effective nucleon-nucleon interaction. Information on the structure of $S_\beta(E)$ is important for different fields of nuclear physics.

For beta transitions of the Gamow-Teller type $S_\beta(E)$ can be written as [1]:

$$S_\beta(E) = \frac{B'_\mp(\mathrm{GT}, E)}{D(g_V^2/g_A^2)}\,, \tag{1}$$

$$B'_\mp(\mathrm{GT}, E) = \frac{4\pi}{g_A^2} B_\mp(\mathrm{GT}, E) = \frac{1}{2I_i + 1} |\langle I_f \| \sum_{k,\mu} t_\mp(k)\sigma_\mu(k) \| I_i \rangle|^2\,, \tag{2}$$

where I_i and I_f are the spins of the initial and final states, g_A and g_V are the coupling constants of the axial-vector and vector components of the β decay, $D = (6260 \pm 60)$ s, and $t_\mp\sigma$ is the product of the isospin and spin operators giving the respective operators of the Gamow-Teller β^- or β^+/EC decays.

Usually $S_\beta(E)$ is measured in MeV^{-1}s^{-1} units, the $B(\mathrm{GT})$ is measured in $g_\mathrm{A}^2/4\pi$ units and ft is in seconds. In this case [1,5]:

$$B(\mathrm{GT}) \;=\; D\left(\frac{g_\mathrm{V}^2}{g_\mathrm{A}^2}\right)\times\frac{1}{ft}\;,\quad D=(6260\pm 60)\mathrm{s}\;, \tag{3}$$

$$\int_{\Delta E} S_\beta(E)dE \;=\; \sum_{E_i\in\Delta E}\frac{1}{(ft)_i}=\left[D\left(\frac{g_\mathrm{V}^2}{g_\mathrm{A}^2}\right)\right]^{-1}\sum_{E_i\in\Delta E}B_i(\mathrm{GT})\;, \tag{4}$$

where ΔE is the energy range, determined by the detector's energy resolution.

The charge-changing elementary excitations with isospin $T=1$ and its z projection $M_T=+1$ can manifest in Gamow-Teller β^+/EC decay. The Gamow-Teller $M_T=+1$ resonance is a coherent superposition of such elementary excitations [1] at high energy. In experiments the $M_T=+1$ Gamow-Teller resonance may manifest as a strong peak in the β^+/EC-decay strength function $S_\beta(E)$ for some nuclei with a high value of decay energy, Q_EC, available for the β^+/EC decay [1,2]. The $M_T=+1$ Gamow-Teller resonance can be experimentally identified as a very strong peak in the high-energy part of $S_\beta(E)$. No experimental data for the fine structure of resonances in $S_\beta(E)$ has been reported yet. Furthermore, no detailed calculation of the fine structure has been published. In this work we present the first detailed experimental and theoretical study of the resonance fine structure of $S_\beta(E)$ for ^{147g}Tb (1.6h), ^{149}Tb (4.15h) and ^{151}Tb (17.6h) β^+/EC decays and in particular the analysis of the $M_T=+1$ Gamow-Teller resonance and its fine structure identification for ^{147g}Tb (1.6h) β^+/EC decay.

2. Experimental β^+/EC decay strength function

In the present work we constructed the $B(\mathrm{GT})$ values according to Eq. (4) using the decay schemes and log(ft) values. For ^{149}Tb (4.15h) and ^{151}Tb (17.6h) we used decay scheme from Ref. [3], for ^{147g}Tb (1.6h) the decay schemes from Ref. [4]. The experimental beta-decay strength function for ^{147g}Tb (1.6h), ^{149}Tb (4.15h) and ^{151}Tb (17.6h) β^+/EC decay are shown in fig.1-fig.4. The strong resonance within the Q_EC window was observed at excitation energy $E\simeq 4$ MeV of ^{147}Gd for the ^{147g}Tb β^+/EC decay , the tail of such type resonance was observed at $E\simeq 3.5$ MeV for ^{149}Tb β^+/EC decay and small resonance at $E\simeq 2$ MeV was observed for ^{151}Tb β^+/EC decay. All these resonances have a fine structure.

For ^{147g}Tb (1.6h)β^+/EC decay strength function was constructed also using total absorption γ-spectroscopy (TAS) data Ref.[5]. This strength function is shown in fig.2. We compared two types of the ^{147g}Tb β^+/EC decay strength functions (fig.1 and fig.2) using Eq.(4). Within the experimental errors both strength functions are in agreement.

From this fact one can conclude that the decay scheme of ^{147g}Tb from Ref. [4]is complete enough .

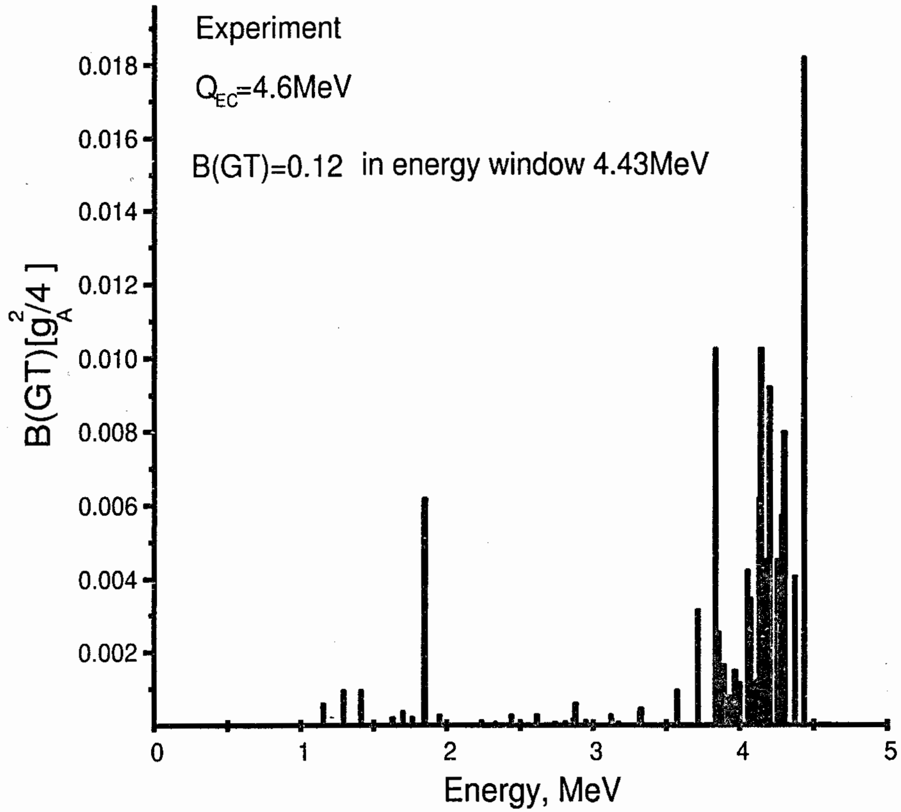

Fig. 1. Strength function for the β^+/EC decay of ^{147g}Tb deduced from the analysis of the decay scheme in [4].

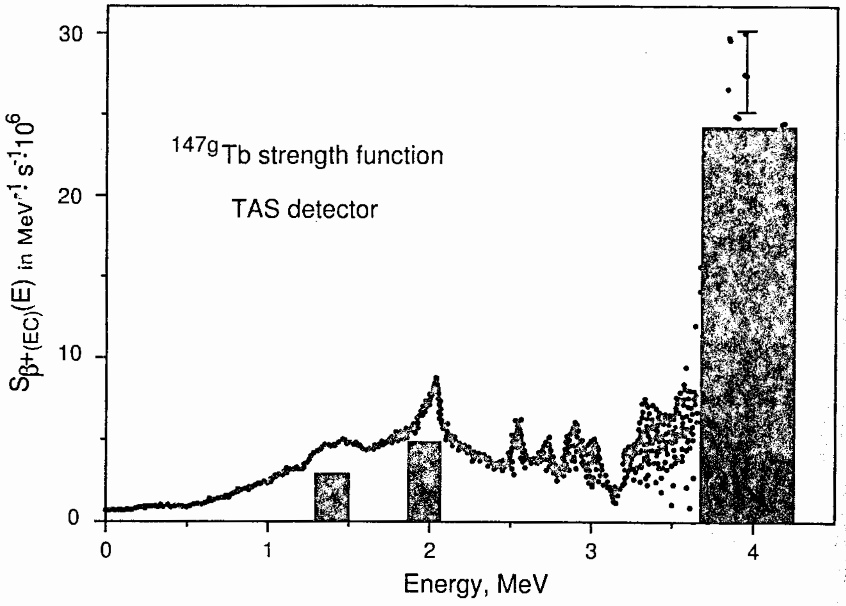

Fig. 2. Strength function for the β^+/EC decay of ^{147g}Tb deduced from the analysis of the TAS-spectrometer data in [5].

3. Theoretical β^+/EC decay strength function

To analyze the fine structure of resonances in beta-decay strength functions we have carried out a theoretical calculation of $B(\mathrm{GT},E)$ using the microscopic quasiparticle-phonon model (MQPM) of [6]. In this model we start from realistic effective two-body forces obtained by G-matrix methods from the Bonn one-meson-exchange potential [7]. We have performed the calculations in the 2s-1d-0g-0h valence space for the protons and in the 2s-1d-0g-2p-1f-0h-0$i_{13/2}$ valence space for the neutrons. For the single-particle part of the hamiltonian we have used the experimental one-particle and one-hole energies with respect to the Gd core for the valence neutrons and Woods-Saxon single-particle energies for the protons. Slight adjustments of the proton single-particle energies were done during the BCS calculation described below. It is worth noting that in the work [5] we used just pure Woods-Saxon energies for the single-particle terms of the hamiltonian and thus the

present calculation is more realistic yielding a much better agreement of the calculated energies with the measured low-energy spectrum of ^{147}Gd.

In the MQPM the approximate ground state of the even-even reference nucleus is obtained from a BCS calculation. After the quasiparticle transformation the nuclear hamiltonian can be written in the form

$$H = \sum_{\alpha} E_a a^{\dagger}_{\alpha} a_{\alpha} + H_{22} + H_{40} + H_{04} + H_{31} + H_{13}\,, \qquad (5)$$

where E_a are the quasiparticle energies and other terms of the hamiltonian are normal-ordered parts of the residual interaction labeled according to the number of quasiparticle creation and annihilation operators which they contain [8]. The optimal quasiparticle energies and occupation factors are obtained by comparing the results of a BCS calculation with the data for the even-even and even-odd nuclei involved in the calculation.

The states of the odd-proton and odd-neutron nuclei discussed in this work are constructed from one-quasiparticle and three-quasiparticle components where the latter are obtained by combining the quasiparticles with the QRPA (quasiparticle random-phase approximation) phonons of various multipolarities, representing excited states in the Gd nucleus. These phonons, in turn, are linear combinations of proton two-quasiparticle and neutron two-quasiparticle states constructed in the adopted valence space. For each value of the angular momentum and parity the spectrum of the Gd nucleus is constructed by diagonalizing the QRPA matrix to obtain the above-mentioned linear combinations. Agreement with the experimental excitation energies is good. The mixing of one- and three-quasiparticle components in the wave functions of the Tb and Gd nuclei was achieved by diagonalization of the $H_{31} + H_{13}$ part of the quasiparticle hamiltonian (5) in the basis containing the relevant one-quasiparticle and quasiparticle-phonon components. Spurious states were removed by inspection of the norm matrix.

For the mass-147 system we have constructed the states of the odd mother and daughter nuclei starting from the ^{146}Gd nucleus, ^{147}Gd being a neutron-quasiparticle nucleus and ^{147}Tb being a proton-quasiparticle nucleus. The initial state is the ^{147}Tb ground state which in our calculation has as a dominating component the structure ^{147}Tb(g.s.) = ^{146}Gd $\otimes$ $\pi 2s_{1/2}$ corresponding to the experimentally observed $1/2^+$ ground state of ^{147}Tb [9]. In ^{147}Gd the agreement of the calculated energy spectrum with the experimental one is excellent for excitation energies up to 2 MeV beyond which the experimental spectrum becomes too messy to enable an unambiguous comparison. The good agreement with the experimental energies was achieved by the carefully chosen valence single-particle energies discussed earlier. A convergence of the excitation energies as a function of the adopted multipolarities and the number of related QRPA phonons was obtained to high energies (roughly to 6 MeV in ecitation energy) leading to diagonalization and construction of large matrices. Similar procedure was also used to describe the β^+/EC decays in the $A = 149$ and $A = 151$ systems.

4. Discussion and conclusions

Our relevant theoretical results, namely the strength functions of the ^{147,149,151}Tb → ^{147,149,151}Gd β^+/EC decays, have been summarized in fig.3 and fig.4. In fig.1 - fig.4 both the experimental and theoretical strengths $B'_+(\mathrm{GT},E)$ of Eq. (2) have been plotted as functions of excitation energy. As can be seen from these figures, there is a qualitative agreement between the theory and the experiment. What is relevant here is that the theory does not predict any significant strength beyond 4.8 MeV of excitation energy for the ^{147g}Tb → ^{147}Gd β^+/EC decay (fig.3). This fact supports the conclusion about the detection of a $M_T = +1$ Gamow-Teller resonance and it's fine structure at the excitation energy $E \simeq 4$ MeV of ^{147}Gd for ^{147g}Tb → ^{147}Gd β^+/EC decay (fig.1).

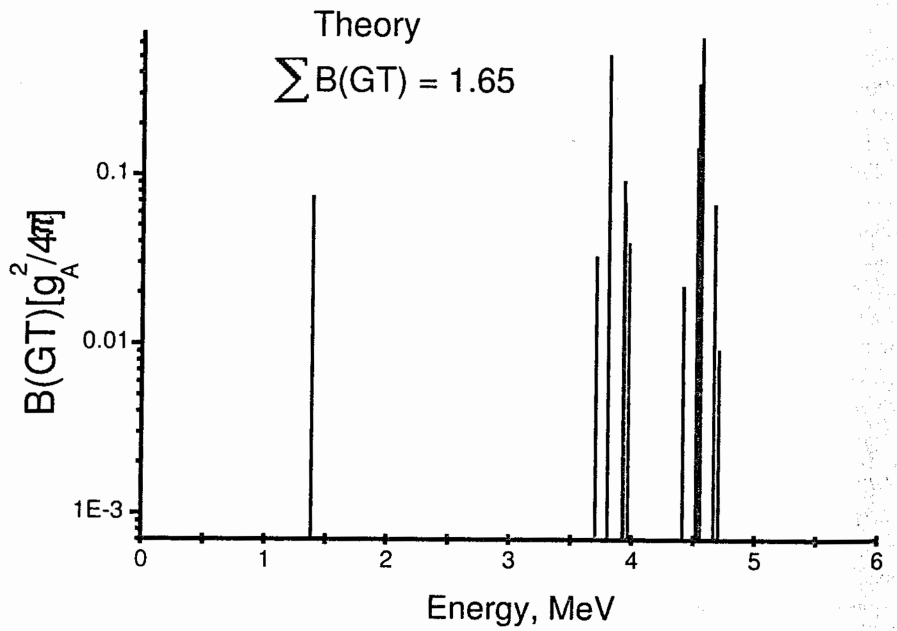

Fig. 3. Calculated (MQPM model)strength $B'_+(\mathrm{GT},E)$ of Eq. (2) for the β^+/EC decay of ^{147g}Tb.

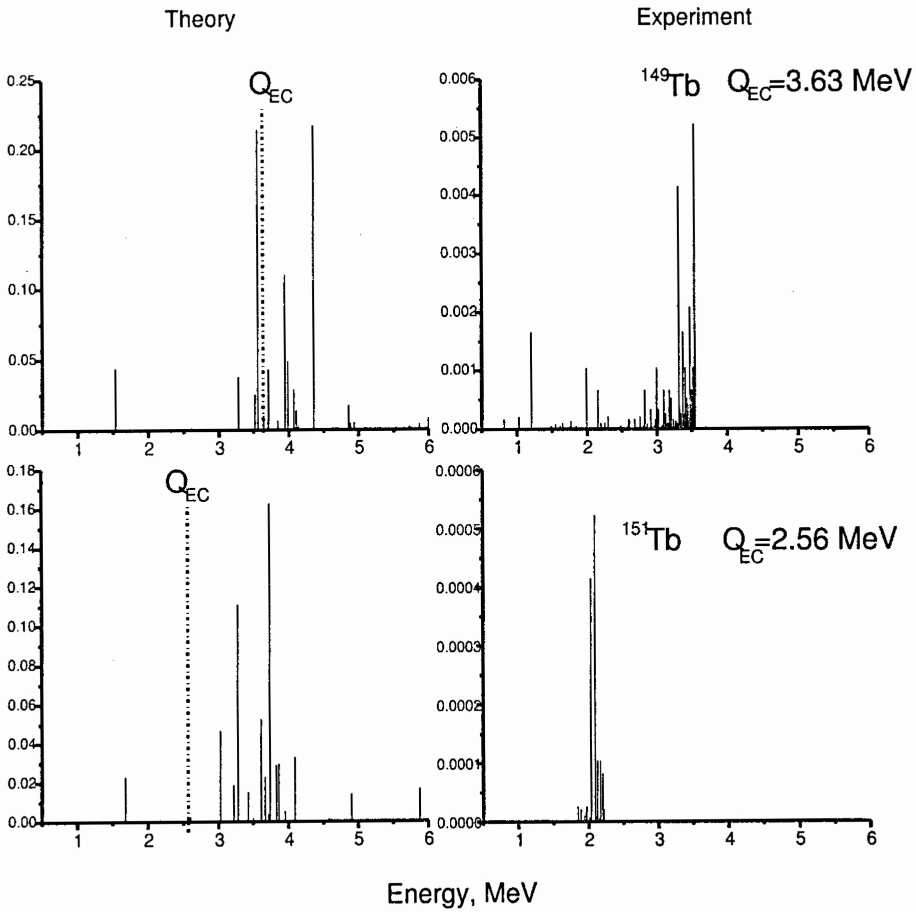

Fig. 4. Experimental (deduced from the analysis of the decay schemes in [3]) and theoretical (MQPM calculations) β^+/EC decay strength functions of ^{149,151}Tb.

For the two other β^+/EC decays (fig.4) the situation is not so fortunate. For the ^{149}Tb → ^{149}Gd case only small part of the fine structure of the gaint resonance can be observed in the decay Q_{EC} window. The situation is still worse in the case of the ^{151}Tb → ^{151}Gd decay because according to the calculations only a very small tail of the gaint resonance falls into the Q_{EC} window. In this case the major part of the resonance can be seen only through an (n,p) charge-exchange reaction.

In conclusion, one can say that the strength functions for the β^+/EC decays of ^{147,149,151}Tb have a distinct resonance character confirmed by the theoretical calculations performed on microscopic level using realistic effective interactions. The fine structure of these resonances has been analyzed both experimentally and in terms of the microscopic quasiparticle-phonon coupling scheme. Both analyses support the identification of the $M_T = +1$ Gamow-Teller resonance and it's fine structure in the ^{147g}Tb electron-capture decay to states of high excitation energy in ^{147}Gd (fig.1).

For a more detailed β^+/EC decay strength function analysis it is necessary to have experimental data on $S_\beta(E)$ in nuclei where all the β^+/EC strength lies within the Q_{EC} window. Such possibility exists for ^{145,143,141}Tb β^+/EC decays.

References

[1] Yu. V. Naumov, A. A. Bykov and I. N. Izosimov, Sov. J. Part. Nucl. 14, 175 (1983)

[2] F. Frisk, I. Hamamoto and X. Z. Zhang, Phys. Rev. C 52, 2468 (1996)

[3] *Table of Isotopes*, Eighth Edition, vol.1. Ed. R.B.Firestone, et al. (Wiley-Interscience, New York, 1996).

[4] J. Wawryszczuk et al., Z. Phys. A 357, 39 (1997)

[5] I. N. Izosimov et al., J. Phys. G 24, 831 (1998)

[6] J. Toivanen and J. Suhonen, J. Phys. G 21, 1491 (1995); Phys. Rev. C 57 1237 (1998)

[7] K. Holinde, Phys. Reports 68, 121 (1981)

[8] J. Suhonen, T. Taigel and A. Faessler, Nucl. Phys. A 486, 91 (1988)

[9] R. Collatz et al., Z. Phys. A 351, 245 (1995)

CHANGES IN NEUTRON MAGIC NUMBERS OF NEUTRON-RICH NUCLEI

Z. Dlouhý, D. Baiborodin, J. Mrázek, G. Thiamová
For the GANIL-Orsay-Dubna-Řež-Bucharest collaboration

Abstract

We present a survey of experimental results obtained at GANIL (Caen, France) resulting in an appearance of new magic number, N=16, in very neutron-rich nuclei. Recent data on mass measurements of neutron-rich nuclei at GANIL and some characteristics of binding energies in this region are discussed. Nuclear binding energies are very sensitive to the existence of nuclear shells and together with the measurements of instability of the doubly magic nucleus ^{28}O they provide new information on changes in neutron shell closures of very neutron-rich isotopes from carbon up to calcium.

The behaviour of the two neutron separation energies S_{2n} gives a very clear evidence for the existence of the new shell closure N=16 for Z=9 and 10 appearing between $2s_{1/2}$ and $1d_{3/2}$ orbitals. This fact, strongly supported by the instability of C, N and O isotopes with N > 16, confirms the magic character of N=16 for the region $6 \leq Z \leq 10$, while the shell closure at N=20 tends to disappear for $Z \leq 13$.

The study of the properties of extremely neutron- or proton-rich nuclei of light elements is a very important topic in the modern nuclear physics. The research in this field has revealed a ”halo” and a ”skin” structure and other unique features. The higher sensitivity of the nuclear models to the choice of the nuclear potential parameters in extreme nucleon matter configurations gives us the opportunity to test the nuclear models. Deformations, shape coexistence or variations in the spin orbit strength as a function of N/Z ratio could result in the modification of magic numbers in very neutron-rich nuclei [1]. A breaking of magicity has already been observed at the N=20 shell closure where an ”island of inversion” in shell ordering has been shown to exist [2]. Such behaviour has very wide consequences that have resulted in the instability of the doubly magic nuclei ^{10}He [3, 4] and ^{28}O [5]. The anomalous behaviour of the binding energy near the shell closure N=20 close to the neutron-drip line is also closely connected to this question. More recently, the determination of the lifetime and of the deformation of ^{44}S has indicated the existence of a similar effect at N=28.

Recently, in an experiment on the LISE3 spectrometer at GANIL, we have used the fragmentation of the neutron-rich projectile ^{36}S to produce and study very neutron-rich nuclei in vicinity of a doubly magic nucleus ^{28}O. However, no events were observed corresponding to even ^{26}O and ^{28}O, odd oxygen isotopes ^{25,27}O and also ^{24,25}N. Till now, the heaviest experimentally found oxygen isotope remains ^{24}O. Our finding that ^{28}O is particle unstable [5] fairly supports the idea that the onset of the deformation found in the Ne-Al region causes the breaking of magicity of the N=20 shell closure in ^{28}O. The instability of ^{25,26,27,28}O and ^{24,25}N was also confirmed by the experiment performed by Sakurai et al. [6] at the fragment separator RIPS at RIKEN in which, however, a new isotope, ^{31}F, was observed for the first time. The calculated and observed yields of isotopes are in a good agreement and provide a strong evidence for the particle instability of ^{24,25}N, ^{25,26,27,28}O and ^{30}F.

We can summarize that the heaviest experimentally found isotopes of carbon, nitrogen and oxygen [5, 6] are ^{22}C, ^{23}N,and ^{24}O, respectively, with the same neutron number, $N=16$, while the heaviest isotope of fluorine was found to be ^{31}F with $N=22$. It should be noted that it is a rather interesting behavior among the light nuclei. Usually, in the region further from the shell closure the neutron numbers of heaviest isotopes of neighbour elements are gradually increasing with Z. Therefore, the sudden step in the largest neutron number from N=16 for carbon, nitrogen and oxygen to N=22 for fluorine may correspond to a substantial change in shell structure.

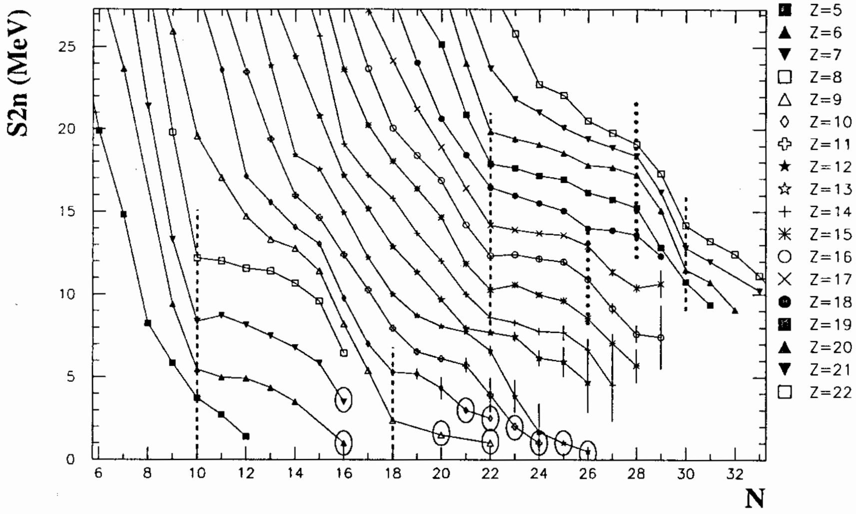

Figure 1: Two-neutron separation energy S_{2n} versus N

The particle stability of nuclei is directly related to the masses and nuclear binding energies, which are very sensitive to the existence of shells and may provide clear signatures of shell closures [7]. An experiment on mass measurement of neutron-rich nuclei using a direct time of flight technique was undertaken by Sarazin et al [8] in order to investigate the N=20 and N=28 shell closures for nuclei from Ne (Z=10) to Ar (Z=18) and thus to bring some clarifications concerning the behaviour of magic numbers far from stability. The nuclei of interest were produced by the fragmentation of a 60 AMeV ^{48}Ca beam on a Ta target. The separation energies of two last neutrons, S_{2n} derived from the measured masses are displayed in fig.1. The new data [8] are presented with error bars while the other, except of the data in circles, are taken from Audi et al. [9]. The Ca, K and Ar isotopes show a behaviour typical of the filling of shells, with the two shell closures at N=20 and N=28 being evidenced by the corresponding sharp decrease of S_{2n} for next two isotopes and a moderate decrease of S_{2n} for subsequent ones as the filling of the next shell starts to influence S_{2n}. The sharp drop at N=22, shown by the dashed vertical line and corresponding to the existence of the shell N_{sh}=20, is clearly visible through all the Si-Ca region while going to lower Z into the Al-Na region this drop seems to move towards the lower N.

This was the reason why we made an attempt to clear up an evolution of two-neutron separation energies in this region. We used a fact that several particle stable nuclei [5, 6, 10] were found to exist in this region, however, their masses are not known yet. Nevertheless,

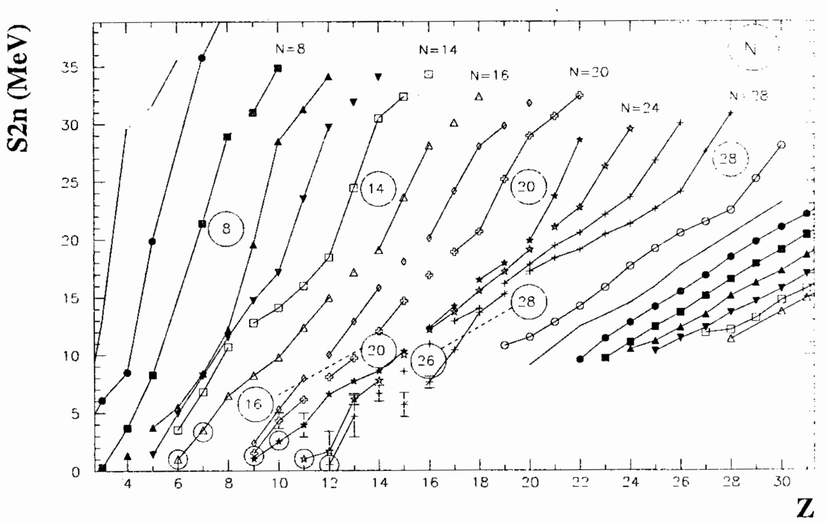

Figure 2: Experimental S_{2n} values versus proton number Z. Dashed lines symbolize the changes of neutron shell closures

their S_{2n} values must be positive and therefore, we included the estimated S_{2n} values of the heaviest ^{23}N, ^{22}C and $^{29,31}F$ particle stable isotopes as well as some others to the graph and marked them by circles. The most important has proved to be the inclusion of S_{2n} values for ^{29}F and ^{31}F that allowed us to observe the sharp drop of ^{27}F value followed by a moderate decrease of S_{2n} values for ^{29}F and ^{31}F giving a very clear evidence for the existence of the new shell closure at N=16 for fluorine. A similar behaviour confirming the N=16 shell closure one can also see at neon isotopes that exhibit a moderate decrease of S_{2n} values for ^{29}Ne and ^{30}Ne. We have already mentioned that in the Al-Na region the sharp drop in S_{2n} values seems to move towards the lower N with decreasing Z. Now, we can make firm conclusion that it finally stabilizes at the vertical line at N=18 (new shell N_{sh}=16) for F and Ne.

It should be noted that the evidence for a new magic number $N = 16$ follows also from fig.2 where the S_{2n} values are plotted versus atomic number Z. The position of various possible shells or pseudo-shells are also shown in the figure. The shells N=20 and 28 appearing in fig.1 are very clearly seen as large gaps in fig.2. The dashed lines in fig.2 symbolize the changes of neutron shell closures from 28 to 26 and from 20 to 16 in neutron-rich nuclei. However, both gaps are narrowing going to lower Z, till finally, at least the gap corresponding to N=20 completely disappears at Z=13, to emerge as the new N=16 gap at Z=10. This new gap governs over most of light Z neutron-rich nuclei and extends from carbon to neon.

So we can state that a new shell closure at N=16 has appeared in neutron-rich nuclei for Z≤10 between the $2s_{1/2}$ and $1d_{3/2}$ orbits in the good agreement with Monte Carlo shell model calculations of Utsuno [11] and Otsuka [12]. This fact, strongly supported by the instability of C, N and O isotopes with N > 16, confirms the magic character of N=16 for the neutron-rich nuclei in the region $6 \leq Z \leq 10$, while the shell closure at N=20 tends to disappear for $Z < 14$.

This is in a good agreement with recently published work of Ozawa et al. [13] where, however, the information on the magicity of N=16 obtained from one neutron separation energies S_{1n} and the measurement of interaction cross section of radioactive beams σ_I is not so well pronounced.

As has been already pointed out in ref. [8] the Cl, S and P isotopes, however, exhibit a pronounced change of slope around N=26. Moreover, this change in the Cl and S isotopes is confirmed by the sharp drop at N=28. The discontinuity observed at N=26 in fig.1 appears in fig.2 as a sufficiently large gap at N=26 for Z=15,16 and 17. It is therefore evident that the representation of the S_{2n} values in dependence of a charge number Z is very usefull. Another gap may appear at N=22 for $13 \geq Z \geq 9$. The measurements [8] demonstrate that the shell structure for Cl, S and P isotopes is modified and that a pseudo-shell closure arising from the onset of the deformation appears at N=26. These findings were reproduced by the shell model and relativistic mean field calculations. In a simple Nilsson picture, for a prolate deformation of $\beta_2 \sim 0.2$, a large gap appears between the lowest three orbits and the fourth orbital belonging to $1f_{7/2}$. Oblate deformations would not be compatible with these observations.

However, this pseudo-shell closure can be considered more probably as an example of shape coexistence and has to be of completely different character than the shell at N=16.

The existence of the N=16 gap should manifest itself in the shell correction ΔM, which reads

$$\Delta M = \Delta M_{exp} - \Delta M^{FRLDM},$$

where ΔM_{exp} is the experimental mass excess and ΔM^{FRLDM} is the spherical macroscopic energy calculated by Moller and Nix [14] in the finite range liquid drop model. Well pronounced minima in the shell corrections appearing at N=16 (or 15) for nuclei from oxygen up to aluminium.

References

[1] Z. Ren et al., Phys. Lett. **B380**, 241 (1996).

[2] C. Thibault et al., Phys. Rev. **C12**, 644 (1975).

[3] A. Korsheninnikov et al., Phys. Lett. **B326**, 31 (1994).

[4] A.N.Ostrowski et al., Phys. Lett. **B338**, 13 (1994).

[5] O. Tarasov et al., Phys. Lett. **B409**, 64 (1997).

[6] H. Sakurai et al., Phys. Lett. **B448**, 180 (1999).

[7] W. Mittig, A. Lépine-Szilly and N. Orr, Annu. Rev. Nucl. Sci. **47**, 27 (1997).

[8] F. Sarazin et al., Phys. Rev. Lett. **84**, 5062 (2000).

[9] G. Audi et al., Nucl. Phys. **A624**, 1 (1997).

[10] H. Sakurai et al., Phys. Rev. **C54**, R2802 (1996).

[11] Y. Otsuno et al., Phys. Rev. **C60**, 054315-1 (1999).

[12] T. Otsuka private communication

[13] A.Ozawa et al., Contr. to RNB2000, 3-8 April 2000, Divonne (France);
Phys. Rev. Lett. **84**, 5493 (2000).

[14] P. Moller and J.R. Nix At. Data Nucl. Data Tables **59**, 185 (1995).

SELECTIVE TRACK RADIOGRAPHY OF HEAVY ELEMENTS WITH ACCELERATED CHARGED PARTICLES

V.P. Perelygin

Join Institute for Nuclear Research, 141980 Dubna, Russia

Abstract

The new combined method of selective alpha-track and fission fragment track radiography of heavy metals (Ir, Os, Pt, Au, Pb, Bi) in solid specimens was developed. It bases on application of accelerated heavy ions ^{2}H, ^{4}He, ^{12}C, ^{16}O, ^{20}Ne with the energy ≥ 6 MeV per nucleon. These ions when struck the heavy metal containing minerals (Ir, Os, Pt, An, Pb, Bi) induce the prompt fission of these nuclei and also produce in reactions (HI, xn) the alpha-active isotopes of ^{210}Po, ^{206}Po, ^{205}Po.

The prompt fission fragments are registered with 15-20 μm thick mica crystal track detectors, close placed to the minerals before irradiation with charged particles beam.

The locations of heavy metal in the ore minerals are clearly seen by f.f. tracks on mica detectors. After heavy ion exposure the minerals were placed in close contact with α-sensitive track detectors (CR-39, cellulose nitrate) for an appropriate time and track density pattern due to α-decay of Po isotopes, produced in (HI, xn) reactions with heavy metals was revealed too.

The intercomparison of f.f. and α-track radiography pattern provides the unambiguous selection of Pb-Bi and Au-Os element containing grains in the ore minerals being investigated.

The sensitivity of the method is at the level of $10^{-6} - 10^{7}$ g/g, the space resolution is about 10 μm.

1. Introduction

The problem of low concentration selective measurements of the elements Bi, Pb and Au, Pt, Ir, Os in rich ore minerals is connected mainly with searching of new ore deposits. In many cases it is necessary to measure not only the average content of the heavy elements, but to determine its distribution in different minerals with the spatial resolution 10-20 μm.

It is especially importation for search and thoroughful investigation of platinum ore deposits. In spite of that Pt content in the Earth is much higher than Pb, due to its unique chemical properties,the geochemistry of platinum was still poorly investigated. It is focusing to investigate properly the Pt content in its ore minerals in order to follow the process of platinum migration and enrichment in each particular minerals of these ores.

The problem of selective determination of the heavy metals in rock minerals could not be solved with the help of neutron activation analysis due to the low spatial resolution, worse than ± 100 μm. The election microprobe analysis provides the necessary spatial resolution, but is rather time-consuming and expensive.

The problem could be solved with the application of the intense beams of accelerated charged particles, which produces the nuclear activation of heavy metal nuclei.

The accelerated heavy ion α-activation technique for high sensitive Pb exploration in solids was first proposed by Hamilton in 1971 (1). He used intense beams of accelerated ^{4}He ions with energy 7.5 MeV/nucleon to produce long-living nuclide ^{210}Po (reaction $^{208}Pb\ (\alpha, 2n)\ ^{210}Po$) in lead-containing solid materials. After helium ion exposure the specimens were placed in close contact with α-sensitive cellulose nitrate track detectors to register α-particles from radioactive decay of ^{210}Po nuclei. In later papers the accelerated ^{3}He ions were used for Pb exploration in solids of non-organic (2) or organic (3) origin. In these experiments the main α-decaying reaction was ^{206}Po, generated in the nuclear reactions with lead isotopes: $^{206}Pb\ (^{3}He,\ 3n)\ ^{206}Po$ and $^{207}Pb\ (^{3}He,\ 4n)\ ^{206}Po$. The different method of Pb exploration in solid ore specimens was first realized in 1974 by Flerov et al. by applying the accelerated ^{12}C ions for producing short-lived α-active nuclei in the region of Ra-Po neutron-deficient isotopes (4). The sensitivity of Pb exploration with α-activation technique is high enough – 10^{-5}-10^{-6} gram of Pb per gram of ore specimens (5).

The latter approach provides the other possibility of charged particle activation analysis. Indeed, the interaction of heavy charged particles with heavy nuclei (Z ≥ 70) realizes both in heavy ion capture cannels and in subsequent prompt fission of compound nuclei obtained. Such a competition in practice realizes in high – yield of prompt fission channel (cross section about 1 barn) and in (xn) evaporation reactions, which produce a number of α-decaying isotopes of Po – Rn isotopes also with rather high cross-sections – about n.10^{2} millibarn.

Both prompt fission fragments and alpha-particles of the same heavy nuclei produced in nuclear reactions can be registered with appropriate solid state track detectors.

The great choice of accelerated heavy ions-from hydrogen and helium isotopes up to ^{12}C-^{40}Ar ions enhanced the possibilities of the combined fission fragment – alpha decay track detection method for selective analysis of Bi-Pb and Au-Pt-Os content in diverse solid specimens.

2. Experimental procedure

In our work we always use the polished samples of heavy metal ores and mineral specimens being investigated and thin metal layers of Bi, Pb, Au, Pt, Ir, Os – for control measurements. The specimens and control metal layers were placed on the cooled massive metal rods mounted at 90° to the beam of accelerated nuclei.

These rods were mounted at the edge of rotating disk with diameter 22 cm, situated inside vacuum chamber, placed at the external beam pattern of heavy ion cyclotrons U-200 or U-400 of Flerov Laboratory of Nuclear Reactions, Joint Institute for Nuclear Research, Dubna. Just before the heavy ion exposure both specimens and control heavy metal foils, mounted onto the massive aluminum rods were covered from the beam side with 15-20 μm thick layers of muscovite mica, used as fission fragment track detector (6-8).

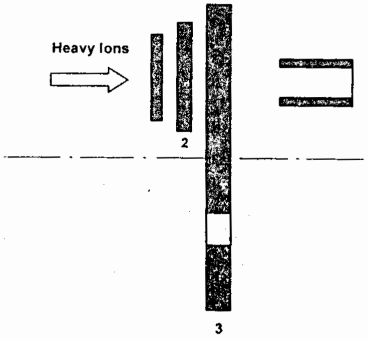

Fig. 1. The experimental setup:
1 – massive mica track detector ~ 20 μm thick;
2 – polished ore specimen;
3 – massive Al rotating disk with a hole;
4 – Faraday cup.

The experimental setup is schematically presented at fig. 1. The 22 cm diameter rotating aluminum disk was placed into vacuum chamber and then bombarded with heavy fluence of accelerated d, He, ^{12}C or ^{16}O ions perpendicularly to the sample surfaces. The rotating Al disk contain a hole though which the heavy ion beam periodically reach the Faraday cup used for permanent control of the beam intensity. Usually up to 20 polished ore specimens were mouthed at the edge of rotating disk. The total fluence of accelerated ions usually was in the range $10^{13} - 10^{14}$ ions per cm^2.

The beam profile was measured with track density of fission fragment due to the induced fission of Pb nuclei with accelerated ^{12}C ions. The beam pattern of fig. 2 proofs the homogeneity of accelerated particles distributions on the surface of target minerals. The ion beam profile was about 25 mm in width as one can see from fig. 2.

Also, because in such a study only "2-backward" geometry can be used, the angular distribution of fission fragment yield (in reaction of 9.1 MeV/nucleon ^{12}C ion with 1 μm Pt foil) was measured. As one can see from fig. 3 the angular distribution of fission fragments generated in the reaction Pt (^{12}C, i.f.) at the energy 9.1 MeV/nucleon in center-of-mass system is quite non-isotropic.

That is why the experimental cross section in "2-backward" geometry does not exceed 0.35 barn out of 1 barn of total induced fission cross section.

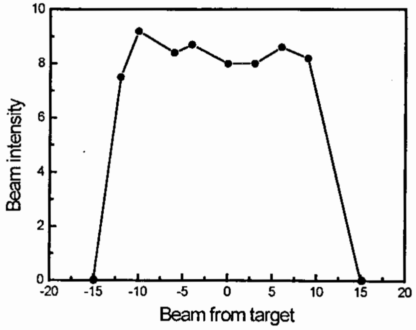

Fig. 2. The ion beam profile on target surface.

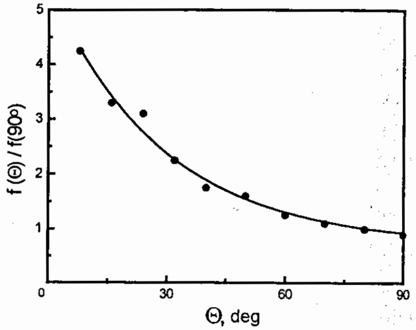

Fig. 3. Angular distribution of fission fragment produced in the interaction of 9.1 MeV/nucleon ^{12}C ions with 1 μm Pt foil.

In order to determine the real yield of fission fragment produced in the thick (~ 10 μm) Pt, Au and Pb metal foils with accelerated 9.1 MeV/nucleon ^{12}C ions we covered these foils with muscovite mice detectors and bombard all the assembly with the effective energies 5.6; 6.7; 7.3; 7.9 and 8.7 MeV per nucleon. The excitation curves for induced fission partial cross-section are presented at fig. 4. One can see, that the fission fragment cross-section in "2-backward" geometry is nearly the same for Pt, Au and Pu nuclei. The application of monitor heavy metal foils allows one to determine the heavy element content in specimens simply by the rate of track density at specimen and heavy metal foils – N_{spec} / N_{eth}, in gram of heavy nuclei per gram of specimen.

After the exposes the muscovite mica layers were removed from the specimens and then annealed at 450°C in order to remove the background tracks due to the compound nuclei formed in the traction of heavy ion beam with mica bulk composing nuclei. The measured background track density for muscovite mica at different time of annealing is presented at fig. 5; the ^{12}C ions fluence was $3\cdot10^{13}$ ions cm^{-2} in that case.

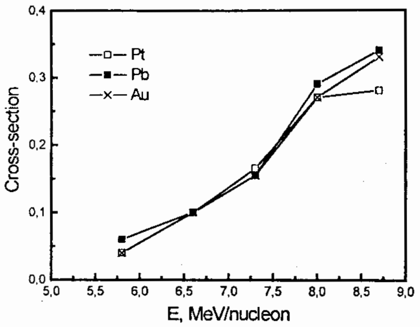

Fig. 4. The backward fission fragment creation cross-section σ_f of Pt, Au, Pb versus the energy of bombarding ions.

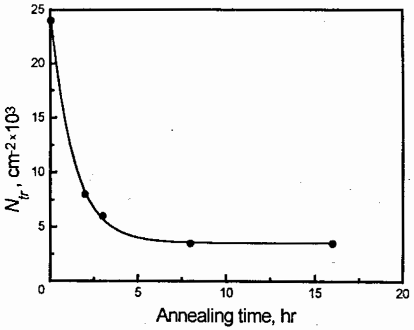

Fig. 5. Annealing behavior of compound nuclei background tracks in muscovite mica.

As one can see from fig. 5, the background track density decreases by factor 5 due to the mica annealing at 450°C during 15 hours. Moreover, the background tracks become to be the shallow etch pits, when the fission fragment tracks still have the length from 2 μm up to 10 μm, and shortens down only by 10%-15% in average, due to annealing at 450°C during 15 hours

The remaining background track density still is at the level of $5\cdot10^{2}$ tr.cm$^{2\cdot}$ These tracks were formed due to the presence of K and also Fe minor admixtures in the natural muscovite mica crystals. The corresponding tracks due to the compound or recoil nuclei with $Z \geq 25$ produced with ^{12}C ions could not be annealed in muscovite mica at any annealing conditions (9). That sets an upper limit for the total fluence of ^{12}C – or heavier ions at the level of (2-3)·10^{14} cm^{-2}, and subsequently, the sensitivity of Pt-Bi element determination with induced fission fragment registration is limited at the level (2-4)·10^{-7} g/g. for natural mica detectors.

In order to increase the sensitivity of the method we have tested at the same ^{12}C ion beam conditions the artificial mica track detector – 10-15 μm thick fluorphlogopite crystals. After the exposure the fluorphlogopite mica foils were properly annealed.

The chosen annealing – 480°C during 6 hours allows one erase completely all the background tracks due to the recoil and compound nuclei in fluorphlogopite. This is due to the much lower sensitivity of this artificial mica which allows to anneal completely all the tracks of compound nuclei with $Z \geq 36$ (10). Fluorphlogopite mica practically contains also no Th-U nuclei ($C_{Th.U} \leq 10^{-13}$ g/g) (10). It allows one to reach in principle the sensitivity for Bi-Pt determination at the level of sensitivity up to $\leq 10^{-8}$ g/g in solid- ore or alloy-specimens.

After the exposure the thin mica track detectors were removed both from specimens and heavy metal layers. Induced alpha-activity was registered with CR-39 plastic track detectors, placed in close contact with all irradiated specimens.

The exposure time varies from 144 hours up to 1000 hours, which allows one to register effectively the alpha – decay of all the known Po isotopes, in our case in experiment with accelerated ^{12}C ions.

The α-activity measurements have demonstrated that Au is the lightest element capable of producing minor amount of α-active isotopes in its reactions with ^{12}C ions. Our calculations of elemental synthesis in the Au (^{12}C, xn) reactions confirmed generation of α-active At and Po isotopes therein. In the Pt (^{12}C, xn) reaction, on the contrary, the α-active isotope yields were found to be negligible. This result enables us that even close elements could be separated by a combined *f.f.* and α-particle detection, simply by comparing *f.f.* tracks and alpha-tracks pattern for the same specimen.

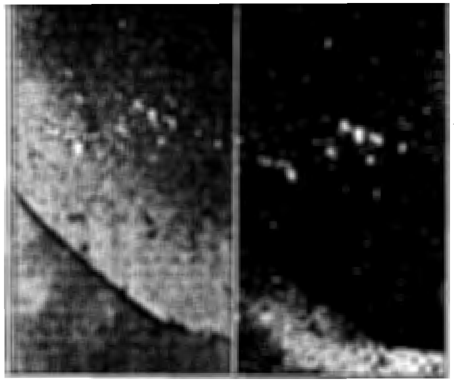

Fig. 6. Ferro-platinum ore specimen (a) and fits fission fragment track replica with muscovite mica detector. The track density (b) is about $3 \cdot 10^6$ tr·cm^{-2}.

Fig. 7. Track radiography of Pt continuing pirite and piridine crystals.

The minimum detectable elemental concentration (i.e., the least numbers of atoms within a local area) depends on the incident ion flux only ($N = 10^{12}$-10^{13} atoms at flux 10^{14} ions·cm^{-2}).

The photomicrograph of the spatial microdistribution of ferro-platinum in the natural ore specimen, and corresponding *f.f.* autoradiograph are shown at fig. 6 (a, b). The autoradiography was obtained by the specimen irradiation with the ^{12}C ion flux $3 \cdot 10^{13}$ cm^{-2}. Platinum concentration was evaluated from the track density on the autoradiography ($3 \cdot 10^6$ tracks per cm^2) and it was found to be (61 ± 7)%.

It is necessary to point out, that the alpha track density at that specimen was less than 10^2 tracks per cm^2, which corresponds to the background level of CR-39 plastic track detectors.

At fig. 7 (a, b) the *f.f.* tracks in mica due to the induced fission of Pt nuclei with ^{12}C ions in pyrite and pyridine crystals are presented. As one can see from fig. 7 (a, b) two lower rather big crystals of pyridine contains Pt homogeneously in the volume, when pyrite crystal contains Pt only at its surface (top crystal).

3. Conclusion

Summarising, the method proposed allows one to use the accelerated charged particles for selective track radiography of Bi, Pb, Au, and the elements of platinum group Pt, Ir, Os in ores (and also alloys) with the sensitivity up to 10^{-7} gram per gram. The fission fragment track radiography provides first the spatial resolution as high as ± 10 μm, which allows to find out a very fine (1 μm) crystals rich with heavy metals. It opens quite new possibilities of investigations of heavy metal containing ores and minerals, which is in particular especially important for detailed investigation of origin and genesis of platinum ore deposits.

References

1. Hamilton, E.L.. New technique for determining the concentration and distribution of lead in materials. Nature 1971, 231, № 5304, pp. 524-525.
2. Fremlin, J.H., Edmonds, M.I. The determination of lead in human teeth. Nucl. Instr. Methods 1972, 173, pp. 211-215.
3. Wipavin, V.T., Thomas, B.I., Khan, H.A. The determination of lead in solids. Int. Journ. Radiat. Phys. Chem. 1974, 6, № 3, p.p. 203-210.
4. Flerov, G.N., Berzina, I.G., Berman, I.B., Melnikov, I.V. Exploration of lead volume distribution in specimens by α-tracks. Atomnaya Energiya 1974, 37, № 6, p.p. 499-500.
5. Flerov, G.N., Berzina, I.G. Radiography of minerals, common rocks and ores. Atomizdat, 1979. Moscow.
6. Perelygin, V.P., Starodub, G.Ya., Stetsenko, S.G. Investigations of lead distribution in common rocks by induced fission method. Atomnaya Energiya 1985, 59, № 6, p.p. 437-439.
7. Ermolaev, A.N., Perelygin, V.P., Starodub, G.Ya., Stetsenko, S.G. Lead redistribution at the formation of study form polymetallic ore bodies in carbonate deposites. Sovetskaya Geologia 1987, № 7, pp. 27-33.
8. Abdullaev, I.G., Belogurov, O.G., Vinokurov, S.F., Khokhlov, N.B., Kushin, V.V., Perelygin, V.P., Petrova, R.I., Stetsenko, S.G. Tracks radiography of heavy elements in minerals. JINR Commun. 1992, E14-92-184, Dubna; Atomnaya Energiya 1993, № 3, p.p. 370-372.
9. Abdullaev, I.G., Bankova, G.G., Enkhjin, L., Murtazaev, Kh., Otgoasuren, O., Perelygin, V.P., Petrova, R.I. On the determination of the track age of some natural crystals. Nucl. Traks Rad. Meas. 1993, 22, № 1-4, p.p. 805-810.
10. Perelygin, V.P. The study of nuclear tracks in crystals. Nucl. Traks Rad. Meas. 1993, 22, № 1-4, p.p. 811-822.

SEARCH FOR RELATIVELY STABLE SUPER-HEAVY ELEMENTS IN NATURE BY FOSSIL TRACK STUDIES OF CRYSTALS FROM METEORITES AND THE LUNAR SURFACE — RESULTS AND PROSPECTS

V.P. Perelygin[1], I.G. Abdullaev[1], Yu.V. Bondar[2], R. Brandt[3], Yu.T. Chuburkov[1], R.L. Fleischer[4], L.L. Kashkarov[5], L.I. Kravets[1], M. Rebetes[6], R. Spohr[3], D. O'Sullivan[7], P. Vater[3]

[1] *Joint Institute for Nuclear Research, Dubna, Russia*
[2] *Ukraine State Scientific Centre on Environmental Radiogeochemistry, Kiev, Ukraine*
[3] *Philipps University, Kernchemie, Marburg, Germany*
[4] *Department of Geology, Union College, Schenectady, New York, USA*
[5] *Vernadsky Institute of Geochemistry and Analytical Chemistry RAN, Moscow, Russia*
[6] *Laboratoire de Microanalyses Nucleares, Universite' de Besancon, France*
[7] *Dublin Institute for Advanced Studies, School of Cosmic Physics, Dublin, Ireland*

Abstract

The main goal of the present work is the search and identification of relatively stable nuclei of Super-Heavy Elements (SHE) ($Z > 110$) in galactic matter by fossil track study of non-conducting crystals from the surface of meteorites and rocks from the lunar regolith. Nuclei of SHE are thought to be the products of nucleosynthesis in explosive processes in our galaxy (supernova r-process nucleosynthesis, and especially neutron-star formation, etc.). When accelerated to relativistic energies in the galaxy, they can produce extended trails of damage in non-conducting extraterrestrial crystals. The lifetime of such SHE in the galactic cosmic rays shall range from 10^3 to 10^7 years to be registered in extraterrestrial crystals.

To search for and to identify the super-heavy nuclei in the galactic cosmic rays it was proposed to use the ability of non-conducting extraterrestrial crystals such as the olivines, pyroxenes and feldspars to register and to store for many million years the trails of damage produced by fast $Z \geq 23$ nuclei coming to rest in the crystalline lattice. The track lengths of fast $Z \geq 23$ nuclei are directly proportional to Z^2 of these nuclei.

The nuclei of SHE shall produce, when coming to rest in a crystal volume, tracks that are a factor of 1.6-1.8 longer than the tracks due to cosmic ray Th and U nuclei. To identify the tracks due to super-heavy nuclei, calibrations of the same crystals were performed with accelerated Au, Pb and U nuclei. For visualization of these tracks inside the crystal volume, proper controlled annealing and chemical etching procedures were developed.

Since 1980 fossil tracks due to Th and U nuclei were observed and unambiguously identified (1988) by subsequent calibrations of the olivine crystals with accelerated U, Au and Pb ions. The number of tracks of Th and U nuclei measured in olivine crystals totaled more than 1600, as compared with the prior 30 events.

The other approach to identifying SHE in nature is to search for tracks in the phosphate crystals from spontaneous fission of $Z \geq 110$ nuclei; these produce 2-prong and 3-prong fission fragment tracks, and differ significantly from the tracks from spontaneous fission of ^{238}U and ^{244}Pu nuclei. Extraterrestrial phosphate crystals of lunar and meteoritic origin will be investigated. Such SHE nuclei can survive in crystals of extraterrestrial rocks and produce the spontaneous fission tracks if the lifetime is more than 5×10^7 years.

I. Introduction – Background and Justification

The existence of relatively stable super-heavy elements (SHE) in nature was predicted theoretically in the mid-1960's by Nilsson, Nix and Sobichevsky (see ref. 1). Basing on the nuclear shell model it was estimated, that double-magic nuclei with atomic number $110 \leq Z \leq 114$ and neutron number $N = 184$ double "magic" closed shells of neclei can possess the lifetimes between 10^3 and 10^9 years. Thus, these elements, like Th and U, could survive in the earth and meteorites since the formation of solar system, about 4.6 G.Y ago.

Experimental attempts to discover long-lived SHE nuclei with the lifetimes $\geq 2 \times 10^8$ years in natural samples undertaken from the late 60s up to the late 70s provided limited evidence of their existence in both terrestrial samples and meteorites. These experiments were done by studying alpha radioactivity and spontaneous fission, which can exceed significantly the effect of spontaneous fission of ^{238}U. Still, no decisive information on the existence of SHE in the nature was obtained.

In the early 70s a completely new approach was proposed to identify SHE nuclei in galactic matter. It was based on the ability of non-conducting crystals to register and to store the trails of damage due to fast, heavy cosmic-ray nuclei for many millions of years. The pioneering work was conducted by R.L. Fleischer, P.B. Price, R.M. Walker and colleagues, who discovered tracks due to trans-iron ($Z \geq 36$, VVH) cosmic-ray nuclei. In spite of many subsequent attempts by P.B. Price, D. Lal, M. Maurette, R.M. Walker and V.P. Perelygin (see ref. 1) during the 60s and 70s, no quantitative information was obtained on the charge spectra and the abundance of $Z \geq 36$ nuclei in cosmic rays.

The new approach, first demonstrated in 1980 (Perelygin, refs. 2-4) was based (1) on partial controlled annealing of both fossil cosmic ray tracks and fresh ones from accelerated Kr, Xe, Au, Pb and U nuclei, and (2) revealing the volume etchable track length (VETL) of these nuclei in olivine crystals from meteorites. Specifically, olivine rich meteorites – the palasites Marjalahti, Eagle Station and Lipovsky Khrutor were chosen for such study. It is worth noting the incredible collecting power of extraterrestrial "natural orbital stations", i.e., meteorites. For example, through every cm^2 of Marjalahti meteorite pre-atmospheric surface during its radiation exposure – 180 M.Y. the fluency of $Z \geq 70$ nuclei corresponds to an exposure of about 20000 m^2 of plastic track detectors in space for one year.

Unfortunately, the ablation of meteorites in the terrestrial atmosphere erased about 90% of such track information for the Marjalahti and Lipovsky meteorites just mentioned. The lunar crystals have a great advantage, the absence of ablation; we propose to choose individual lunar crystals that were situated in the upper 2 cm of the lunar regolith for many million years.

Such crystals can be used to search not only for SHE nuclei ($Z \geq 110$-114, $N = 184$), and also for SSHE nuclei (Z about 160-180, $N \approx 320$-360) – the possible long-lived double-magic nuclear remnants of desintegration and decay of pure neutron matter, ejected during the formation of neutron stars.

Freshly formed nuclei with $Z \geq 36$, up to $Z \approx 110$ and above, as it has been recently stated by S. Slavatinsky (5), are accelerated by the intense electromagnetic fields of exploding neutron star, to energies 10^6 GeV per nucleon. These nuclei can reach the solar system in as few as 10^3 years and produce very long latent tracks in non-conducting crystals.

Thus, we can seek SHE nuclei with a lifetime $T \geq 10^3$ years in extraterrestrial crystals that have been exposed for many million of years at the surface of meteorites and the lunar regolith. Another way to identify SHE in nature is to search in phosphate crystals for tracks from spontaneous fission of $Z \geq 110$ nuclei; they produce 2-prong and 3-prong tracks, and differ significantly from the spontaneous fission tracks of ^{238}U and ^{244}Pu nuclei.

Extraterrestrial phosphate crystals of lunar and meteoritic origin will be investigated in future studies because these crystals began to register fission fragment tracks about 4.2-4.3 billion years ago – after the parent body of these extraterrestrial objects cooled (6). Such nuclei of SHE can survive in extraterrestrial rocks and produce tracks from spontaneous fission, if their lifetime is more than 5×10^7 years.

2. Experimental

2.1. Milestones

Recent synthesis and discoveries of very stable isotopes of elements 110 – 116 stimulated the present project. During 1999-2000 in the Flerov Laboratory of Nuclear Reactions, JINR, Dubna, Professor Yu.Ts. Oganessian and his colleagues succeed in obtaining a number of rather neutron-rich isotopes of elements 112, 114 and 116 in reactions of high-intensity breams of ^{48}Ca with mono-isotopic targets of ^{238}U, ^{244}Pu and ^{248}Cm, respectively (7). The most stable isotope obtained was the odd-even nuclide ^{285}112, which has a lifetime between 10 and 30 min, compared to 10-60 sec for neighboring nuclei of Z = 110, 114 and milliseconds to seconds for Z = 116 or Z = 106-109 nuclei. Still the isotope ^{285}112 has only 173 neutrons – 11 less than the magic number N = 184.

For the known actinide nuclei (Z = 89-98) such a neutron difference for the lightest and most stable isotopes provides a stabilization factor of 10^{10}-10^{13} in lifetime. The discovery of new very stable isotope of element 112 provides final, unambiguous proof of the existence of a new island of relatively stable SHE nuclei; the island was predicted theoretically much earlier. Now we point out that there is no way to produce a neutron number of 184 using present-day accelerators and target nuclei. The only way to find double-magic SHE nuclei is to seek these nuclei in natural samples.

2.2. Registration of the heaviest cosmic-ray nuclei

There are two approaches to understanding registration of ultra-heavy (Z ≥ 36) galactic cosmic-ray nuclei. The traditional investigation of ultra-heavy nuclei in galactic cosmic rays was based on present-day registration of these nuclei in space using large-area stacks of nuclear emulsions and/or plastic track detectors. Historically, the study of the heaviest cosmic-ray component was initiated by Fowler et al. in 1967, using 4.5 m^2 stack of nuclear emulsions exposed near the top of the atmosphere with a balloon for a few days.

Then, in the late sixties to the mid-seventies a number of research groups exposed large stacks of nuclear emulsions and plastic detectors on balloons and in the orbital station Skylab. From the start of the 80s, two systems of big electronic detectors started to register cosmic-ray nuclei on the orbital stations Ariel-6 and HEAO-3 (2-4). The main disadvantage of that approach is a very low flux of the heaviest cosmic-ray nuclei. As a result, during 1981-1984 only 3 cosmic-ray nuclei with Z ≥ 89 were definitely registered with the two electronic detectors. During 1985-1990, using the NASA LDEF, a large stack of plastics was exposed by the Dyblin-ESTEC group (7). In spite of an exposure for 69 months of 46 m^2 of plastic track detectors, only 27 actinide nuclei were registered (see ref. 4). No track of Z ≥ 110 cosmic-ray nuclei was found.

The other type of galactic cosmic-ray investigation used the ability of non-conducting meteoritic crystals – pyroxenes, olivine, feldspars, phosphates – to register and to store for many tens and hundreds M.Y. tracks of nuclei with Z ≥ 20 (the Fe group and heavier nuclei).

But obtaining quantitative information on the charge and energy spectra of ultra-heavy cosmic-ray nuclei from fossil tracks in extraterrestrial crystals encounters methodological problems. One is the very high background of Fe-group nuclei, (10^{10}-10^{12} tracks per cm^2); another problem is partial annealing of track in silicate crystals that occurs under the conditions of outer space. This annealing prevents direct comparison of the etchable track length of fossil tracks and those of fresh tracks (used to calibrate the same crystals using accelerated heavy ions (Z = 20-92). Thus attempts made in the late of the 60s to the early 70s to study the heaviest galactic cosmic-ray nuclei by tracks in meteoritic and lunar crystals yielded only qualitative results for cosmic-ray nuclei with Z > 83 (for a review see ref. 1).

Freshly synthesized SHE nuclei in our galaxy, accelerated to relativistic energies, can produce extended trails of damage in meteoritic and lunar crystals. The volume attachable track length (VETL) of these nuclei is proportional to Z^2. Thus, the Z = 110 – 114 super heavy nuclei produce tracks that are a factor 1.6 – 1.8 longer than tracks due to fast Th or U ions. The main advantage of fossil track studies in extraterrestrial olivine crystals is the very long exposure time – about 200 M.Y. for Marjalahti and Lipovsky meteorites. Crystals in these meteorites contain up to 10^2 Th and U cosmic-ray tracks per cm^3.

For quantitative information, the technique of controlled annealing technique of tracks in crystals prior to etching was originally applied to olivines from the meteorites Marjalahati and Eagle Station. The procedure chosen for annealing olivine, at 430°C for 32 hr, erased fossil tracks from Fe nuclei (10^{10}-10^{11} cm^{-3}), and shorted tracks of Z > 50 nuclei by a factor of 6-8. More importantly differences were removed in the thermal history of the tracks, which had been recorded during the space exposure of these meteorites, over a few tens to hundreds of M.Y.

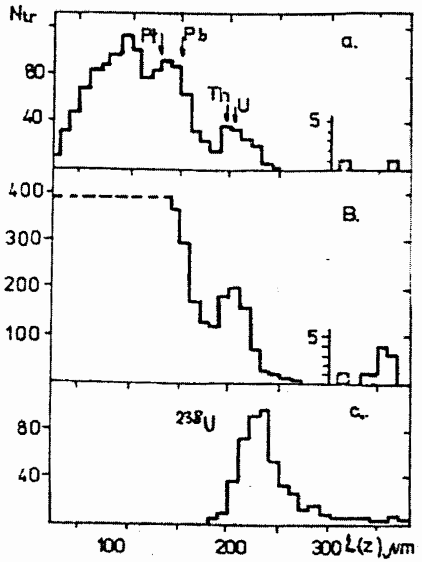

Fig. 1. The VETL spectrum of fossil tracks due to galactic cosmic-ray nuclei and due to accelerated ^{238}U in meteoritic olivine crystals annealed at 430°C for 32 hr before etching 90% of the tracks were measured in crystals from the Marjalahti meteorite:

- a – fossil track-length spectra (ref. 2);
- b – fossil track-length spectra (refs. 3 , 4);
- c – track-length spectra due to accelerated ^{238}U nuclei (ref. 3).

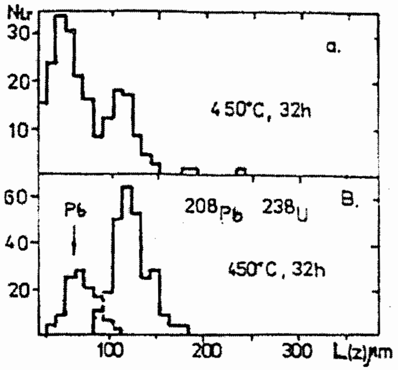

Fig. 2. VETL spectrum of fossil tracks due to galactic cosmic-ray nuclei and due to accelerated ^{208}Pb and ^{238}U in Marjalahti olivine crystals annealed at 450°C for 32 hr before etching:

- a – fossil track-length spectra;
- b – track-length spectra due to accelerated ^{208}Pb and ^{238}U nuclei (ref. 4).

In 1980 Perelygin (ref. 2) found the VETLs of Pt-Pb and Th and U galactic cosmic-ray nuclei in meteoritic olivine crystals annealed at 430°C for 32 hr were about 100-130 μm and 160-180 μm respectively (Fig. 1a).

These tracks of different lengths were unambiguously identified in 1988 by calibrations of the same olivine crystals with accelerated Au, Pb and U nuclei. In further studies, more than 1600 fossil tracks of Th and U nuclei were measured (Fig. 1b). For these annealing conditions 11 extra-long tracks ($L = 340\text{-}380$ μm) were found (ref. 3, 4). The correspondence of fossil and fresh ^{208}Pb and ^{238}U tracks was clear after annealing at 450°C for 32 hr, as seen in Fig. 2a, b. In spite of the limited statistics in Fig. 2, a single fossil track with the length of ≥ 250 μm was seen. The maximum track length of Th or U nuclei can not exceed 200 μm under these annealing conditions at any orientation in olivine. Detailed X-ray and optical analysis show that 5 of the 11 anomalously long tracks could not be from Th or U cosmic rays. Thus we have the evidence of SHE nuclei; their abundance relative to the actinide elements is $\sim (3\text{-}10)\times 10^{-3}$.

The proposed main goal of future studies is to obtain conclusive necessary and sufficient, proofs of the existence of SHE nuclei in galactic matter for lifetimes $T \geq 10^3$ years.

2.3. Spontaneous fission of $Z \geq 110$ nuclei

The other possibility for study is the search for and identification of fossil tracks from spontaneous fission of $Z \geq 110$ nuclei in extraterrestrial phosphate crystals. There are two possibilities:

1. The annealing behavior of tracks from spontaneous fission differs drastically in phosphates for actinides and for SHE. The proper annealing (for instance, at 450°C for 32 hr for Marjalahti whitlockite) provides separation of fission fragment tracks of ^{238}U and ^{244}Pu spontaneous fission from those of spontaneous fission of to $Z \geq 110$ nuclei. The volume etchable track lengths differ by a factor of 2. The fossil track-length spectra must be compared with those from thermal-neutron-induced fission of ^{235}U in the same crystals annealed under the same conditions. Such tracks should provide proof of spontaneous fission of $Z \geq 110$ nuclei, if present.
2. The estimated probability of ternary spontaneous fission of $Z = 110\text{-}114$ nuclei as compared with binary fission is 10^{-3} to 10^{-4}. For actinide nuclei that ratio is $\leq 10^{-7}$. These 3-prong tracks also will have mean length 20% greater than those of binary tracks due to spontaneous fission of actinide nuclei. Thus, the observation and measurements of such 3-prong spontaneous fission tracks in phosphate crystals would provide unambiguous proofs of SHE nuclei in solar system.

In both cases we must revel spontaneous fission tracks on polished surfaces of the crystals. For such a study we shall use the accelerated $Z \geq 30$ ions with energy ≥ 10 MeV per nucleon at 90° to the surface. The fluency of accelerated ions will be in the range $5\times 10^5\text{-}2\times 10^6$ ions per cm^2. Such bombardments could be performed at cyclotrons U-400, FLNR, JINR, Dubna, GSI UNILAC, Darmstadt, GANIL Tandem Cyclotrons, Caen.

3. Research Milestones

The basic method of the proposed studies is the controlled partial annealing of both fossil cosmic-ray tracks and fresh ones accelerated Kr, Xe, Au, Pb and U nuclei, the revelation of these tracks inside meteoritic and lunar silicates and phosphates, and measurement and analysis of the volume etchable track-length (VETL) spectra.

For that purpose the etching solution must be delivered inside crystal volume either by artificial cracks, produced by a well-focused Nd laser beam, or (better) by bombarding of polished crystals with $Z \geq 26$ nuclei accelerated at JINR Dubna; GANIL, Caen tandem cyclotron, SIS-UNILAC accelerator, Darmstadt. Also these facilities shall be used for calibrating the sensitivity of meteoritic and lunar silicates with accelerated ^{197}Au, ^{208}Pb and ^{238}U of energies 20-50 MeV per nucleon. There are two main ways to releaze the proposed goal of unambiguous discovery and identification of long-lived SHE nuclei in natural samples.

First is the search for and identification of anomalously long tracks produced by $Z \geq 110$ galactic cosmic-ray nuclei in extraterrestrial olivine crystals. For that purpose the main object of study will be the Eagle Station pallasite, which contains positions that were only 2-3 cm from the pre-atmospheric surface. Olivine crystals from these locations are very rich in $Z \geq 50$ nuclei, many more than were found in the Marjalahti pallasite. We estimate that in 10-12 cm^3 of these olivines we will be able to find and identify up to 10 anomalously long tracks. The annealing of these crystals at 440-450°C will eliminate the background of Th and U nuclei at any orientation in olivine, but not the $Z \geq 110$ nuclei.

Second, we plan to identify of tracks from spontaneous fission of SHE in extraterrestrial phosphate crystals. These will be in the presence of a significant background from spontaneous fission of ^{238}U. Also in old extraterrestrial samples ^{244}Pu must be dealt with. To distinguish the SHE tracks we will use the track-in-track (TINT) technique to reveal 3-prong spontaneous fission tracks and will employ controlled annealing of these crystals (in the case of 2-prong events). In our study we shall choose whitlocite and stanfildite crystals from the meteorites Marjalahti, Lipovsky Khutor, Omolon; and phosphates from Luna-16, Luna-24 probes.

Acknowledgement

The authors are very grateful to Russian Foundation of Basic Research for providing us the grant № 01-02-16410.

References

1. Flescher R.L., Price P.B., Walker R.M. (1975): *Nuclear Tracks in Solids; Principles and Applications.* Univ. of Calif. Press, Berkeley, 1975, pp. 1 – 605.
2. Perelygin V.P., Stetsenko S.G. The search for tracks due to $Z \geq 110$ Galactic cosmic ray nuclei in olivine crystals from meteorites. JETP Pisma, 1980, v. 32, pp. 622-625.
3. Perelygin V.P., Stetsenko S.G., Crawford H.J., Symons T.J.M. Analysis of the results of calibration of meteoritic olivine crystals with ^{238}U nuclei at the Bevelac accelerator. Z. Phys., 1991, v. A388, pp. 435-439.
4. Perelygin V.P., Petrova R.I., Stetsenko S.G., Brandt R., Vater P., Rebetez M., Spohr R., Vetter I., Perron C. Study of fossil tracks due to $50 \leq Z \leq 92$ galactic cosmic ray nuclei in meteoritic crystals. Radiat. Meas., 1999, v. 31. pp. 609-614.
5. Slavatinsku S.A. Cosmic rays and their role in the development of high-energy physics and astrophysics. Soros Teaching Mag., 1999, v. 10, pp. 68-74.
6. Perelygin V.P., Petrova R.I., Enkhjin L., Abdullaev I.G., Otgonsuren O. Determination of the track age of some terrestrial and meteoritic miacrals. Radiat. Meas., 1995, v. 25, pp. 525-526.
7. Oganessian Yu.Ts., Utyonkov V.K., Lobanov Yu.V. The synthesis of super-heavy nuclei in the ^{48}Ca – ^{244}Pu reaction. JINR Commun. E7-99-53, Dubna, 1999.

EXPERIMENTAL APPROACH TO THE TARGET RADIOTHERAPY USING ^{211}AT

Shmakova N.L. [1], *Norseev Yu.V.* [1], *Kutsalo P.V.* [1], *Fadeeva T.A.* [1], *Krasavin E.A.* [1],
Kodina G.E. [2], *Goltyapin Yu.V.* [2], *Sorokin V.P.* [2], *Slobodjanik I.I.* [2], *Korsunskji V.N.* [2]
[1]Department of Radiation and Radiobiological Research, JINR, Dubna, Russia
[2]Institute of Biophysics, Moscow

Usage of different kinds of radionuclides becomes more wide-spread in the present radiotherapy, and particularly in the tumor therapy. However irradiation of the tumors with external radiation sources or brachytherapy usually lacks specificity. As a result, these sources often cannot be applied at potentially curative levels because their toxicity to normal tissues. Targeted radionuclide therapy, also called endoradiotherapy, is an attractive alternative to external beam radiotherapy because it attempts to exploit anatomical and biochemical features in order to enhance specificity of tumor cell cytotoxicity. An advantage of targeted radiotherapy is that radionuclides are available with a wide variety of emission types and energies. Thus, it is possible to select a radionuclide whose radiation is most appropriate for the treatment of certain type of tumor.

The vast majority of clinical applications of targeted radiotherapy have involved β-emitting radionuclides such as ^{131}I and ^{90}Y. They deposit their energy over the distance of several millimeters, resulting in the fact that this type of radiation can be applied for the treatment of relatively large tumors. At the present time Auger-electron emitters and α-emitters also seem to be perspective for the proposes of radiotherapy. These approaches are attractive because their radiation is of more confined range in tissue and of higher relative biological effectiveness.

Actually, α-emitters possess two general advantages. First, it is the short range of particles emitted in tissue (60-65 μm, which equals several diameters of a cell). It provides targeted damage of the cells and it decreases normal tissue irradiation. Second, it is the high linear energy transfer (LET, 80-120 keV/μm). It induces damages in the cell which the cell cannot repair, it provides minimal difference between normal and tumor tissue oxygenation with oxygen enchacement ratio (OER) close to 1. The latter fact makes it possible to achieve maximum relative biological effectiveness (RBE).

While selecting an α-emitting radionuclides for therapeutic applications a number of factors must be considered:

1. Regarding nuclear properties of a radionuclide, the fraction of decays involving the emission of α-particles should be high.
2. For many applications the absence of β-particles is advantageous.
3. The radionuclide should have stable or long-lived decay products.
4. The emission of γ- or x-rays with the energy appropriate for external imaging would be helpful for *in vivo* monitoring.
5. The physical half-life of the radionuclide should be long enough for convenient radiosynthesis. The radionuclide should also be compatible with the dynamics of tumor localization and retention of the intended carrier molecule.
6. Radiochemical strategies must be available to label the carrier molecule with reasonable yield and in such a way that the labeled molecule has adequate stability *in vivo*, as well as the labeled products of catabolism are excreted rapidly.

7. The radionuclide should be produced in sufficient quantity and possess isotopic purity to permit clinical use.

As a result of these requirements, the only α-emitters which have received serious attention in endoradiotherapy are ^{225}Ac, ^{212}Bi, ^{213}Bi, ^{211}At, ^{149}Tb, ^{225}Fm. For our investigations we have chosen an ^{211}At and the iodine isotopes.

Astatine is the last element in the group VII (halogens) in the Periodic Table of chemical elements. Astatine doesn't have natural and stable isotopes as well. From the two of most long-lived isotopes, ^{210}At and ^{211}At (half-life periods are 8.3 and 7.2 h respectively), only the last one is suitable for the clinical application. The reason for this is the fact that the neighboring ^{210}At decays to the long-lived α-particle emitter ^{210}Po (138 d), whose presence must be strictly avoided according to the practical radiation protection standards. For the same reason, the high purity of ^{211}At for the experimental work and possible *in vivo* use is mandatory.

^{211}At is a pure α-emitter (half-life period is 7,2 h), which is suitable for damage of targeted cells in vivo. ^{211}At decays by two pathways: by direct α-particle emission with transition to long-lived ^{207}Bi (41.8 %, 5.78 MeV; $T_{1/2\ Bi}$ = 38 years), and by electron capture with conversion to ^{211}Po ($T_{1/2}$ = 0.5 s), which also decays via α-particle emission with mean particle energy at about 7.45 MeV. Both of ^{211}At decay pathways result in the production of stable ^{207}Pb. ^{211}At emits one α-particle per disintegration with a mean energy of 6.72 MeV. Emitted α-particles possess high LET at about 98.84 keV/μm.

Organ and tissue specificity of ^{211}At proves to be very close to the nearest halogen in the Periodic Table - iodine. For example, ^{211}At also naturally accumulates in thyroid gland, however to a less extent than iodine does (the thyroid:blood ratio is 180:1 and 220:1, respectively). As for pure ^{211}At, it doesn't possess any organ or tissue affinity.

As far as the specificity of the α-emitted radionuclide therapy with confined range of α-particles is concerned, this kind of irradiation can be effective in two cases: in the treatment of small colonies of metastatic cells or disseminated tumors (such as lymphoma and melanoma), and in the treatment of the cavitary cancers. In the first case a tumor-specific carrier has to be used for direct delivery of the radionuclide to the tumor cells. Targeting effect in the second case is achieved by retaining the radionuclide in the cancer cavity during all period of decay.

In our Department we have carried out research in two different directions. The first works included experiments with the Ehrlich ascitic carcinoma (EAC) cells. Our presented works are dedicated to experimental substantiating of targeted therapy of human pigmented melanoma.

As one may know, *melanoma* is an aggressive and rather wide-spread kind of tumors. This cancer is the disease of melanocytes, special cells that produce a pigment, called melanin. Besides for the skin, melanin-producing cells are also found in the mouth, eye, gut and some other areas. The property which makes melanoma exceptionally malignant tumor, is its active metastatic ability. Disseminated melanoma cells arise in early stages of the cancer development, often before the primary tumor diagnosis, and spread through blood or lymphatic vessels residing in lungs and in other places of the body which are hard to predict given any certain case of the disease. Besides, melanoma cells are characterized by well-developed repair system and high redioresistance which makes it exceptionally difficult for the common tumor therapy as well as external beam irradiation to be applied.

Melanoma is not an uncommon type of cancer and the number of new cases of melanoma has tended to rise each year. The higher risk of melanoma development occurs in fair skinned persons. This cancer is most wide-spread among white inhabitants of Australia.

As it happens to any cancer, the results of the treatment often depend on the stage of the tumor progression. Thus, diagnostics plays one of the primary roles. The vast majority of the presented cancer diagnostic has proven to be non-effective for melanoma, because they are unable to differentiate malignant cancer from non-malignancies of the skin. Radioisotope diagnostic seems to be more accurate. Today the method of choice for melanoma therapy is chemotherapy, but it allows to obtain the remission in 20% of the cases only. Immunotherapy as well as radioimmunotherapy seem to be alternative methods, however, at the present time they are in the stage of development.

Our experiments were based on the fact that melanoma cells contain pigment melanin which possesses high binding affinity to some polycyclic compounds, particularly phenothiazine derivatives. One of them, 3,7-(dimethylamino)-phenazathionium chloride, or methylene blue (MTB), seems to be useful in clinical application due to its low general toxicity. It is widely useful for clinical application with a respective dose equal to 1-4 mg/kg of body weight per day. The idea to investigate radionuclide in complex with MTB belongs to English scientists. Some works that they have presented confirm high affinity of MTB to the pigmented melanoma cells, and show encouraging results. The topics becomes very urgent if to take into consideration an existing demand in a radiopharmaceutical of this kind.

First our experiments were aimed at studying the therapeutic efficacy of the ^{211}At-tellurium colloid towards EAC cells *in vivo*. Experiments with human melanoma were aimed at obtaining a direct quantitative evaluation of *in vitro* damage induced in pigmented melanoma cells and non-pigmented normal cells. The distinct question was to compare the survival of cells after treatment with ^{211}At and ^{211}At-MTB, and to compare the accumulation levels of these compounds in the cells. Experiments *in vivo* were proposed to obtain qualitative results of accumulation of MTB and its kinetics in complex with iodine isotopes. The choice of the iodine is caused by the reasons of: 1) the most worked out methods of usage of this isotope; 2) close biochemical features of iodine and astatine; 3) a possibility of iodine application in diagnostic and treatment of large tumors of pigmented melanoma.

Experimental part

^{211}At and ^{211}At-MTB production

^{211}At was produced by the ^{209}Bi(α,2n)^{211}At reaction on U-200 cyclotron in Laboratory of Nuclear Reactions, JINR, Dubna. Today it is the most suitable way of the astatine production for the experimental work because of a high purity grade of the produced isotope. Another possible production process via proton irradiation of tritium target (^{232}Th(p,xn)^{211}Rn) with separation of ^{211}At from radon isotopes seems to be not useful for medical application because of high contamination with the neighboring radioisotope ^{210}At ($T_{1/2}$ = 8.3 h). Maximum activity yield achieved was about 400 kBq.

^{211}At sorbtion on tellurium crystals (20-25 mkm diameter) was passed in HNO_3 solution during 2-3 min. Then tellurium particles were washed with NaCl solution and injected into the mice in this form.

Binding of ^{211}At to methylene blue was carried out through electrophylic exchange.

Investigations of ^{211}At-Te colloid at EAC cells in vivo

^{211}At adsorbed by tellurium particles was administered into the peritoneal cavity of mice 2 days after the intraperitoneal injection of $1x10^7$ ascitic cells. At the same time different number of EAC cells (from 10 to 10^7) were implanted into control mice. The life and death rate of control and experimental animals was determined, which allowed survival of radiation-affected EAC cells to be calculated in our model.

The results show that mice with transplanted ascitic tumors had longer life after intraperitoneal injection of 0.1-1.5 MBq of ^{211}At-Te colloid (see table). 25-30% of mice were cured after injection of 1.5-2.0 MBq. Autopsy of cured mice after 3 months did not show either ascites or large tumors.

Table. Influence of ^{211}At-Te activity on the mean life rate and survival of mice with EAC.

^{211}At activity, MBq	Number of animals	Mean survival, days	Number of cured animals
0.10	10	16.6	0
0.18	10	22.2	0
0.30	10	25.6	0
0.74	7	33.4	0
1.5	7	51.0	2
2.0	6	46.8	3
Control	40	14.6	0

We think that ^{211}At is not excreted from the peritoneal cavity because of the large size of the tellurium particles and remains in contact with tumor cells for all its decay time. As we suppose, some of the tumor cells could avoid contact with ^{211}At-Te particles. In the experiments the cell irradiation intensity depended only on the ^{211}At concentration in the medium surrounding the cells.

Experimental approach to human melanoma therapy

Experiments were carried out on pigmented Human melanoma BRO and Chinese hamster V-79 fibroblasts. Both cell lines were incubated in standard conditions.

To study the accumulation of ^{211}At and ^{211}At-MTB melanoma cells were plated and grown as monolayer during 2 days, and after that ^{211}At-MTB as well as ^{211}At in ionic form were injected with activity of 18,5 kBq/ml. The activity accumulated by cells was measured in different time after injection. The results are presented on fig. 1.

The maximum accumulation of ^{211}At-MTB by melanoma cells occurs in 2 h after injection and is two times higher than that of non-pigmented cells. At the same time ^{211}At in ionic form is accumulated by both cell lines in similar and insignificant way.

The effectiveness of ^{211}At and ^{211}At-MTB treatments was evaluated by cells clonogenic ability with the aid of method proposed by T.T. Puck and P.I. Marcus. Cells maintained as monolayer were resuspended and plated into the fresh medium. After 10 or 24 hours cells were incubated in medium containing various radioactive concentrations -

from 0 to 370 kBq/ml of ^{211}At and ^{211}At-MTB for 3 h. Non-toxic concentration of MTB was estimated to be about 5 mg/ml which limits the injection of the compound. Control incubations were carried out with all conditions kept the same except for radiation injections. After that flasks were washed for three times and cells were allowed to proliferate in a fresh medium for 8 to 10 days. Mature colonies were fixed by 10% formalin solution and dyed with methylene blue. The number of grown clones was calculated manually. Cells survival was estimated as correlation:

[plating efficiency in the experiment] / [plating efficiency in control],

where [plating efficiency] is defined as correlation of a number of surviving cells to that have been plated.

Treatment with ^{211}At and ^{211}At-MTB (results were presented on dose-survival curves, fig. 2) shows considerable decrease of survival of melanoma cells after ^{211}At-MTB injections. The dose modifying factor (DMF), defined as correlation of equal activities of ^{211}At and ^{211}At-MTB, was estimated close to 30. The dose, required for 37% cells survival is about 4.8 kBq/ml of medium.

At the same time the Chinese hamster cells survival after the ^{211}At and ^{211}At-MTB treatment shows mean value of dose modifying factor 2 (fig. 3), since dose decreasing survival of the cells was 44.4 kBq/ml. Observed differences in non-pigmented cells survival may be attributed to negligible uptake of radioactive MTB by these cells. The survival of cells after treatment with ^{211}At in ionic form was similar (and one order of magnitude higher) for each cell type.

In general terms, the presented experiments on both cell lines shown obvious difference between ^{211}At and ^{211}At-MTB influence on normal and pigmented cells survival. The results let us to report one order of magnitude lower cell survival after ^{211}At-MTB injection on pigmented melanoma cells as compared to normal fibroblasts.

Preliminary experiments with iodinated MTB in vivo were carried out on white rats and black mice. ^{131}I-MTB was injected into the tail vein of the animals. The first experiment was carried out on healthy animals, the last - on the tumor bearing mice at the 9th-11th day after tumor transplantation. In some experiments the thyroid gland was blocked by previous injection of KI solution. At different points of time since the injection the treated mice were sacrificed and a radioactivity of each organ was calculated.

The results show rapid accumulation of radioiodinated methylene blue practically in all tissues and organs (fig. 4).

Rapid excretion of the compound from all the organs was observed during first 24 h. However, its accumulation in tumor was maximal in 24 h and stayed at a high level at least first 2 days after the injection. We have not the possibility to observe the pharmacokinetics for a longer time in a case of absence of a large amount of tumor-bearing animals in one experiment.

The obtained results allow to affirm that ^{211}At-MTB is capable to act selectively, damaging melanoma cells with selective accumulation in pigmented cells. Thus, the MTB tagged ^{211}At can be regarded as an affective adjuvant aimed at preventing the metastatic process, in the complex therapy of disseminated melanoma. For diagnostic of the melanoma ^{123}I seems to be quite suitable; as for the treatment, well-known isotopes ^{131}I and ^{125}I, β-emitters, and the ^{211}At, an α-emitter, also proves to be curative.

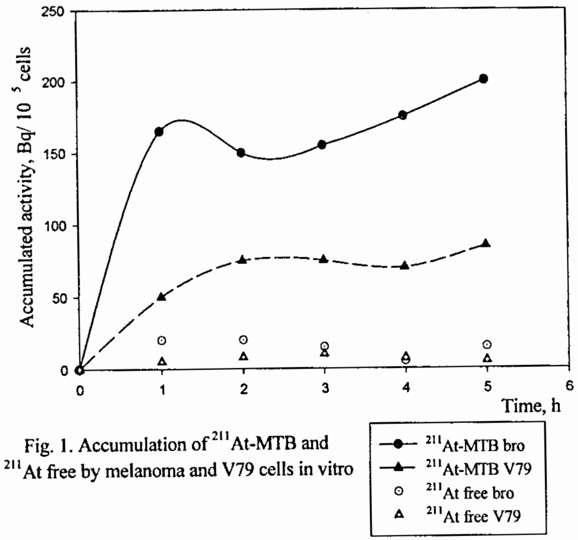

Fig. 1. Accumulation of ^{211}At-MTB and ^{211}At free by melanoma and V79 cells in vitro

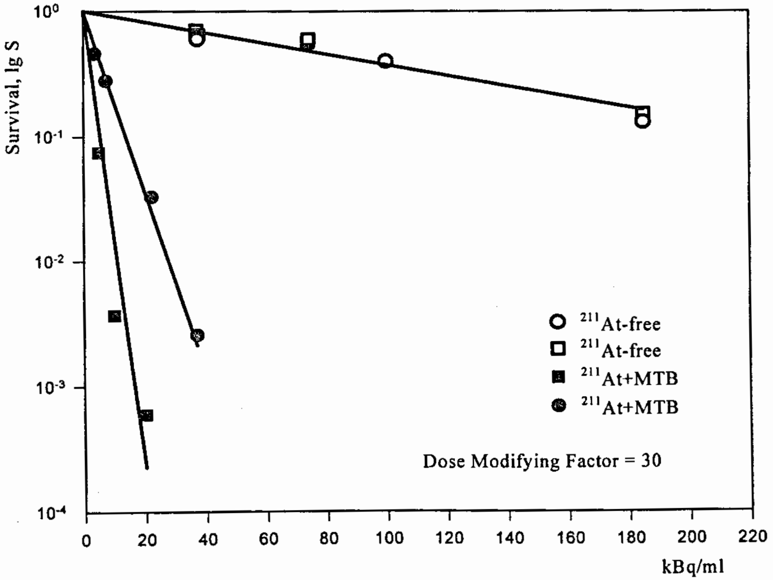

Fig. 2. Survival of human melanoma cells after in vitro ^{211}At and ^{211}At-MTB irradiation

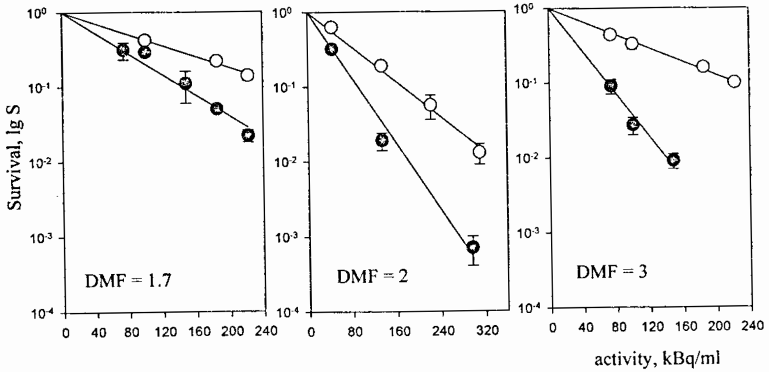

Fig. 3. Survival of non-pigmented fibroblasts after ^{211}At-MTB and ^{211}At free treatment in vitro

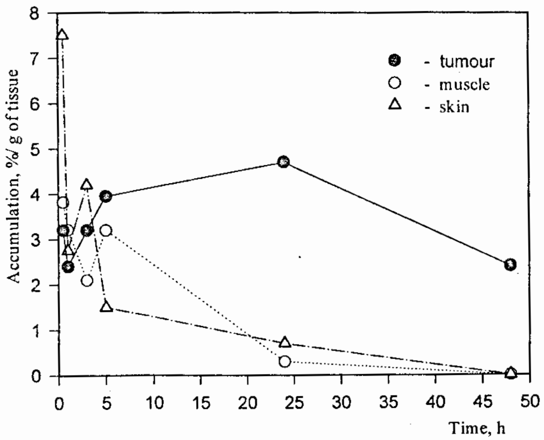

Fig. 4. Accumulation of ^{131}I-MTB in tissues of tumor-bearing animals

Conclusions

The results illustrate possibilities of ^{211}At α-radiation in radiotherapy of the tumors application.

^{211}At adsorbed on tellurium particles proves to be curative in the treatment of cavitary cancers, particularly, of Ehrlich ascitic carcinoma.

Compounds based on methylene blue (MTB) seem to be perspective in diagnostics and treatment of pigmented melanoma. The accumulation of ^{211}At-MTB compound in pigmented melanoma cells *in vitro* is two times higher than its accumulation in non-pigmented cells. The results obtained after the ^{211}At-MTB treatment *in vitro* show one order of magnitude higher treatment efficiency on pigmented melanoma cells relative to normal cells, while action of ^{211}At-MTB irradiation on normal non-pigmented cells was practically non-effective. The experiments *in vivo* show rapid excretion of ^{131}I-MTB from all tissues, while an observed accumulation of the compound in pigmented melanomas is high enough during at least first 24 hours.

Thus, we suggest a possibility of *^{211}At-MTB* application in targeted therapy of some types of cancer (i. e. ascitic carcinomas or pigmented melanoma). The present work confirms this possibility with qualitative and quantitative results and promotes further experimental projects in this field of research.

References

1. *Wheldon T.E.* Targeting Radiation to Tumours, Int J Radiat Biol, 1994, V. 65, № 1, P.109-116
2. *Vaidyanathan G., Zalutsky M.R.*, Targeted Therapy Using Alpha-emitters, Phys Med Biol, 1996, 41, P. 1915-1931.
3. *Brown I.* At-211: Its possible applications in cancer therapy, Appl Rad Isot, 1986, 37, № 8.
4. *Amaldi U., Larsson B., Lemoigne Y.*(editors), Advances in Hadrontherapy, Proceedings of the Int. Week on Hadrontherapy, Archamps, France, 1995, and of the 2nd International Symposium on Hadrontherapy, PSI and CERN, Switzerland, 1996, Elsevier Science B.V., 1997.
5. *Hoefnagel C.A.* Role of nuclear medicine in melanoma, Eur J Nucl Med, 1998, Vol. 25, № 11, Nov.
6. *Link E.M., Lukewicz S.* A new radioactive drug selectively accumulating in melanoma cells, Eur J Nucl Med, 1982, 7.
7. *Link E., Blower P.J., Costa D.C., Lane D.M., Lui D., Brown R.S.D., Ell P.J., Spittle M.F.* Early detection of melanoma metastases with radioiodinated methylene blue, Eur.J.Nucl.Med., 1998, 25(9), P. 1322-1329.
8. *Puck T.T., Marcus P.I.* Action of X-rays on mammalian cells, J Exp Med, 1956, 103.

MAGNETO-OPTICAL CHARACTERISTICS OF HUMAN SERUM

M. SURMA, Optics Laboratory,Institute of Physics,A.Mickiewicz University
Poznań, Poland

Summary

The magneto-optical circular birefringence of human serum is presented in the work. The serum samples investigated came from 50 disease patients. The patients were clinically diagnosed with: rectal cancer, prostate cancer, ovarian cancer, brest cancer, plasmocytoma, sarcoma and 12 of these patients were in clinical observation within a period of 3-12 months. Blood serum samples of these patients and 23 qualified blood donors have been analysed by the high magnetic field circular birefringence effect. Results of high magnetic field -induced circular birefringence in serum proved an unquestionable indication of disease development.

The intra-centrifuged blood is optically active. Apart from its natural optical activity (NOA), the serum shows the magneto–optical circular birefringence (MOCB) induced by the magnetic field **B**. The induced circular birefringence rotation α of the light polarization plane is a superposition of the linear (B), quadratic (B^2) and cubic (B^3) field dependent terms. In a magnetic field of high intensity (B>10 Tesla) the natural rotation $\alpha_o(0)$ in a chiral medium (serum) becomes quadratic (B^2) field dependent. The quadratic field dependent rotation in serum might be recognized as a quantitative oncological marker.

PATIENTS AND METHOD

For all disease patients whose serum samples were subjected to magneto–optical studies their individual medical treatment results were monitored at the Greater Poland Cancer Center. The patients with malignant cases were under clinical observation for 3-12 months. Clinical response to treatment was evaluated on the basis of physical examination; blood tests, serum markers, X–ray, Ultrasonography or CT–computed tomography. The study of the MOCB effect was performed at the Adam Mickiewicz University , Optics Laboratory.

The total rotation of the light polarization plane in a chiral medium (serum) is $\alpha^{\uparrow\uparrow}$ for the parallel configuration $[(\mathbf{B}//\mathbf{k})]$ and $\alpha^{\uparrow\downarrow}$ for the antiparallel $[(-\mathbf{B}//\mathbf{k})]$ configuration of **B** and **k**. The light polarization planes of the beams $\alpha^{\uparrow\uparrow}$, $[(\mathbf{B}//\mathbf{k})]$, and $\alpha^{\uparrow\downarrow}$, $[(-\mathbf{B}//\mathbf{k})]$, leaving the medium with $a>0$, $b>0$, $c>0$ are rotated, respectively by(1):

$$\alpha^{\uparrow\uparrow} = (aB + bB^2 + cB^3 + \ldots)L, \qquad (1)$$
$$\alpha^{\uparrow\downarrow} = (-aB + bB^2 - cB^3 + \ldots)L.$$

In eqs.1 the term cB^3 describes the non-linear Faraday effect, the term bB^2 is a measure of the change of NOA of the chiral medium in magnetic field(2,3,4), the term aB is the linear Faraday effect, and L is the length of the chiral medium subjected to the magnetic field induction **B** vector and **k** light propagation vector, $\mathbf{k}//\mathbf{L}$. The natural rotation $\alpha_o(B=0)\equiv \alpha_o$ is not introduced in eqs.1.

Any change in the a, b and c coefficients of the chiral medium investigated i.e. serum, can be an indicator of structural deformation/mutation of the chiral molecules (proteins) and/or as an indicator of the process leading to an increase in the number (density) of structurally defected chiral molecules (proteins) with respect to the values corresponding to standard metabolism.

Among 85 samples investigated(5,6), 50 came from cancer patients and 23 from patients recognized as perfect blood donors. From the group of 50 patients the magneto-optical measurement were performed for 12 patients again, after several months, in order to detect changes (if any) of the magneto-optical coefficients a, b

and *c* values of their serum. Measurements were performed in strong pulse magnetic fields up to $B\cong30$ Tesla and laser light beam of the wavelength of λ=488nm. All of the serum samples subjected to the *B* magnetic field and the electromagnetic field of the laser beam were placed in cells of L=5mm in length. Detailed description of the experimental set-up is given in paper[1)]. The magneto-optical circular birefringence per unit path length according to eqs.1, can be expressed in the units of *a, b, c* coefficients:deg T^{-1} m^{-1}, degT^{-2} m^{-1} and deg T^{-3} m^{-1}, respectively. The effects of the quadratic magnetic field-induced circular birefringence (bB^2L) and non-linear Faraday (cB^3L) rotation in a chiral medium i.e. serum are clearly observed[1)] for $B>10$ Tesla. The NOA (natural circular birefringence α_o of the investigated serum samples: L=5mm) was measured by the classical method with an accuracy of ±0.01 degree and expressed in deg m^{-1} (degrees in arc of rotation related to 1m of thickness of a serum sample). The error in the determination of coefficients *a, b* and *c* is ±0.5%, ±2% and ±10%, respectively[2)]. For all of the serum samples investigated, their NOA was positive, $\alpha_o>0$. In order to calculate MOCB effect in degrees of rotation: $\alpha(B) = aBL$, $\alpha(B^2) = bB^2L$ and $\alpha(B^3) = cB^3L$ the values of *a, b, c* given in Tables I - IV are to be multiplied by $2\cdot10^2$ for $L = 1$m.

RESULTS

MOCB of serum from qualified donors

Blood serum samples from qualified donors of blood for transfusion were subjected to magneto-optical studies in order to determine the *a, b, c* coefficients and α_o of their serum to be used as reference. The results of the measurements for exemplary 8 samples are displayed in Table I. The serum samples from these 8 donors are characterized by positive natural optical activity ($\alpha_o>1$) and positive values of *a, b* and *c* magneto-optical coefficients. So, the sings of α_o, *a, b* and *c* are the same as those observed for dextrorotatory chiral mirror image molecules[4)]. From the data given in the Table I we notice that the values of coefficient *a* do not differ from one another by more then a few percent. These results indicate that the *a* coefficient (linear Faraday effect) is not very sensitive to the change of molecular structure of serum (proteins). On the other hand, the values of *b* and *c* coefficients are more scattered. However, the observed scatter of results of *b* and *c* values could

serum samples investigated. The differences between *b* and *c* values have no correlation to the *Rh*-identification of the blood (Table I).

MOCB of Serum From Rectal Cancer Patients

The data presented in Table II, for exemplary 3 rectal cancer patients, indicate the changes of the α_o and *a, b, c* magneto-optical coefficents within the time of the patient medical control.

For the rectal cancer patient (Table II; No.1), the magneto-optical studies gave $\alpha_o>0$, $b<0$, $c>0$ on Oct.1st,1996, while his serum marker determination was CEA:452ng/l (carcinoembryonic antigen). After radiation treatment (Feb.13th, 1997) CEA marker dropped to 195 and magneto–optical analysis of serum gave: $\alpha_o>0$, $b>0$, $c>0$. Medical report stated a considerable improvement of the patient health. Four months later, on June 12th, 1997 the results of the magneto-optical study were $\alpha_o>0$, $b<0$, $c<0$, and the CEA marker value of 375. Medical report stated a significant deterioration of the patient health. The correlation between the changes in *a, b, c* coefficients and the medical examination results is obvious. A similar correlation between the medical diagnosis and MOCB patient serum studies was noted for patient No.2, Table II, with recognized rectal cancer (Feb.24, 1997). On June 11, 1997, after 4 months therapy, a significant decrease in *b* and *c* coefficients was noted which signalled unsuccessful response to the therapy confirmed by the marker determination (CEA:7.9). The magneto-optical coefficients *a, b, c* of the serum of the patient with rectal cancer (Table II; No3) also well correlate to the medical diagnossis.

MOCB of Serum from Cancerous Patients: Prostate Cancer, Ovarian Cancer, Testicular Cancer and Sarcoma, Plasmocytoma

The data in Table III present medical diagnosis and the MOCB, NOA results for cancer patients serum. The patient No.1 (Table III) was diagnosed with prostate cancer and patients: No 2, 3, 4 with ovarian cancer, sarcoma with distant metastases and plasmocytoma, respectively. The results presented indicate a very good correlation between the medical diagnosis and the data of the proposed method of quantitative physical identification of malignant disease expressed as a correlation between the medical marker (patients 1 and 2) and the b coefficient value. The results of magneto-optical measurements of serum samples presented in Table IV; patients 1, 2, 3, 4 gave $b<0$ and $\alpha_o/b<0$.

DISCUSSION

For all the patients investigated their MOCB's are displayed as a quantitative relation between the value of α_o/b parameter versus b coefficient value observed for healthy (Fig.1A), recovered (Fig.1B) and unrecovered patients (Fig.1C). The data presented in Tables II and III illustrate the changes in the α_o, a, b and c values in the time of 3 to 12 months when the patient's status was under control. These changes were characterized by the NOA, (α_o), and the MOCB, (a, b, c) structure of the blood serum of cancer cases.

As follows from the data given in Tables II, III and IV, results of the magneto-optical analysis of blood serum of the patients are very sensitive indicators of a change in the health status. Fig.1.A, presents an exemplification of the b coefficient ($b>0$) and α_o/b values of the qualified donors. Moreover, an increase from $b<0$ to $b>0$ in the value of magneto-optical coefficient b characterizing the serum of cancer patient (Fig.1.,B) indicates an improvement in the patients' health and a successful, ($b>0$), medical treatment. On the other hand, a decrease in the value of b coefficient on a series of subsequent tests, ($b<0$), indicates the deterioration of the patient's health (Fig.1.,C) and progress of the disease. On the basis of the results of magneto-optical studies and their comparison with the outcome of medical tests and diagnoses we can put forward a thesis that the results of b coefficient measurements are indicative of the health status and presence of a malignant disease. These findings are clearly demonstrated by the data of Tables II, III and IV .

CONCLUSION

The fact that MOCB effect measurement in human blood serum may provide the information regarding cancer (malignant disease) presence and development and serve for early diagnosis of cancerous changes. The results of this study showed that human blood serum chirality α_o is positive while the quadratic magnetic

TABLE I

The NOA α_o and values of MOCB a, b, c coefficients characterizing serum from qualified donors

No	α_o (deg m^{-1})	a (degT^{-1}m^{-1})	$b\cdot10^3$ (degT^{-2}m^{-1})	$c\cdot10^5$ (degT^{-3}m^{-1})	$(\alpha_o/b)\cdot10^{-5}$ (T^2)	Rh (identification)
1	56	1.66	0.08	13.1	7.00	0/+
2	61	1.62	0.1	8.0	6.10	A/–
3	66	1.63	0.25	15.2	2.64	A_1/+
4	58	1.69	0.32	3.8	1.81	0/+
5	75	1.62	0.83	8.8	0.90	B/+
6	57	1.67	0.95	2.9	0.60	A_1/+
7	62	1.63	1.0	6.0	0.62	0/–
8	49	1.64	1.5	10.0	0.32	AB/–

TABLE II

The MOCB *a*, *b* and *c* coefficients, NOA α_o of serum from rectal cancer patients under long period of medical treatment

No/ Medical control data	Medical diagnosis	Serum marker (ng/ml)	α_o (deg m^{-1})	*a* (deg$T^{-1}m^{-1}$)	$b \cdot 10^3$ (deg$T^{-2}m^{-1}$)	$c \cdot 10^5$ (deg$T^{-3}m^{-1}$)	$\alpha_o/b \cdot 10^{-5}$ (T^2)
1 Male 01.10.96.	Rectal cancer −after operation Local recurrence of disease in course of radiation treatment	CEA:452	72	1.68	−1.37	14.0	−0.53
13.02.97.	Partial remission after radiation treatment	CEA:195	60	1.66	0.80	5.59	0.75
12.06.97.	Local progression of the disease	CEA:375	65	1.60	−0.90	−0.65	−0.72
2 Male 24.02.97.	Rectal cancer with primary tumor after radiotherapy	CEA:3.3	72	1.63	0.76	0.8	0.95
11.06.97.	Local progression of the disease	CEA:7.9	59	1.56	−1.3	−1.8	−0.45
20.09.97.	Local progression	CEA:5.0	66	1.56	−2.0	15.0	−0.33
3 Female 06.03.97.	Rectal cancer after operation and radiation treatment with complete remission	CEA:1.0	64	1.64	−0.99	−9.5	−0.65
21.05.97.	Breast cancer[a] treated with hormonotherapy[b]	−	67	1.60	−0.70	0.76	−0.96

CEA −Carcinoembryonic Antigen

[a] Seen by the MOCB method earlier then by the traditional medical treatment

[b] Non marker control

TABLE III

The MOCB *a*, *b*, *c* coefficients, NOA α_o characterizing serum of cancerous patients: prostate cancer, ovarian cancer and sarcoma, plasmocytoma under a long period of medical treatment

No/ Medical control data	Medical diagnosis	Serum marker (ng/ml)	α_o (deg m^{-1})	*a* (deg$T^{-1}m^{-1}$)	$b \cdot 10^3$ (deg$T^{-2}m^{-1}$)	$c \cdot 10^5$ (deg$T^{-3}m^{-1}$)	$(\alpha_o/b) \cdot 10^{-5}$ (T^2)
1 Male 29.10.97.	Prostate cancer −treated with hormonotherapy	PSA:27.6	54	1.62	−0.13	−5.0	−4.2
10.12.97.	Progression	PSA:29	69	1.65	−1.6	−10.0	−0.43
2 Female 24.09.96.	Ovarian cancer after operation	Ca−125:1.4	65	1.63	−0.80	2.98	−0.81
29.10.97.	After chemotherapy	Ca−125:4.6	72	1.64	−1.33	1.2	−0.54
3 Female 02.10.96.	Sarcoma after operation and radiation Local progression - disease treated with short course of radiotherapy		65	1.70	0.89	17.6	0.73
12.02.97.	Distant metastases		78	1.67	−1.13	7.82	−0.69
23.10.97.	Stabilization		64	1.65	−0.77	4.0	−0.83
4 Male 25.06.97.	Plasmocytoma treated with chemotherapy	−	68	1.65	−0.39	−9.5	−1.74
23.10.97.	Stabilization	−	71	1.68	−0.75	−12.0	−0.95

PSA −Prostate Specific Antigen
Ca −Cancer antigen

TABLE IV

Summary of the data obtained for patients whose medical records NOA and MOCB investigations were not continued after the first dated clinical diagnosis

No	Medical Record	Medical diagnosis	α_0 (deg m^{-1})	a (degT^{-1}m^{-1})	$b \cdot 10^3$ (deg T^{-2}m^{-1})	$c \cdot 10^5$ (degT^{-3}m^{-1})	$(\alpha_0/b) \cdot 10^{-5}$ (T^2)
1 Female	17.11.95.	Ovarian cancer	65	1.50	–6.00	–30.0	–0.11
2 Female	17.11.95.	Ovarian cancer	69	1.50	–2.72	–16.5	–0.25
3 Male	04.10.96.	Malignant tumor of the submandibular salivary gland	53	1.69	–0.79	18.1	–0.67
4 Male	29.10.97. (CEA:2.4 AFP:4.8 β–hCG:0.3)	Testicular cancer	76	1.65	–1.70	–2.5	–0.45

AFP –Alpha Fetoprotein
β–hCG –Human Chorionic Gonadotropin

Figure 1. Quantitative relation between the value of the parameter α_0/b and the B^2 –induced circular birefringence coefficient b.

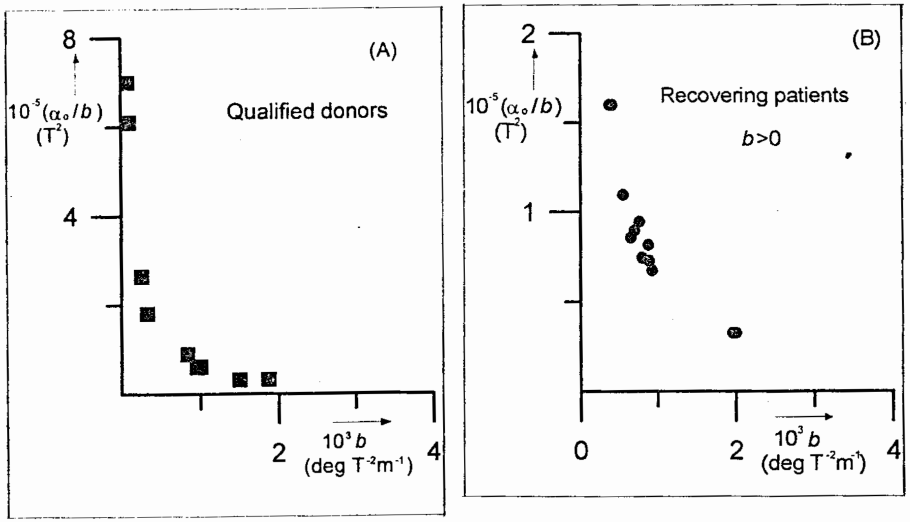

Figure 1A. Donors of blood for transfusion: b>0.

Figure 1B. Recovering patients: b>0.

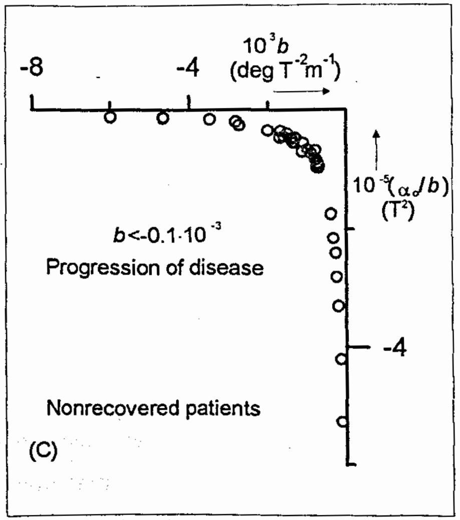

Figure 1C. Nonrecovering patients: b<0.

field–induced circular birefringence bB^2L of the serum strongly depends on the health status of man.The quadratic magnetic field–induced circular birefringence of serum of healthy man is observed as positive, while it is negative in the serum of the malignant cases. Also, the observed non-linear (B^3) Faraday effect in human blood serum is correlated to the health status. Both, the induced–quadratic magnetic field and the non-linear Faraday circular birefringences, directly indicate the progression and/or regression of the disease status. The magneto–optical analysis of a human blood serum should be recognized in the near future as a useful monitoring technique of the man health condition and the magneto-optical coefficient *b* might be recognized as a quantitative oncological marker.

The test requires a small volume of blood serum ca 0.5ml. High threshold of detectability of the quadratic magnetic field–induced circular birefringence is corresponding roughly to the presence of 10^{15} chiral biopolymers (+) or (–) in the volume of the laser beam. The values of the coefficient *b* recorded by the MOCB method are determined by the characteristics of the structure of biopolymers, e.g. proteins in blood serum.

REFERENCES

1) Surma, M. Magneto–optical circular birefringence of a chiral medium in high magnetic field. Molec. Phys. **90**, 993–997(1997).

2) Surma, M. Experimental evidence of the B^2 and B^3 dependent circular birefringence of chiral molecules in high magnetic fields. Molec. Phys. **93**, 271–278 (1998).

3) Zawodny, R., Woźniak, S. and Wagnière, G. On quadratic dc magnetic field–induced circular birefringence and dichroism in isotropic chiral media. Molec. Phys. **91**, 165–172 (1997).

4) Surma, M. Correlation between quadratic magnetic field induced birefringence and the natural optical activity of chiral media. Molec. Phys. **96**, 429–433 (1999).

5) Surma, M., Bućko, J., Bąk, G., Ciszek, M. Magneto-optical characteristics of human serum. Acta Phys.Polon. A **98**, 533-542 (2000).

6) Marian Surma, Jerzy Bućko, Grażyna Bąk , Mariusz Ciszek Natural and high magnetic field induced optical activity of human serum. Polish J Med.Phys&Eng **7**,No 1, 25-33 (2001).

7) Miura, N., Asaka. N., Shinyashiki, N. and Mashimo, S. Microwave dielectric study on bound water of globule proteins in aqueous solution. Biopolimers. **34**, 357–367 (1994).

8) Bohr, J., Bohr, H.G. and Brunak, S. The formation of protein structure. Europhysics News **27**, 50–54 (1996).

LIST OF PARTICIPANTS

Bronislaw Arcimowicz
Poznan University of Technology,
Piotrowo 3, 60-965, Poznan, Poland.
Tel. +48-61-665-23-32
Fax:
E-mail: arcimow@phys.put.poznan.pl

Zdzislaw Blaszczak (Chairman)
Division of Optics
Faculty of Physics, Adam Mickiewicz University,
ul. Umultowska 85, 61-614 Poznan, Poland.
Tel: +48-61-827-30-03
Fax: +48-61-825-77-58
E-mail: zetbe@main.amu.edu.pl

Alfred Budziak
Institute of Physics
30-059 Krakow, Poland
Tel: +48-12-633-63-77
Fax: +48-12-33-84-94
E-mail: fred@castor.if.edu.pl

Paul Campbell
Department of Physics and Astronomy, University of Manchester,
Schuster Laboratory, Brunswick St., Manchester M13 9PL, UK.
Tel: +44-161-275-4157
Fax: +44-161-275-5509
E-mail: pc@mags.ph.man.ac.uk

S.Chojnacki
Institute of Physics, Pedagogical University of Kielce,
ul. Konopnickiej 15, 24-406 Kielce, Poland.
Tel./Fax: +48-41-362-64-52
Heavy Ion Laboratory, Warsaw University
Poland, 02-097 Warsaw, Pastuera 5A
Tel:+48-22-822-21-23 ; +48-22-658-20-21
Fax: +48-22-659-27-14
E-mail: schojn@pu.kielce.pl

Miroslaw Drozdowski
Institute of Physics, Poznan University of Technology,
Piotrowo 3, 60-965, Poznan, Poland.
Tel: +48-61-878-25-97
Fax: +48-61-878-23-24
E-mail: mirdrozd@phys.put.poznan.pl

David Forest
University of Birmingham
Edgbaston, Birmingham
B15 2TT , United Kingdom
Tel: +44-121-414-4580
Fax: +44-121-414-4577
E-mail: D.H.FOREST@BHAM.AC.UK

Boguslaw Furman
Chair of Atomic Physics,
Poznan University of Technology,
Poznan, Poland.
Tel: +48-665-28-34
Fax: +48-665-21-00
E-mail: furman@phys.put.poznan.pl

Iouri Gangrsky
Flerov Laboratory of Nuclear Reactions, JINR,
Joliot Curie str.6, 141980 Dubna, Moscow Region, Russia.
Tel: +7-09621-64896
Fax: +7-09621-65-083, +7-09621-65-599
E-mail: gangr@cv.jinr.ru

Agnieszka Gluzicka
Faculty of Physics, Warsaw University
Hoza 69, 00-681 Warsaw, Poland
Tel: +48-022-554-62-04
Fax: +48-022-625-64-06
E-mail: gluzicka@nor.slej.uw.edu.pl

Marek Halas (secretary)
Division of Optics
Faculty of Physics, Adam Mickiewicz University,
ul. Umultowska 85, 61-614 Poznan, Poland.
Tel: + 48-61-827-30-08
Fax: +48-61-825-77-58
E-mail: halas@main.amu.edu.pl

Harry Hühnermann
Fachbereich Physik, Marburg University
Renthof 7 Str.
D-35041 Marburg, Germany
Tel: +49-6421-282-41-53
Fax: +49-6421-32163 (private fax + phone)
E-mail: huehnermann@Physik.Uni-Marburg.De

Igor Izosimov
V.G.Khlopin Radium Institute
194021 St. Petersburg, 2 Murinski av.28, Russia
Tel: +7-812-247-80-95
Fax: +7-812-247-80-95
E-mail: izosimov@atom.nw.ru

Iwona Iwaszkiewicz-Kostka (secretary)
Division of Optics
Faculty of Physics, Adam Mickiewicz University,
ul. Umultowska 85, 61-614 Poznan, Poland.
Tel: + 48-61-827-30-08
Fax: +48-61-825-77-58
E-mail: kostka@main.amu.edu.pl

Andrzej Jarosz
Chair of Atomic Physics, Poznan University of Technology,
Poznan, Poland.
Tel: +48-665-28-34
Fax: +48-665-21-00
E-mail:

Michal Kaczmarek
Division of Optics
Faculty of Physics, Adam Mickiewicz University,
ul. Umultowska 85, 61-614 Poznan, Poland.
Tel: + 48-61-827-31-08
Fax: +48-61-825-77-58
E-mail: asan@main.amu.edu.pl

Ryszard Kaluski
Division of Optics
Faculty of Physics, Adam Mickiewicz University,
ul. Umultowska 85, 61-614 Poznan, Poland.
Tel: + 48-61-827-31-08
Fax: +48-61-825-77-58
E-mail: asan@main.amu.edu.pl

F. Karpeshin
St. Petersburg State University
St. Petersburg, Russia
Tel: +7-812-428-44-96
Fax: +7-812-428-42-70
E-mail: karpesh@nuclpc1.phys.spbu.ru

Aleksandra Leliwa-Kopystynska
Institute of Experimental Physics, Warsaw University,
Hoza 69, 00-681 Warsaw, Poland.
Tel: +48-22-55-32-346, 621-09-85
Fax: +48-22-625-64-06
E-mail: akopyst@fuw.edu.pl

Polina Kutsalo
Department of Radiation and Radiobiological Research
OU&U, JINR
141980 Dubna, Russia
Tel: + 7-09621-658-96
Fax: +7-09621-655-99
E-mail: polina@cv.jinr.ru

Boris Markov
Flerov Laboratory of Nuclear Reactions, JINR,
Joliot Curie str.6, 141980 Dubna, Moscow Region, Russia.
Tel: +7-09621-64-586
Fax: +7-09621-65-083
E-mail: markov@flnr.jinr.ru.

Gennadi Mishinsky
Flerov Laboratory of Nuclear Reactions, JINR,
Joliot Curie str.6, 141980 Dubna, Moscow Region, Russia.
Tel: +7-09621-63-659
Fax: +7-09621-65-083, (-65-599)
E-mail: laser@bcv.jinr.dubna.ru

Wojciech Nawrocik
Faculty of Physics, Adam Mickiewicz University,
ul. Umultowska 85, 61-614 Poznan, Poland.
Tel. +48-61-827-32-02
Fax: +48-61-825-77-58
E-mail: nawrocik@main.amu.edu.pl

Wiefried Nörtershäuser
GSI Darmstadt
Planchstr. 1, D-64220 Darmstadt
Tel: +49-0-6159-71-2459
Fax: +49-0-6159-71-2785
E-mail: W.Noertershaeuser@gsi.de

Vladimir Perelygin
Laboratory of Nuclear Reactions
JINR, Dubna, Russia
Tel: 09621-62-102
Fax: 09621-65-083
E-mail: pergam@cv.jinr.ru

Yu.E.Penionzhkevich
Flerov Laboratory of Nuclear Reactions, JINR,
Joliot Curie str.6, 141980 Dubna, Moscow Region, Russia.
Tel: +7-09621-64-857
Fax: +7-09621-65-083
E-mail: pyuer@nrsun.jinr.dubna.ru

Jonas Persson
Department of Mathematics and Natural Sciences
University Kristianstad
SE-29188 Kristianstad, Sweden
Tel: + 46-44-203450
Fax: + 46-44-203403
E-mail: Jonas.Persson@MNA.HKR.SE

Brigitte Roussiere
Institut de Physique Nucliare 91406 Orsay, France
Tel: 01-69-15-62-65
Fax: 01-69-15-71-96
E-mail: roussier@ipno.in2p3.fr

Elena Rusakovich
JINR,
141980, Dubna, Russia
Tel: +7-09621-63890
Fax: +7-09621-65599
E-mail: pankova@cv.jinr.ru

Stanislav Sazonov
Kurchatov Institute
Moscow, 123182, Russia
Tel: 095-196-98-91
Fax:
E-mail: zaretsky@imp.kiae.ru

Maxim Seliverstov
Petersburg Nuclear Physics Institute,
188350, Gatchina, Russia
Tel: +7-812-713-60-41
Fax: +7-812-713-60-41
E-mail: MSELIVER@RECO#.PNPI.SPB.RU

Michael Sewtz
University Mainz
J.J.Becher Weg 45, D-55128 Mainz, Germany
Tel: +49-6131-392-51-99
Fax: +49-6131-392-29-46
E-mail: sewtz@kph.uni-mainz.de

Alexander Solnyshkin
Laboratory of Nuclear Problems, JINR,
Joliot Curie str.6, 141980 Dubna, Moscow Region, Russia.
Tel: 62-495, 33943
Fax: +7-09621-65-083, 65599
E-mail:

Ewa Stachowska
Chair of Atomic Physics, Poznan University of Technology,
Poznan, Poland.
Tel: + 48-61-665-23-43
Fax:
E-mail: stachows@phys.put.poznan.pl.

Marian Surma
Division of Optics
Faculty of Physics, Adam Mickiewicz University,
ul. Umultowska 85, 61-614 Poznan, Poland.
Tel: +48-61-827-31-04
Fax: +48-61-825-77-58
E-mail:

Valentin Nesterenko
Flerov Laboratory of Nuclear Reactions, JINR,
Joliot Curie str.6, 141980 Dubna, Moscow Region, Russia.
Tel: +7-09621-63-383
Fax: +7-09621-63-584
E-mail: nester@thsun1.jinr.dubna.ru

A.Wojtasiewicz
Institute of Experimental Physics, Warsaw University,
ul. Hoza 69, 00-681 Warsaw, Poland.
Tel: +48-22-628-30-31 ext.128
Fax: +48-22-625-14-96
E-mail: wojtasie@zfyavs.fuw.edu.pl

Zenon Wozniak
Division of Optics
Faculty of Physics, Adam Mickiewicz University,
ul. Umultowska 85, 61-614 Poznan, Poland.
Tel: + 48-61-827-31-08
Fax: +48-61-825-77-58
E-mail: asan@main.amu.edu.pl

120 р

Научное издание

Application of Lasers in Atomic Nuclei Research. Prospects for the Development of Laser Methods in the Study of Nuclear Matter

Proceedings of the V International Workshop

Применение лазеров в исследовании атомных ядер. Перспективы развития лазерных методов исследования ядерной материи

Труды V международного рабочего совещания

E15-2002-84

Сборник отпечатан методом прямого репродуцирования
с оригиналов, предоставленных оргкомитетом.

Ответственный за подготовку сборника к печати *Б. Н. Марков.*

Обложка *Е. А. Минина.*

ЛР № 020579 от 23.06.97.
Подписано в печать 04.06.2002.
Формат 60 × 90/16. Бумага офсетная. Печать офсетная.
Усл. печ. л. 16,06. Уч.-изд. л. 28,89. Тираж 150 экз. Заказ № 53336.

Издательский отдел Объединенного института ядерных исследований
141980, г. Дубна, Московская обл., ул. Жолио-Кюри, 6.